

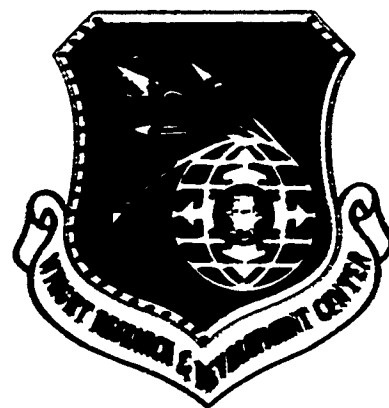
WRDC-TR-90-4125

AD-A237 064



2

LIGHTWEIGHT DISK ALLOY DEVELOPMENT



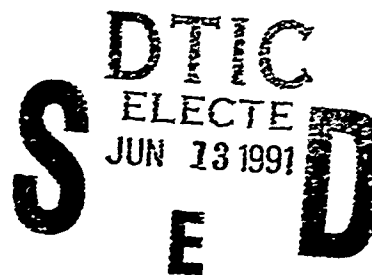
S. M. Russell, C. C. Law and M. J. Blackburn

United Technologies Corporation
Pratt & Whitney
Government Engines & Space Propulsion
P. O. Box 109600
West Palm Beach, FL 33410-9600

P. C. Clapp and D. M. Pease

Institute of Materials Science
University of Connecticut
Storrs, Connecticut 06268

April 1991



Final Report for Period September 1986 — April 1990

Approved for public release; distribution unlimited.

91-01995



**MATERIALS LABORATORY
WRIGHT RESEARCH AND DEVELOPMENT CENTER
AIR FORCE SYSTEMS COMMAND
WRIGHT-PATTERSON AIR FORCE BASE, OHIO 45433-6533**

91 6 12 074

NOTICE

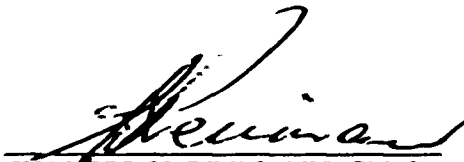
When Government drawings, specifications, or other data are used for any purpose other than in connection with a definitely Government-related procurement, the United States Government incurs no responsibility or any obligation whatsoever. The fact that the government may have formulated or in any way supplied the said drawings, specifications, or other data, is not to be regarded by implication, or otherwise in any manner construed, as licensing the holder, or any other person or corporation; or as conveying any rights or permission to manufacture, use, or sell any patented invention that may in any way be related thereto.

This report is releasable to the National Technical Information Service (NTIS). At NTIS, it will be available to the general public, including foreign nations.

This technical report has been reviewed and is approved for publication.



DANIEL B. MIRACLE, Project Engineer
Materials Development Branch
Metals and Ceramics Division



WALTER H. REIMANN, Chief
Materials Development Branch
Metals and Ceramics Division

FOR THE COMMANDER



NORMAN M. TALLAN, Director
Metals and Ceramics Division

If your address has changed, if you wish to be removed from our mailing list, or if the addressee is no longer employed by your organization, please notify WL/MLLM, WPAFB, OH 45433-6533 to help us maintain a current mailing list.

Copies of this report should not be returned unless return is required by security considerations, contractual obligations, or notice on a specific document.

REPORT DOCUMENTATION PAGE

Form Approved
OMB No. 0704-0188

1a. REPORT SECURITY CLASSIFICATION Unclassified			1b. RESTRICTIVE MARKINGS		
2a. SECURITY CLASSIFICATION AUTHORITY USAF/AFMIL			3. DISTRIBUTION/AVAILABILITY OF REPORT Approved for public release; distribution is unlimited.		
2b. DECLASSIFICATION/DOWNGRADING SCHEDULE					
4. PERFORMING ORGANIZATION REPORT NUMBER(S) FR 21413			5. MONITORING ORGANIZATION REPORT NUMBER(S) WRDC-TR-90-4125		
6a. NAME OF PERFORMING ORGANIZATION UTC, Pratt & Whitney Government Engines & Space Propulsion		6b. OFFICE SYMBOL (If applicable) UTC-P&W		7a. NAME OF MONITORING ORGANIZATION Wright Research and Development Center Materials Laboratory	
6c. ADDRESS (City, State and ZIP Code) P. O. Box 109600 West Palm Beach, FL 33410-9600			7b. ADDRESS (City, State and ZIP Code) Wright-Patterson AFB Dayton, OH 45433-6533		
8a. NAME OF FUNDING/SPONSORING ORGANIZATION Wright Research & Development Center		8b. OFFICE SYMBOL (If applicable) WRDC/MLLM		9. PROCUREMENT INSTRUMENT IDENTIFICATION NUMBER F33615-86-C-5037	
8c. ADDRESS (City, State and ZIP Code) Wright-Patterson AFB Dayton, OH 45433-6533			10. SOURCE OF FUNDING NUMBERS		
			PROGRAM ELEMENT NO. 62102F	PROJECT NO. 2420	TASK NO. 01
			WORK UNIT ACCESSION NO. 76		
11. TITLE (Include Security Classification) Lightweight Disk Alloy Development					
12. PERSONAL AUTHOR(S) S. M. Russell, C. C. Law, M. J. Blackburn, P. C. Clapp and D. M. Pease					
13a. TYPE OF REPORT Final		13b. TIME COVERED FROM 09/15/86 TO 04/15/90		14. DATE OF REPORT (Year, Month, Day) 1991 April 5	
15. PAGE COUNT 223					
16. SUPPLEMENTARY NOTATION					
17. COSATI CODES			18. SUBJECT TERMS (Continue on reverse if necessary and identify by block number)		
FIELD	GROUP	SUB-GROUP	Nickel Aluminide, Ordered Alloys, Intermetallic, Ductility, Disk Alloy, Bond Strength, Simulation of Deformation		
19. ABSTRACT (Continue on reverse if necessary and identify by block number)					
<p>A 3-year program was conducted with the intention of developing NiAl-base alloys with properties suitable for use as a turbine disk material. The program emphasized overcoming the room temperature brittleness problem and enhancing high-temperature strength and creep resistance. Two approaches were utilized to address the room temperature brittleness problem: alloying to change the ordering energy to modify the slip behavior and exploiting a variety of martensitic transformation mechanisms. In order to explore the first approach, ternary additions of Cr, Co, Fe, and V were studied at a variety of NiAl compositions. Both Cr and Co additions modify the room temperature slip behavior of NiAl toward one more favorable with respect to Von Mises criterion. However, a change in slip system alone is apparently insufficient for room temperature ductility. Therefore, this approach requires further study. The martensitic transformation mechanisms in Co-modified NiAl alloys were also studied as a means of overcoming the room temperature brittleness problem. The mechanisms of stress-induced martensite, nucleation of additional martensitic variants under stress, and rearrangement of twin lamellae within existing martensitic variants were all beneficial and enhance the room temperature ductility and toughness. Room temperature ductility and fracture toughness values as high as 2.2% and 33 MPa\sqrt{m}, respectively, were directly attributable to the operation of martensitic transformation mechanisms in these alloys. In addition to the alloy development studies, this program contained fundamental studies of the atomic bond characteristics of B2 compounds as well as computer simulation of flow and fracture of stoichiometric NiAl.</p>					
20. DISTRIBUTION/AVAILABILITY OF ABSTRACT <input type="checkbox"/> UNCLASSIFIED/UNLIMITED <input type="checkbox"/> SAME AS RPT. <input checked="" type="checkbox"/> DTIC USERS			21. ABSTRACT SECURITY CLASSIFICATION Unclassified		
22a. NAME OF RESPONSIBLE INDIVIDUAL D. B. Miracle			22b. TELEPHONE (Include Area Code) (513) 255-9833		22c. OFFICE SYMBOL WRDC/MLLM

19. ABSTRACT (continued)

The atomic bonding studies were performed on a series of B2 compounds using extended X-ray absorption edge fine structure (EXAFS) and X-ray absorption near edge spectroscopy (XANES) techniques. Important differences in the bond strengths of the various compounds were noted from the EXAFS results. In particular, the bonding in CoAl as compared to NiAl was much stronger (5 to 7 times) for the second and third nearest-neighbor bonds, while the first nearest-neighbor bond strengths were similar. Further Cr additions to NiAl, which modify the slip behavior, reduce the first nearest-neighbor bond strength while leaving the second nearest-neighbor bonding unchanged, offering a clue for the change in slip behavior. XANES studies of B2 aluminides revealed that CoAl has more charge transfer from the Al atoms to the transition metal atoms than either NiAl or FeAl, indicating greater covalency of the bonding. Finally, in the course of this program, a new technique for EXAFS of major species in bulk samples was developed which eliminates many of the problems associated with conventional EXAFS techniques.

Embedded Atom Method (EAM) computer simulations were conducted on stoichiometric NiAl to determine the flow and fracture characteristics at various temperatures from 0 to 1000K. Lattice energy, surface energy, APB energies, and melting points were determined by the EAM in order to check the validity of the simulation. Much of the flow and fracture simulations were devoted to developing the EAM technique to produce realistic results by utilizing increasingly larger array sizes (up to 9000 atoms), center crack arrays, periodic boundary conditions, and constant strain rate loading. From this work, the fracture plane of NiAl was determined to be (100), a DBTT was observed between 300 and 800K, and the importance of short-range surface diffusion as a crack blunting mechanism was revealed. In addition, a new strategy for recognizing dislocations was created which exploits the unique characteristics of the strain gradient in the vicinity of a dislocation.

Strength characteristics of NiAlCo alloys were studied as a function of phase structures of the types B2, L1₀ and L1₂. The strength of these alloys depended upon a variety of factors, including the B2 phase composition, L1₂-phase (γ) volume fraction and the width of fine twin lamellae within the martensitic phase (L1₀) structures. Selected ternary NiAlCo alloys were subsequently strengthened with either small quaternary additions of Hf (0.5 at/o) and Ti (5 at/o) or with chopped PRD-166 fibers (10 to 15 vol/o). The yield strength was enhanced by Ti additions over a broad temperature range (20°C to 800°C), but by Hf additions only at high temperatures. Unfortunately, these alloying additions, however small, resulted in degradation of the room temperature fracture toughness, indicating practical difficulties in simultaneously achieving strength and ductility through alloying. The compositing approach for strengthening resulted in orientation-dependent strength and stiffness benefits at all temperatures, which could be further improved through better consolidation. Unfortunately, room temperature ductility and fracture toughness were degraded because of a shortening of the fibers during the consolidation process.

TABLE OF CONTENTS

<i>Section</i>	<i>Page</i>
1. INTRODUCTION	1
1.1 Background and Approach	1
1.2 Program Outline	2
1.3 Program Overview	3
2. EXPERIMENTAL	4
2.1 Preparation of Materials	4
2.2 Evaluation of Mechanical Properties	4
2.3 Preparation of Samples for Transmission Electron Microscopy	5
3. PHASE I ALLOYS	6
3.1 Baseline Alloy Selection	6
3.2 Baseline Alloy Results and Discussion	6
3.2.1 Alloy Characterization	6
3.2.2 Tensile Ductility and Strength	6
3.3 Formulation of Modified Alloys	7
3.3.1 Ni-Al-V-Cr System	7
3.3.2 Ni-Al-Fe System	7
3.3.3 Ni-Al-Co System	7
3.3.4 Ni-Al-Ti System	8
3.4 Modified Alloys Results and Discussion	8
3.4.1 Alloy Characterization	8
3.4.2 Compressive Strength	11
3.4.3 Deformability and Tensile Ductility	11
3.4.3.1 NiAlCo Alloys	11
3.4.3.1.1 Deformation Behavior of Alloy A	12
3.4.3.1.2 Deformation Behavior of Alloy B	13
3.4.3.1.3 Deformation Behavior of Alloy C	13
3.4.3.2 NiAlFe Alloys	14
3.4.3.3 NiAl(V, Cr) Alloys	14
3.4.3.4 NiAlTi Alloys	15

TABLE OF CONTENTS (continued)

<i>Section</i>	<i>Page</i>
4. PHASE II ALLOYS	16
4.1 Alloy Selection	16
4.1.1 Macroalloying for Toughening	16
4.1.2 Macroalloying for Strengthening	16
4.1.3 Compositing with Superalloy Additions	17
4.2 Results and Discussion	17
4.2.1 Alloy Characterization	17
4.2.2 Tensile Properties	19
4.2.2.1 Ternary NiAlCo Alloys	19
4.2.2.2 Quaternary NiAlCo(Hf, Ti) Alloys	20
4.2.2.3 Composite Mixture of NiAl + Ni-Base Superalloy	20
4.2.3 Compressive Strength	20
4.2.3.1 Strengthening Mechanisms in NiAlCo Alloys	20
4.2.3.2 Strengthening Mechanisms in Modified NiAlCo Alloys	21
4.2.3.2.1 Effect of Hf Additions	22
4.2.3.2.2 Effect of Ti Additions	22
4.2.3.2.3 Effect of Superalloy Particle Compositing	23
4.2.3.2.4 Summary of Strengthening Approaches	23
4.2.4 Room Temperature Fracture Toughness and Fracture Energy	23
4.2.4.1 Binary NiAl Alloys	23
4.2.4.2 Cobalt-Modified Ternary Alloys	24
4.2.4.3 Cobalt-Modified Quaternary Alloys and NiAl Composite	25
4.2.4.4 Effect of Boron on the Fracture Toughness Behavior	25
4.2.4.5 Effect of Heat Treatment on Fracture Toughness of Alloys B2 and C	26
4.2.4.5.1 Effect of Gamma Prime Volume Fraction	26
4.2.4.5.2 Effect of Grain Size	27
4.2.5 Martensitic Phenomena in NiAlCo Alloys	27
4.2.5.1 Preyield Deformation in Martensitic Alloys	28
4.2.5.2 Postyield Deformation in Martensitic Alloys	30
4.2.6 Secondary Properties	30
4.2.6.1 Compressive Creep	30
4.2.6.2 Low Cycle Fatigue Testing	31

TABLE OF CONTENTS (continued)

<i>Section</i>	<i>Page</i>
5. PHASE III ALLOYS	33
5.1 Matrix Selection	33
5.2 Reinforcement Selection	33
5.3 Results and Discussion	33
5.3.1 Material Characterization	33
5.3.2 Compressive Strength and Modulus	34
5.3.3 Tensile Ductility	35
5.3.4 Fracture Toughness	35
5.3.5 Compressive Creep Strength	35
5.3.6 Low Cycle Fatigue	36
6. STUDY OF ATOMIC BONDING	37
6.1 Techniques for Studying Atomic Bonding	37
6.2 Alloys for EXAFS Studies	39
6.3 Development of the Low Exit Angle Method of Measuring EXAFS	39
6.4 Results and Discussion	40
6.4.1 Stoichiometric B2 Alloys	40
6.4.2 Effect of Stoichiometry and Alloying Additions on NiAl	41
6.4.3 Annealed Versus Cold-Worked FeAl	41
6.4.4 XANES of NiAl, CoAl and FeAl	41
7. COMPUTER SIMULATION STUDY	43
7.1 Introduction	43
7.2 Computer Modeling and Simulation Results	44
7.2.1 Physical Property Calculations	44
7.2.1.1 Lattice Energy	44
7.2.1.2 Surface Energies	44
7.2.1.3 Anti-Phase Boundary Energies	45
7.2.1.4 Melting Points	45
7.2.2 Simulation of Crack Propagation	45
7.2.2.1 1000 Atom Array Results	45
7.2.2.2 4000 Atom Array Results	47
7.2.2.3 9000 Atom Array Results	48

TABLE OF CONTENTS (continued)

<i>Section</i>	<i>Page</i>
8. CONCLUSIONS	50
8.1 Alloy Development	50
8.2 Atomic Bonding Studies	51
8.3 Computer Simulation Studies	51
REFERENCES	53

Accession For	
NTIS GRA&I	<input checked="" type="checkbox"/>
DTIC TAB	<input type="checkbox"/>
Unannounced	<input type="checkbox"/>
Justification	
By _____	
Distribution/	
Availability Codes	
Dist	Avail and/or Special
A-1	



LIST OF ILLUSTRATIONS

<i>Figure</i>	<i>Page</i>
1. Schematic of the Approach Used in this Program Showing the Relationship Between the Various Types of Studies	82
2. Specimen Geometries Used in Mechanical Testing for: (a) Tensile Strength and Ductility, (b) Compressive Strength and Deformability and Compressive Creep, and (c) Fracture Toughness	83
3. Ni-Al-Cr Isothermal Section at 750°C (Reference 5)	83
4. Microstructures of the Baseline Alloy Produced as VIM Ingot After Extrusion at 1000°C, Extrusion Ratio 9:1 (top) and After Heat Treatment for 2 Hours at 1300°C (bottom); Left-Transverse Section, Right-Longitudinal Section	84
5. Microstructures of the Baseline Alloy Produced in Powder Form After Extrusion at 1000°C, Extrusion Ratio 9:1 (top) and After Heat Treatment for 2 Hours at 1300°C (bottom); Left-Transverse Section, Right-Longitudinal Section	85
6. Microstructure of the Extruded and Heat Treated Baseline Alloy Showing a Uniform Distribution of Fine Alpha Chromium Particles and Denuded Zones at Grain Boundaries	86
7. Tensile Elongation Versus Temperature Plots for the Baseline Alloy Initially in Powder Form (top) and Produced as Cast Ingot (bottom)	87
8. Tensile Yield Strength of the P/M Baseline Alloy in As-Extruded Condition (circles) and After Heat Treatment for 2 Hours at 1300°C (triangles)	88
9. Microstructures of the Alloy A (Ni-30 a/o Al-35 a/o Co) Produced as a VIM Ingot After Extrusion at 1000°C, Extrusion Ratio 9:1 (top) and After Heat Treatment for 2 Hours at 1050°C (bottom); Left-Transverse Section, Right-Longitudinal Section	89
10. Microstructures of the Alloy B (Ni-30 a/o Al-25 a/o Co-0.25 a/o B) Produced as a VIM Ingot After Extrusion at 1000°C, Extrusion Ratio 9:1 (top) and After Heat Treatment for 2 Hours at 1050°C (bottom); Left-Transverse Section, Right-Longitudinal Section	90
11. Microstructures of the Alloy C (Ni-29 a/o Al-21 a/o Co) Produced as a VIM Ingot After Extrusion at 1000°C, Extrusion Ratio 9:1 (top) and After Heat Treatment for 2 Hours at 1050°C (bottom); Left-Transverse Section, Right-Longitudinal Section	91

LIST OF ILLUSTRATIONS (continued)

<i>Figure</i>	<i>Page</i>
12. Microstructures of the Alloy D (Ni-35 a/o Al-10 a/o Co) Produced as a VIM Ingot After Extrusion at 1000°C, Extrusion Ratio 9:1; Top-Transverse Section, Bottom-Longitudinal Section. Note that numerous grains have been liberated from the surface indicating weak grain boundaries.	92
13. Microstructures of the Alloy E (Ni-33 a/o Al-28 a/o Fe) Produced as a VIM Ingot After Extrusion at 1000°C, Extrusion Ratio 9:1 (top) and After Heat Treatment for 2 Hours at 1050°C (bottom); Left-Transverse Section, Right-Longitudinal Section	93
14. Microstructures of the Alloy F (Ni-33 a/o Al-20 a/o Fe) Produced as a VIM Ingot After Extrusion at 1000°C, Extrusion Ratio 9:1 (top) and After Heat Treatment for 2 Hours at 1050°C (bottom); Left-Transverse Section, Right-Longitudinal Section	94
15. Microstructures of the Alloy G (Ni-35 a/o Al-5 a/o V) Produced as a VIM Ingot After Extrusion at 1000°C, Extrusion Ratio 9:1 (top) and After Heat Treatment for 2 Hours at 1050°C (bottom); Left-Transverse Section, Right-Longitudinal Section	95
16. Microstructures of the Alloy H (Ni-35 a/o Al-5 a/o V-3 a/o Cr) Produced as a VIM Ingot After Extrusion at 1000°C, Extrusion Ratio 9:1 (top) and After Heat Treatment for 2 Hours at 1050°C (bottom); Left-Transverse Section, Right-Longitudinal Section	96
17. Microstructures of the Alloy I (Ni-35 a/o Al-5 a/o Ti) Produced in Powder Form After Extrusion at 1000°C, Extrusion Ratio 9:1; Top-Transverse Section, Bottom-Longitudinal Section	97
18. Microstructures of the Alloy J (Ni-40 a/o Al-10 a/o Ti) Produced as a VIM Ingot: (a) As Cast, and (b) As Partially Extruded. Alloy J exceeded the load capacity of the extrusion press and was not extruded. The microstructures shown are from the leading end of the extrusion preform from one of the attempted extrusions.	98
19. Ni-Co-Al Phase Diagram at 800K (Reference 9) with Estimated Martensitic Transformation Temperature Contours (from References 10 and 11)	99
20. Scanning Electron Micrographs of NiAlCo Alloys A, B and C (a, b and c, respectively). The compositions of the phases indicated are given in Table 6.	100
21. Optical Micrographs of Alloy A After Compression at Room Temperature (top) and 760°C (1400°F) (bottom)	101

LIST OF ILLUSTRATIONS (continued)

<i>Figure</i>	<i>Page</i>
22. TEM of VIM Alloy A, As Extruded + Heat Treatment of 2 Hrs/1050°C/Air Cool After Compression at 760°C (1400°F). (a) Micrograph of matrix containing a high density of prism-shaped precipitates. (b) Higher magnification micrograph of grain boundary showing elongated gamma prime.	102
23. TEM of VIM Alloy A, As Extruded + Heat Treatment of 2 Hrs/1050°C/Air Cool After Compression at 760°C (1400°F) to 0.2% Strain. (a) Higher magnification micrograph of matrix showing the prism-shaped precipitates which are seen to lie predominantly along $\langle 110 \rangle$ B2 directions. (b) Micrograph of blocky matrix precipitate with the same structure (L_{12}) as the grain boundary phase seen in Figure 22.	103
24. Selected Area Diffraction of VIM Alloy A (As Extruded + Heat Treatment at 2 Hrs/1050°C/Air Cool After Compression at 760°C (1400°F) to 0.2% Strain) on the Phases Seen in Figure 23. (a) Matrix, (001) zone axis pattern - ordered bcc (B_2) with $a = 0.286$ nm. (b) Blocky precipitate, (011) zone axis pattern - ordered fcc (L_{12}) with $a = 0.355$ nm. (c) Prism precipitate, (011) zone axis pattern - fcc (Al) with $a = 0.355$ nm.	104
25. Microstructures of VIM Alloy B After Extrusion and a Heat Treatment at 2 Hrs/1050°C/Air Cool. (a) TEM micrograph of the martensitic plates, corresponding to the (b) selected area diffraction pattern, showing that the plates are twin related. Subscripts "m" and "t" correspond to arbitrary selection of "matrix" and "twin." (c) Optical micrograph showing parallel martensitic plates in various grains.	105
26. TEM Micrographs of Fine Twin Lamellae within the Martensitic Plates of VIM Alloy B. The orientation of the lamellae is related to the orientation of the larger martensitic plates.	106
27. (a) TEM Micrograph of Grain Boundary Precipitates in VIM Alloy B, with Corresponding Selected Area Diffraction Patterns with Zone Axes of (b) (001) and (c) (123). The precipitates are identified as $(Ni,Co)_{20}Al_3B_6$	107
28. TEM of VIM Alloy C, As Extruded + Heat Treatment of 2 Hrs/1050°C/Air Cool. (a) TEM micrograph of grain boundary phases. (b) Higher magnification TEM dark field micrograph of gamma/gamma prime phase mixture.	108
29. TEM of Powder Alloy G, As Heat Treated (2 Hrs/1050°C/Air Cool) and After Tensile Testing at 760°C (1400°F) to $> 30\%$ Strain, Showing the Beta Phase Matrix Containing Gamma Prime in Equiaxed and Rod-Shaped Morphologies	109
30. Isothermal Section of the Ni-V-Al Phase Diagram at 1150°C (Reference 13), Showing the Location of Phase I Alloy G and the Pseudo-Ternary Location of Alloy H	110

LIST OF ILLUSTRATIONS (continued)

<i>Figure</i>	<i>Page</i>
31. TEM of Powder Alloy G, As Heat Treated (2 Hrs/1050°C/Air Cool) and After Tensile Testing at 760°C (1400°F) to > 30% Strain, Showing Microstructure in Greater Detail. Note the mottled matrix and the rod-shaped and planar gamma prime phases.	111
32. {111} Electron Diffraction Pattern Taken from Powder Alloy G, As Heat Treated (2 Hrs/1050°C/Air Cool) and After Tensile Testing at 760°C (1400°F) to > 30% Strain. The pattern was taken from a region of the mottled matrix free of gamma prime phase. Note the $\langle 01\bar{1} \rangle$ streaking indicative of lattice instability and the $\langle 11\bar{2} \rangle$ streaking associated with the higher order diffraction spots.	112
33. Electron Diffraction Pattern of the {111} NiAl Matrix and the $\langle 101 \rangle$ Gamma Prime Precipitates Taken from Powder Alloy G, As Heat Treated (2 Hrs/1050°C/Air Cool) and After Tensile Testing at 760°C (1400°F) to > 30% Strain	113
34. 0.2% Compressive Tensile Yield Strength Versus Temperature Curves for NiAl VIM Alloys A, B, C, E, F and G, Tested After a Homogenization Heat Treatment (2 Hrs/1050°C/Air Cool)	114
35. Tensile Elongation Versus Temperature Curves for Phase I NiAl Alloys Produced as VIM Ingots and Extruded at 1000°C with an Extrusion Ratio of 9:1. Specimens were tested as-extruded (circles) and after a homogenization heat treatment for 2 hours at 1050°C and air cooled (triangles). (Data points which correspond to both forms are designated as squares.) The fracture locations in the specimens are indicated by "g" for gage fracture, "s" for fracture at the shoulder or grip section of the specimen, and "p.o." for specimens deformed at the shoulder and pulled out of the grip without fracture.	115
36. Tensile Elongation Versus Temperature Curves for Phase I NiAl Alloys Produced in Powder Form and Extruded at 1000°C with an Extrusion Ratio of 9:1. Specimens were tested as-extruded (circles) and after a homogenization heat treatment for 2 hours at 1050°C and air cooled (triangles). Overlapping data points are indicated by squares.	118
37. Typical Examples of Tensile Fracture Surfaces of Phase I VIM Alloys. (a) Intergranular fracture (Alloy E, tested at 760°C), (b) transgranular cleavage (Alloy F, tested at 540°C), (c) mixed mode (Alloy A, tested at 540°C), and (d) ductile tearing (Alloy A, tested at 760°C). All alloys tested after a homogenization heat treatment at 1050°C for 2 hours, air cooled.	121
38. Optical Micrographs of Alloy A Compression Specimens Before Deformation (top) and After 4% Strain at Room Temperature (bottom). Note the stress-induced martensite (arrow).	122

LIST OF ILLUSTRATIONS (continued)

<i>Figure</i>	<i>Page</i>
39. Room Temperature Tensile Stress-Strain Curve for Extruded VIM Alloy A Showing Evidence of a Stress-Induced Martensitic Transformation at About 80 MPa	123
40. TEM of VIM Alloy A, As-Extruded + Heat Treatment of 2 Hrs/1050°C/Air Cool After Compression at Room Temperature to 0.2% Strain. (a) Micrograph of matrix showing dislocation bands along $\langle 112 \rangle$ and $\langle 110 \rangle$ B2 directions. (b) Micrograph of blocky phase with stacking faults on the same structure (L_{12}) as the grain boundary phase. Note the poorly defined tweed contrast in the matrix. .	124
41. Optical Micrographs of Alloy B Room Temperature Compression Specimen (top) After 0.35% Strain, and (bottom) After 1.65% Strain. Note the nucleation of the intergranular crack labeled #2 after 1.65% strain. (Applied force direction - horizontal to the photographs.)	125
42. Optical Micrographs of Alloy B Room Temperature Compression Specimen (top) After 4.0% Strain, and (bottom) After 7.5% Strain. Note that at 4.0%, cracks #1 and #2 have widened and both cracks continue to widen with 7.5% strain. However, the grains exhibit good toughness as seen by the blunting of the crack and resistance to propagation into the grain at the point indicated by #2. (Applied force direction - horizontal to the photographs.)	126
43. TEM Micrographs of VIM Alloy B After Compression to 3% at Room Temperature. (a) Bright field image showing lamellae of different orientations—A: $\bar{1}\bar{1}2$, B: $1\bar{5}2$, C: $1\bar{1}2$, D: $1\bar{3}2$. (b) Dark field image of the same area. Note that the twin lamellae maintain their orientation as they continue through martensitic plates of different (twin related) orientations. The average thickness of the twin lamellae is 65 nm.	127
44. TEM Micrographs of VIM Alloy B After Compression to 3% at Room Temperature. (a) Bright field image showing lamellae of different orientations. Selected area diffraction patterns using a convergent beam and zone axes of (b) $(\bar{1}\bar{1}2)$ and (c) $(0\bar{1}1)$, indicating the structure of the martensite to be face-center tetragonal with lattice parameters of $a = 0.384$ nm and $c = 0.314$ nm.	128
45. Optical Micrographs of Alloy C Room Temperature Compression Specimen After 1.5% Strain (top left), After 4.0% Strain (top right), and After 9.0% Strain (bottom). Note the origination of what appears to be cross-twinning at 1.5% strain (#1). At 4.0% strain, the number of cross-twins has increased (#2). A different grain shown at 9.0% strain contains a very large number of these features. #3 and #4 indicate areas to be examined in greater detail in Figure 46. (Applied force direction - horizontal to the photographs.)	129

LIST OF ILLUSTRATIONS (continued)

<i>Figure</i>	<i>Page</i>
46. Optical Micrographs of Alloy C Room Temperature Compression Specimen After 9.0% Strain Showing the Detail in Figure 45 at (top) #3 and (bottom) #4. The top micrograph shows the region at the grain boundary, with the secondary grain boundary phase seen here at #1. The crack (#2) is typical of cracks in Alloy C, which appear at the interface between the martensitic grains and the secondary phase. The bottom micrograph shows the lines which appear to be cross-twinning. (Applied force direction - horizontal to the photographs.)	130
47. TEM Micrographs of VIM Alloy C, As Extruded ÷ Heat Treatment of 2 Hrs/1050°C/Air Cool. (a) Undeformed microstructure of parallel martensitic laths. (b) Intersecting martensitic laths produced by plastic deformation.	131
48. Microstructures of Alloy A2 (Ni-32 a/o Al-29 a/o Co) Produced as a VIM Ingot After Extrusion at 1000°C, Extrusion Ratio 9:1 (top) and After Heat Treatment for 2 Hrs/1050°C/Air Cool (bottom): Left-Transverse Section, Right-Longitudinal Section	132
49. Microstructures of Alloy A3 (Ni-32 a/o Al-25 a/o Co) Produced as a VIM Ingot After Extrusion at 1000°C, Extrusion Ratio 9:1 (top) and After Heat Treatment for 2 Hrs/1050°C/Air Cool (bottom): Left-Transverse Section, Right-Longitudinal Section	133
50. Microstructures of Alloy B2 (Ni-30 a/o Al-25 a/o Co) Produced as a VIM Ingot After Extrusion at 1000°C, Extrusion Ratio 9:1 (top) and After Heat Treatment for 2 Hrs/1050°C/Air Cool (bottom): Left-Transverse Section, Right-Longitudinal Section	134
51. Microstructures of Alloy C2 (Ni-31 a/o Al-16 a/o Co) Produced as a VIM Ingot After Extrusion at 1000°C, Extrusion Ratio 9:1 (top) and After Heat Treatment for 2 Hrs/1050°C/Air Cool (bottom): Left-Transverse Section, Right-Longitudinal Section	135
52. Microstructures of Alloy C3 (Ni-30 a/o Al-15 a/o Co) Produced as a VIM Ingot After Extrusion at 1000°C, Extrusion Ratio 9:1 (top) and After Heat Treatment for 2 Hrs/1050°C/Air Cool (bottom): Left-Transverse Section, Right-Longitudinal Section	136
53. Microstructures of Alloy AH (Ni-30 a/o Al-34.5 a/o Co-0.5 a/o Hf) Produced as a VIM Ingot After Extrusion at 1000°C, Extrusion Ratio 9:1 (top) and After Heat Treatment for 2 Hrs/1050°C/Air Cool (bottom): Left-Transverse Section, Right-Longitudinal Section	137

LIST OF ILLUSTRATIONS (continued)

<i>Figure</i>	<i>Page</i>
54. Microstructures of Alloy CH (Ni-29 a/o Al-21 a/o Co-0.5 a/o Hf) Produced as a VIM Ingot After Extrusion at 1000°C, Extrusion Ratio 9:1 (top) and After Heat Treatment for 2 Hrs/1050°C/Air Cool (bottom); Left-Transverse Section, Right-Longitudinal Section	138
55. Microstructures of Alloy CT (Ni-29 a/o Al-21 a/o Co-5 a/o Ti) Produced as a VIM Ingot After Extrusion at 1000°C, Extrusion Ratio 9:1 (top) and After Heat Treatment for 2 Hrs/1050°C/Air Cool (bottom); Left-Transverse Section, Right-Longitudinal Section	139
56. Microstructures of Alloy M1 (Ni-50 a/o Al-20 v/o MERL 76 Particles) After Extrusion at 1000°C, Extrusion Ratio 9:1 (top) and After Heat Treatment for 2 Hrs/1050°C/Air Cool (bottom); Left-Transverse Section, Right-Longitudinal Section	140
57. Microstructures of Alloy AT (Ni-30 a/o Al-32.5 a/o Co-5 a/o Ti) Produced as a VIM Ingot. Alloy AT broke apart during the canning stage and was not extruded. . .	141
58. (a) Optical Micrograph, and (b) TEM Micrograph of Alloy C3 After Compression at Room Temperature Showing Gamma Prime Distribution and Fine Twin Lamellae	142
59. Higher Magnification of the Fine Twin Lamellae Seen in Figure 58b: (a) Bright Field, and (b) Dark Field	143
60. Alloy CT After Compression at Room Temperature: (a) Optical Micrograph, and (b) TEM Micrographs of Matrix (Region A) Showing a Tweed Structure	144
61. SAD of Matrix Region of Alloy CT as Shown in Figure 60 After Compression at Room Temperature Showing $\langle 111 \rangle$ Streaking Corresponding to the Tweed Structure: (a) $\langle 111 \rangle$ Zone Axis, and (b) $\langle 311 \rangle$ Zone Axis	145
62. TEM Micrographs of Alloy CT After Compression at Room Temperature Showing the Gamma Prime Morphologies at the Grain Boundaries: (a) Regions of Equiaxed Grains at Areas B and C Indicated in Figure 60a, and (b) Stringers at Area D of Figure 60a	146
63. (a) Optical Micrograph, and (b) TEM Micrograph of Alloy CT After Compression at 760°C (1400°F) Showing the Gamma Prime at the Grain Boundaries and Randomly-Oriented, Elongated Gamma Prime in the Grain Interior	147

LIST OF ILLUSTRATIONS (continued)

<i>Figure</i>	<i>Page</i>
64. TEM of VIM Alloy AH, As Extruded + Heat Treatment of 2 Hrs/1050°C/Air Cool After Compression at Room Temperature to 0.2% Strain. (a) Micrograph of matrix showing dislocation bands. (b) Higher magnification micrograph of stringer of a Hf-rich hexagonal blocky phase with numerous stacking faults.	148
65. TEM of VIM Alloy AH, As Extruded + Heat Treatment of 2 Hrs/1050°C/Air Cool After Compression at 760°C (1400°F). (a) Micrograph of matrix containing a small amount of Hf-rich rod-shaped precipitates and a high dislocation density. (b) Higher magnification micrograph of grain boundary showing small Hf-rich particles (open arrows) and a disordered fcc (A1) blocky phase (solid arrows).	149
66. Tensile Elongation Versus Temperature Curves for Phase II NiAl Alloys. Specimens were tested as-extruded (circles) and after a recrystallization heat treatment for 2 hrs/1050°C/Air Cool (triangles)	150
67. 0.2% Compressive Yield Strength Versus Temperature of Selected Phase II Ternary Alloys	152
68. 0.2% Compressive Yield Strength Versus Temperature of Selected Phase II Alloys Formulated for Strengthening	152
69. Load Versus Load Point Displacement Traces of Chevron-Notched Precracked Specimens Tested at 20°C. (A): A cobalt-modified martensitic alloy (B2). Note the apparent yielding during loading and slow rates of the load drop as the crack propagates. (B) A nonmartensitic (stoichiometric) binary alloy.	153
70. Stress-Strain Curve for: (a) a Martensitic Alloy that Undergoes Preyield Deformation, and (b) an Alloy that Does Not	153
71. Ratio of Unloading/Loading Stiffness Versus A_f Temperature for Various Martensitic NiAlCo Alloys. Note the abrupt change in stiffness ratio when the test temperature is near the A_f temperature of the material.	154
72. Ratio of Unloading/Loading Stiffness and 0.2% Compressive Yield Strength Versus Temperature for Alloy B2. Note the abrupt changes near the A_f temperature.	154
73. Compressive Creep Strength Versus Secondary Creep Rate at 760°C (1400°F) of Selected Alloys	155
74. Compressive Creep Strength Versus Secondary Creep Rate at 980°C (1800°F) of Selected Alloys	155

LIST OF ILLUSTRATIONS (continued)

<i>Figure</i>	<i>Page</i>
75. Optical Micrographs of Ni-29 Al-21 Co + PRD-166 Mixture. Note the fine grain size and uniform reinforcement distribution. (a) Transverse section, and (b) longitudinal section.	156
76. Scanning Electron Micrographs of Ni-29 Al-21 Co + PRD-166 Mixture. Note the martensitic structure of the NiAlCo matrix and the blocky gamma prime at the grain boundaries. (a) Transverse section showing no reaction zone between the reinforcement and the matrix. (b) Longitudinal section showing evidence of fiber breakup and void formation at the ends of the fibers during extrusion.	157
77. 0.2% Compressive Yield Strength of the Phase III Material Tested with the Stress Direction Both Parallel and Perpendicular to the Fiber/Extrusion Axis. Alloy C (Ni-29 a/o Al-21 a/o Co) is the matrix alloy.	158
78. Elastic Modulus of the Phase III Material Tested in Compression with the Stress Direction Both Parallel and Perpendicular to the Fiber/Extrusion Axis. Alloy C (Ni-29 a/o Al-21 a/o Co) is the matrix alloy.	158
79. Elongation Versus Temperature of the Phase III Material Tested Parallel to the Extrusion Axis Compared to the Matrix Material (Ni-29 a/o Al-21 a/o Co) in Extruded Powder Form	159
80. Tensile Fracture Surfaces of the Phase III Material at Room Temperature (a through c) and 760°C (d)	160
81. Room Temperature Fracture Toughness Specimen Fracture Surfaces of the Phase III Material Showing Fiber Breakage and Limited Fiber Pull-Out	161
82. Compressive Creep Rate as a Function of Applied Stress of the Phase III Material at Different Temperatures Tested with the Stress Direction Both Parallel and Perpendicular to the Fiber/Extrusion Axis. Ni-29 a/o Al-21 a/o Co is the matrix material.	162
83. Room Temperature Low Cycle Fatigue Behavior of the Phase III Material. The stress was cycled between zero and the maximum stress at 40 cpm.	162
84. Fracture Surface of Room Temperature LCF Specimen of the Phase III Material. Note the chisel-edge fracture of the gamma prime precipitates (b and c).....	163
85. Plot from EXAFS of $\Delta\sigma^2$ Versus Temperature for the First, Second and Third Nearest-Neighbor Bonds for CoAl	164
86. Comparison of Standard Geometry (a) and the Improved Geometry (b) for Performing EXAFS on Bulk Samples Using Fluorescence Detection	164

LIST OF ILLUSTRATIONS (continued)

<i>Figure</i>	<i>Page</i>
87. k^3 Transforms for (a) Ni-Edge in NiAl and (b) Co-Edge in CoAl, Both at 7°K	165
88. k^3 Transform of EXAFS Data for Ni-50Al and Ni-43Al. The reduced amplitude for the Ni-43Al alloy is indicative of structural disorder in the material.	166
89. k^3 Transforms of EXAFS Data for: (a) the Ni-Edge in Ni-50Al, (b) the Ni-Edge in Ni-42Al-6Cr, and (c) the Cr-Edge in Ni-42Al-6Cr. Addition of Cr to NiAl reduces the first nearest-neighbor bond strength and the Cr atoms are seen to occupy Al sites.	167
90. Comparison of EXAFS Spectra from Annealed and Cold-Worked FeAl. Note the decreased amplitude in the cold-worked case indicative of disorder.	168
91. $L_{3,2}$ Edge XANES Data from EELS Measurements. The splitting of the transition metal L_3 and L_2 edge white lines becomes more pronounced going from FeAl to CoAl to NiAl, indicating a filling of the third band as electrons are added across the series. It also appears that the effect of the Al in CoAl is to increase the Co occupied states (References 35 and 36); this is not seen in the FeAl or NiAl.	169
92. Lattice Energy Versus Bain Strain for NiAl Using the Embedded Atom Method ...	169
93. Surface Energies (γ) of: (a) NiAl, and (b) Ni as Calculated from the Embedded Atom Method Simulation Arrays	170
94. Anti-Phase Boundary Energy of NiAl as Calculated from the Embedded Atom Method Simulation Arrays	171
95. Appearance of the: (a) {110}, and (b) {112} Anti-Phase Boundaries in NiAl at 1K as Determined from the Embedded Atom Method Simulation Array. Ni atoms are marked by circles and Al atoms by triangles. The diagrammed movements are 4X and 16X the actual movements for the {110} and {112} boundaries, respectively.	172
96. Potential Energy Versus Temperature Plots from the Embedded Atom Method Simulation Arrays of: (a) NiAl, and (b) Ni for Determination of the Melting Points .	173
97. Three-Dimensional Diagram of the Simulated Lattice Containing a Crack. The white circles represent Al atoms, while the grey circles represent Ni atoms. The arrows indicate the direction of the applied force. Note that the force is being applied only to the outermost layer of atoms. In the $\langle 001 \rangle$ direction, the force is acting only on the Ni atoms (grey arrow), while in the $\langle 00\bar{1} \rangle$ direction, the force is acting only on the Al atoms (white arrow).	174

LIST OF ILLUSTRATIONS (continued)

<i>Figure</i>	<i>Page</i>
98. Typical Layers in EAM Simulation Array at 100°K, Showing the Array at Various Simulation Steps (40 Steps = 1 Atomic Vibration). Some rebonding of atoms after bond breaking can be seen in the vicinity of the crack tip in the later steps. At #1, the middle layer has separated from the top and bottom sections of the array. At #2, the middle layer has rebonded to the top portion. The "tails" attached to the atoms show displacements from their initial positions.	175
99. EAM Simulation Array at 300°K, Showing the Array at Step 2000. Rebonding of atoms after bond breaking can be seen in the vicinity of the crack tip. The "tails" attached to the atoms show displacements from their initial positions.	176
100. Typical Layers in EAM Simulation Array at 1000°K, Showing the Array at Various Simulation Steps (1 Step = 40 Atomic Vibrations). A description of the deformation processes in this simulation is provided in the text. Note: Step 3000 is plotted with displacements indicated relative to Step 2500 (not shown) and at a different scale (2.5X smaller). The "tails" attached to the atoms show displacements from their initial positions.	177
101. EAM Simulation Array at 1°K, Showing the Array at Step 4000. Ni atoms are represented by circles and Al atoms by squares. At this step, there is evidence of slip on the (001) plane (arrows), for the outermost layer of atoms has apparently shifted down a layer. The "tails" attached to the atoms show displacements from their initial positions.	178
102. {1 $\bar{1}$ 0} Slices through the Initial Embedded Atom Method Simulation Array for a Stress Applied in the <112> direction. Ni atoms are marked by circles and Al atoms by triangles. A load of 1250 MPa is applied to the top and bottom of the array at Step 0. This stress orientation should favor dislocation generation as the (110) planes are at 45° to the stress axis, making the resolved shear stress on these planes high.	179
103. {1 $\bar{1}$ 0} Slices through the Embedded Atom Method Simulation Array at 100K After 400 Steps. Only elastic distortions are present at this time. The stress of 1250 MPa is applied in the <112> direction and Ni atoms are marked by circles and Al atoms by triangles. Note: the array has been redrawn for ease of interpretation.	180
104. {1 $\bar{1}$ 0} Slices through the Embedded Atom Method Simulation Array at 100K After 800 Steps. Some sort of dislocation has propagated in the array as seen from the jog that has appeared in the lower left corner of some of the slices. The stress of 1250 MPa is applied in the <112> direction and Ni atoms are marked by circles and Al atoms by triangles. Note: the array has been redrawn for ease of interpretation.	181

LIST OF ILLUSTRATIONS (continued)

<i>Figure</i>	<i>Page</i>
105. {110} Slices through the Embedded Atom Method Simulation Array at 100K After 1400 Steps. Some new dislocations have propagated in the array as seen from the new jogs that have appeared in the upper right-hand side of some of the slices. The stress of 1250 MPa is applied in the $\langle 112 \rangle$ direction and Ni atoms are marked by circles and Al atoms by triangles. Note: the array has been redrawn for ease of interpretation.	182
106. Typical {110} Slices through the Embedded Atom Method Simulation Array at 100K After 0, 400 and 1000 Steps. The stress of 5000 MPa has been applied in the $\langle 112 \rangle$ direction by coordinated atomic movements on (110) planes in a $\langle 001 \rangle$ direction in the lower portion of the array, and slip on (112) planes in a $\langle 111 \rangle$ direction in the upper portion of the array. However, no dislocations are evident. At 1000 steps, slip appears to be well advanced, but still no dislocations are evident. Ni atoms are marked by circles and Al atoms by triangles.	183
107. Typical {110} Slices through the 4000 Atom Embedded Atom Method Simulation Array at 100K After 100, 1500, 1800, 2000, 2500 and 2700 Steps. A stress of 2500 MPa was applied in the $\langle 112 \rangle$ direction at Step 0, which was increased to 3750 MPa after Step 1500. In Steps 2000 through 2700, there appear to be dislocation events occurring in the form of coordinated slip. Further details of this simulation are provided in the text. Ni atoms are marked by circles and Al atoms by triangles.	184
108. Typical {110} Slices through the 4000 Atom Embedded Atom Method Simulation Array at 100K After 500, 1000, 1500 and 2000 Steps. The array is loaded at a constant strain rate, with a center crack and periodic boundary conditions between the left and right faces. The strains are applied in the $\langle 112 \rangle$ direction and Ni atoms are marked by circles and Al atoms by triangles.	187
109. Lattice Energy Versus Simulation Time Plot for the Simulation Shown in Figure 108. The lattice energy is topping out and beginning to drop near Step 2000 owing to the fracture that is becoming evident in Figure 108(d).	189
110. {001} Slices through the Embedded Atom Array at 100K After: (a) 1500, (b) 2000, (c) 3500, and (d) 6000 Steps. Ni atoms are marked by circles and Al atoms by triangles.	190
111. {001} Slices through the Embedded Atom Array at 300K After: (a) 1500, (b) 2500, (c) 5000, and (d) 6000 Steps. Ni atoms are marked by circles and Al atoms by triangles.	191

LIST OF ILLUSTRATIONS (continued)

<i>Figure</i>	<i>Page</i>
112. {001} Slices through the Embedded Atom Array at 800K After: (a) 500, (b) 3500, (c) 4000, and (d) 6000 Steps. Ni atoms are marked by circles and Al atoms by triangles.	192
113. {001} Slices through the Embedded Atom Array at: (a) 100K, (b) 300K, and (c) 800K After 8000 Steps. Ni atoms are marked by circles and Al atoms by triangles.	193
114. Potential Energy Versus Simulation Time Plot for the Simulations Shown in Figures 110 through 113	194
115. {110} Slices through the Embedded Atom Array Strained in the $\langle 112 \rangle$ Direction at 100K After: (a) 500, (b) 1000, (c) 1500, and (d) 2000 Steps. Ni atoms are marked by circles and Al atoms by triangles.	195
116. Side View (Looking at a {111} Plane) of the Array Shown in Figure 115(b) After 1000 Steps	196
117. Slice through the Embedded Atom Method 9000 Atom Array at 300K After 2000 Steps, Showing the Atomic Displacements in the Form of "Tails" on the Atoms. Ni atoms are marked by circles and Al atoms by triangles.	197
118. Slice through the Embedded Atom Method 9000 Atom Array at 300K After 2000 Steps, Showing the Strain Field. Ni atoms are marked by circles and Al atoms by triangles.	198
119. Slice through the Embedded Atom Method 9000 Atom Array at 300K After 2000 Steps, Showing the Strain Gradient Field and the Dislocation Loops Present in the Array. Ni atoms are marked by circles and Al atoms by triangles. ...	199
120. Potential Energy Versus Simulation Time Plot for a 9000 Atom Simulation, Recorded for: (a) the Total Simulation Array, and (b) a Few Hundred Atoms at Either Side of the Crack. The observed peaks have been seen to correspond fairly well with dislocation nucleation and/or bond breaking events.	200

LIST OF TABLES

<i>Table</i>	<i>Page</i>
1. Modified Phase I Alloys	56
2. Modified Phase I Cast Alloys	56
3. Phase I Alloy Densities	57
4. Homogenized Cast and Extruded Phase I Alloy Structures	57
5. Martensite Transformation Temperatures in Phase I NiAl-Co Alloys	58
6. Electron Microprobe Analysis of Phase I NiAl-Co Alloys	58
7. Tensile Data of Phase I VIM Alloys	59
8. Tensile Data of Phase I Powder Alloys	61
9. Tensile Fracture Behavior of Phase I VIM Alloys	63
10. Tensile Fracture Behavior of Phase I Powder Alloys	64
11. Phase II Alloys	65
12. Phase II Alloy Compositions (atom percent)	66
13. X-Ray Diffraction Results for Phase II Alloys	67
14. Martensitic Transformation Temperatures of NiAl-Co Alloys	68
15. Phase II Alloys Metallography Results	68
16. Gamma Prime Compositions in Alloy CT at 760°C (1400°F)	69
17. Morphology and Structure of the Phases Present in Alloys A and AH at Room Temperature and 760°C (1400°F)	69
18. Compositions of Phases Present in Alloys A and AH at 760°C (1400°F)	69
19. Tensile Data of Phase II NiAlCo Alloys	70
20. Tensile Data of Strengthening Modifications of Alloy A	71
21. Tensile Data of Strengthening Modifications of Alloy C	72
22. Tensile Data of Alloy M1 with MERL 76 Reinforcement	73

LIST OF TABLES (continued)

<i>Table</i>	<i>Page</i>
23. Compression Data of First Series of Phase II Alloys	73
24. Compression Data of Second Series of Phase II Alloys	74
25. Room Temperature Fracture Toughness and Fracture Energy of Selected Alloys	75
26. Room Temperature Fracture Toughness and Fracture Energy of Selected Quaternary Alloys and a NiAl Composite	76
27. Heat Treatment Studies of NiAlCo Alloys	76
28. Compressive Stiffness of Martensitic and Nonmartensitic Alloys	77
29. Creep Stress Exponents for Selected Alloys at 760°C (1400°F)	77
30. Low Cycle Fatigue Data of Selected Alloys	78
31. Metallography of As-Extruded Phase III and Baseline Materials	78
32. 0.2% Compressive Yield Strength of the Phase III Material	79
33. Elastic Modulus of the Phase III Material	79
34. Tensile Ductility of the Phase III Material	80
35. Fracture Toughness of the Phase III Material and Selected Alloys	80
36. $\Delta\sigma^2$ Values for 300°K Versus 77°K, Taken on Bulk, Annealed CoAl and NiAl by Glancing Exit Angle Fluorescence	81
37. Third Nearest-Neighbor $\Delta T/\Delta\sigma^2$ from EXAFS	81

1. INTRODUCTION

1.1 BACKGROUND AND APPROACH

The benefits that could be achieved by the development and application of nickel aluminide (NiAl) base alloys in the gas turbine engine are extensive. For example, it has been calculated that weight savings of over 100 pounds could be achieved by the substitution of such alloys for disks in an F100 type engine. However, the alloy development challenge is exceptionally demanding, and a much greater level of understanding will be required before any real progress can be achieved.

It is usually stated that the ductility problem in NiAl can be traced to an insufficient number of slip systems to satisfy the Von Mises criterion for plastic flow in polycrystalline aggregates. NiAl deforms by the movement of $\langle 001 \rangle$ glide elements which are inadequate for general plasticity.

In a previous study of NiAl alloys at Pratt & Whitney (Air Force Contract F33615-84-C-5067, Reference 1), the addition of manganese (Mn) and chromium (Cr) to NiAl modified the slip systems. In compression at room temperature, plastic flow occurred by the movement of $\langle 111 \rangle$ dislocations, indicating that the Von Mises criterion was apparently satisfied. However, the alloys were still brittle in tension. This observation shows that the factors controlling plastic flow and fracture are obviously not understood. The mere presence of $\langle 111 \rangle$ type glide is insufficient to guarantee plasticity. A similar situation is found in the iron aluminide (FeAl) which also exhibits $\langle 111 \rangle$ type slip. In the iron-base system, if the concentration of aluminum is reduced to 40 atom percent, then ductility at room temperature is observed, whereas the equiatomic alloy is brittle (Reference 2). This observation indicates that the ductility problem may be tractable in this class of alloys. However, although quite extensive alloy development activity has centered on NiAl alloys, little progress has been made in overcoming the intrinsic brittleness of the compound. Traditionally, the search for useful alloys has been based on an empirical approach coupled with metallurgical intuition. However, it became clear that if real progress were to be made, a fresh approach was needed.

The first step in this approach was to critically review the previous work on B2 compounds which consisted of a wide range of studies undertaken by a disparate group of investigators ranging from theoretical physicists to practicing blacksmiths. Because each investigator analyzed a specific feature of the B2 compounds from a narrow perspective, it was difficult to meld all the results into a coherent or comprehensive whole. Therefore, it was clear that the problem must be attacked on a broader front rather than by the methods used to define alloys in the past. In our approach to the problem, we attempted to couple both basic and applied studies as follows.

The objectives of the present program were to gain insights into intrinsic factors controlling ductility of NiAl alloys and to develop NiAl alloys with a balance of properties suitable for advanced gas turbine engine applications. Pratt & Whitney, in collaboration with the University of Connecticut, constructed a program which involved three coupled studies:

- The use of advanced X-ray spectroscopic techniques such as extended X-ray absorption edge fine structure (EXAFS) and X-ray absorption near edge spectroscopy (XANES) to determine the nature of atomic bonding in the B2 lattice.
- Computer modeling and simulation of dislocation stability and mobility.
- Experimental studies of the mechanical properties of selected alloys.

The relationship between the three studies, as initially conceived, is depicted in Figure 1. It was anticipated that results from these studies would provide insight into the effects of alloying additions on the nature of atomic bonding and the resulting mechanical properties. Further, one of the objectives of the modeling and simulation studies was to identify favorable alloying directives for increasing the ductility of NiAl at ambient temperatures.

The experimental study of the ductility and deformation behavior of selected NiAl alloys was conducted by Pratt & Whitney in East Hartford, Connecticut; the EXAFS and XANES study by Professor Douglas Pease of the University of Connecticut at Brookhaven National Laboratory; and the deformation modeling and computer simulation by Professor Philip Clapp at the University of Connecticut.

1.2 PROGRAM OUTLINE

The program consisted of three phases which were conducted over a period of 3 years. The objectives of Phase I, ductility enhancement/mechanisms, were to:

- Determine the ductility and deformation behavior of selected NiAl alloys.
- Develop EXAFS and XANES techniques for characterizing atomic bonding in NiAl alloys.
- Develop deformation model and computer simulation techniques for predicting ductility and deformation behavior of NiAl alloys.

The ductility and deformation study in Phase I involved the initial selection of one baseline alloy for study and later, the formulation of 10 more alloys for improved fracture resistance. These alloys were characterized in terms of microstructure, ductility, fracture, and strength in tensile and compression tests from room temperature to 1000°C.

The EXAFS and XANES study involved the selection of several binary B2 phase alloys, which exhibit a range of ductility and deformation behavior, and the development of the EXAFS and XANES techniques for analysis of atomic bonding characteristics in the selected B2 phase alloys. The binary B2 phase alloys selected included NiAl, CoAl, FeAl, FeCo, and CuZn. The EXAFS analyses were then extended to evaluate the effects of a ternary addition on the atomic bonding of NiAl.

At the outset, the deformation behavior of the B2 compound NiAl, for which experimental data are available from the literature, was modeled and simulated. The goal of the initial study was to develop the interatomic potentials to perform simulations of NiAl deformation behavior, with the goal of predicting the fracture strengths, slip systems and ductile-brittle transition temperature (DBTT) in this type of alloy. Some of the critical steps in this study included:

- Development of Embedded Atom Method (EAM) equations using input data from pure Ni and Ni₃Al.
- Calculation of crack surface free energy which depends on atomic bond-breaking energy.
- Calculation of work of plastic deformation per unit crack extension which depends on the rate of dislocation generation at the crack tip and work done moving dislocations away from the crack tip.

Results from these calculations and computer simulations were used to determine various properties, including the DBTT and dominant slip systems which were then compared with experimental observations.

Following Phase I, the objectives of Phase II, alloy improvements, were to:

- Determine ductility and deformation behavior of selected NiAl alloys based on promising results of Phase I, concentrating on a good balance of properties.
- Continue development and application of EXAFS and XANES techniques for characterizing atomic bonding in NiAl alloys.
- Apply deformation model and computer simulation techniques for predicting ductility and deformation behavior of NiAl alloys.

Phase II involved the selection of an additional 10 modified alloys based on promising alloys from Phase I of the program. These alloys were modified with the intention of obtaining a useful balance of secondary properties such as creep rupture, low cycle fatigue, and fatigue crack growth.

Finally, Phase III involved selection of the most promising alloy from Phase II for further evaluation. The Phase III material was characterized in detail for tensile ductility and fracture behavior, strength, creep resistance, fracture toughness, and low cycle fatigue.

1.3 PROGRAM OVERVIEW

A new approach in alloy development was taken in this program which involved joint efforts of metallurgists and physicists attempting to gain insight into and modify the brittle nature of intermetallics by coupled experimental and theoretical studies. The approach, shown schematically in Figure 1, turned out to be overly optimistic since neither the EXAFS nor the computer simulation techniques were sufficiently developed at the onset of this program to meet the program schedule. The development of both basic approaches was longer than expected and, in the case of the EXAFS study, it was further delayed for 8 months because of shutdown of the synchrotron beamlines at Brookhaven National Laboratories for equipment upgrading. As a result, the anticipated integration and potential synergism of the three companion studies as originally conceived (Figure 1) was not realized. In spite of the initial difficulties, remarkable progress was made in both basic studies. Differences in atomic bonding among B2 compounds were clearly demonstrated in EXAFS results and a technique was developed for obtaining EXAFS from bulk samples (rather than the traditional powder or thin foil samples) by Professor Pease's team. The use of bulk samples eliminates the lattice disordering and contaminations associated with the powder and the foil making processes. A realistic computer simulation technique for plastic deformation using the Embedded Atom Method, as well as a technique for identifying dislocations in a large atom array, were developed by Professor Clapp. The results of the basic studies are described in detail in Sections 6 and 7. It is gratifying to note that both Professors Clapp and Pease are currently pursuing further understanding on the fundamental brittleness problem in intermetallics under ONR and DoE funding using the techniques developed in this program.

2. EXPERIMENTAL

2.1 PREPARATION OF MATERIALS

Phase I alloys were produced in both cast and powder form. Vacuum induction melting (VIM) was used to produce 10 kg cast ingots of each of the alloys. Powder was produced by vacuum atomization using the processes and facilities at Homogeneous Metals Incorporated. To achieve a fully recrystallized microstructure, both product forms were canned and extruded at the Air Force Metals Processing Lab. The extrusion cycle consisted of controlled heating at a rate of 80°C per hour to 600°C, soaking at temperature for several hours, followed by heating at a more rapid rate (200°C per hour) to the extrusion temperature of 1000°C. An extrusion ratio of 9:1 was used. Heat treatments of 800, 1000 and 1200°C for 2 hours each were performed on selected alloys to determine an appropriate homogenization treatment for the alloys. A temperature of 1050°C was chosen because the exposure did not cause substantial grain growth. This heat treatment was used throughout all phases of the program. Phase II alloys were made either as extruded VIM ingots or as an extruded composite powder mixture. The extrusion cycle was similar to that of the Phase I alloys.

The Phase III material was produced in the form of an extruded, mechanically blended mixture of -80 mesh Ni - 29 a/o Al - 21 a/o Co powder and about 12 v/o chopped PRD-166 ($\text{Al}_2\text{O}_3 + 20\% \text{ZrO}_2$) fibers. The extrusion cycle was similar to that of the Phase I and Phase II alloys with the exception that the extrusion was performed at the higher temperature of 1100°C to ensure metal flow around the fibers.

2.2 EVALUATION OF MECHANICAL PROPERTIES

Mechanical properties testing was performed on sections of selected extruded bars of Phase I and Phase II alloys in both the extruded and extruded plus homogenized (2 hr/1050°C/air cool) conditions. The Phase III material was tested in the as-extruded form using similar test procedures. Tests were carried out for tensile strength and ductility, compressive strength and deformability, compressive creep strength, fracture toughness, and low cycle fatigue. The specimen configurations used for the above tests are shown in Figure 2. Tensile testing was performed using modified "dogbone" specimens (Figure 2a) at various temperatures using a strain rate of approximately 0.02/min. The specimens had scribe marks, which were measured before and after testing to determine the extent of the deformation. For those materials which fractured before yielding and with no apparent ductility in tension, compression testing was used to determine the yield strength and deformation behavior of the materials. Compression specimens (Figure 2b) were tested at various temperatures at a strain rate of approximately 0.04/min. Strains were measured using an extensometer attached to alumina buttons above and below the specimen. Using similar specimens and a similar experimental setup, compressive creep testing was performed at various elevated temperatures and creep rates were determined for various stress levels. Room temperature fracture toughness testing was performed on chevron-notched, fatigue pre-cracked slow bend specimens (Figure 2c) following ASTM Standard E399. The fracture energy, i.e., the ability of the material to resist crack propagation, was determined by calculating the area under the loading curve and dividing by the specimen area in front of the pre-crack. Load controlled low cycle fatigue testing was performed on cylindrical specimens tested in tension with smooth grip sections. The specimens were tested in a servohydraulic testing machine equipped with hydraulic grips. The temperature was controlled with induction heating and an infrared radiation pyrometer.

23 PREPARATION OF SAMPLES FOR TRANSMISSION ELECTRON MICROSCOPY

Thin foils were prepared for transmission electron microscopy (TEM) using a Fischione Twin Jet Electropolisher and electropolishing solution of perchloric acid, methanol, ethanol, and butanol in ratios of 1:10:10:10. Samples were thinned at -20°C using 30 V (25–30 mA current) or at -30°C using 70 V (25–30 mA current). A brief ion milling was used on selected samples to eliminate any surface film from the electrojet thinning process. Specimens were examined in either a Philips EM400 or in a Philips CM12 Transmission Electron Microscope.

3. PHASE I ALLOYS

As described in Section 1.1, this program included both basic and applied studies. Phase I involved selection of B2 alloys for EXAFS studies of the atomic bonding as well as alloys for mechanical evaluation. The latter alloys consisted of 1 baseline alloy, later followed by 10 modified alloys. Alloys selected for EXAFS studies are given in Section 6.2.

3.1 BASELINE ALLOY SELECTION

To ductilize NiAl, it was considered necessary to reduce the ordering energy of this compound by alloying. An examination of the available heats of formation of various transition metal (TM) aluminides (Reference 3) suggests that alloying NiAl with elements to the left of Ni in the periodic table should reduce the ordering energy of NiAl by increasing amounts. Indeed, CrAl exists only as an unstable B2 compound.

In terms of bonding, the densities of states calculations of Müller, et al., indicate that the stability of the TM aluminides is related to the charge transfer from Al to TM (Reference 4). Müller, et al., determined that charge transfer is: (1) quite small for CrAl and even slightly negative for VAl (another unstable B2 compound), and (2) maximum for CoAl which has the highest melting point of the TM aluminide series. An intriguing point made by Müller, et al., is that the addition of 10 atomic percent Cr would stabilize $V_{40}Cr_{10}Al_{50}$ in the B2 phase, suggesting an interaction effect of the alloying additions.

Positive indications of this alloying strategy were observed in a previous program at Pratt & Whitney, which indicated that in Mn- and Cr-modified ternary NiAl alloys, the slip at ambient temperatures tends to be along $\langle 111 \rangle$ instead of $\langle 001 \rangle$ as is normally observed in binary NiAl (Reference 1). This alloying strategy was pursued further in this program. A hypostoichiometric alloy 52 a/o Ni, 42 a/o Al, 6 a/o Cr was selected as a baseline alloy for initial studies in Phase I. The selected composition lies in the B2 single phase field of the Ni-Al-Cr ternary phase diagram (Reference 5) (Figure 3).

3.2 BASELINE ALLOY RESULTS AND DISCUSSION

3.2.1 Alloy Characterization

The microstructure of the baseline alloy (Ni-42 a/o Al-6 a/o Cr) in as-extruded and extrusion plus recrystallization heat treatment conditions is shown in Figures 4 (cast material) and 5 (powder material). A rather unusual microstructure was observed in the as-extruded cast material (Figure 4 - top) which may be related to the cast structure. For both the cast and the powder materials, recrystallization and considerable grain growth were observed after a heat treatment for 2 hours at 1300°C. A uniform dispersion of fine particles was observed in the baseline alloy in both as-extruded and heat-treated conditions (Figure 6). The particles were determined to be alpha chromium by Miracle, et al. (Reference 6) which is consistent with precipitates seen in the previous program in Cr-modified alloys (Reference 1). These particles appear to have an affect on the mechanical properties as described below.

3.2.2 Tensile Ductility and Strength

The baseline alloy in both powder and cast forms was tested at various temperatures in both as-extruded and extrusion plus recrystallization heat treatment conditions. Plots of the tensile elongation at fracture as a function of temperature are shown in Figure 7. The ductile brittle transition temperatures (DBTT) are generally above 600°C. For comparison, the DBTT is around 500°C for binary

NiAl alloys with similar processing. Tensile fracture in the baseline alloy occurred transgranularly at temperatures below the DBTT, but predominantly intergranularly above the DBTT. The tensile yield strengths of the baseline alloy near the DBTT are shown in Figure 8.

A separate study was performed by Miracle, et al. on the baseline alloy in single crystal form (Reference 6) in order to elucidate the deformation characteristics of the baseline alloy. It was determined that the Cr addition succeeded in modifying the slip behavior of NiAl by enhancing slip via a $\langle 111 \rangle$ type Burger's vector with respect to slip via $\langle 001 \rangle$ Burger's vectors. Further, stoichiometric FeAl, which slips via a $\langle 111 \rangle$ Burger's vector, is also brittle at room temperature (Reference 2). Therefore, slip system modification alone is not sufficient to impart ambient temperature ductility to NiAl alloys.

3.3 FORMULATION OF MODIFIED ALLOYS

The Cr-addition to NiAl in the baseline alloy succeeded in enhancing $\{110\} \langle 111 \rangle$ slip at room temperature with respect to $\{110\} \langle 001 \rangle$ slip, which theoretically satisfies von Mises criterion for plasticity. However, the material was still brittle at room temperature. Therefore, modified Phase I alloys were selected both to further explore slip system modification in NiAl and to investigate alternative means of enhancing the room temperature ductility and toughness of NiAl. The alloys and their rationales are given in Table 1 and described in detail below.

3.3.1 Ni-Al-V-Cr System

In the baseline alloy studies and in the previous NiAl program (Reference 1), it was shown that additions of manganese or chromium change the slip behavior of NiAl at room temperature. However, all the alloys were still brittle. The origin of the change was considered to be a reduction in the ordering energy of the B2 lattice. Additions of vanadium were thought to follow the same trend as chromium and manganese with an even more pronounced effect. Therefore, it was proposed that additions of vanadium be studied as a single addition (Alloy G) and also in combination with chromium (Alloy H). Vanadium additions to NiAl were studied in the previous NiAl program (Reference 1), but all the alloys also contained boron, an element which was found to be detrimental to the room temperature ductility of NiAl. Phase I Ni-Al-V(Cr) alloys were studied without boron.

3.3.2 Ni-Al-Fe System

The selection of iron-modified NiAl alloys for further study was based on good ductility observed in a Ni-27 a/o Fe-22 a/o Al alloy studied in the previous program (Reference 1). The microstructure of the aforementioned alloy consisted of about 85% B2 phase with the remainder an $L1_2$ -type phase which formed as equiaxed grains in the B2 phase grain boundary regions. It was assumed that the B2 phase was responsible, at least in part, for the observed ductility.

The composition of the B2 phase in the alloy was determined via electron microprobe, and an alloy based on this composition but with a higher Al content was proposed (Alloy F). An alloy with further additions of iron at the expense of nickel was also prepared (Alloy E).

3.3.3 Ni-Al-Co System

Some room temperature ductility was observed in cobalt-modified NiAl alloys with low Al contents from the previous program (Reference 1). In particular, an alloy of Ni-25 a/o Al-25a/o Co exhibited 10% plastic elongation at room temperature. Such alloys contain a mixture of phases: Ni_3Al , martensitic NiAl and B2 NiAl in various proportions. The presence of NiAl martensite in these alloys was considered a major factor for their ductility. Further, binary B2 NiAl single crystals are brittle

at room temperature while martensitic NiAl single crystals have been shown to exhibit elongations of up to 13% at room temperature as a result of the transformation and/or rearrangement of martensite variants under an applied stress (References 7 and 8). Ductility in the isostructural compound NiTi is attributed to a like transformation. Therefore, the martensitic transformation is considered to be a means of obtaining room temperature ductility and toughness in NiAl alloys.

Higher aluminum alloys (relative to the previously studied alloy Ni-25 a/o Al-25 a/o Co) were studied in order to reduce the density of the material. To explore transformation toughening, an alloy was selected to exploit a stress-induced martensitic transformation at room temperature (Alloy A). In addition, alloys were formulated to be martensitic at room temperature based on the composition of the martensitic phase from the Ni-25 a/o Al-25 a/o Co alloy (Alloys C and D). It was thought that the martensitic phase might prove to be inherently tougher than the B2 phase. At the same time, there is the possibility for ductility enhancement due to martensite-to-martensite transformations under stress. Plasticity can be accommodated in a fully martensitic alloy by switching of martensite variants to those with more favorable orientations with respect to the imposed strain. Finally, an additional alloy was formulated to be martensitic at room temperature, but with the addition of boron in an attempt to counteract embrittling effects of the Ni₃Al phase containing higher aluminum concentrations (Alloy B).

3.3.4 Ni-Al-Ti System

It was proposed that NiAl alloys be developed with a mechanism for ductility similar to that of the isostructural compound NiTi. The good ductility of NiTi at ambient temperature is often attributed to stress-induced martensitic transformation. The nature of the nickel-titanium atomic bonding may also be a contributing factor. Thus, it was proposed that alloys based on the Ni-Al-Ti system be studied. Certain titanium-modified NiAl alloys were studied in the previous NiAl alloy development program (Reference 1). However, the combination of Al and Ti in the alloys studied was such that no martensitic transformation occurred at ambient temperatures. Further, all of the titanium-modified NiAl alloys studied were doped with boron, an element which was found to lower the ductility of NiAl alloys.

Alloys I and J were formulated to explore primarily martensitic transformation induced plasticity. Alloy I was formulated specifically to exploit the martensite-to-martensite phenomenon. The M_s temperature of binary Ni, 35 a/o Al is around 300K. Replacing 5 a/o Ni with Ti (Alloy I) was expected to raise the M_s temperature and render the alloy fully martensitic at room temperature.

Alternatively, plasticity can be accommodated by the stress-induced transformation of a B2 phase to martensite if the B2 phase is sufficiently unstable. This situation may be created in Ni-40 a/o Al which has a M_s temperature near 0K. By replacing 10 a/o Ni with Ti (Alloy J), the M_s temperature was expected to be raised to somewhere near 300K. Further, the addition of a moderate amount of Ti was thought to destabilize the B2 lattice sufficiently for a stress-induced martensitic transformation to occur around room temperature.

3.4 MODIFIED ALLOYS RESULTS AND DISCUSSION

3.4.1 Alloy Characterization

Chemical analyses of the cast alloys are shown in Table 2. The accuracy of the determination is ± 1 to 2% of the reported values. In general, the Al contents are slightly higher than the aim while the Ni and ternary additions slightly lower. Al is easily lost during casting due to its high vapor pressure. Therefore, an extra amount of Al charge is commonly added to the melt to compensate for this, in these cases, it appears to have overcompensated. The compositions of the powder alloys (not shown)

were all found to be within 3% of the desired value, with most varying only about 1% of the desired composition. Al values tended to be slightly on the low side. In addition, the densities of selected Phase I alloys were determined by a gravimetric technique and results are given in Table 3. Note that most of the alloys represent a moderate weight savings over a typical superalloy.

In order to characterize the microstructure, metallography and X-ray diffractometry were used for phase determination and lattice parameters; the results are presented in Table 4. Further, the microstructures of the cast alloys in the as-extruded and extruded plus homogenization heat treatment (2 hours/1050°C/air cooled) conditions are shown in Figures 9 through 17. The extruded powder alloys have similar microstructures to their cast counterparts, but with significantly smaller grain sizes (about a factor of 10). Alloy J (Ni-40 a/o Al-10 a/o Ti) exceeded the load capacity of the extrusion press and was only partially extruded (Figure 18). Therefore, this alloy was not fully characterized.

The microstructures of the Phase I modified alloys did not all meet the expectations as outlined in Section 3.3 and Table 1. In fact, only the Fe-modified alloys (E and F) and V- and Cr-modified alloys (G and H) had their intended phase structure, which was a virtually single phase B2 structure. On the other hand, the Ti-modified alloys (I and J), which were formulated to exploit martensitic transformation mechanisms, exhibited no martensite before or after deformation. Alloy J was also found to contain a small amount of the high strength Heusler Phase (Ni_2AlTi -type), rendering it unextrudable.

As a group, the Co-modified alloys possessed the most interesting microstructures. The alloys were originally formulated for two different ductilizing approaches: the formation of γ' , Ni_3Al -type phase (A and B), and the operation of a stress-induced transformation (C and D). However, the operation of martensitic transformation mechanisms are active in all four of the alloys and all but Alloy B contained γ' . The boron addition to Alloy B suppresses the formation of γ' in favor of a small amount of a boride phase of the form $(\text{Ni},\text{Co})_{20}\text{Al}_3\text{B}_6$. The martensitic transformation in NiAlCo alloys became the major toughening approach in later phases of the program, and so the NiAlCo alloys underwent more detailed characterization. In particular, martensitic transformation temperatures were determined; electron microprobe and transmission electron microscopy (TEM) analyses were performed on specimens of Alloys A, B and C, the results from which are summarized below.

Martensitic transformation temperatures were determined for the Phase I NiAlCo alloys using dilatometry measurements (Table 5). These results were combined with data from literature (References 9 through 11) in order to plot M_s temperature contours on the Ni-Al-Co phase diagram (Figure 19). It is evident that small variations in composition result in quite large variations in the transformation temperatures. A more comprehensive treatment of the effect of composition on M_s temperature in NiAlCo alloys was performed by Russell, et al. (Reference 12), where it was determined that the Al content has about 4X the effect that Co does on the M_s temperature.

Electron microprobe characterization of the phase compositions was performed on Alloys A, B and C. The results are summarized in Table 6 and Figure 20. The result for Alloy B was unexpected, with the grain boundary precipitate being revealed as a boride of the form $(\text{Ni},\text{Co})_{20}\text{Al}_3\text{B}_6$. Boron evidently is insoluble in the NiAlCo alloy as it was only found in the precipitate. Without boron, Alloy B would be expected to consist of a martensitic matrix with gamma prime-type precipitates. However, the boride precipitate, which is a low-Al phase, enriches the remaining alloy in Al so that no gamma prime phase is observed.

Alloy A (Ni-30 a/o Al-35 a/o Co) will undergo a stress-induced martensitic transformation and exhibit a high degree of fracture toughness at room temperature (Section 4.2.4.2). Further, Alloy A was the baseline alloy for a number of the Phase II alloys; in particular, for alloys modified for improvement in high temperature strength. Therefore, compression specimens tested at both room

temperature and 760°C (1400°F) were sliced perpendicular to the stress axis for further characterization with TEM.

Optical micrographs of Alloy A after testing at both temperatures are shown in Figure 21. Some stress-induced martensite ($L1_0$) can be seen optically in the specimen tested at room temperature. In addition, martensite laths were occasionally seen in the TEM specimen. However, the majority of the matrix grains were identified via electron diffraction to be an ordered bcc (B2) phase. Some of the grains contain a tweed structure accompanied by diffuse streaking in $[1\bar{1}\bar{2}]$ and $[1\bar{1}\bar{2}]$ B2 directions in the (110) B2 diffraction patterns. The tweed structure is considered a precursor of a martensitic transformation. Stringers of blocky precipitates are seen at the grain boundaries. These were identified to be ordered fcc ($L1_2$, Ni_3Al -type).

After testing at 760°C (1400°F), the microstructure of Alloy A looks much different than at room temperature (Figures 21 through 24). The $L1_2$ particles on the stringers have coarsened. In addition, Alloy A now contains about 34 volume percent of an elongated prism-shaped disordered fcc phase (Al) within the matrix with the lengths aligned along $\langle 011 \rangle$ B2 directions and the short sides along $\langle 112 \rangle$ B2 directions (Figure 23). Evidently, at 760°C (1400°F) Alloy A is in a three phase region of the Al-Co-Ni phase diagram.

Alloy B (Ni-30 a/o Al-25 a/o B) and Alloy C (Ni-29 a/o Al-21 a/o Co) are both martensitic at room temperature, and deformation microstructure and mechanical testing results (Section 4.2) indicated the presence of stress-induced martensite-martensite transformation behavior in these alloys at ambient temperatures. Therefore, TEM specimens were prepared of both alloys from compression specimens both before and after testing at room temperature. The deformed microstructures are discussed in Section 3.4.3.1.

Transmission electron microscopy of Alloy B reveals twin related martensite plates which formed during cooling (Figure 25). Selected area diffraction (SAD) from these plates reveals an ordered fct $L1_0$ (CuAuI-type) structure with $a = 0.384$ and $c = 0.324$ nm and twinning on the $(11\bar{1}) \langle 112 \rangle$ face-center tetragonal system. The thickness of the martensitic plates ranges from 0.1 to 0.3 microns. In some areas of the material, a modulated tweed structure is seen within the parallel martensite plates. Further, at higher magnification, fine lamellae are observed in many of the plates (Figure 26). Precipitates are observed at the grain boundaries of the material (Figure 27). Micro diffraction using a 60 nm spot size revealed the precipitates to have a face-center cubic structure with $a = 1.0582$ nm, supporting the microprobe results which suggested the precipitate to be of the form $(Ni,Co)_{20}Al_3B_6$.

The TEM photographs of Alloy C reveal similar parallel martensitic laths containing fine twin-related lamellae. SAD reveals the material to be $L1_0$ with $a = 0.370$ and $c = 0.318$ nm. Precipitates are found at the grain boundaries, consisting of equiaxed grains containing very fine ($0.08 \mu m$) precipitates (Figure 28). These were revealed to be ordered fcc with $a = 0.35$ nm. However, the lattice parameters of gamma (fcc Ni) and gamma prime (ordered fcc Ni_3Al) are virtually identical. Therefore, their diffraction spots will be inseparable. This fact, along with relatively weak ordering spots, suggest this to be a gamma/gamma prime phase mixture with an appearance similar to many nickel-base superalloys.

TEM was also performed on Alloy G (Ni-35 a/o Al-5 a/o V) in order to explain the reason for its relatively high strength (Section 3.4.2) with respect to the rest of the Phase I alloys. Thin foils were prepared from tensile specimens deformed at room temperature and 760°C (1400°F). Figure 29 shows the microstructure to consist of equiaxed gamma prime particles located primarily at the grain boundaries and rod-shaped gamma prime particles in the interior of the grains. The matrix is ordered bcc (B2). This phase mixture is consistent with the Al-Ni-V phase diagram (Reference 13) (Figure

30). At higher magnification (Figure 31), the matrix exhibits a mottled structure which was observed in both undeformed and deformed samples. Electron diffraction revealed streaking along $\langle 011 \rangle$ directions in the $\langle 111 \rangle$ diffraction pattern (Figure 32). The $\langle 011 \rangle$ streaks are indicative of an instability in the matrix $\{011\}$ planes. Closer inspection of the gamma prime precipitates in the interior of the grain, along with diffraction results from the precipitates (Figure 33), indicates that the gamma prime particles are oriented along the matrix $\{011\}$ planes. Therefore, it appears that the $\langle 011 \rangle$ streaking in the matrix is associated with the instability toward formation of the gamma prime phase. In addition, the crystallographic relationship between the NiAl matrix and the gamma prime phase is $\langle 111 \rangle_{\text{NiAl}} / \langle 101 \rangle_{\gamma'}$, similar to that reported by Moskovic (Reference 14). The cause for the high strength of this alloy is still unclear; it may be related to the precipitation of gamma prime which may provide some strengthening effects.

3.4.2 Compressive Strength

The 0.2% yield strengths of the Phase I alloys were measured in compression, and results for the cast alloys are given in Figure 34. In general, the powder forms of the alloys are slightly stronger. There were no differences in strength based on alloy system except for the Ni-Al-Ti system which showed high strength. Instead, some individual alloys are strong. Alloy A (Ni-30 a/o Al-35 a/o Co) and Alloy G (Ni-35 a/o Al-5 a/o V) were the strongest of the tested Phase I alloys. The high strength of Alloy A is due to the large amount of cobalt in the alloy. CoAl is known to be stronger than its isostructural counterpart NiAl, and so a larger amount of Co in the NiAl phase should result in higher strength. On the other hand, the reason for the high strength of Alloy G may be related to precipitation of fine gamma prime particles.

The strongest of all Phase I alloys may actually be Alloy J (Ni-40 a/o Al-10 a/o Ti). However, it was not tested as it exceeded the load capability of the extrusion press. Therefore, the yield strength of this alloy was estimated from the extrusion data to be greater from 1275 MPa (185 ksi) at 1150°C (2100°F). A Ni₂AlTi-type Heusler phase was discovered by X-ray diffraction of a section of the cast material. This phase is very strong and must be responsible for the apparent high strength of Alloy J.

3.4.3 Deformability and Tensile Ductility

Tensile testing was performed on both as-extruded and heat treated (2 hours/1050°C/air cooled) forms of Phase I modified alloys. Results are summarized in Tables 7 and 8 and Figures 35 and 36. The fracture modes of these alloys are given in Tables 9 and 10, and typical fracture surfaces are shown in Figure 37. Tensile ductility at room temperature of any significant amount was only observed in the cast alloys of NiAlCo, A, B and C, all of which have martensitic characteristics. The powder forms of these alloys, however, showed little or no room temperature ductility. The powder forms of the NiAlFe alloys, E and F, showed some minor room temperature ductility although none was seen in cast form. The fracture modes of all Phase I alloys were similar in both cast and powder forms. The tensile properties are described in more detail, in terms of the alloy system, in the following sections.

3.4.3.1 NiAlCo Alloys

Note that, although the cast forms of Alloys A, B and C possess a modicum of room temperature ductility, these same alloys when produced in powder form are brittle (Table 8). At first inclination, one would suspect that the ductility loss in the finer grain powder materials can be attributed to a grain size phenomenon. Martensitic transformations can result in stress concentrations because of poor strain accommodation at the grain boundaries. The larger number of grain boundaries in the finer grain powder material may, therefore, result in an increase in brittleness. However, the powder alloys of A, B, and C, which were heat-treated in air at 1050°C for 2 hours, had similar grain sizes

to the as-extruded cast alloys but were still brittle. It is possible that the heat treatment in air introduced interstitials which may have counteracted the larger grain size.

The room temperature ductility in Alloys A, B, and C in extruded cast form is apparently linked to the operation of martensitic transformation mechanisms in these materials. Alloy C (Ni-29 a/o Al-21 a/o Co) was the most ductile with 2.2% elongation recorded at room temperature. Alloy D (Ni-35 a/o Al-10 a/o Co) was the only NiAlCo alloy to exhibit no elongation at room temperature. This is most likely due to its high Al content, which is well known to be a cause of brittleness in NiAl alloys. The room temperature ductility of Alloy B, while measurable, is low (0.3%) with respect to that of Alloys A and C (1.8 and 7.2%, respectively). Further, the fracture mode of Alloy B at room temperature is more intergranular than that of Alloys A or C (Tables 9 and 10).

Room temperature compression testing was performed on Alloys A, B, and C to further characterize their deformation behavior and cracking tendencies. These studies focused on potential martensitic transformation deformation mechanisms. The martensitic transformation is generally regarded as a deformation mode that competes with slip (Reference 15). In general, strain accommodation occurs by: (1) plastic deformation of tough martensitic grains, as seen in martensitic steels; (2) a stress-induced parent to martensite transformation; (3) nucleation of additional martensitic variants in the material; or (4) the growth of selected variants with a preferred orientation at the expense of non-preferred variants (Reference 16). The mechanisms will all be considered as the deformation behavior of Alloys A, B, and C are examined in more detail.

3.4.3.1.1 Deformation Behavior of Alloy A

Alloy A shows an equiaxed, homogeneous B2 grain structure with some grain boundary γ' in the as-extruded plus heat-treated (2 hours/1050°C/air cooled) condition (Figure 38). After 4.0% compressive strain at room temperature, extensive intergranular cracking occurs. This is in contrast to the tensile results which showed transgranular fracture (Tables 9 and 10). The grains in Alloy A are aligned along the extrusion direction, which is also the stress direction for the tensile and compressive testing. Therefore, there are more grain boundaries which experience a normal tensile stress in the compressed sample, explaining the shift to more intergranular cracking in the compression specimen. Stress-induced martensite (SIM) is observed in Alloy A after 4.0% strain at room temperature (Figure 38). Examination of the room temperature tensile stress-strain curves reveals evidence of SIM in tension also (Figure 39).

TEM was performed on Alloy A for further deformation microstructure characterization on specimens tested in compression at room temperature and 760°C (1400°F). A general description of the microstructures has been given in Section 3.4.1. It is evident from the deformation microstructures that, at room temperature, Alloy A deforms via the formation of dislocation bands, which are oriented along $[0\bar{1}1]$ and $[\bar{2}1\bar{1}]$ B2 directions (Figure 40). Further using the $\bar{g} \cdot \bar{b}$ invisibility criterion, the slip system in Alloy A was determined to be $\langle 111 \rangle \{011\}$ at room temperature. NiAl is known to slip via $\langle 100 \rangle \{011\}$ slip at room temperature, which does not satisfy Von Mises criterion for plasticity, which has been given as a cause of the brittleness of NiAl. However, the $\langle 111 \rangle \{011\}$ slip system of Alloy A does satisfy Von Mises criterion.

As much as 1.8% tensile ductility was recorded on Alloy A at room temperature. However, it is somewhat unclear whether the recorded ductility is due to a stress-induced martensitic transformation or to the change to a more favorable slip system for plasticity. However, based on the tensile stress-displacement curve shown in Figure 39 and the fact there was no macroscopic plastic yielding at a high stress prior to fracture, the measured elongation is considered to be attributable primarily to the apparent martensitic transformation strain.

3.4.3.1.2 Deformation Behavior of Alloy B

In the room temperature compression studies of Alloy B, the deformation of individual grains was monitored throughout the test by removing and photographing the specimen after different amounts of strain. Grain boundary cracking is seen to begin at yielding and more cracks are observed at higher strains (Figures 41 and 42). The cracking occurs primarily at the interfaces between the grain boundary borides and the martensitic grains. At 7.5% strain, the cracks have widened but appear to be halted by the martensitic grains. No martensitic transformation processes can be observed at these magnifications, but the blunting of cracks by the martensitic grains indicates reasonable toughness. TEM studies were, therefore, performed to examine the deformation of Alloy B in more detail.

TEM thin foils were prepared from compression specimens of Alloy B in the untested and tested at room temperature to 3% strain conditions. The undeformed microstructure has been described in Section 3.4.1 (see Figures 25 and 27). The microstructure consists of martensitic plates containing fine twin lamellae. The microstructure of Alloy B after room temperature compression to 3% plastic strain is shown in Figures 43 and 44. The fine twin lamellae are continuous across the martensitic plates, which is in contrast to the microstructure before deformation where the fine lamellae were discontinuous at the boundaries of the plates and formed a sharp angle with the lamellae of the neighboring martensitic plates (Figure 26). It is evident that, under compression, the martensitic structure of Alloy B accommodates the deformation by the formation and/or rearrangement of the fine twin lamellae within the larger plates. The plates themselves remain relatively unchanged, which is why there was no apparent martensitic mechanism observed in the optical studies. The rearrangement/formation of the lamellae must provide the toughness to the martensitic grains. However, the material ultimately fails because of cracking along the interface between the matrix and the grain boundary borides. The tensile results show Alloy B to have very little ductility and to be the only NiAlCo alloy to fail predominantly intergranularly in extruded cast form.

There are two potential explanations for the low ductility and change in fracture mode in Alloy B: the grain boundary borides and martensitic transformation temperatures below the DBTT (about 600°C). First, Alloy B is the only NiAlCo alloy with grain boundary borides rather than gamma prime. As noted above, cracks tended to nucleate at the interface between the boride and the martensitic grains. This grain boundary cracking is perhaps enhanced by the low M_s temperature in this alloy. Since the martensitic transformation occurs below the DBTT, the alloy cannot easily accommodate the strain incompatibilities across the grain boundaries resulting from the transformation. Stress concentrations result which can increase the susceptibility to grain boundary cracking and intergranular fracture.

3.4.3.1.3 Deformation Behavior of Alloy C

Alloy C possessed the largest amount of room temperature ductility (2.2%) of any alloy tested in this program. Further, as discovered in Phase II, it also possessed a remarkably high fracture toughness (Section 4.2.4). Therefore, compression studies were performed to evaluate the deformation of Alloy C in more detail. The change in microstructure of individual grains was monitored periodically throughout a room temperature compression test via optical metallography. No change was observed in the microstructure prior to yield. However, following plastic yield, linear features began to appear perpendicular to existing martensitic plates, which intersected those plates (Figures 45 and 46). These features appear primarily in martensitic plates oriented parallel to the direction of the applied stress and the number of the features increased with increasing strain. Further examination of these features led to the proposition that these represented cross-twinning of the martensite, i.e., new martensitic variants, which intersect the existing variants, nucleate to accommodate the

deformation. Delaey, et al. (Reference 17) have shown the formation of similar intersection of martensitic plates in a CuZn alloy, which is isostructural with NiAlCo martensite. Some cracking also occurred in Alloy C, but not until about 9% strain and the cracks were confined to the interface between the martensitic grains and the grain boundary gamma prime.

In order to further study the martensitic deformation of Alloy C, TEM foils were taken from compression specimens, both untested and after compression at room temperature to 8% strain. The undeformed microstructure was described in Section 3.4.1. An example of the crossing martensitic variants is shown in Figure 47.

These variants appeared only after plastic yielding of the material. The other NiAlCo alloys fractured prior to or just at yield. Therefore, the fracture strength of Alloy C must be higher than the other NiAlCo alloys in order to allow yielding and the post-yield martensitic processes to occur. The tensile fracture strengths recorded for Alloy C are 820 and 587 MPa for the as-extruded and heat-treated forms of the alloy, respectively. The measured compressive yield strength is 754 MPa. Therefore, the high fracture strengths, i.e., high toughness, of Alloy C allows the material to take advantage of the post-yield martensitic transformation processes.

3.4.3.2 NiAlFe Alloys

Alloys E (Ni-33 a/o Al-28 a/o Fe) and F (Ni-33 a/o Al-20 a/o Fe) are both essentially single phase B2 alloys containing fine Fe-rich particles. Neither alloy exhibited any room temperature ductility in cast form (Table 7 and Figure 35). However, both alloys exhibited a small amount of plastic elongation at room temperature when produced in powder form (Table 8 and Figure 36). Both Alloys E and F also exhibited an unusual ductility dependence with temperature, with a local ductility maximum at about 540°C and a local ductility minimum at about 760°C. Similar ductility dependence has been reported in the literature for FeAl alloys (Reference 18). In FeAl, the initial brittle-ductile transition has been attributed to the activation of $\langle 111 \rangle$ slip and the intermediate loss of ductility attributed to the onset of grain boundary cavitation and the presence of mostly $\langle 100 \rangle$ type slip in the material. The observed resumption of increasing ductility with increasing temperature was attributed to the activation of diffusion-assisted processes at these higher temperatures. The initial brittle-ductile transition in Alloys E and F occurs at about 400°C to 500°C while the subsequent brittle-ductile transition occurred at about 750°C. The slip characteristics of Alloys E and F were not determined in this program, so a complete comparison with FeAl cannot be made.

3.4.3.3 NiAl(V, Cr) Alloys

The alloys in the NiAl(V, Cr) system were formulated with the intention of lowering the ordering energy of the lattice and potentially modify the slip behavior to $\langle 111 \rangle$ type in order to satisfy Von Mises criterion for general plasticity. Previous work with chromium and manganese modified alloys succeeded in modifying the slip behavior of NiAl. However, the resultant materials were still brittle (References 1 and 6). Vanadium additions (alone or in conjunction with chromium) apparently follow the same trend and perhaps cause an even greater change in order to achieve room temperature ductility. Unfortunately, no ductility was observed in the V and Cr modified alloys, G and H (Tables 7 and 8 and Figures 35 and 36). In fact, extensive cracking in Alloy H prohibited testing in the heat-treated condition (2 hours/1050°C/air cool). The fracture modes in both alloys were transgranular cleavage at lower temperatures in both cast and powder forms (Tables 9 and 10).

3.4.3.4 NiAlTi Alloys

Alloy I (Ni-35 a/o Al-5 a/o Ti) was the only alloy of this system tested in this program for Alloy J (Ni-40 a/o Al-10 a/o Ti) was unextrudable up to 1150°C (2100°F) as it exceeded the load capability of the extrusion press used. However, cylindrical compression specimens were wire electrical discharge machined from a portion of the cast material for testing. These compression specimens fractured prior to yielding up to 760°C, indicating no hope of room temperature tensile ductility. X-ray diffraction indicated the presence of a Heusler phase (Table 4) which seems to be responsible for the brittleness. No ductility was observed in the cast alloy at room temperature; however, the heat-treated form of the powder alloy elongated about 1% at room temperature and 540°C (Tables 7 and 8 and Figures 35 and 36). Both alloy forms fractured transgranularly up to the DBTT at about 700°C (Tables 9 and 10).

4. PHASE II ALLOYS

Two series of alloys were explored in Phase II of this program, both of which were based on the two best alloys from Phase I, Alloys A and C. The first series consisted of ternary alloys selected to further explore martensitic toughening in the NiAlCo system. The second series involved the addition of Hf and Ti to Alloys A and C in order to enhance the strength and creep resistance of the alloys. The rationale for alloy selection is described below and summarized in Table 11.

4.1 ALLOY SELECTION

The alloys selected for Phase II (Table 11) study were based primarily on positive results of Ni-Co-Al alloys from Phase I of the program. Alloys were formulated with the intention of exploring further ductilizing within the NiAl-Co system and utilizing the techniques of strengthening via solid-solution and precipitation hardening. In addition, toughening of a brittle matrix with superalloy particle additions was also considered. Ten alloys were evaluated in Phase II of this program, and the rationale behind the selection of the specific methods and alloys is explained in the following sections.

4.1.1 Macroalloying for Toughening

Alloys of the Ni-Co-Al system showed the most promise for room temperature elongation in Phase I of this program. The best alloys were Alloy A (Ni-30 a/o Al-35 a/o Co) which undergoes a stress-induced martensitic transformation, and Alloy C (Ni-29 a/o Al-21 a/o Co) which has an M_s temperature of about 700°C. Based on these promising alloys, four alloy compositions were formulated for Phase II of this program and are identified as A2, A3, C2, and C3.

The "A-series" alloys (A2 and A3) were based on Alloy A and were designed to utilize the stress-induced martensitic transformation and the associated transformation strains in order to obtain room temperature ductility in the material. With proper control of texture, NiAl-base materials have been known to produce as much as 13% elongation owing solely to transformation strains (References 7 and 8). Also, the alloys were formulated with slightly higher aluminum contents than Alloy A in order to gain a 13% to 14% weight savings over the current superalloys. The "C-series" alloys (C2 and C3) were based on Alloy C, which exhibited the most room temperature elongation of all the Phase I alloys. Alloys C2 and C3 were formulated with similar M_s temperatures to Alloy C, but with slightly higher aluminum contents for lower density, resulting in an estimated weight savings of 12% to 13% over current superalloys. In addition to the above alloys, another alloy in the Ni-Co-Al system was proposed for Phase II and is designated B2. In Phase I, Alloy B (Ni-30 a/o Al-25 a/o Co-0.25 a/o B) also showed some promise. However, the alloy failed prematurely because of cracking along the boride-matrix boundaries (see Section 3.4.3.1.2). Therefore, elimination of boron may improve the ductility of this alloy.

4.1.2 Macroalloying for Strengthening

The purpose of Phase II was to alloy for a more useful balance of properties, including strength. In the previous NiAl development program (Reference 1), it was determined that of all the alloying additions investigated for NiAl, titanium, and hafnium were the most potent strengtheners. Therefore, Alloys AT, CT, AH, and CH were formulated with the intention of using titanium and hafnium to strengthen the somewhat ductile Ni-Co-Al Alloys A and C. The amounts of titanium and hafnium added to Alloys A and C were based on the results of the previous program and were intentionally kept small so as to avoid degrading the ductility of the alloys as much as possible, while still being able to provide sufficient strengthening.

4.1.3 Compositing with Superalloy Additions

In Phase II, compositing with superalloy particles was used in an attempt to both toughen and strengthen NiAl-base alloys. The reinforcing material, MERL 76, is a nickel-base superalloy with elongations of greater than 20% through 815°C (1500°F). In addition, its tensile yield strength is greater than 960 MPa (140 ksi) to about 700°C (1290°F) and remains greater than 620 MPa (90 ksi) to 815°C (1500°F). If this material showed promise, it was proposed to make the material again, but with coated superalloy particles in order to prevent degradation of the composite structure during fabrication and service at temperature. The superalloy addition would be coated with a stable oxide (either alumina or yttria) to act as a diffusion barrier between the constituents. M1 was formulated as a baseline test of this compositing approach for the NiAl system. Stoichiometric NiAl was chosen for the matrix because of its low density.

4.2 RESULTS AND DISCUSSION

4.2.1 Alloy Characterization

Chemical analysis was performed on the received ingots of Phase II alloys, and the results are summarized in Table 12. As with the Phase I alloys, the aluminum compositions are higher than the aim (by 0.5 to 2 a/o) while the cobalt values are low (by 0.4 to 1.7 a/o). X-ray diffraction analysis was performed on Phase II alloys in the extruded plus heat-treated condition (2 hours/1050°C/air cool), and the results are given in Table 13. The X-ray results confirm the phases expected from the available phase diagrams. Although Alloys AT and CT were formulated for precipitate strengthening, the presence of strengthening precipitates was not detected by X-ray diffraction.

Recall that the ternary Phase II alloys were based on promising room temperature ductility results from Phase I NiAlCo Alloys A and C. Martensitic transformation mechanisms were determined to play a role in the enhanced room temperature properties. Therefore, martensitic transformation temperatures were determined for the ternary NiAlCo alloys using dilatometry, and results are given in Table 14. Note that all but Alloy A2 are martensitic at room temperature. Alloy A2 transforms just below room temperature ($M_s \approx 15^\circ\text{C}$) and was used to further explore stress-induced martensite at room temperature.

Metallography was performed on the extruded Phase II ingots and the powder composite of M1; the results are presented in Table 15 and Figures 48 through 56. The ingot of Alloy AT is very brittle and was unextrudable. Metallography of this alloy was, therefore, performed only on the cast ingot (Figure 57).

The microstructures of the quaternary NiAlCo(Hf, Ti) alloys were not all as planned. In particular, Alloys AT (Ni-30 a/o Al-32.5 a/o Co-5 a/o Ti) and CT (Ni-29 a/o Al-21 a/o Co-5 a/o Ti) were both formulated with the intention of forming strengthening precipitates. However, none were observed with either optical metallography or X-ray diffraction. Further, among the ternary NiAlCo alloys, Alloy A3 (Ni-32 a/o Al-25 a/o Co) was intended to have an M_s temperature just below room temperature in order to undergo a stress-induced martensitic transformation. Instead, it turned out to be martensitic with an M_s temperature just above room temperature.

The composite mixture, M1, consisting of MERL 76 superalloy particles in an NiAl matrix, was formulated for toughening. Figure 56 shows the composite mixture microstructure after extrusion with and without a subsequent heat treatment (2 hours/1050°C/air cooled). Relatively little interaction occurred between the superalloy particles and the NiAl matrix during the extrusion consolidation

process, but extensive reaction after the heat treatment formed what is assumed to be Ni_3Al . A coating of alumina or yttria on the superalloy particles should prevent the reaction, but this was not pursued since the mechanical properties of the mixture did not show great promise (see Section 4.2.2.3).

In addition to the optical metallography, more detailed characterization with TEM was performed on Alloys AH (to explain its high-temperature strength), CT (to look for strengthening precipitates) and C3 (to discover the cause of its low-temperature strength).

Thin foils of Alloy C3 (Ni-30 a/o Al-15 a/o Co) were prepared from a compression specimen that had been tested at room temperature. TEM analysis confirmed the identification of the martensitic L_{10} and gamma prime L_{12} phases as reported by X-ray diffraction, similar to those of Alloy C from Phase I (Section 3.4.1). However, an interesting difference between this alloy and both isostructural Phase I Alloys B and C is seen in the nature of the fine twin lamellae contained within the larger martensitic laths of the matrix (Figures 58 and 59). All three alloys contain the fine, parallel, twin-related lamellae within the laths, but the lamellae in Alloy C3 are of a much finer scale than in either of the other two alloys. The widths of the lamellae in Alloys B and C vary from 30 to 130 nm, while the lamellae in Alloy C3 are 3.5 to 5 nm wide – a factor of 6 to 37 difference. Possible effects this may have on strength are discussed in Section 4.2.3.1.

In order to look for the presence of strengthening Heusler precipitates, thin foils of Alloy CT were cut from compression specimens which were tested at room temperature and 760°C (1400°F). Optical metallography and X-ray diffraction of these specimens indicated the presence of only ordered bcc (B2) and gamma prime (L_{12}) phases (Figures 55 and 60a), with lattice parameters of $a = 0.288$ and $a = 0.36$ nm, respectively, as determined by electron diffraction (Figure 61). At room temperature, the gamma prime (20 v/o) appears primarily at the grain boundaries as stringers or in regions containing very fine equiaxed grains (Figure 62). Small isolated grains of gamma prime occasionally are seen away from the grain boundary. At 760°C (1400°F), the test specimen underwent a heating cycle equivalent to slow heating to 760°C (at approximately $15^\circ\text{C}/\text{minute}$), holding at 760°C for about 5 minutes, followed by furnace cooling (at about 5°C to $10^\circ\text{C}/\text{minute}$). After this process, the amount of gamma prime increased from 20 to about 40 v/o, much of which is rod-shaped with the rod axis randomly oriented with respect to the matrix in the interior of the grains (Figure 63). The composition of the gamma prime at both the grain boundaries and within the grains is given in Table 16. No Heusler phase was found in either condition, indicating the solubility of Ti to be greater than 5a/o in Ni-29 a/o Al-21 a/o Co at room temperature and 760°C .

Alloy AH (Ni-30 a/o Al-34.5 a/o Co-0.5 a/o Hf) was examined in TEM after compression testing at both room temperature and 760°C (1400°F). These results can be compared to those of Phase I Alloy A (Ni-30 a/o Al-35 a/o Co) which was studied under the same conditions (Section 3.4.3.1.1) and is similar to AH but without the Hf addition. Optical micrographs of Alloy AH after testing at both temperatures are shown in Figures 64 and 65. Like Alloy A, the room temperature specimen matrix was identified via electron diffraction as ordered bcc (B2) containing some tweed structure and diffuse streaking in the $[1\bar{1}2]$ and $[1\bar{1}\bar{2}]$ B2 directions in the (110) B2 diffraction patterns. The tweed structure and streaking are indicative of pre-martensitic phenomena and, in fact, stress-induced martensitic laths are occasionally encountered as well in both alloys. Blocky precipitates were found along the grain boundaries of Alloy AH, similar in appearance to Alloy A (Figure 64). However, the precipitates were found to be Hf-rich hexagonal precipitates, not gamma prime as in Alloy A. Evidently, Hf is relatively insoluble in NiAlCo and forms Hf-rich precipitates at the expense of gamma prime.

At 760°C (1400°F), the microstructure of Alloy AH has changed (Figure 65). Evidently, the alloy is now in a three-phase region of its phase diagram with the addition of a disordered fcc (A1) phase at the grain boundaries at the expense of some of the hexagonal (A3) grain boundary precipitate

(Figure 65b). In addition, a small amount (about 8 v/o) of rod-shaped precipitates with a hexagonal crystal structure (A3) now also appear in the matrix (Figure 65a). Recall (Section 3.4.1) that A1 precipitates were also found in the 760°C (1400°F) sample of Alloy A, but to a much larger extent, indicating that it is also in a three phase region at this temperature (see Table 17).

The compositions of the phases present in both Alloys A and AH at 760°C (1400°F), as determined by analytical electron microscopy, are given in Table 18. Of primary interest is the apparently very low solubility of Hf in the NiAlCo B2 and A1 phases in Alloy AH. All the Hf appears to be within the hexagonal (A3) phase. This is consistent with the work of Vedula, et al. (Reference 19) who reported low Hf solubility in NiAl alloys, resulting in Hf-rich particles in NiAl-Hf alloys. The presence of the Hf-rich precipitate also serves to alter the remaining matrix composition. Using the measured composition and volume fraction (8%) of the precipitate, the remaining composition of the alloy can be calculated and determined to be 34.7 a/o Ni-32.6 a/o Al-32.7 a/o Co. This composition appears to be in a two-phase fcc (A1) and ordered bcc (B2) region of the NiAlCo phase diagram (Figure 19), which is the reason no gamma prime is found in this alloy.

4.2.2 Tensile Properties

The Phase II alloy compositions were based on Phase I Alloys A and C, which exhibited 1.8 and 2.2 % ductility at room temperature, respectively. The ternary NiAlCo alloys (A2, A3, C2, C3) were formulated to extend the ductility to alloys with higher Al contents and, therefore, lower densities. The quaternary NiAlCo (Hf, Ti) alloys (AH, CH, AT, CT) were formulated with the intention of maintaining the ductility while improving the strength and creep resistance of the alloys. Finally, the composite mixture M1 was formulated in order to explore superalloy reinforcement of NiAl as an alternative to alloying. In general, both increasing the Al content and additions of Hf and Ti resulted in degradation of the room temperature ductility observed in Alloys A and C. Further, the composite mixture properties were no better than some of the ternary NiAlCo alloys.

No apparent plastic yielding was recorded in any Phase II alloy at temperatures below 540°C (1000°F) as indicated by the stress-strain curves. However, large tensile elongations were recorded in all the alloys tested at temperatures of 760°C (1400°F) and above, indicating the ductility transition to be between 540°C and 760°C. In spite of the lack of yielding in the stress-strain curves, some of the Phase II alloys exhibited small tensile elongations at room temperature as calculated from measured spacings of lines scribed on the gage sections before and after the tensile tests. Since the stress-strain curves showed no apparent yielding of the material, the measured strains must have accumulated during the loading prior to yielding. This "pre-yield" strain is thought to be associated with the martensitic transformation in these alloys. The origin of this phenomenon is discussed in greater detail in Section 4.2.5.1.

4.2.2.1 Ternary NiAlCo Alloys

Tensile properties of the ternary NiAlCo alloys modified for enhanced lower temperature ductility and toughness were determined and results are given in Table 19 and Figure 66. As previously discussed, all the specimens tested at 540°C (1000°F) and below, fractured without yielding. However, the as-extruded form of Alloy A3 and the heat-treated form of Alloy C3 each elongated a small amount (0.6% and 1.3%, respectively) at room temperature as calculated from scribe marks on the specimens measured before and after testing. These alloys were based on Phase I Alloys A and C which elongated 1.8% and 2.2%, respectively, at room temperature. Evidently the increased Al and/or decreased Co contents degrades the room temperature ductility. Further, the observed ductility in Alloy A was attributed to a stress-induced martensitic transformation which was evident in both the shape of the stress-strain curve and in the microstructure. This was not seen in any Phase II alloys,

not even in Alloy A2 which has an M_s temperature of about 15°C. However, the elongations in Alloys A3 and C3 are attributed to "pre-yield" martensitic phenomena as discussed in detail in Section 4.2.5.1.

4.2.2.2 Quaternary NiAlCo(Hf, Ti) Alloys

Tensile properties of Phase II alloys modified for improved strength and creep resistance (Alloys AH, CH and CT) are recorded in Tables 20 and 21. Tensile testing was not performed on Alloy AT as it was extremely brittle and broke apart during machining prior to extrusion, although based on this experience, no low temperature ductility is expected in Alloy AT. Small Hf and Ti additions were used for these Phase II alloys in the hope that the ductility observed in the baseline alloys A and C could be maintained. Unfortunately, the Hf and Ti additions to Alloy C (in CH and CT, respectively) succeeded in totally eliminating the room temperature ductility, while the addition of 0.5 at% Hf to Alloy A (in AH) reduced the room temperature ductility by 50%. TEM results after compression at room temperature of Alloy AH revealed the presence of stress-induced martensite (Section 4.2.3.2.1), although no martensitic discontinuity was seen in either tensile or compressive stress-strain curves. However, the recorded tensile ductility is apparently due to the operation of martensitic transformation mechanisms in Alloy AH.

4.2.2.3 Composite Mixture of NiAl + Ni-Base Superalloy

Tensile results on the extruded powder mixture composite, M1, do not show any room temperature ductility (Table 22). However, in both the as-extruded and heat-treated forms of the material, ductility was observed at 540°C (1000°F), which is consistent with stoichiometric NiAl which has a DBTT of 400 to 500°C (Reference 1).

It is also interesting to compare the tensile yield strengths of the as-extruded and heat-treated forms of this material above the DBTT (Table 22). The heat-treated form of the material is 77% stronger at 760°C (1400°F) and 20% stronger at 980°C (1800°F) than the as-extruded material. Recall (Section 4.2.1) that the superalloy particles reacted with the NiAl matrix to form an intermediate Ni_3Al -type phase during the heat treatment. The difference in strengths between the two forms of material can perhaps be attributed to gamma prime strengthening effects.

4.2.3 Compressive Strength

Compression testing was performed on Phase II alloys in heat-treated form (2 hours/1050°C/air cool) to determine the yield strengths of the materials below the ductility transition temperature. The results are summarized in Tables 23 and 24 and Figures 67 and 68 along with yield strengths of the alloys at higher temperature for additional reference. The strengths of Alloys A and C, upon which the Phase II alloy compositions were based, are also provided for comparison. The Phase II alloys consisted of a series of ternary NiAlCo alloys formulated for room temperature ductility and toughness, a series of quaternary NiAlCo(Hf, Ti) alloys formulated for strength and creep resistance, and a composite powder mixture of NiAl and a Ni-base superalloy. These series are treated separately below.

4.2.3.1 Strengthening Mechanisms in NiAlCo Alloys

There are notable differences between the strengths of the various ternary NiAlCo alloys as seen in Table 23 and Figure 67. The room temperature strength trends appear to be related to the phase structures, and the alloys can be divided into four separate categories by strength/structure. First, the weakest of the alloys are A3 and B2, both of which have unstable structures with respect to a martensitic transformation at room temperature. In Alloy A3, this is evidenced by a partially

transformed structure, while Alloy B2 has shown instability in the form of extensive pre-yield deformability (Section 4.2.5.1). The next two categories of alloys are those with a stable martensitic structure (Alloys C and C2) and those with a stable B2 structure (Alloys A and A2). From the compression data, it is evident that at room temperature, the B2 structure is stronger than the martensitic structure as expected. Finally, Alloy C3 has the highest room temperature strength of all the ternary alloys tested in this program, and it also contains the largest volume fraction (30 to 35 v/o) of gamma prime which is most likely responsible for the high strength. However, owing to the blocky nature and incoherence of the gamma prime precipitate in the $L1_0$ matrix, the recorded strength is abnormally high. Therefore, TEM was used to further investigate the reasons for the abnormally high strength of Alloy C3.

TEM thin foils of Alloy C3 were prepared from a compression specimen that had been tested at room temperature. The microstructure is described in detail in Section 4.2.1. The most striking feature of the microstructure was that the fine twin lamellae within the larger martensitic laths were a factor of 6 to 37 times narrower than those seen in Alloys B and C. The lamellae are twin-related and so, in a given area, we see a much greater number of twin boundaries in Alloy C3 than in Alloys B and C. It is possible that a large number of twin boundaries may resist propagation of dislocations through the alloy and therefore provide strengthening, but this would only be effective at temperatures below the martensitic transformation temperature of the material. The A_s temperature of Alloy C3 is about 330°C, but high strength is still observed at 540°C (1000°F) and above. Therefore, the narrower lamellae, and hence increased number of twin boundaries, cannot totally account for the high strength of this alloy. Perhaps there is a combined effect with the gamma prime in the alloy.

At the highest test temperature of 980°C (1800°F), the strengths of the ternary NiAlCo alloys are all rather low and fall within a narrow range. In this case, no microstructure-strength relationship can be established. However, at the next highest test temperature of 760°C (1400°F), there are considerable differences in strengths among the alloys. It is particularly interesting to examine the 760°C yield strengths of Alloys A, B2 and C3, which are 316, 195 and 303 MPa, respectively. The compositions of Alloys A, B2 and C3, which have the same Al contents, differ only in the nickel-to-cobalt atom ratios which are 1.0, 1.8 and 3.7, respectively. The lowest yield strength is associated with the intermediate cobalt content. Note that at 760°C, the phases present in these alloys are primarily of the B2 and $L1_2$ types. For a given aluminum content, the amount of the $L1_2$ phase decreases with increasing cobalt content. The higher strength of Alloy C3, which has the lowest cobalt content, may well be related to the largest quantity of $L1_2$ precipitate formed in this alloy. On the other hand, Alloy A is as strong and has equiatomic concentrations of nickel and cobalt. The high strength of Alloy A is thought to be related to the higher strength of the (Ni,Co)Al B2 phase. The B2 phase CoAl is known to be stronger than NiAl (Reference 20). Therefore, a higher Co (Ni,Co)Al B2 phase should possess higher strength than an equivalent lower Co (Ni,Co)Al phase.

In summary, it appears as if the room temperature strengths of ternary NiAlCo alloys are controlled by the phase structures and stabilities of these structures and, in general, stable B2 alloys are stronger than stable martensitic alloys. At higher temperatures, the Co content appears to control the strengths of the alloys. At high Co contents, a stronger B2 phase may be providing strength, while at low Co contents, the presence of gamma prime appears to be important. A strength minimum appears at intermediate Co contents where neither of the two above circumstances applies.

4.2.3.2 Strengthening Mechanisms in Modified NiAlCo Alloys

The second series of alloys was formulated for purposes of strengthening via mechanisms of solid-solution strengthening with Hf additions (Alloys AH and CH), precipitate strengthening with Ti additions (Alloy CT) and particulate composite strengthening/toughening with MERL 76 superalloy additions to stoichiometric NiAl (Alloy Mixture M1). Unfortunately, the Hf did not remain

in solution in Alloy AH and no precipitates were observed in Alloy CT (Section 4.2.1). Compressive yield strength data for these alloys are listed in Table 24 and plotted in Figure 68 along with Alloys A and C, upon which they are based, for comparison.

4.2.3.2.1 Effect of Hf Additions

Hf additions were made to Alloys A (in AH) and C (in CH) for solid solution strengthening purposes. Hf appears to have a high temperature strengthening effect on both Alloys A and C as seen in the results for Alloys AH and CH (Table 24). For example, at 760°C (1400°F) Alloy CH is 96% stronger than Alloy C while Alloy AH is about 30% stronger than Alloy A. Alloy A is much stronger than Alloy C at 760°C to begin with, so the strengthening effects of the Hf were not expected to be as large. However, the room temperature strength of Alloy C is actually much larger than that of Alloy CH. Alloy C contains a larger amount of gamma prime (25 to 30 v/o) than Alloy CH (20 v/o) which may have had an effect on the room temperature strength. At room temperature, the strengths of Alloys A and AH are similar. Therefore, the Hf strengthening effects must be confined to higher temperatures.

Among all the alloys tested in this program, Alloy AH possesses the best balance of high and low temperature strengths. Therefore, in order to examine this alloy further, thin foils were cut from Alloy AH which had been tested in compression at both room temperature and 760°C (1400°F) for TEM studies. The high- and low-temperature microstructures were characterized thoroughly and presented previously in Section 4.2.1. Recall that at room temperature, Alloy AH contains an Hf-rich hexagonal grain boundary phase in a B2 matrix, but no gamma prime as seen in Alloy A. At 760°C, the grain boundary precipitate is reduced in size and replaced, in part, by a disordered fcc (A1) phase. In addition, a small amount (about 8 v/o) of rod-shaped hexagonal precipitates appeared in the matrix. The presence of the Hf-rich precipitate served to alter the remaining alloy composition such that it was in a B2 + A1 region of the phase diagram and was closer to the CoAl side of the B2 (Ni,Co)Al phase field, providing additional strengthening at all temperatures.

At 760°C (1400°F), the only major notable difference between Alloys A and AH (besides the phases present) is the larger number of dislocations observed in Alloy AH as compared to Alloy A (Figures 22 and 65). In addition, the dislocations in Alloy AH exhibit more curvature than those in Alloy A. In a study by Vedula, et al. (Reference 19), Hf was shown to strengthen NiAl. It was postulated that the strengthening was due to the interaction of dislocations and insoluble Hf particles. In the present work, though, pinning of dislocations of the Hf-rich precipitates in Alloy AH was not observed. However, the large number of dislocations in Alloy AH indicates less recovery in this material. Perhaps this is related to the CoAl characteristics of the (Ni,Co)Al phase rather than any precipitate effects.

4.2.3.2.2 Effect of Ti Additions

Contrary to the highly temperature-dependent strengthening effect of Hf as previously described, Ti additions to Alloy C as seen in Alloy CT appear to have significant strengthening effects at all temperatures (Figure 68 and Table 24). Although Ti was added in order to form strengthening precipitates (e.g., Heusler), aside from gamma prime, no precipitates were noted in Alloy CT as determined by metallography, X-ray diffraction and TEM (Section 4.2.1). Further, the amount of gamma prime in Alloy CT is less than or about the same as Alloy C. Therefore, the Ti is thought to provide strengthening via solid solution mechanisms.

4.2.3.2.3 Effect of Superalloy Particle Compositing

About 20 v/o of Ni-base superalloy (MERL 76) particles were added to a binary stoichiometric NiAl matrix for the purpose of particulate strengthening and toughening. Compressive yield strength data for the mixture are given in Table 24 along with data for binary NiAl. It is evident that the superalloy additions succeeded in strengthening the alloy at all temperatures as expected, but not to as significant an extent as the alloying additions of Ti and Hf when the increases in strength per unit addition are compared. Further, Section 4.2.4 shows that the fracture toughness at room temperature was not significantly improved either. Additional development of this approach would require coating of the particles to prevent reaction with the matrix. However, since the mechanical property gains from such an approach do not appear to be significant, further development of this approach was not pursued.

4.2.3.2.4 Summary of Strengthening Approaches

It appears from this work that Hf is a very potent strengthener of NiAlCo alloys, especially at high temperatures, although the strengthening mechanism is unclear. Precipitate strengthening with Ti may be a viable approach; however, more Ti (> 5 a/o) is needed to produce strengthening precipitates such as the Heusler phase. Unfortunately, the Hf-modified Alloy AH and Ti-modified Alloys AT and CT are brittle in tension at room temperature, which may discourage further strengthening developments through alloying.

4.2.4 Room Temperature Fracture Toughness and Fracture Energy

Fracture toughness testing was conducted at room temperature on selected binary and cobalt-modified ternary alloys using pre-cracked, chevron-notched specimens. All the binary NiAl alloys were tested in the as-extruded condition and the ternary NiAlCo alloys in the heat treated condition (2 hours/1050°C/air cooled) as well, except for alloys A, B, and C, which were tested only in the as-extruded condition. The binary alloys tested under these conditions were Ni-43 a/o Al and Ni-50 a/o Al, both of which are single-phase B2 alloys, while most of the ternary alloys contained martensite and gamma prime. It is of interest to compare the fracture toughness of ternary NiAlCo alloys with binary NiAl alloys on an isostructural basis. Binary alloys with lower aluminum contents which undergo a martensitic transformation were studied by Kumar and Mannan (Reference 21). These alloys were prepared by hot-pressing of pre-alloyed powders, and their fracture toughnesses were determined in the as-hot pressed condition using chevron-notched cylindrical specimens (Reference 22). The data from these alloys are given along with those of this program in Table 25.

The fracture toughness represents the critical stress intensity for propagating a crack. It is calculated from the load required for a precrack of a specified length to begin propagating through the material. A related value is the fracture energy, which represents the total energy required to propagate the crack through the material and is calculated from the area under the load versus load-point displacement curve. In addition, as shown in Section 4.2.5, the shape of the load-displacement curve itself provides important clues to the martensitic toughening mechanisms. These items are discussed in terms of microstructure and phase structures in the following sections.

4.2.4.1 Binary NiAl Alloys

Table 25 shows that the fracture toughness of binary NiAl alloys is 4 to 9 $\text{MPa}\sqrt{\text{m}}$ and is relatively independent of aluminum content in the range of 37 to 50 a/o Al. In addition, small boron additions have little effect on the room temperature fracture toughness. The microstructures observed in all the

binary alloys consist entirely of a single B2 phase. However, the B2 phase in the binary alloys with the lowest aluminum contents (37 and 38.5 a/o) tends to be unstable at room temperature under stress since the M_s temperatures of these alloys are close to room temperature. In fact, martensite was observed in electron microscopy to form at a crack tip in thin foil samples of Ni-37 a/o Al (Reference 23). The slightly higher fracture toughnesses of the binary alloys Ni-37 a/o Al and Ni-38.5 a/o Al can, therefore, be attributed to a stress-induced transformation occurring in these alloys during the fracture toughness testing.

Fracture energies were only able to be determined for Ni-43 a/o Al and Ni-50 a/o Al because of the nature of the testing technique used on the lower Al alloys. The fracture energies were calculated to be 3 to 7 N-cm/cm² for these alloys, providing a baseline for comparison for the various NiAlCo alloys.

4.2.4.2 Cobalt-Modified Ternary Alloys

The fracture toughness and energy of fracture, given in Table 25, show that the ternary alloys studied are generally more fracture resistant than the binary alloys. However, there are considerable variations among the ternary alloys. The fracture toughness of the best ternary alloy (C) is about 3 times higher, and the fracture energy about 20 times higher, than the highest values measured in the binary alloys. In contrast, the fracture toughness values of the ternary alloys A2, A3, B, and D are marginally superior and their fracture energy values only several times higher than the highest values measured in the binary alloys.

To gain insight into the origin of these differences, the fracture behavior of the binary and ternary alloys during the fracture toughness testing and the effect of microstructure on the fracture resistance will be discussed. Discussion on the binary alloys is limited to the alloys with stable B2 phase since load-load point displacement data, which can be directly compared with those from the ternary alloys, are available only on these alloys. Typical load-displacement data for such alloys are reproduced as Curve B in Figure 69, which shows that the load in the chevron-notched precracked specimen increases monotonically with the displacement until a critical level is reached when the crack becomes unstable and propagates rapidly, resulting in an abrupt decrease in load. Such behavior is rather typical of brittle materials. In contrast, the fracture behavior of the cobalt-modified alloys is quite different. The fracture characteristics of such alloys are best illustrated by the load-displacement data from a more fracture-resistant alloy (Alloy B2) which is shown as Curve A in Figure 69. Two significant differences are obvious: an apparent "yielding" at a low stress during loading and a gradual decrease in load after the maximum is reached. The apparent yielding is thought to be associated with the onset of martensitic deformation or stress-induced martensitic transformation for alloys with unstable B2 phase at the crack tip zone. The plastic deformation at the crack tip zone continues after yielding by martensitic mechanisms and, at higher stresses, may include dislocation slip activities as well until a critical stress intensity is reached. The gradual decrease in load after the load peak suggests significant crack-tip plasticity also occurs during the crack propagation stage, presumably by a similar mix of martensitic and dislocation mechanisms as in loading. High plasticity at the crack tip generally results in blunting of the crack and contributes toward crack resistance.

Although the fracture behavior of all the ternary NiAlCo alloys in Table 25 shares the characteristics of Alloy B2 just described, there are considerable variations in the measured fracture resistance among them. For example, the K_{IC} of Alloy B2 is about 2 times higher and the fracture energy 5 times higher than for the isostructural alloys A3 and D. There is no obvious correlation of these differences with processing (as-extruded versus 2 hours/1050°C heat treatment) and grain size in these alloys. However, important differences in the fracture behavior of the precracked specimens of Alloy B2 and Alloys A3 and D as a group have been noted. In Alloys A3 and D, the yielding is much less pronounced and the crack propagated considerably faster as evidenced by considerably faster rates of load

decrease. This led to the conclusion that the differences in fracture behavior among the martensitic alloys are related to the intrinsic deformability and fracture resistance of the martensitic phase. This topic is discussed further in Section 4.2.5.

4.2.4.3 Cobalt-Modified Quaternary Alloys and NiAl Composite

This section focuses on the fracture toughness values of the Hf and Ti-modified alloys AH, CH and CT as compared to their baseline alloys A and C and the composite mixture M1 (Table 26). In Alloys AH, CT and M1, the fatigue precracking did not result in a linear crack front as specified by the ASTM standards. In these cases, average positions of the precracks were used in the fracture toughness calculations. Therefore, the fracture toughness value does not qualify as a K_{IC} number and is referred to as K_{max} . These values should be used cautiously.

As previously discussed (Section 4.2.3.2.1), Alloy AH represents a significant strengthening advantage over Alloy A at high temperatures. However, based on the tensile ductility results, the addition of Hf embrittled the material at room temperature. Further, the fracture toughness value dropped from 18.5 for Alloy A to 10.9 $\text{MPa}\sqrt{\text{m}}$ for Alloy AH. Following the same trend, the fracture energy dropped from 77 to 12 $\text{N}\cdot\text{cm}/\text{cm}^2$. This value for Alloy AH is still higher than for the best binary alloy. In addition, the Ti-modified form of Alloy A (Alloy AT) was so brittle in cast form that the ingot cracked during the canning stage and was not extruded. The fracture toughness values for Alloy AT are therefore expected to be even lower than for Alloy AH.

Recall (Section 4.2.3.2) that both Alloys CH and CT appeared to offer some strengthening advantages over their baseline (Alloy C) in the as-extruded condition. However, these two alloys are very different from Alloy C in their toughness characteristics. First, Alloy CT is very brittle. In fact, the fracture toughness and fracture energy values for Alloy CT are comparable to binary NiAl alloy values. In contrast, the fracture toughness values for Alloy CH are quite high (17.7 and 22.8 $\text{MPa}\sqrt{\text{m}}$ for as-extruded and heat-treated alloys, respectively). Further, the fracture energy value for the heat-treated form of Alloy CH is 229 $\text{N}\cdot\text{cm}/\text{cm}^2$, which is the highest recorded for any alloy in this program. This is especially interesting in light of the fact that the as-extruded form of this alloy produced a fracture energy of only 37 $\text{N}\cdot\text{cm}/\text{cm}^2$. Examination of the microstructures of Alloy CH in both conditions (Figure 54) reveals a small amount (about 10 to 15 v/o) of gamma prime decorating the grain boundaries of the martensitic NiAlCo phase. However, during the 2 hours/1050°C heat treatment, the gamma prime particles coalesce to form a duplex grain structure with a larger amount (about 20 v/o) of gamma prime. Evidently, this duplex gamma prime plus martensite structure is much more fracture resistant than the as-extruded structure. Perhaps the gamma prime phase aids in crack blunting which would cause the alloy to resist propagation of a crack and therefore increase the fracture energy of the material.

In addition to the alloying modifications, a powder mixture of Ni-50Al with 20 v/o MERL 76 (a Ni-base superalloy) was made to explore the effects of superalloy compositing on NiAl. The superalloy particles were expected to improve the toughness of NiAl and, in fact, the fracture toughness of the powder mixture is about 2.5x and the fracture energy about 3x the values for binary NiAl alloys. However, these improvements are not as great as have been achieved through alloying with cobalt. Further, the stability of the superalloy particles in NiAl is a problem that can be addressed only through the expensive process of coating the particles with alumina or yttria as a diffusion barrier prior to consolidation. Because of this and the marginal improvements in strength (Section 4.2.3.2.3), this approach was not further pursued in this program.

4.2.4.4 Effect of Boron on the Fracture Toughness Behavior

Table 25 shows that a small boron addition has essentially no effect on the K_{IC} and the fracture energy of the stoichiometric binary alloy. In contrast, a comparison of the fracture properties between

Alloys B and B2 (Table 25) shows a deleterious effect of the boron addition on K_{IC} although the fracture mode was the same for both alloys (intergranular). These apparently inconsistent boron effects can be rationalized in terms of the phase microstructure in these alloys. First, the binary alloys have a B2 structure while the ternary alloys are martensitic at room temperature. Further, the addition of boron to the ternary alloy changes the type of secondary phase formed in the alloy. In the boron-free ternary alloy (Alloy B2), about 5% of an Ni_3Al -type phase is formed as stringers along the grain boundaries. On the other hand, when boron is added (in Alloy B), a boride phase forms as a grain boundary film and no Ni_3Al -type phase is seen. The binary alloy, with and without boron, was a single phase B2 alloy.

The fracture toughness differences between Alloys B and B2 are apparently indirectly related to the presence of different secondary phases in the material through their effects on the matrix composition, especially the Al content. The aluminum content of the boride phase in Alloy B was determined via electron microprobe to be 11 a/o, while the aluminum content of the Ni_3Al -type phase in Alloy B2 is estimated to be slightly higher from results on similar alloys. Precipitation of a lower Al phase will result in enrichment of the matrix in Al which has a strong effect on the properties of the martensitic phase. There is 2 to 5 times as much precipitate in Alloy B2 as in Alloy B (5 v/o as compared to <2 v/o). Therefore, more Al enrichment is expected in Alloy B2 which should manifest itself in slightly lower transformation temperatures for Alloy B2 as compared to Alloy B which is the case (Table 14).

Further, there are differences between Alloys B and B2 in the shape of the load-displacement curves from the fracture toughness test. Specifically, the boron-free alloy (Alloy B2) shows a pronounced "yielding" in the curve well below the stress required for the precrack to begin propagating (Figure 69, Curve A). A similar "yielding" in Alloy B is barely discernible. This "yielding" is considered a characteristic of the martensitic transformation in the alloys acting to accommodate the applied stress/strain. The operation of such martensitic transformation mechanisms is generally easier near the transformation temperatures of the material (Section 4.2.5). Therefore, transformation temperatures closer to room temperature (as in Alloy B2) should make the operation of such mechanisms more likely.

4.2.4.5 Effect of Heat Treatment on Fracture Toughness of Alloys B2 and C

The observations in the previous section are intriguing for they suggest that the fracture properties of these martensitic alloys can be optimized through adjustment of the martensitic matrix composition via controlled precipitation of selected secondary phases. The amount of secondary phase, e.g., gamma prime, can be varied by heat treatment in order to affect the stability of the martensitic phase in the alloys. For example, in Ni-36 a/o Al, the amount of gamma prime phase was changed from 0 to 30 v/o by heat treatment (Reference 1). In the process, the structure of the matrix changed from martensitic to a stable B2 phase. It has been estimated that the precipitation of 30 v/o Ni_3Al enriched the matrix by about 4 a/o in aluminum, stabilizing the B2 phase against martensitic transformation at room temperature. As the stability of the martensitic phase at room temperature appears to have an influence on the fracture toughness, heat treatment studies were performed on Alloys B2 and C to examine the influence of microstructure on the room temperature fracture toughness. Both alloys were originally prepared as cast ingots which were extruded at 980°C (1800°F) with a 9:1 reduction in area. Each alloy was then subjected to a series of heat treatments followed by metallography and fracture toughness testing. The results are presented in Table 27.

4.2.4.5.1 Effect of Gamma Prime Volume Fraction

The results for Alloy C show that, for a similar grain size (ASTM 5, 0.06-mm diameter), increasing the amount of gamma prime phase from 20 to 33 v/o appears to have little effect on the

fracture toughness values which range from 23 to 33 MPa $\sqrt{\text{m}}$. Similarly, increasing the volume fraction of gamma prime from 3 to 13 percent in Alloy B2 has no effect on the fracture toughness which remains 17.7 MPa $\sqrt{\text{m}}$. Therefore, in spite of the predicted effect of controlled precipitation on the martensitic transformation mechanisms (and therefore fracture behavior), no great effect was seen. Evidently, the effects are much more complex than suspected.

4.2.4.5.2 Effect of Grain Size

For both Alloys B2 and C, the heat treatment at 1300°C resulted in materials with very little gamma prime and a very coarse grain size of ASTM -3 (1.0 mm diameter). The coarse-grained material of Alloy B2 fractured intergranularly prior to testing, suggesting that a coarse grain size is extremely detrimental to the fracture toughness of this alloy. In contrast, a specimen of the coarse-grained Alloy C showed a fracture toughness value similar to the fine-grained material, although a separate specimen exhibited a considerably lower value. The following section attempts to explain the large differences in fracture behavior between the coarse-grained forms of Alloys C and B2 as well as the large scatter in fracture toughness values observed in the coarse-grained Alloy C.

Both Alloys B2 and C form martensite upon cooling to room temperature. However, an important difference between the two is the temperature at which this occurs. The M_s temperature of Alloy B2 is about 110°C, which is below the ductile-brittle transition temperature (DBTT) of the material. On the other hand, the M_s of Alloy C is 665°C which is above its DBTT. During the transformation of neighboring grains of different orientations, there can be problems with accommodation of the transformation strains across the grain boundaries, especially in coarse-grained materials. If the transformation occurs above the DBTT of the material, the grains of the material can deform to accommodate the strain. However, below the DBTT, the grains are brittle and will not deform, resulting in stress concentrations at the grain boundaries and increased susceptibility to grain boundary cracking. The presence of a more ductile grain boundary precipitate may help to alleviate this problem by deforming to reduce the grain boundary stresses. Therefore, the extreme brittleness of coarse-grained Alloy B2, which lacks any potentially helpful grain boundary precipitates, may be due to these problems associated with transformation below the DBTT.

Another important consideration is the higher propensity for grain boundary embrittlement, with increasing grain size, due to segregation of impurities. Further, it is known that both grain boundary segregation and the accommodation of transformation strain across grain boundaries depend on the specific orientation relationship between the adjacent grains. This anisotropic effect could result in large scatter in fracture resistance in very coarse-grained materials.

4.2.5 Martensitic Phenomena in NiAlCo Alloys

The martensitic B2 to L1₀ transformation appears to play a significant role in the mechanical properties of NiAlCo alloys as seen from a variety of results from this program. In particular, martensitic NiAlCo alloys have shown superior room temperature ductility and fracture toughness properties as compared to non-martensitic alloys in other ternary systems. Further, the martensitic transformation plays a role in enhancing these properties by:

- Accommodating the imposed strain via a stress-induced B2 to martensite transformation in Alloy A.
- Blunting cracks in Alloy B.
- Nucleating new martensitic variants to accommodate strain in Alloy C.
- Martensitic "yielding" behavior in the fracture toughness curves of Alloy B2.

Ductility in the isostructural compound NiTi is attributed to a similar transformation, indicating good potential for exploiting the martensitic transformation in NiAl for enhanced ductility and/or toughness. However, not all martensitic alloys are ductile. Therefore, it is evident that the important factors which govern martensite-induced plasticity must be identified in order to choose favorable alloying directions for NiAl. In a separate study (Reference 12), a comprehensive review of the literature was undertaken, using NiTi as a model system, and the specific effects of cobalt on the martensitic transformation characteristics of NiAl were determined. The important martensitic toughening parameters are:

- The mobility of the martensitic variant interfaces. The magnitude of the stress required to nucleate and/or rearrange martensitic variants in the alloy, σ_m , provides an indicator of the mobility. σ_m is lowest (mobility highest) near the M_s temperature.
- Transformation strain anisotropy. A large anisotropy in the transformation strain results in problems with accommodating strain at grain boundaries. The anisotropy can be calculated from the lattice parameters of the parent and martensitic phases.
- The magnitude of the fracture stress, σ_f . σ_f must be greater than σ_m to allow the martensitic transformation mechanisms to operate.

For a fixed Al content, cobalt additions to NiAl:

- Reduce the M_s temperature.
- Reduce the transformation strain anisotropy.
- Increase the fracture strength of NiAl.

These results were used to formulate some of the ternary NiAlCo alloys that were studied in Phase II of this program.

In order to characterize the martensitic transformation behavior in the NiAlCo alloys studied in this program, martensitic transformation temperatures were determined using dilatometry. Results are given in Table 14, and approximate M_s temperature contours are drawn on the NiAlCo phase diagram in Figure 19. In addition, the deformation characteristics of the Phase II alloys were explored by critically examining the stress-strain behavior and performing TEM analysis on selected alloys the results are presented in the following sections.

4.2.5.1 Preyield Deformation in Martensitic Alloys

A number of alloys tested in this program exhibited room temperature elongations as measured on the specimens after testing. However, no plastic yield point was observed on the tensile stress-strain curves. In addition, with the exception of Alloy A, no martensitic yield stress or "shelf" was observed in tension either. This measurable "preyield" plastic strain, therefore, is a, parently associated with the martensitic transformation, but the transformation/deformation occurs throughout a broad range of stresses below the plastic yield point, σ_y , of the material rather than at one specific stress, σ_m .

To study these effects more thoroughly, compression data from martensitic alloys as well as stable B2 phase, non-martensitic alloys were studied in detail. In particular, the slopes of the compressive stress versus strain curves in loading and unloading were analyzed. The slope of the stress-strain

curve in loading, in the absence of preyield plastic deformation, should be the same as that in unloading, and both approach the Young's Modulus for the alloy. In contrast, a smaller slope in loading than in unloading is indicative of preyield deformation in the material (Figure 70). The loading and unloading slopes from various alloys are recorded in Table 28.

Alloys E, F, and J, which do not undergo a martensitic transformation, do not show any preyield plastic deformation and have an average stiffness of about 136 GPa (19.8 Msi). This is in reasonable agreement with the dynamic Young's Modulus of a nonmartensitic binary NiAl alloy (135 GPa, 19.6 Msi) with comparable aluminum content (40 a/o) (Reference 24). However, there are some important differences among the alloys which do undergo martensitic transformation. First, the room temperature unloading stiffnesses (83 to 118 GPa, 12 to 17 Msi) measured for martensitic NiAlCo alloys (Alloys A3, B, B2, C, and C2) are considerably lower than for the B2 phase alloys. Further, the measured stiffnesses are in reasonable agreement with the dynamic Young's Modulus (100 GPa, 14.5 Msi) of a martensitic binary NiAl alloy with comparable aluminum content (37.5 a/o) (Reference 24).

An exception to the martensitic NiAlCo alloys is Alloy C3 which, though martensitic at room temperature, has an unloading stiffness (126 GPa, 18 Msi) which more closely resembles that of a B2 alloy. This is most likely due to the large volume fraction of gamma prime (30 to 35 v/o) in this alloy. The dynamic Young's Modulus of stoichiometric Ni₃Al is about 180 GPa (26 Msi) (Reference 24). An estimate of the Young's Modulus of martensitic NiAl containing 30 v/o gamma prime, using Rule of Mixtures and values of 100 GPa for the martensitic phase and 180 GPa for the gamma prime phase, is 128 GPa (18.6 Msi) for the mixture, which is very close to the stiffness value measured for Alloy C3.

The measured stiffness in unloading should approach the Young's Modulus of the material, while the stiffness in loading may include the effects of any preyield martensitic transformation/deformation behavior. Therefore, to study the preyield deformability of the various alloys, one should compare the value of the stiffness in unloading with that in loading. The ratio of the stiffnesses is given in Table 28 and provides a quantitative measure of the ease of preyield martensitic deformation in the material. In addition, the stiffness ratios for a number of alloys are plotted as a function of the A_f temperature of the alloys in Figure 71. In order to simplify the analysis, quaternary alloys and alloys with very large amounts of gamma prime (> 30 v/o) were not included. Note that the ratio is highest for an alloy with its A_f temperature just below the test temperature. Further, if one plots the ratio as a function of the test temperature for an alloy (as done for Alloy B2 in Figure 72), the ratio is again seen to be highest just above the A_f temperature.

Near the A_f/M_s temperatures of a material, the thermodynamic driving force for the martensite to parent transformation is the highest. Therefore, martensitic transformation/deformation processes can favorably occur, which explains the increased preyield deformation near these temperatures. In addition, martensite deformability is apparently related to the mobility of martensitic interfaces in the material, which in turn should be related to the mobility of dislocations within the materials. The strength of an alloy is indicative of the difficulty in moving dislocations through the alloy. Note in Figure 72 that the strength of the material also drops in the A_f/M_s temperature region of the material, indicating perhaps higher dislocation mobility in the material.

As previously described, the preyield deformation of various NiAlCo alloys was studied via the loading and unloading slopes in the compressive stress-strain curves. VIM Alloy B (Ni-30 a/o Al-25 a/o Co-0.25 a/o B) exhibited a relatively large hysteresis between the loading and unloading slopes, indicating the deformability of the martensite in this alloy to be high. To explore the microstructural features accompanying the deformation, TEM was performed on compression samples of VIM Alloy B both before and after deformation (to 2% plastic strain) at room temperature. These results are described in Section 3.4.3.1.2. Under compression, the martensitic plates in the material accommodate the deformation by the formation and/or rearrangement of the fine twin lamellae within the plates.

The material ultimately fails because of cracking between the martensitic matrix and the grain boundary boride phase. Since Alloy B2 is the same composition as Alloy B, but without the boron, it is possible that Alloy B2 is less susceptible to this type of cracking and will be more fracture resistant. Table 25 shows that the fracture toughness of Alloy B2 is indeed greater than that of Alloy B.

4.2.5.2 Postyield Deformation in Martensitic Alloys

In contrast to some of the above alloys is Alloy C (Ni-29 a/o Al-21 a/o Co), an alloy with relatively high fracture toughness (up to $33.3 \text{ MPa}\sqrt{\text{m}}$) and some measurable room temperature ductility (up to 2.2%). However, this alloy shows no noticeable preyield deformation at room temperature as observed in either the loading and unloading slopes (Table 28) or the microstructure. However, examination of the microstructure of Alloy C throughout a room temperature compression test revealed martensitic transformation mechanisms operating at or just after plastic yield in the material (Section 3.4.3.1.3). At yield, new martensitic variants nucleated which intersected the existing variants. These did not appear prior to yield in the material. The new variants nucleated only in existing variants which were aligned parallel with the applied stress. The new variants grew perpendicular to those particular variants and were, therefore, normal to the applied stress. Obviously, this was the most desirable orientation with which to accommodate the applied stress.

The tensile fracture strengths recorded for this alloy (820 MPa and 587 MPa for the as-extruded and heat-treated conditions, respectively) are very close to the compressive yield strength of the heat-treated material (754 MPa). Therefore, it is the relatively high fracture strengths of Alloy C which allow the martensitic transformation mechanism (which only operates at higher stress) to accommodate the stress/strain and provide the observed room temperature toughness and ductility.

4.2.6 Secondary Properties

Based on earlier data generated in this program, including tensile strength and ductility, compressive strength and deformability, and fracture toughness and fracture energy, alloys were selected which appeared to warrant further testing for secondary properties, including creep resistance and low cycle fatigue. Alloys were selected, which were in the top half of all alloys tested in strength as well as fracture toughness and fracture energy. Using these criteria, five alloys were selected for further evaluation: Alloys A, AH, C, C2, and CH.

4.2.6.1 Compressive Creep

Secondary creep rate was determined as a function of stress at 760°C (1400°F) and 980°C (1800°F) for selected Phase I and Phase II alloys. The results are given in Figures 73 and 74 along with data for binary NiAl for comparison (Reference 25). An idea of the relative creep resistance of the alloys can be determined by comparing the creep rates at a similar stress level for all the alloys. Note that, in general, the ternary NiAlCo alloys tested (Alloys A, C and C2) are no more (and sometimes less) creep resistant than binary NiAl. On the other hand, at 760°C (1400°F) and 34.5 MPa (5 ksi), the alloys with Hf additions exhibit the lowest creep rates of the series and show a noticeable improvement over the binary and ternary alloys. Therefore, it appears that Hf succeeds in increasing the creep resistance of NiAlCo alloys at this temperature, and preliminary results on AH (a Hf-modified form of Alloy A) at 980°C (1800°F) appear to indicate that Hf additions are effective at still higher temperatures as well. This is consistent with the results of Vedula, et al. (Reference 19) on the effect of Hf additions on binary NiAl.

However, the results at both temperatures seem to indicate that 5% Ti does not offer much hope for increasing the creep resistance of NiAlCo alloys, as the creep strength of Alloy CT is much worse

than the binary NiAl at 760°C (1400°F) and about the same at 980°C (1800°F). Strutt and Kear (Reference 26) showed that Ti is effective in greatly improving the creep strength of NiAl when enough Ti is added to form a sufficient amount of Heusler phase in the alloy. However, no Heusler precipitates were observed in Alloy CT. Therefore, in order to precipitate a Heusler phase and utilize its strengthening and creep resistant benefits, more Ti must be added to this alloy.

Note also that the stress exponents for Alloys AH, C2, and CT are different than for the rest of the ternary alloys. The measured stress exponents at 760°C (1400°F) are given in Table 29 along with stress exponents for various binary NiAl alloys. The aluminum contents for the ternary and quaternary alloys are all about 30 a/o. Unfortunately, no data are available for lower aluminum NiAl alloys for accurate comparison. It is apparent that the stress exponent of NiAl gradually decreases with decreasing Al content, but it is unclear what the stress exponent will be in a binary alloy near 30 a/o Al. However, it is clear that the ternary and quaternary alloys fall into two distinct groups – those with exponents from 3–4 and those with exponents from 1–2. The amounts of various precipitates in these two groups (including gamma prime, fcc, and hexagonal types) do not vary greatly from each other. Therefore, the differences in stress exponents do not appear to be a precipitate effect. Further, it does not appear to be structurally dependent as all alloys are of the B2 structure at the test temperature.

Vandervoort, et al. (Reference 27) reported that binary NiAl alloys with 44, 50.4 and 54 a/o Al had stress exponents (n) between 3 and 4 and activation enthalpies (ΔH) between 64 and 78 kcal/mole at temperatures of 1000°C and above. The mechanism for creep in these alloys was determined to be the viscous motion of dislocations. At temperatures from 1000 to 900°C, the activation enthalpies for the alloys with 44 and 50.4 a/o Al decreased with decreasing temperature, while that of Ni – 54 Al remained relatively constant. In all three alloys, the stress exponent increased with decreasing temperature between 1000 and 800°C to a value of about 7 in the stoichiometric and Ni-rich alloys. The creep mechanism in this intermediate temperature region was undetermined.

The stress exponent of Alloy A at 760°C was determined to be about 3. Therefore, the creep mechanism of Alloy A is apparently the same as was determined by Vandervoort, et al. for the binary alloys above 1000°C, namely the diffusion-controlled viscous motion of dislocations. The melting temperature of Alloy A was determined to be about 1775K, while that of the binary alloys is about 1910K. Therefore, although the test temperatures of the binary alloys and Alloy A are different, they represent similar fractions of the melting point, namely 0.6 T_m and 0.7 T_m for Alloy A and the binary alloys, respectively. Therefore, the creep mechanisms may well be similar. However, the activation enthalpy for creep in Alloy A is only 38 kcal/mole (159 kJ/mole) which is about half that of the binary alloys.

In contrast to Alloy A, creep in Alloy AH appears to be governed by a different mechanism. The stress exponent of Alloy AH was measured to be about 1, which implies a change in the creep mechanism. The creep mechanism at work in this alloy has yet to be determined. Furthermore, the activation enthalpy for creep was calculated to be about 16 kcal/mole (68 kJ/mole), which is about half the magnitude of Alloy A.

4.2.6.2 Low Cycle Fatigue Testing

Low cycle fatigue (LCF) data were generated at room temperature and/or 760°C (1400°F) for selected alloys which showed some promise in terms of strength and room temperature ductility/toughness. The results are given in Table 30. The number of specimens tested was limited, for by this point in the program, only a small section remained of the extruded bar of each alloy. Specimens were fatigue tested at a frequency of 0.75 Hz and an R ratio of zero. The test was considered a run-out

if the specimen exceeded 50,000 cycles at a given stress level. The maximum tensile stress achieved, along with the number of cycles at that stress, is given in the table. The alloys tested included Alloys A, C, C2, and CH, although no data were obtained for Alloy A. Owing to an insufficient amount of material remaining, the room temperature specimen of Alloy A was machined from a section of the extruded bar corresponding to the top section of the cast extrusion preform. The presence of unhealed porosity in the specimen resulted in premature failure and no results were obtained.

All the alloys tested at room temperature (C, C2, and CH) failed at 60 ksi, although the actual number of cycles to failure varied. Therefore, the room temperature fatigue strength of these NiAlCo alloys is about 60 ksi with little or no dependence on composition from 29 to 31 a/o Al and 16 to 21 a/o Co. Also, based on the results for Alloys C and CH, Hf additions do not appear to affect the room temperature fatigue strength of Ni-29 a/o Al-21 a/o Co. However, the fatigue life at 60 ksi has been improved tremendously (from 20 to 14,160 cycles). At 760°C (1400°F), only Alloys C and C2 were tested. It appears that Alloy C2 (Ni-31 a/o Al-16 a/o Co) is more fatigue resistant at 760°C than Alloy C (Ni-29 a/o Al-21 a/o Co). The reasons for the improved fatigue resistance are unknown.

5. PHASE III ALLOYS

The Phase I and Phase II studies showed that the fracture toughness of some ternary martensitic NiAlCo alloys was significantly better than the binary NiAl alloys. However, the ternary martensitic alloys are weak at high temperatures. Attempts to strengthen these tough base alloys with quaternary additions invariably debited the fracture toughness even with small quaternary additions. With the concurrence of the Air Force, a compositing approach was used to improve the strength characteristics of a selected NiAlCo alloy.

5.1 MATRIX SELECTION

After careful review of all Phase I and II alloys, Alloy C (Ni-21 a/o Co-29 a/o Al) was selected for the Phase III matrix material based on its superior room temperature toughness (as high as $33 \text{ MPa}\sqrt{\text{m}}$) and ductility (2.2%). However, Alloy C was shown to be weak at all temperatures and have poor creep resistance. The reinforcement material was chosen to address these deficiencies.

5.2 REINFORCEMENT SELECTION

Chopped PRD-166 (80% alumina + 20% zirconia) fibers were chosen as the reinforcement phase because of a variety of factors:

- Thermal stability in NiAl alloys.
- Commercial availability at relatively low cost.
- Good strength at high temperatures.
- Chopped fiber approach provides more options for processing and consolidation of the materials.

Further, the chopped fiber additions were expected to have some of the following beneficial effects on the chosen matrix materials:

- Improve the creep resistance.
- Improve the strength, especially at high temperature.
- Toughen via crack deflection.
- Increase the modulus.
- Lower the overall density of the material.

5.3 RESULTS AND DISCUSSION

5.3.1 Material Characterization

Optical metallography and scanning electron microscopy were performed on the Phase III material, and results are summarized and compared with results from the baseline NiAlCo alloy in Table 31. The microstructure of the Phase III material is presented in Figures 75 and 76.

Note that the phase distribution within the NiAlCo alloy matrix is the same with and without reinforcement. However, the reinforcement does change the grain size significantly. This fine grain size also can be seen clearly in Figure 75. In addition, Figure 75(a) shows the reinforcement to be distributed uniformly throughout the cross section of the specimen. This uniformity was seen

throughout the entire length of the extruded bar. The fiber diameter is about 15 to 25 microns. The fibers were initially chopped to lengths of about 5 mm, corresponding to an aspect ratio of about 250. However, as seen in Figure 75(b), the fibers were fractured during the consolidation process, i.e., in the mechanical blending and/or extrusion processes. The result is fiber lengths ranging from 20 to 100 microns, corresponding to an average aspect ratio of about 2.5 to 3, which is 100 times smaller than the aspect ratio of the initial chopped fibers. The material should be considered particulate rather than chopped fiber reinforced.

Scanning electron microscopy (SEM) was performed on sections of the Phase III material to further study the microstructure, especially to determine the chemical reactivity and mechanical integrity between the reinforcement and the matrix. The SEM secondary electron images are shown in Figure 76. Figure 76(a) shows the cross section of a fiber and the lack of any interfacial reaction zone. More detailed SEM examination confirmed that no reaction layer exists. This is consistent with various studies of the compatibility of alumina-based reinforcements and NiAl alloys (References 28 and 29). Figure 76(b) reveals that there were occasional voids that formed in the material at the ends of the fibers. These voids seem to be due to lack of sufficient metal flow around the fibers during extrusion. The influence of these voids on the mechanical properties of the material is described in Section 5.3.2.

5.3.2 Compressive Strength and Modulus

Compression testing to determine the 0.2% yield strength and elastic modulus was performed on specimens of the Phase III material. The material was tested with the stress axis both perpendicular and parallel to the extrusion direction to study the effect of fiber orientation on strength. The strength results are given in Table 32 and Figure 77 along with results for the matrix alloy (Alloy C, Ni-29a/oAl-21a/oCo) for comparison. The elastic modulus data are given in Table 33 and Figure 78.

The Phase III material is stronger and stiffer than the baseline matrix Alloy C in both orientations and at all temperatures tested. However, there are important differences between the two orientations of the Phase III material. First, the strength is greater in the material tested parallel to the extrusion direction than in the perpendicular direction at all temperatures. This result is not clearly understood. Particulate strengthening theories can be applied which state that the strength of the composite is inversely proportional to the square root of the interparticle spacing (Reference 30). In this theory, the role of the particles is to impede the movement of dislocations in the material. The particles are slightly elongated, resulting in different interparticle spacings for different slip planes. Therefore, it is possible that the difference in strength between the two test conditions is due to different interparticle spacings on the slip planes. However, it is difficult to provide a more definitive reason for the strength differences.

On the other hand, the elastic modulus results (Figure 78) can be readily linked to the presence and morphology of the PRD-166 fibers. Using a simple Rule of Mixtures formula, the room temperature modulus of an NiAlCo alloy ($E = 90$ GPa) containing about 15 v/o of PRD-166 fibers ($E = 380$ GPa) should be 134 GPa, which is exactly the modulus of the material tested perpendicular to the fiber/extrusion direction. In contrast, the modulus of the material tested parallel to the fiber/extrusion direction is not very different from the unreinforced NiAlCo material. These differences can be explained by examining the bonding of the fibers with the surrounding matrix material. Recall (Section 5.3.1) that the Phase III material frequently contained voids in the matrix material at the ends of the fibers. Further, as shown in Section 5.3.3, the fibers are weakly bonded to the matrix. The result of these two features is that when the material is stressed parallel to the fibers, the fibers support little to none of the load and provide no modulus enhancement. On the other hand, when the material is compressed normal to the fibers, the fibers can contribute fully and enhance the modulus to the theoretical extent

expected. Perhaps with better processing, the voids can be eliminated and the modulus can be enhanced in all orientations of the material.

5.3.3 Tensile Ductility

The Phase III material was tested in tension to determine the ductility as a function of temperature. Results are given in Table 34 and Figure 79 along with equivalent data for the powder processed matrix material (Ni-29 a/o Al-21 a/o Co). The Phase III material was tested with the stress axis parallel to the extrusion/fiber direction. It is apparent that the addition of the PRD-166 fibers degrades the ductility of the material at all temperatures. A ductility transition is observed between 500°C to 600°C, which is higher than the matrix material alone (~400°C). However, below the ductility transition, some small amount of ductility is still noted in both materials ($\leq 2.5\%$). Figure 80 shows the fracture behavior of the Phase III material both below and above the ductility transition. Note there is some evidence of fiber pull-out below the ductility transition, although fiber breakage is also prevalent. The mixture fails via transgranular cleavage. Cracks appear to originate at the fiber matrix interface, especially at the corners and voids at the ends of the fibers. Above the ductility transition (Figure 80d), the matrix fails in a ductile mode around the reinforcement. It appears that the ductility of this material may be improved somewhat by optimizing the processing in order to maintain sufficient fiber length for fiber pull-out mechanisms to contribute significantly.

5.3.4 Fracture Toughness

Two tests were performed to measure the room temperature fracture toughness of the Phase III material: a slow bend K_{IC} test and a Charpy Impact test. K_{IC} and Charpy Impact Energy values of 18.9 to 20.5 $\text{MPa}\sqrt{\text{m}}$ and 0.84 N-m were measured for the Phase III material at room temperature. While Charpy Impact data were not generated for other alloys in this program, the K_{IC} values can be compared to some of the best alloys from earlier phases of the program (Table 35). The highest toughness values (22.8 to 33.3 $\text{MPa}\sqrt{\text{m}}$) were recorded for the extruded ingot of Alloy C (Ni-29 a/o Al-21 a/o Co) which is the matrix alloy for the Phase III material. However, the Phase III material exhibited the next highest toughness values (18.9 to 20.5 $\text{MPa}\sqrt{\text{m}}$) of all the materials tested in this program. An examination of the fracture surfaces (Figure 81) reveals some limited fiber pull-out, but primarily fiber breakage with the matrix undergoing transgranular cleavage, similar to the tensile results. The very short fiber length prohibits fiber pull-out mechanisms from contributing significantly to toughen the material. Further, the tensile results showed that the voids at the end of the fibers and the weak interface serve as crack nucleation sites. By optimizing the consolidation process to maintain a large aspect ratio of the fibers and eliminate the voids, it may be possible to realize the expected toughening benefits.

5.3.5 Compressive Creep Strength

The Phase III material was tested for compressive creep with the stress axis both parallel and perpendicular to the extrusion/fiber axis. Results are provided in Figure 82 along with some data for the matrix alloy alone (Ni-29 a/o Al-21 a/o Co). No trend can be seen between the two orientations of the Phase III material at all temperatures. However, it appears at the higher temperatures that the material tested parallel to the extrusion/fiber axis is more creep-resistant than the material tested perpendicular. Further, based on the results at 980°C (1800°F), the Phase III material is less creep-resistant than the monolithic matrix material.

It is generally known that grain boundary sliding is an important creep mechanism in high temperature creep which results in a direct relationship between creep resistance and grain size. Apparently, in the present case, the fiber reinforcement is more than offset by the faster grain boundary creep in the fine grain composite material.

5.3.6 Low Cycle Fatigue

Room temperature low cycle fatigue (LCF) testing was performed on specimens of the Phase III material. The specimen was cycled between zero stress and the maximum stress at 40 cycles per minute at four different stresses. The results are presented in Figure 83. Some of the data points can be compared to other alloys from this program (see Table 30). It appears that the PRD-166 addition succeeds in greatly improving the LCF life. In particular, Alloy C (Ni-29 a/o Al-21 a/o Co) failed after 20 cycles at 414 MPa. Extrapolating the curve for the Phase III material reveals that, for the same stress (414 MPa), the LCF life will be over 600,000 cycles. Of course, the comparison is not totally valid because the specimen of Alloy C was tested at lower stress levels prior to the test at 414 MPa. However, even adding the cycles achieved at lower stress levels to those achieved at 414 MPa still results in a total of only 150,020 cycles, which represents a fourfold improvement for the Phase III material. The fracture surface is shown in Figure 84 and reveals extensive fiber pull-out with some fiber breakage. Further, close examination of a martensitic grain in the fracture surface (Figures 84b and 84c) reveals chisel-edge fracture of the grain boundary gamma prime particles. This ductile phase may be a contributor to some of the good room temperature properties of these materials.

6. STUDY OF ATOMIC BONDING

6.1 TECHNIQUES FOR STUDYING ATOMIC BONDING

Extended X-ray Absorption Edge Fine Structure (EXAFS) studies were used to determine the local atomic bond strengths in selected ordered alloys. The EXAFS spectrum shows the influence of neighboring atoms (including atom species, spacial arrangement and motion) on the absorption of X-ray photons and resultant photoelectron ejections in the material. The spectrum is obtained by measuring the linear absorption coefficient for X-rays in the vicinity of an absorption edge as a function of the wave number k of the ejected electron, which is seen as an oscillatory modulation which is superimposed on the monotonic absorption-edge background. To determine atomic bond strengths, the main EXAFS peaks must undergo a Fourier transform and are then back-transformed, thus eliminating the higher order EXAFS peaks in the process.

The EXAFS corresponding to the first three atomic shells are compared with a theoretical expression derived by Stern, et al. (Reference 31), which describes the oscillatory portion of the fine structure as follows:

$$X(k) = \frac{1}{k} \sum_j \frac{N_j}{R_j^2} t_j(2k) e^{-2R_j/\lambda} \sin[2[kR_j + \delta_j(k)]] e^{-2k^2\sigma_j^2}$$

where: $X(k)$ = the oscillatory portion of the fine structure.
 k = the wave number of the ejected electron.
 R_j = the average distance between the origin atom and the j th atom.
 σ_j = the rms deviation from R_j , t_j .
 $t_j(2k)$ = the magnitude of the amplitude for back-scattering from the j th atom.
 λ = a mean free path for inelastic scattering.
 N_j = the number of atoms in the coordination shell corresponding to R_j .
 δ_j = a phase shift, which includes both outgoing and back-scattered wave components.

This procedure allows the disorder parameter, σ , which is a measure of atomic vibrations from the equilibrium positions, to be determined. The disorder parameter contains both a static and thermal component. The static disorder arises from a spread of average distances of the j th shell. Any change in σ_j^2 with temperature is due to thermal disorder changes. Therefore, for an isolated shell at two temperatures, T_1 and T_2 , one can obtain:

$$\ln \frac{X_{T_1}(k)}{X_{T_2}(k)} \approx -2k^2 [\sigma_{T_1}^2 - \sigma_{T_2}^2]$$

assuming that other quantities are equivalent for T_1 and T_2 which is a good approximation. By plotting $\ln(X_T/X_{T_0})$ versus k^2 for a series of temperatures, a plot of σ^2 as a function of temperature can be obtained and the slope of $\Delta\sigma^2/\Delta T$ can be determined. Additionally, in a rough approximation, the height of an isolated transform peak varies inversely with σ , so that qualitative information on changes in σ between samples may be deduced from the transform directly.

For a classical oscillator where k is a spring constant and $\langle u^2 \rangle$ a mean square displacement, the average potential energy is:

$$V \approx \frac{1}{2} k \langle u^2 \rangle$$

For higher temperatures, where the equipartition energy theorem is valid, one vibrational degree of freedom contributes $\frac{1}{2} k_B T$ to the thermal energy; and therefore, if one assumes independent oscillators (Einstein model), one obtains:

$$\frac{1}{2} k \langle u^2 \rangle \approx \frac{1}{2} k_B T$$

where k_B is Boltzmann's constant. It follows that:

$$\frac{\Delta \langle u^2 \rangle}{\Delta T} \propto \frac{1}{k}$$

σ^2 from EXAFS is closely related to $\langle u^2 \rangle$ and so if the local bond stiffness is represented by an equivalent spring constant, it is obvious that $\Delta \sigma^2 / \Delta T$ obtained from EXAFS can be considered inversely proportional to the local atomic bond stiffness, if the ΔT values are near room temperature. With more sophisticated forms of data analysis, such as fitting the EXAFS and using phase corrected transforms (Reference 32), the disorder parameters of the first, second, and third shells can be determined. The atomic vibrations for β phase structures were further analyzed to obtain an expression for $\langle u^2 \rangle$ which does not depend on the Einstein model. This more exact expression shows that transition metal-aluminum vibrations contribute to a different portion of the phonon spectrum than do transition metal-transition metal vibrations. This point is further discussed below.

A plot of σ^2 versus temperature is approximately linear near room temperature, but the curve bends so as to approach a constant value at very low temperatures, for which one approaches the zero point vibration condition. (See Figure 85 for plots of σ^2 versus temperature obtained for transmission powders of CoAl, using a CoSi₂ standard.) Some of our data are taken for the linear portion of the σ^2 versus T curve using several different temperatures and samples which are foils made from powders, and other data are taken at room temperature versus liquid nitrogen temperature on solid samples. Since liquid nitrogen temperature is near the zero point vibration portion of the σ^2 versus T curve, we do not directly compare data taken by the two methods, although changes in the $\Delta T / \Delta \sigma^2$ values between different samples, using data taken by the same method, are significant.

X-ray Absorption Near Edge Spectroscopy (XANES) can be considered part of high resolution EXAFS, but for near threshold energies. The most common use of XANES spectra is to obtain information on electronic structure. By studying the XANES spectra as a function of alloy compositions, insight into the nature of the atomic bonding can be obtained.

6.2 ALLOYS FOR EXAFS STUDIES

To facilitate the initial study of atomic bonding characteristics in B2 compounds, EXAFS and XANES experiments were conducted on a set of well-ordered equiatomic binary alloys NiAl, CoAl, FeAl, FeCo, and CuZn. This selection featured compounds with extremes in ordering energy and ductility. The transition metal (TM) aluminides are ordered up to their respective melting temperatures, while FeCo and CuZn undergo an order-disorder transformation prior to melting. CuZn is ductile, while FeCo and the equiatomic TM aluminides are all brittle at ambient temperatures.

6.3 DEVELOPMENT OF THE LOW EXIT ANGLE METHOD OF MEASURING EXAFS

Much of the effort spent on this contract was devoted to overcoming problems associated with the standard method of obtaining EXAFS by transmission, for which sample foils made of several layers of finely ground powder are required. NiAl and CoAl disorder upon cold working, and difficulty was found in producing transmission samples that were simultaneously well ordered, uniform, sufficiently thin to avoid thickness effects, and sufficiently free of surface oxides. Electron yield methods have recently been developed for studying EXAFS of bulk materials, and one possibility might have been to construct a device for measuring temperature dependent electron yield EXAFS. Such a technique may be overly surface sensitive, however, and difficult to apply at low temperatures. By using a normal incidence, glancing angle detection mode of measuring EXAFS by fluorescence, the experimental distortion, usually present in fluorescence EXAFS measurements of concentrated elements, could be largely eliminated.

Ordinarily, a bulk sample appears infinitely thick to an incident X-ray beam. All incident X-rays are absorbed and no fine structure appears in the fluorescence spectrum, for the emitted fluorescence spectrum lies below the absorption edge and the fine structure is not seen. However, the average penetration depth before absorption of the X-ray photons differs and the emitted fluorescence photons can have slightly different absorption probabilities. The absorption probability near the surface can be decreased by using an X-ray beam of normal incidence, which maximizes the penetration depth of the incident photon. Further, the escape depth of the emitted fluorescence is minimized by using a very small exit angle. By utilizing such a geometry, fine structure can be observed and EXAFS spectra can be obtained.

The standard geometry for fluorescence detection of EXAFS from a bulk sample, which is used successfully for detection of dilute species, is shown in Figure 86a. With this geometry, however, no fine structure is detected in EXAFS of major species in bulk samples because of the large amount of absorption of the X-rays, even near the surface. On the other hand, the new geometry (Figure 86b), with the incident beam normal to the surface of the specimen and a very small exit angle, has proven to work very well for collecting EXAFS of major species in bulk samples. By this method, some of the signal is lost because of noise, but with bulk samples the signal is large to start with. Data from the new method were verified by comparing them with data from transmission EXAFS of ductile copper foils. The data were identical, and the new procedure was adopted for all subsequent studies. Our initial development of this detector geometry, described in Reference 33, was limited to room and liquid nitrogen temperatures. An improved version has been constructed in cooperation with the National Institute of Science and Technology. The new apparatus improves the signal to noise ratio by using an annular photodiode detector array which eventually will be used with a dispersive refrigerator system to measure EXAFS at a wide range of temperatures on solid specimens.

6.4 RESULTS AND DISCUSSION

6.4.1 Stoichiometric B2 Alloys

Results were obtained at both room and liquid nitrogen temperatures on bulk ingots of NiAl, CoAl, and FeAl. These ingots had been given long homogenization anneals, were mechanically polished flat and then were given a final electropolish to remove any mechanical strain. (Previous studies by transmission EXAFS on powder samples had revealed that mechanical strain results in considerable site disorder in these samples. The problem is particularly acute for powders of FeAl.) EXAFS parameters for the three nearest atomic shells were determined, using a CoSi₂ standard sample. For CoAl and NiAl, numerous self-consistency checks insured the parameters obtained to be quite reliable. For FeAl, we find surprising evidence that may indicate disorder even in annealed specimens.

The k^3 weighted Fourier transforms of the EXAFS χ functions of CoAl and NiAl are shown in Figure 87. The heights of the peaks in the transforms may be compared directly because of the similarity in the backscattering amplitudes of Co and Ni. (Of course, this is also true for the peaks due to Al backscatterers.) The figure shows that the disorder in CoAl is significantly less than in NiAl at each temperature. However, this disorder has a negligible effect on the temperature dependence. It is also apparent that the temperature dependence of the EXAFS in the two materials is quite different. The results of the analysis are listed in Table 36. The numbers agree with the qualitative picture obtained from examination of Figure 87, and indicate that the temperature dependence of the first coordination shell is similar in the two materials, while the temperature dependencies of the second and third shells in NiAl are much stronger. The stronger temperature dependencies of the second and third shells in NiAl indicate more excitation of lattice vibrations, and therefore lower phonon frequencies as compared to CoAl. This is consistent with stronger interatomic forces in CoAl (a larger "spring constant" produces higher characteristic frequencies). Other evidence, such as that obtained from Young's modulus measurements, is consistent with our result that the CoAl is a "stiffer" material than NiAl. However, our experiment is the first to show that the enhanced stiffness of CoAl relative to NiAl comes from the TM-TM bonds (second or third neighbor to a TM absorber) rather than the TM-Al (first neighbor) bonds. These results are especially interesting when one considers that the cohesive energies of CoAl and NiAl are very similar, with the CoAl cohesive energy being slightly less than that of NiAl, despite the much stiffer TM-TM bonding in CoAl. We point out that the first coordination shell is sensitive to a somewhat different range of phonon frequencies compared to the second and third shells. For instance, σ^2 between an absorber and an equivalent atom (which is the case for the second and third shells in these materials) is insensitive to lattice vibrations near the center of the Brillouin zone ($k \rightarrow 0$) because in these vibrations the atoms move nearly in-phase. This will not be the case when the backscatterer is the nonequivalent near-neighbor (as in the first shell here), since it may be expected that there are optical modes in which the two atoms vibrate out-of-phase, as in the simple diatomic chain, in which near-neighbors vibrate exactly out-of-phase for $k = 0$. The similarity of the temperature dependence of the first shell EXAFS in NiAl and CoAl indicates that the portion of the phonon spectrum to which the first shell is most sensitive is similar in the two materials.

Anomalous phonon frequencies may also have an effect. NiAl has been shown to exhibit anomalously low phonon frequencies in the TA [110] phonon branch. Others have speculated that precursor martensitic phenomena in NiAl are due to special characteristics of the NiAl Fermi surface as deduced from the calculations of Connally and Johnson (Reference 34). Müller, et al., have calculated the local partial density of states (DOS) for NiAl and CoAl (Reference 35). Although the Fermi surfaces or energy bands are not shown, a comparison of the DOS indicates a rigid band behavior when going from NiAl to CoAl, with the CoAl Fermi level closer to the bottom of the band and

intersecting quite different DOS features than does the Fermi level of NiAl. Therefore, if Fermi surface features are indeed important to the vibrational behavior of NiAl, it would be reasonable that quite different vibrational behavior between CoAl and NiAl, such as we have found, could be associated with pronounced differences in the Fermi surfaces of the two materials.

Since the third shell is isolatable in the Fourier transform for the β phase alloys, one may use the \ln ratio technique to determine the temperature dependence of σ^2 . The \ln ratio technique should yield results that are less sensitive to static disorder (as occur in powdered samples) than are results based on fitting all three shells to theory. Therefore, such results on third shell bonds, as listed in Table 37, can be used to estimate the relative bond stiffness even though these data were obtained on transmission samples. Since the data in Table 37 were obtained using a displac unit operated at several temperatures, we were able to obtain $\Delta T/\Delta\sigma^2$ from the linear portion of the σ^2 versus temperature curve. The values of $\Delta T/\Delta\sigma^2$ so obtained will be greater than $\Delta T/\Delta\sigma^2$ obtained between room and liquid nitrogen temperature only, for bulk samples. The ratio of the $\Delta T/\Delta\sigma^2$ (300°K versus 77°K) values for NiAl versus CoAl obtained on bulk, annealed samples is close to the ratio of $\Delta T/\Delta\sigma^2$ for NiAl versus CoAl listed in Table 37. We note that the Zn-Zn bonds in β brass are much softer than bonds in the other materials, in agreement with expectations.

6.4.2 Effect of Stoichiometry and Alloying Additions on NiAl

EXAFS spectra were obtained from samples of NiAl of varying stoichiometries and with ternary Cr additions. When one compares EXAFS spectra from Ni-43Al with Ni-50Al (Figure 88), it is evident that the excess Ni results in a lowering of all the peak heights, indicative of structural disorder in the material. On the other hand, Cr additions have a much more specific effect. Comparing the Ni-edges in Ni-50Al and in Ni-42Al-6Cr (Figures 89a and 89b, respectively) shows that the addition of Cr reduces the first nearest-neighbor bond stiffness of NiAl and leaves the second nearest-neighbor bond strength essentially unchanged. Recall that Cr additions have been found to modify the room temperature slip behavior of NiAl (References 1 and 6) from a slip vector of $\langle 001 \rangle$ to $\langle 111 \rangle$. The reduction of the Ni-Al first neighbor bond can now be identified as the likely cause of the change in slip system. EXAFS also shows that the Cr atoms in the Ni-42Al-6Cr alloy occupy Al sites, for the Cr edge in the alloy (Figure 89c) appears much different from the Ni edge in the same alloy (Figure 89b). If the Cr atoms were on Ni sites, the spectra would appear similar.

6.4.3 Annealed Versus Cold-Worked FeAl

It became evident from earlier results that FeAl readily disordered when ground into powder which made analysis of the EXAFS data difficult. Results on the FeAl show a marked increase in amplitude of the annealed specimen EXAFS spectrum over the unannealed result (Figure 90). However, the shape of the electron yield spectrum of FeAl remained unchanged. The low amplitude of the FeAl spectrum in the cold-worked case seems to be due to a disordering (i.e., randomness in lattice site occupancy) of the material as it was ground into powder. However, a similar comparison of annealed and unannealed spectra of CoAl showed little difference between them, indicating a stronger bonding in CoAl, making it harder to disorder. Data on the slow cooled, ordered FeCo and quenched, disordered FeCo show similar changes as in FeAl.

6.4.4 XANES of NiAl, CoAl and FeAl

XANES spectra on NiAl, CoAl and FeAl alloys were obtained using the Electron Energy-Loss Spectroscopy (EELS) at Argonne National Labs and are shown in Figure 91. A splitting of the transition metal L_3 and L_2 edge white lines systematically becomes more pronounced as one goes from FeAl to CoAl to NiAl, consistent with a filling of the third band as one adds electrons across the series

(References 35 and 36). In addition, it appears that the effect of the Al in CoAl is to increase the Co occupied states. This same effect is not seen in either the NiAl or the FeAl. The indication is that CoAl may have more charge transfer to TM sites as compared to the NiAl or FeAl. While preparing the samples for the XANES, we found that the FeAl is readily disordered. This fact may cause the FeAl data to be slightly inaccurate.

7. COMPUTER SIMULATION STUDY

7.1 INTRODUCTION

Computer simulations were used to study the deformation characteristics of binary 50–50 NiAl. The Embedded Atom Method (EAM) was chosen for the simulations for its flexibility and ease of use. Most computer simulation approaches have certain limitations and are therefore not suitable for a wide variety of applications. For example, pair-potential methods use volume-dependent energy to describe the elastic behavior of a material (Reference 37). Therefore, the volume must be known precisely for accurate calculations, which causes problems with simulations of surfaces and defects. Further, pair-potentials cannot be applied to chemically active impurities.

On the other hand, the EAM, as described in great detail by Daw and Baskes (Reference 37), views each atom as an impurity atom embedded within a "host" consisting of all other atoms. It is electron density dependent, rather than volume dependent, so that it can be applied to a variety of simulations, including alloying additions, surfaces, cracks, and chemically active impurities. Further, it is not much more difficult to apply than most pair-potential methods.

Since the EAM considers each atom an impurity within a host of other atoms, a total energy can be calculated,

$$E_{tot} = \sum_i F_i (\rho_{h,i})$$

where F_i is the embedding energy and $\rho_{h,i}$ the density of the host at the given site, but without atom i . However, this equation assumes complete uniformity, while neglecting core-core repulsions which lead to unrealistic results. The former is addressed by using a density averaged over a finite region, as follows:

$$\bar{\rho}_i = \sum_{j(\neq i)}^n \rho(r_{ij})$$

where r_{ij} is the distance between atoms i and j . The core-core repulsions are corrected for by assuming a short-range pair-wise repulsion between the atomic cores, ϕ_v . The EAM equation becomes:

$$E_{tot} = \sum_i^n F(\bar{\rho}_i) + \frac{1}{2} \sum_{i,j}^n \phi_{ij}(r_{ij}) \quad (i \neq j)$$

If alloys are formed, the embedding function, F_i , must be known for each element as well as the pair potential, ϕ_{ij} , for each type of atomic pair. For example, in the Ni–Al system, pair potentials must be developed for Ni–Ni, Al–Al and Ni–Al pairs. The elemental values for F and ϕ are determined from properties of the pure metals. However, the interactions between the unlike atomic species must be determined. In many instances, the repulsive pair potential is of the form:

$$\phi_{ij}(r) = Z_i(r) Z_j(r)/r$$

where Z represents the effective charge of the given atomic species. Selected physical constants are used to fit the functions F and Z for each element. These constants include lattice parameters, elastic constants, vacancy formation energy, cohesive energy, and anti-phase boundary energy. In the B2

NiAl simulations, the functions were derived from fitting mostly to Ni_3Al properties. The only B2 NiAl properties used to develop the potentials were lattice parameter and cohesive energy.

7.2 COMPUTER MODELING AND SIMULATION RESULTS

The Embedded Atom Method (EAM), as described in References 37 through 43, was applied to the case of 50-50 ordered (B2) NiAl. The EAM has the advantage over other methods, e.g., the semi-empirical approach of Maeda, et al. (Reference 44) by incorporating a number of theoretical inputs which allow the construction of potentials for each chemical type of interatomic pair from experimental data for the pure species and one binary alloy composition. This immediately gives the advantage in the case of 50-50 NiAl, say, to treat it as an ordered alloy or as a disordered alloy if one prefers. It also facilitated fine tuning the interatomic potentials via input from the EXAFS results as they became available.

7.2.1 Physical Property Calculations

7.2.1.1 Lattice Energy

It is known that certain NiAl alloys undergo a martensitic transformation at low temperatures. The EAM simulation revealed quite an interesting feature while recording the lattice energy as a function of Bain strain in testing for this type of lattice instability. The Bain strain is an expansion of the $\langle 001 \rangle$ cubic axis while simultaneously compressing the $\langle 100 \rangle$ and $\langle 010 \rangle$ axes equally while maintaining constant volume. This strain will homogeneously deform an ordered bcc crystal into an ordered fcc crystal if carried far enough. The result is shown in Figure 92 and the ideal bcc and fcc positions are marked on the horizontal axis. The fcc lattice energy is known to be higher than the bcc energy, but the energy minimum actually occurs for a tetragonally distorted ordered bct lattice (also marked) which has been calculated to have a c/a ratio of about 1.30. The martensitic phase which is known to form in the NiAl β phase field from 30 to 40 atom percent Al is also ordered bct and is found to have a c/a of approximately 1.25 (References 14, 45 and 46). The ideal fcc may be regarded as bct with a c/a of 1.414. It can be concluded that the EAM predicts that the martensitic bct phase should be the lowest energy phase at 50 atom percent Al at very low temperatures. The data that exist indicate that the M_s temperature at 30 atom percent Al is about 600K; and by 40 atom percent Al, it is below 100K (Reference 46). Thus, the EAM prediction may be close to reality.

7.2.1.2 Surface Energies

Simulations were also performed to allow the calculation of the surface energy for purely brittle fracture, γ (usually thought of in terms of 2γ), as a function of temperature. For a $\{100\}$ surface orientation, it was found that $\gamma = 0.92 \text{ J/m}^2$ at 1K, 10K, and 100K, but at 1000K it rises to a value in excess of 1.2 J/m^2 . On careful examination it appears that, at this higher temperature, the free surface is undergoing some type of reconstruction, probably analogous to that which has been recently determined for $\{110\}$ surfaces in NiAl by J. Noonan and H. Davis at ORNL using LEEDS measurements.

Additional surface energy determinations were made for NiAl, and also for pure fcc Ni to be used as a baseline for comparison. The results of these surface energy calculations are shown in Figure 93. For comparison, experimental (001) surface energy values for Ni can be found in the literature. Maiya and Blakely (Reference 47) report a value of $1.8 \text{ J/m}^2 \pm 10\%$ for the (100) orientation at about 1500K. Our results, if linearly extrapolated to that temperature, give about 2.0 J/m^2 , in fairly satisfactory agreement. Hayward and Greenough (Reference 48) measured a value of $1.85 \text{ J/m}^2 \pm 10\%$ at about 1525K, but their measurement, being by the zero creep method, was an average over orientations. For beta NiAl, the surface energy predictions were judged to be accurate within 10 to 20%, based

on the Ni comparison. Note that all orientations show an increase with increasing temperature, and that the (100) orientation is substantially lower in value than the other orientations. This would provide some basis for a prediction that (100) should be a preferred fracture plane in transgranular cleavage. There are, as yet, no experimental measurements for NiAl available with which to compare these results, to the best of our knowledge (References 49 and 50). However, these results may stimulate some experiments.

7.2.1.3 Anti-Phase Boundary Energies

Anti-phase boundary (APB) energies for NiAl were determined by utilizing approximately equiaxed arrays of about 1000 atoms, inserting APBs of the desired orientation, and comparing equilibrated total energies to the same array without APBs. The results are shown in Figure 94. Periodic boundary conditions were invoked in all three directions, thus mandating APB pairs in each case. Note that their energies are substantially below that of the free surfaces as expected. The {112} APB energy shows a definite decrease with increasing temperature, in opposition to the trend of the surface energies. The {110} APB energy shows mixed behavior. Both APBs show systematic atomic shifts across the boundary, at least at low temperature (Figure 95). In the {110} APB at 1K, the atoms above the APB shift to the right and the Al atoms move slightly away from the boundary whereas the Ni atoms move toward the APB. The diagrammed movements are drawn at 4X the actual movements for visibility. The {112} APB at 1K also shows systematic displacements, although they are more complicated and not as large (actual displacements are 1/16th those shown) as for the {110} APB. To the best of our knowledge, no experimental data exist to compare with these predictions. These simulations should provide a useful basis for predicting the separation of super-dislocation pairs and also the hypothetical disordering temperature of NiAl. However, at this time, no predictions of this kind have been made.

7.2.1.4 Melting Points

Melting point determination for Ni and NiAl were also made using the Embedded Atom Method (EAM) potentials and the results are shown in Figure 96. The melting point of Ni was determined in the simulations by several methods, all giving very similar results. The method shown here involves finding the discontinuity in energy of the array as a function of temperature. This discontinuity occurs at about 1570K in these simulations. This value is about 10% lower than the true value of 1728K, but it is nevertheless a very difficult and sensitive test for any interatomic potential, which was the main point of the exercise. A similar determination for NiAl yields a value again of about 1570K, which is well below the known value of 1911K by 18%, rather worse than for pure Ni, but not surprising since the EAM potential as constructed by Voter and Chen (References 38 through 42) used much more data from pure Ni than from beta NiAl.

7.2.2 Simulation of Crack Propagation

EAM simulations were performed on an ordered NiAl lattice containing a crack to study the deformation and crack propagation characteristics. Arrays of 1000, 4000, and 9000 atoms were studied in various orientations and crack morphologies under constant load and constant strain rate conditions.

7.2.2.1 1000 Atom Array Results

Initially, an array consisting of alternating (010) layers of Ni and Al with a side crack was simulated using a constant force applied in the $\langle 001 \rangle$ direction (Figure 97). In the first simulation trials, the externally applied force was too large and was applied too rapidly, so that the outer layer of atoms was torn off the crystal and the more internal atoms were relatively unaffected. The simulations were

subsequently altered so that the force was applied more gradually in order to yield more physically realistic results. A stress of 1250 MPa was applied to the array for Steps 0 through 1000 and increased to 5000 MPa for Steps 1000 through 3000. Forty steps is the equivalent of one atomic vibration period (10^{-13} seconds).

Figure 98 represents the simulation array at 100K at various simulation steps. Some rebonding of atoms after bond breaking can be seen to have occurred in the vicinity of the crack tip in some of the later simulation steps. This rebonding probably provided additional resistance to crack propagation through the material. In the 300K simulation (Figure 99), similar rebonding of atoms after bond breaking at the crack tip was observed; however, the rebonding occurred at a much earlier point in the simulation. The greater tendency for rebonding at this higher temperature was expected, for the atomic mobility is greater. At 1000K (Figure 100), a noticeable rounding of the crack tip occurred very early on in the simulation and continued throughout the deformation process. By Step 800, significant atomic rearrangements at the crack tip had already begun to occur and Step 1000 showed a large degree of the bond breaking and rebonding behavior seen in the lower-temperature simulations. In Step 2000, very large atomic displacements were seen. These continued to increase until in Step 3000 we saw significant elongation and necking in the array prior to fracture.

Apparently, short-range diffusion was very active as part of the response to the applied stress and contributed greatly to the plastic response of the alloy at this temperature. This may be an important factor in attempts to lower the ductile-brittle transition temperature (DBTT) of the alloy, i.e., perhaps elements should be added which promote the diffusion of the major species, or themselves are rapid diffusers. From these data, a rough estimate of the DBTT of NiAl was obtained. The marked difference in the deformation behavior from 300K to 1000K indicates that the DBTT falls somewhere within that range.

An interesting result is shown in the simulation at 1K (Figure 101), which shows evidence of slip occurring in the simulation array. The outermost (001) planes appear to be slipping "downward" by one layer in the array. However, it is not possible from this orientation to determine the specific slip system(s) at work.

A second set of simulations of crack propagation in the NiAl lattice at various temperatures was instituted with the stress direction changed to $\langle 112 \rangle$ and the direction of the crack to $\langle 111 \rangle$. This resulted in a large resolved shear stress on {110} planes in a $\langle 001 \rangle$ direction designed to make dislocation generation at the crack tip a much easier process than in the previous orientation. Results at 100K using applied stresses of 1250 and 5000 MPa are shown in Figures 102 through 106.

The initial starting array of the 1250 MPa simulation is shown in Figure 100. The load was applied to the top and bottom layers at Step 0. At Step 400 (Figure 103), only elastic distortions were apparent. (Note: The array layers for Steps 400, 800, and 1400 are presented in a different configuration for ease of presentation only.) At Step 800 (Figure 104), some sort of dislocation appeared to have propagated as could be seen by the jog which started to appear in the lower left corner of some of the slices. After 1400 steps (Figure 105), several new dislocations were generated and had propagated to the outer surfaces as evidenced by the new jogs on the upper right-hand side and on the lower right.

The simulation shown in Figure 106 is similar to the one previously described, with the exception that the load imposed at the start was increased fourfold to 5000 MPa. As seen in Figure 106 in Steps 400 and 1000, an important difference appeared in the plastic response of the array, namely slip produced by the coordinated movement of atoms (or possibly twinning) became the dominant process, and no dislocation generation was observed to occur. The slip (or twinning) appeared to be on (110) planes in a $\langle 001 \rangle$ direction in the lower portion of the array and on (112) planes in a $\langle 111 \rangle$ direction in the upper portion of the array. Apparently, although the activation energy for nucleation

of slip by coordinated atomic movement (or twinning) is higher than that for dislocations, the propagation speed of slip is also substantially higher and so will win out on a kinetics basis once this mode is activated. This is unquestionably an important result to bear in mind under shock loading conditions such as in the earlier simulations.

7.2.2.2 4000 Atom Array Results

Since it is the dislocation process that is of primary interest in these studies, the array size was increased to bring the coordinated slip activation energy up to more realistic levels relative to the dislocation generation energy. The increased size of the array required adapting the simulation for use with the Cray supercomputer at Wright-Patterson Air Force Base. A number of programming and design changes were found necessary to accommodate the approximately 4000 atoms in the new simulations and much of the early work focused on debugging the larger array simulations.

The first test runs (Figure 107) were begun with a stress of 2500 MPa applied in the $\langle 112 \rangle$ direction. However, after 1500 simulation steps (40 steps = 1 atomic vibration period), only elastic strains were apparent and the stress was increased to 3750 MPa to encourage the onset of plastic processes. By Step 2000, a plastic event appeared to have occurred in the array. Either a dislocation nucleated at a point on the surface and ran through the array or cooperative slip occurred. Similar events on a larger scale continued to occur through Step 2700, with the apparent activation of some slip systems oblique to the plane of the simulation as well.

Subsequent work concentrated on making the large array simulations more representative of macroscopic sample sizes. The first step in this direction was to try the effects of constant strain rate loading. This was accomplished by rigidly "moving" the top and bottom layers apart at some fixed velocity, and had the advantage of eliminating the top and bottom layers as free surfaces also. The second step was to eliminate the free surfaces at the left and right faces by moving the crack into the center of the array and then applying periodic boundary conditions between left and right faces.

Figure 108 shows the larger (4000 atoms) $\langle 112 \rangle$ array with the crack at the center, periodic boundary conditions at the left and right surfaces and constant strain rate loading. Figure 109 gives the lattice energy for this run, and the fracture that is becoming evident in Figure 108d is the cause of the lattice energy topping off and beginning to drop by Step 2000.

Center crack, constant strain rate studies were performed on two different array orientations ($\langle 100 \rangle$, $\langle 010 \rangle$, $\langle 001 \rangle$ and $\langle 11-1 \rangle$, $\langle 112 \rangle$, $\langle 1-10 \rangle$) with 4000 atom arrays. Figures 110 through 112 show time sequences for the first orientation at 100, 300, and 800K, respectively. At 100K (Figure 110), atoms began moving after 1500 steps and an edge dislocation appears to have nucleated at about Step 3500 in the upper part of the crack, as evident by an extra half plane of atoms in the upper portion of the array. By Step 6000, extensive dislocation activity was apparent. At 300K (Figure 111), dislocations were first seen at Step 5000, where numerous atoms had shifted in and out of the plane of the simulation shown. Extensive activity was seen by Step 6000 and the crack appeared to be propagating from the lower right-hand corner. In this, the "hard" orientation for NiAl, the crack propagation occurred in the plane of maximum shear stress rather than maximum tensile stress. In the 800K simulation (Figure 112), there appeared to be atomic movements and surface diffusion occurring at earlier steps, but it was not until Step 6000 that any dislocations were noted (in the upper part of the array).

Figure 113 compares the arrays at all three temperatures at Step 8000. Note that there appears to be extensive dislocation activity and crack propagation in the 100 and 300K arrays; but in the 800K array, all that has occurred is an enlargement of the crack/hole. One can deduce from this that the ductile-brittle transition of the material must occur between 300 and 800K. The potential energy of

the array as a function of time step is plotted in Figure 114. The changes in slope of the curves, especially as seen for the 300K simulation, appear to correspond to the nucleation of dislocations in the material. Recall that the first dislocation was observed in the 300K simulation at about 5000 steps, and a large "hill" occurs in the potential energy curve at 4900 steps. The other "hill" that occurs at about Step 2400 corresponds to the breaking of several bonds in the vicinity of the crack tip. Similar behavior is observed in the 100 and 800K simulations. A correlation may exist between the area under the "hill" and the activation energy for the formation of dislocations and/or the propagation of a crack via the breaking of bonds. However, it is impossible to quantify such a relationship at this time.

Figure 115 shows a simulation using the ($\langle 11-1 \rangle$, $\langle 112 \rangle$, $\langle 1-10 \rangle$) orientation at 100K. A constant strain rate was applied in the $\langle 112 \rangle$ direction. The response of the array was much different from that of the previous orientation at the same temperature. Plastic deformation of some complexity is already evident by 1000 steps. Figure 116 is a side view of the same array at Step 1000. A large cooperative shear is shown at 45 degrees to the strain axis. This is especially pronounced to the left of the crack plane in the side view and is the result of a $\langle 1-10 \rangle$ (110) shear type lattice instability momentarily induced by the tensile strain. Such instabilities are well known in the field of martensitic transformations, and the relevance here is that the resistance to this type of instability in bcc crystals comes from the C11-C12 shear elastic constant, which is known to be low (relative to C44) in NiAl and is probably related to the occurrence of a martensitic transformation in Ni-rich NiAl. Further, C11-C12 will be reduced as (110) planes are pulled apart, such as occurs in our high strain rate simulations. This may be sufficient to momentarily trigger this type of cooperative shear instability in this orientation. In the later time steps, the fracture mode indicates that short range diffusion and reattachment occurs near the crack tip, undoubtedly increasing the work necessary for fracture. The fracture plane is seen to be (112) or perhaps (111).

7.2.2.3 9000 Atom Array Results

The array size was increased to 9000 atoms in order to reduce the possibility of significant interactions between the strain fields of the crack and its periodic images. In addition, a new set of programs was instituted for determination of the strain distributions, determination of energy changes near the crack tip, and recognition of dislocations in the array. The latter involves a new strategy which represents a major improvement over previous methods in that it does not require any prior knowledge of where the dislocations might be, and it is quite efficient in terms of computer time. Discussions with Murray Baskes of Sandia National Laboratories revealed that the strategy used by his group involved running Burgers circuits around regions believed to contain dislocations. This method often missed dislocations, required constant human intuition, and also was fairly expensive in terms of computer time. The new strategy is, to our knowledge, the only currently existing algorithm for finding dislocations in simulation arrays and determining their Burgers vectors.

The new strategy is based on the observation that the strain gradient function becomes a maximum as the slip plane of a dislocation loop is approached from a direction normal to the plane, and then changes sign as one passes through the plane. The difference in the strain gradient on either side of the slip plane is directly proportional to the Burgers vector of the dislocation. Furthermore, the strain gradient will have very small values everywhere in the lattice except near a dislocation slip plane or other major discontinuity. As a result, by plotting the strain gradient, the position of dislocation loops becomes readily apparent, without any prior assumptions or guesswork on the part of the investigator.

A simulation was performed at 300K using the new array size of 9000 atoms and the new dislocation recognition strategy, and results are shown in Figures 117 through 119. Figure 117 shows the displacement field of the array after 2000 steps with respect to the initial starting positions of the atoms. Figure 118 shows the corresponding strain field and Figure 119 the strain gradient field. In

Figure 119, the dislocation loops have been marked for easy recognition. Recall that the simulation arrays were created with periodic boundary conditions on the left and right faces and so the dislocation loop that ends at the left side continues into the array from the right side where it eventually ends.

Dislocation generation at the crack surfaces is clearly seen, but some spontaneous dislocation creation is also occurring in the lattice away from the crack tip. These loops often self-annihilate at later times as the strain distribution continues to change, but the crack-initiated dislocations are generally permanent and propagate outwards from the crack.

A new set of programs was also instituted to determine the energy changes near the crack tip. The energy change measurements were done by having the computer continuously monitor the potential energy of a small number of atoms all within several atom distances of the crack tip on the right side of the array, and separately, a small group on the left side. This technique provided much finer resolution of the events occurring in the immediate vicinity of the crack tip such as dislocation nucleation or bond breaking. The difference is quite evident in comparing Figure 120a, which shows the potential energy of the total 9000 atom array under constant strain conditions, and Figure 120b, which shows the potential energy of just a few hundred atoms at either side of the crack. Fairly good correlation has been seen between the energy peaks in Figure 120b and the time when either dislocations are first formed in these regions, or just before additional bonds are broken. As a result, the activation energies for dislocation generation and for crack propagation may eventually be measurable with some degree of accuracy. If so, this would provide essential numbers for estimating the plastic work, γ_p . When γ_p is added to the surface energy, 2γ , one can get the total work of propagating a crack and thus a direct measure of the toughness of the material.

8. CONCLUSIONS

8.1 ALLOY DEVELOPMENT

This program was conducted with the intention of developing NiAl-base alloys with properties suitable for use as a turbine disk material. The program emphasized overcoming the room temperature brittleness problem as well as enhancing the high-temperature strength and creep resistance. The former goal was addressed primarily through alloying to change the ordering energy and thus modify the room temperature slip behavior and through the use of a variety of martensitic transformation mechanisms. The latter goals were addressed through both ternary and quaternary alloying approaches, including solid-solution precipitation and martensitic strengthening mechanisms. Significant progress was made in this program with respect to improvements in the room temperature ductility and fracture toughness. However, an acceptable combination of low-temperature ductility/fracture resistance and high-temperature strength and creep resistance has not yet been achieved. Further development is needed in order to overcome the remaining deficiencies. The main areas of progress in this program can be summarized as follows:

- Cr and Co additions to NiAl modify the slip behavior and enhance $\langle 111 \rangle$ slip with respect to $\langle 001 \rangle$ slip. However, the modified alloys are still brittle at room temperature, indicating that the presence of sufficient slip systems does not guarantee ductility.
- Fe-modified NiAl alloys exhibit unusual tensile elongation versus temperature behavior similar to that seen in binary FeAl alloys.
- The operation of martensitic transformation mechanisms in Co-modified NiAl alloys resulted in enhanced room temperature ductility (up to 2.2%) and fracture toughness (up to $33.3 \text{ MPa}\sqrt{\text{m}}$). The enhanced properties were controlled by a variety of mechanisms, including:
 - A stress-induced parent-to-martensite transformation.
 - The rearrangement, under an applied stress/strain, of fine twin lamellae within the existing martensitic variants.
 - The nucleation of alternate martensitic variants under stress.
- Ternary additions to NiAl strengthen via:
 - The precipitation of fine gamma prime (γ').
 - Heusler precipitates (with 10 a/o Ti).
 - The presence of a high-Co (Ni,Co)Al B2 phase (Co).
 - The presence of extremely fine twin lamellae in the martensitic structure (Co).
- The quaternary elements Hf and Ti were added to selected tough NiAlCo alloys to improve the strength and creep resistance with the following results:
 - 0.51 a/o Hf additions improve the strength and creep resistance at high temperatures.
 - 5 a/o Ti additions strengthen at all temperatures via solid-solution mechanisms.
 - Both Ti and Hf additions reduce the room temperature ductility and fracture toughness considerably.

- The addition of chopped PRD-166 fibers to Ni-29 a/o Al-21 a/o Co in Phase III improves the strength, stiffness and LCF life, but degrades the room temperature ductility and fracture toughness and high-temperature creep resistance. The lower ductility and fracture toughness of the composite are attributed to shortening of the fibers during consolidation and the lower creep resistance to the finer grain size.

8.2 ATOMIC BONDING STUDIES

EXAFS and XANES studies were performed on selected B2 compounds to determine the strength and character of the bonding. Important results are summarized as follows:

- A new method was developed for obtaining EXAFS spectra of major species in bulk samples which provides significant sample preparation advantages over conventional powder or thin-film methods.
- EXAFS studies of selected B2 compounds revealed:
 - The first neighbor bond strengths of NiAl and CoAl are similar while the second and third nearest neighbor bond strengths are 5 and 6.6 times as strong, respectively, in CoAl as compared to NiAl.
 - FeAl is readily disordered by cold-working.
 - Cr additions to NiAl alloys reduce the first nearest neighbor bond strength, but do not affect the second nearest neighbor bond strength.
 - Cr additions to NiAl occupy Al sites.
- XANES studies showed that there is more charge transfer from the Al to the transition metal atoms in CoAl than in either NiAl or FeAl, indicating greater bond covalency.

8.3 COMPUTER SIMULATION STUDIES

Embedded Atom Method (EAM) simulations were conducted on stoichiometric ordered NiAl using EAM potentials developed for Ni₃Al. Much of the effort was focused on making the simulations as realistic as possible by using increasingly larger array sizes (up to 9000 atoms), center cracks, periodic boundary conditions, and constant strain rate loading. Notable results gained from this effort are as follows:

- Various physical properties were determined for NiAl as a means of checking the validity of the simulation. All properties were in excellent agreement with data from the literature where available. The simulated properties included lattice energy as a function of Bain strain, surface energies for NiAl and Ni, Anti-Phase Boundaries (APB) and APB energies, and melting points.
- EAM simulations of NiAl lattice deformation and crack propagation at various temperatures revealed:
 - Short-range surface diffusion plays a major role in crack blunting.
 - When the lattice was stressed in a $\langle 112 \rangle$ direction, a $\langle 1\bar{1}0 \rangle$ (110) shear-type martensitic lattice instability was observed.
 - The potential energy of the lattice experienced local maxima corresponding to the breaking of bonds and the generation of dislocations.

- The fracture plane of NiAl is predicted to be (100).
- The ductile-brittle transition temperature (DBTT) of NiAl is between 300 and 800K.
- A new dislocation recognition strategy was created which exploits the unique characteristics of the strain gradient near a dislocation. This method is superior to other methods because it does not require any prior knowledge of potential dislocation sites and is therefore ideal for larger array sizes.

REFERENCES

1. C. C. Law and M. J. Blackburn, "Rapidly Solidified Lightweight Durable Disk Material," Final Technical Report, F33615-84-C-5067, July 1987.
2. M. G. Mendiratta, T. I. Mah and S. K. Ehlers, "Mechanisms of Ductility and Fracture in Complex High-Temperature Materials," Final Technical Report, AFWAL-TR-85-4061, July 1985.
3. M. Ettenberg, K. L. Komareh and E. Miller in "Ordered Alloys," eds. B. H. Kear, C. T. Sims, N. S. Stoloff and J. H. Westbrook, Proc. 3rd Bolton Landing Conference, 1969, p. 49.
4. C. Müller, W. Blau and P. Ziesche, *Phys. Stat. Sol. (b)*, **116**, 561 (1983).
5. A. Taylor and R. W. Floyd, *J. Inst. Metals*, **81**, 451 (1952-1953).
6. D. B. Miracle, S. Russell and C. C. Law, *Mat. Res. Soc. Symp. Proc.*, **133**, 225 (1989).
7. T. Saburi and S. Nenno in *Proc. Int. Conf. 'Solid-Solid Phase Transformations'*, ed. H. I. Aaronson, et al., Pittsburgh, Pennsylvania, 1981, pp. 1455-1479.
8. K. Enami, V. V. Martynov, T. Tomie, L. G. Khandros and S. Nenno, *Trans. Japan Inst. Metals*, **22**, 357 (1981).
9. L. Kaufman and H. Nesor, *Met. Trans. A*, **6A**, 2123 (1975).
10. S. Chakravorty and C. M. Wayman, *Met. Trans. A*, **7A**, 555 (1976).
11. V. S. Litvinov and A. A. Arkhangel'skaya, *Fiz. Metal. Metalloved.*, **44**, 826 (1977).
12. S. M. Russell, C. C. Law and M. J. Blackburn, *Mat. Res. Soc. Symp. Proc.*, **133**, 627 (1989).
13. A. Taylor and R. W. Floyd, *J. Inst. Metals*, **81**, 25 (1952-1953).
14. R. Moskovic, *J. Mat. Sci.*, **12**, 1895-1902 (1977).
15. J. R. Patel and M. Cohen, *Acta Met.*, **1**, 531 (1953).
16. K. Otsuka and K. Shimizu, *Internat. Met. Rev.*, **31**, 93 (1986).
17. L. Delaey, F. Van de Voorde and R. V. Krishnan in *Shape Memory Effects in Alloys*, ed. J. Perkins, Plenum Press (1975), p. 351.
18. I. Baker and D. J. Gaydosch, *Mat. Sci. and Eng.*, **96**, 147-158 (1987).
19. K. Vedula, V. Pathare, I. Aslanidis and R. H. Titran, *Mat. Res. Soc. Symp. Proc.*, **39**, 411 (1985).
20. D. L. Yaney and W. D. Nix, *J. Mat. Sci.*, **23**, 3088 (1988).
21. K. S. Kumar and S. K. Mannan, ONR Report: MML TR88-66C, June 1988.
22. L. M. Barker in *Chevron-Notched Specimens: Testing and Stress Analysis*, eds. J. H. Underwood, S. W. Freiman and F. I. Baratta, ASTM Symposium, Lexington, Kentucky, 1983.

23. Private communications with S. Kumar, Martin Marietta Laboratories, February 1989.
24. N. Rusovic and H. Warlimont, *Phys. Stat. Sol. (a)*, **53**, 283 (1979).
25. W. J. Yang and R. A. Dodd, *Metal Science Journal*, **7**, 41 (1973).
26. P. R. Strutt and B. H. Kear, *Mat. Res. Soc. Symp. Proc.*, **39**, 279 (1985).
27. R. R. Vandervoort, A. K. Mukherjee and J. E. Dorn, *Trans. ASM*, **59**, 930 (1966).
28. L. Yang, J. H. Norman and G. H. Reynolds, "Thermodynamic Compatibility of Selected Reinforcing Phases in Advanced Intermetallic Matrices," Interim Progress Report for AFWAL Contract No. F33615-88-C-5403, prepared under Pratt & Whitney Subcontract No. 5405-2, September 1988.
29. A. K. Misra, "Thermodynamic Analysis of Compatibility of Several Reinforcement Materials with Beta Phase NiAl Alloys," NASA Contractor Report 4171, November 1988.
30. R. H. Krock and L. J. Broutman in *Modern Composite Materials*, eds. L. J. Broutman and R. H. Krock, Addison-Wesley Publishing Co. (1967), pp. 13-16.
31. F. W. Lytle, D. E. Sayers and E. A. Stern in *Advances in X-ray Spectroscopy*, eds. C. Bonnelle and C. Maude, Pergamon (1982).
32. D. R. Sandstrom, E. C. Marques, V. A. Biebesheimer, F. W. Lytle and R. B. Gregor, *Phys. Rev.*, **B32**, 3541 (1985).
33. D. M. Pease, D. L. Brewster, Z. Tan, J. I. Budnick and C. C. Law, *Phys. Lett.*, **A138**, 230 (1989).
34. M. Mostoller, R. M. Nicklow and D. M. Zehner, *Phys. Rev. B*, **40**, 2856 (1989).
35. C. Müller, W. Blau and P. Zieche, *Phys. Stat. Sol. (b)*, **116**, 561 (1983).
36. D. M. Pease and L. V. Azaroff, *J. Appl. Phys.*, **50**, 6605 (1979).
37. M. S. Daw and M. I. Baskes, *Phys. Rev. B*, **29**, 6443 (1984).
38. S. P. Chen, A. F. Voter and D. J. Srolovitz, *Phys. Rev. Letts.*, **57**, 1308 (1986).
39. S. P. Chen, A. F. Voter and D. J. Srolovitz, *Scripta Met.*, **20**, 1389 (1986).
40. S. P. Chen, A. F. Voter and D. J. Srolovitz, "Atomistic Simulations of <001> Symmetric Tilt Boundaries in Ni₃Al," MRS Proceedings Winter 1986.
41. S. P. Chen, A. F. Voter and D. J. Srolovitz, "Atomistic Simulations of Surface Relaxations in Ni, Al, and Their Ordered Alloys," MRS Proceedings Winter 1986.
42. A. F. Voter and S. P. Chen, "Accurate Interatomic Potentials for Ni, Al and Ni₃Al," MRS Proceedings Winter 1986.
43. S. Charpenay, P. C. Clapp, J. A. Rifkin, Z. Z. Yu and A. F. Voter in *Atomic Scale Calculations in Materials Science*, eds. J. Tersoff, D. Vanderbilt and V. Vitek, MRS Proceedings Volume 141 (1989).

44. K. Maeda, V. Vitek and A. P. Sutton, *Acta. Met.*, 30, 2001 (1982).
45. K. C. Russell and J. W. Eddington, *J. Mat. Sci.*, 6, 20 (1972).
46. M. J. Lequeux, Ph.D. Thesis, Univ. de Paris-Sud (1979).
47. P. S. Maiya and J. M. Blakely, *J. Appl. Phys.*, 38, 698 (1967).
48. E. R. Hayward and A. P. Greenough, *J. Inst. Met.*, 88, 217 (1959-1960).
49. H. Jones, *Met. Sci. J.*, 5, 15 (1971).
50. J. R. Rice and R. Thomson, *Phil. Mag.*, 29, 73 (1974).

Table 1. Modified Phase I Alloys

Alloy	Nominal Composition (atom percent)				Ductilizing Approach
A	35.0 Ni	30.0 Al	35.0 Co	}	Formation of a (Ni,Co) ₃ (Al,Co) Phase
B	44.75 Ni	30.0 Al	25.0 Co 0.25 B		
C	50.0 Ni	29.0 Al	21.0 Co	}	Stress-Induced Martensitic Transformation
D	55.0 Ni	35.0 Al	10.0 Co		
E	39.0 Ni	33.0 Al	28.0 Fe	}	Formation of (Ni,Fe)(Al,Fe) B2 Phase
F	47.0 Ni	33.0 Al	20.0 Fe		
G	60.0 Ni	35.0 Al	5.0 V	}	Change Slip Behavior to <111> Type
H	57.0 Ni	35.0 Al	5.0 V 3.0 Cr		
I	60.0 Ni	35.0 Al	5.0 Ti	}	Change of Martensite Variants
J	50.0 Ni	40.0 Al	10.0 Ti	}	Stress-Induced Martensitic Transformation

Table 2. Modified Phase I Cast Alloys

Alloy		Composition (atom percent)					Ductilizing Approach
A	<u>Aim</u> <u>Chem. Anal.</u>	35.0 Ni	30.0 Al	35.0 Co		}	Formation of (Ni,Co) ₃ (Al,Co) Phase
		34.0 Ni	29.3 Al	36.7 Co			
B	<u>Aim</u> <u>Chem. Anal.</u>	44.75 Ni	30.0 Al	25.0 Co	0.25 B	}	
		45.4 Ni	31.5 Al	23.1 Co			
C	<u>Aim</u> <u>Chem. Anal.</u>	50.0 Ni	29.0 Al	21.0 Co		}	Stress-Induced Martensitic Transformation
		49.9 Ni	29.3 Al	20.8 Co			
D	<u>Aim</u> <u>Chem. Anal.</u>	55.0 Ni	35.0 Al	10.0 Co		}	
		54.8 Ni	35.7 Al	9.5 Co			
E	<u>Aim</u> <u>Chem. Anal.</u>	39.0 Ni	33.0 Al	28.0 Fe		}	Formation of (Ni,Fe)(Al,Fe) B2 Phase
		36.8 Ni	32.6 Al	30.6 Fe			
F	<u>Aim</u> <u>Chem. Anal.</u>	47.0 Ni	33.0 Al	20.0 Fe		}	
		46.3 Ni	34.2 Al	19.5 Fe			
G	<u>Aim</u> <u>Chem. Anal.</u>	60.0 Ni	35.0 Al	5.0 V		}	Change Slip Behavior to <111> Type
		60.5 Ni	34.4 Al	5.1 V			
H	<u>Aim</u> <u>Chem. Anal.</u>	57.0 Ni	35.0 Al	5.0 V	3.0 Cr	}	
		55.8 Ni	35.7 Al	4.9 V	3.6 Cr		
I	<u>Aim</u> <u>Chem. Anal.</u>	60.0 Ni	35.0 Al	5.0 Ti		}	Change of Martensite Variants
		59.3 Ni	35.9 Al	4.8 Ti			
J	<u>Aim</u> <u>Chem. Anal.</u>	50.0 Ni	40.0 Al	10.0 Ti		}	Stress-Induced Martensitic Transformation
		49.9 Ni	40.6 Al	9.9 Ti			

Table 3. Phase I Alloy Densities

Alloy	Density (gram/cm ³)	Weight Savings (%)
Current Superalloy Disk Materials	8.0	—
Ni-43 a/o Al	6.0	25
Baseline (NiCrAl)	6.2	22
A	7.0	12
B	6.9	13
C	7.1	11
E	6.6	17
F	6.6	17
G	6.6	17

Table 4. Homogenized Cast and Extruded Phase I Alloy Structures

Alloy	Nominal Composition (atom percent)	X-Ray Diffraction Results		Optical/SEM Observations
		Phase Structure	Lattice Parameter (nm)	
A	35Ni-30Al-35Co	80% beta NiAl 20% fcc Ni solid solution	a = 0.285473	NiAl grains with a small amount of a Co-rich grain boundary phase
B	44.75Ni-30Al-25Co-.25B	100% tetragonal	a = 0.3847 c = 0.3158	Martensitic grains with a very small amount of a Co-rich grain boundary phase
C	50Ni-29Al-21Co	70-75% tetragonal 30-25% fcc Ni solid solution	a = 0.3784 c = 0.3232 a = 0.3587	Martensitic grains with a small amount of a Co-rich grain boundary phase
E	39Ni-33Al-28Fe	100% beta NiAl	a = 0.288135	Equiaxed grains with fine, widely dispersed Fe-rich particles
F	47Ni-33Al-20Fe	100% beta NiAl	a = 0.288028	Equiaxed grains with fine, widely dispersed Fe-rich particles
G	60Ni-35Al-5V	100% beta NiAl	a = 0.287225	Equiaxed grains
H	57Ni-35Al-5V-3Cr	100% beta NiAl	a = 0.287802	Equiaxed grains with widely dispersed Al-poor particles
J	50Ni-40Al-10Ti	70-80% ord. fcc Heusler Ni ₂ AlTi-type 30-20% ord. bcc Ni(Ti,Al)	a = 0.58088 a = 0.29359	Dendritic with an inter-dendritic secondary phase

Table 5. Martensite Transformation Temperatures in Phase I NiAl-Co Alloys

Alloy	Composition (atom percent)					Transformation Temperatures (°C)		
	Ni	Co	Al	B	As	Af	Ms	Mf
VIM A	35	35	30	—	-70	-55	-25	-50
VIM B	44.75	25	30	0.25	170	215	180	150
VIM C	50	21	29	—	675	695	665*	
P/M D	55	10	35	—	270*		165	150

* Only one transformation temperature observed on dilatometer trace in the form of a change in slope only

Table 6. Electron Microprobe Analysis of Phase I NiAl-Co Alloys

Alloy	Phase*	Composition (atom percent)				Phase Structure
		Ni	Co	Al	B	
A	Bulk	35	35	30		
	1	34	34	32		(Ni,Co)(Co,Al), B2
	2	29	55	16		(Ni,Co) ₃ (Al,Co), L1 ₂
B	Bulk	44.75	25	30	0.25	
	1	45	21	34		Ni(Al,Co), L1 ₀
	2	36	32	11	21	possibly (Ni,Co) ₂₀ Al ₃ B ₆ **
C	Bulk	50	21	29		
	1	48	21	31		Ni(Al,Co), L1 ₀
	2	49	33	18		(Ni,Co) ₃ (Al,Co), L1 ₂

* See Figure 20 for identity of phases within the microstructure.

** Boride identity deduced from electron microprobe results.

Table 7. Tensile Data of Phase I VIM Alloys

Alloy	Heat Treatment Condition	Temperature °C (F)	Percent Elongation	Ductility Transition Temp. °C (°F)	0.2% Yield MPa (ksi)
Cast A	As-extruded	Room Temp.	1.8	650 (1200)	*
		540 (1000)	0.3		*
		760 (1400)	113.6		93 (14)
Cast A	1050°C/2hr/Air Cool	Room Temp.	0.0	650 (1200)	*
		540 (1000)	1.3		*
		760 (1400)	79.4		127 (18)
Cast B	As-extruded	Room Temp.	0.3	600 (1100)	*
		540 (1000)	1.2		552 (80)
		760 (1400)	172.8		180 (26)
Cast B	1050°C/2hr/Air Cool	Room Temp.	0.3	600 (1100)	*
		540 (1000)	1.3		409 (59)
		760 (1400)	105.3		142 (21)
Cast C	As-extruded	Room Temp.	2.2	600 (1100)	820 (119)
		540 (1000)	3.7		625 (91)
		760 (1400)	133.0		186 (27)
		980 (1800)	191.4		20 (3)
Cast C	1050°C/2hr/Air Cool	Room Temp.	1.7	750 (1400)	*
		540 (1000)	2.3		864 (125)
		760 (1400)	19.1		303 (44)
		980 (1800)	149.2		28 (4)
Cast D	As-extruded	Room Temp.	0.0	700 (1300)	*
		540 (1000)	0.0		*
		760 (1400)	190.0		152 (22)
Cast D	1050°C/2hr/Air Cool	Room Temp.	0.0	700 (1300)	*
		540 (1000)	0.0		*
		760 (1400)	94.0		95 (14)
Cast E	As-extruded	Room Temp.	0.0	++	*
		540 (1000)	26.6		342 (50)
		760 (1400)	20.7		178 (26)
		980 (1800)	38.6		47 (7)
		1120 (2050)	118.0		26 (4)
Cast E	1050°C/2hr/Air Cool	Room Temp.	0.0	++	*
		540 (1000)	6.7		282 (41)
		760 (1400)	5.7		161 (23)
		980 (1800)	5.4		53 (8)
		1120 (2050)	12.7		15 (2)
Cast F	As-extruded	Room Temp.	0.0	++	*
		540 (1000)	26.5		370 (54)
		760 (1400)	34.4		169 (25)
		980 (1800)	96.7		29 (4)
Cast F	1050°C/2hr/Air Cool	Room Temp.	0.0	++	*
		540 (1000)	10.0		389 (56)
		760 (1400)	10.6		185 (27)
		980 (1800)	114.4		25 (4)

* = Fractured before yielding

++ = Unusual ductility versus temperature dependence; see text

Table 7. Tensile Data of Phase I VIM Alloys (continued)

<u>Alloy</u>	<u>Heat Treatment Condition</u>	<u>Temperature °C (F)</u>	<u>Percent Elongation</u>	<u>Ductility Transition Temp. °C (°F)</u>	<u>0.2% Yield MPa (ksi)</u>
Cast G	As-extruded	Room Temp.	0.0	600 (1100)	*
		540 (1000)	0.0		398 (58)
		760 (1400)	129.1		194 (28)
		980 (1800)	193.3		35 (5)
Cast H	As-extruded	Room Temp.	0.0	600 (1100)	*
		540 (1000)	0.4		704 (102)
		760 (1400)	25.5		220 (32)
		980 (1800)	135.5		34 (5)
Cast I	As-extruded	Room Temp.	0.0	600 (1100)	*
		540 (1000) ⁺	0.7		540 (78)
		760 (1400)	55.0		309 (45)
Cast I	1050°C/2hr/Air Cool	Room Temp.	0.0	650 (1200)	*
		540 (1000)	0.0		*
		760 (1400)	92.5		372 (54)
* = Fractured before yielding					
++ = Unusual ductility versus temperature dependence; see text					

Table 8. Tensile Data of Phase I Powder Alloys

Alloy	Heat Treatment Condition	Temperature °C (°F)	Percent Elongation	Fracture Strength MPa (ksi)	0.2% Yield MPa (ksi)
P/M A	As-extruded	Room Temp.	0.0	791 (115)	*
		540 (1000)	24.8	905 (131)	794 (115)
		760 (1400)	25.7	99 (14)	131 (19)
		980 (1800)	218.0	13 (2)	16 (2)
P/M A	1050°C/2hr/Air Cool	Room Temp.	0.4	850 (123)	850 (123)
		540 (1000)	18.8	876 (127)	503 (73)
		760 (1400)	43.0	71 (10)	114 (16)
		980 (1800)	106.0	20 (3)	24 (3)
P/M B	As-extruded	Room Temp.	0.0	358 (52)	*
		540 (1000)	13.9	919 (133)	560 (81)
		760 (1400)	45.0	76 (11)	135 (20)
		980 (1800)	80.0	8 (1)	31 (4)
P/M B	1050°C/2hr/Air Cool	Room Temp.	0.0	690 (100)	*
		540 (1000)	11.0	813 (118)	493 (71)
		760 (1400)	78.4	55 (8)	124 (18)
P/M C	As-extruded	Room Temp.	0.7	1087 (158)	968 (140)
		540 (1000)	18.6	1041 (151)	611 (89)
		765 (1410)	76.3	53 (8)	80 (12)
P/M C	1050°C/2hr/Air Cool	Room Temp.	0.0	717 (104)	717 (104)
		540 (1000)	1.2	823 (119)	492 (71)
		760 (1400)	48.0	54 (8)	135 (20)
P/M D	As-extruded	Room Temp.	0.0	283 (41)	*
		540 (1000)	0.0	462 (67)	*
		760 (1400)	107.0	193 (28)	166 (24)
		980 (1800)	183.0	34 (5)	14 (2)
P/M D	1050°C/2hr/Air Cool	Room Temp.	0.0	269 (39)	*
		540 (1000)	0.0	290 (42)	*
		760 (1400)	82.5	214 (31)	166 (24)
		980 (1800)	167.0	41 (6)	34 (5)
P/M E	As-extruded	Room Temp.	1.1	633 (92)	*
		540 (1000)	49.8	411 (60)	371 (54)
		760 (1400)	10.0	169 (25)	190 (28)
		980 (1800)	42.4	26 (4)	59 (8)
P/M E	1050°C/2hr/Air Cool	Room Temp.	0.0	783 (114)	*
		430 (800)	5.2	740 (107)	571 (83)
		540 (1000)	51.3	380 (55)	295 (43)
		650 (1200)	26.9	223 (32)	208 (30)
		760 (1400)	14.7	205 (30)	213 (31)
		980 (1800)	77.1	22 (3)	57 (8)
P/M F	As-extruded	Room Temp.	0.7	852 (124)	852 (124)
		430 (800)	3.5	640 (93)	486 (70)
		540 (1000)	42.3	460 (67)	541 (78)
		650 (1200)	15.5	334 (48)	346 (50)
		760 (1400)	5.9	179 (26)	241 (35)
		980 (1800)	82.5	2 (0)	33 (5)

* = Fractured before yielding.

Table 8. Tensile Data of Phase I Powder Alloys (continued)

Alloy	Heat Treatment Condition	Temperature °C (°F)	Percent Elongation	Fracture Strength MPa (ksi)	0.2% Yield MPa (ksi)
P/M F	1050°C/2hr/Air Cool	Room Temp.	0.7	683 (99)	683 (99)
		430 (800)	9.8	760 (112)	611 (89)
		540 (1000)	29.0	552 (80)	544 (79)
		650 (1200)	12.1	332 (48)	320 (46)
		760 (1400)	6.6	197 (29)	232 (34)
		980 (1800)	81.0	31 (5)	34 (5)
P/M G	As-extruded	Room Temp.	0.0	332 (49)	*
		540 (1000)	0.0	541 (79)	*
		760 (1400)	42.6	142 (21)	263 (38)
		980 (1800)	84.7	13 (2)	33 (5)
P/M G	1050°C/2hr/Air Cool	Room Temp.	0.0	446 (65)	*
		540 (1000)	8.6	823 (119)	725 (105)
		760 (1400)	55.4	95 (14)	196 (29)
		980 (1800)	89.3	11 (2)	40 (6)
P/M H	As-extruded	Room Temp.	0.0	181 (26)	*
		540 (1000)	0.0	633 (92)	*
		760 (1400)	18.7	87 (13)	203 (29)
		980 (1800)	85.5	14 (2)	41 (6)
P/M I	As-extruded	Room Temp.	0.0	176 (26)	*
		540 (1000)	0.0	330 (48)	*
		760 (1400)	81.8	123 (18)	219 (32)
P/M I	1050°C/2hr/Air Cool	Room Temp.	1.3	154 (22)	154 (22)
		540 (1000)	1.0	241 (35)	241 (35)
		760 (1400)	65.6	162 (24)	263 (38)

* = Fractured before yielding.

Table 9. Tensile Fracture Behavior of Phase I VIN Alloys

Alloy	Heat Treatment Condition	Fracture Mode				
		Room Temp.	540°C	760°C	980°C	1120°C
A	As-extruded	mostly T	mixed	D	—	—
	1050°C/2hr/Air Cool	T	mixed	D	—	—
B	As-extruded	mostly I	mostly T	DI	—	—
	1050°C/2hr/Air Cool	mostly I	mostly T	D	—	—
C	As-extruded	mixed	T	D	D	—
	1050°C/2hr/Air Cool	mixed	mixed	DI	D	—
D	As-extruded	mostly I	mostly I	D	—	—
	2h/1050°C/AC	I	mixed	DI	—	—
E	As-extruded	mixed	mixed	mostly I	mostly I	DI
	1050°C/2hr/Air Cool	mostly I	mixed	I	I	DI
F	As-extruded	T	mostly T	DI	D	—
	1050°C/2hr/Air Cool	T	mostly T	I	D	—
G	As-extruded	T	T	D	D	—
H	As-extruded	T	mixed	I	D	—
I	As-extruded	T	mostly T	D	—	—
	1050°C/2hr/Air Cool	mostly T	mostly T	D	—	—

I = Intergranular fracture

T = Transgranular cleavage

mixed = Both transgranular cleavage and intergranular fracture

D = Ductile tearing

DI = Ductile tearing plus intergranular separation

Table 10. Tensile Fracture Behavior of Phase I Powder Alloys

Alloy	Heat Treatment Condition	Fracture Mode			
		Room Temp.	540°C	760°C	980°C
P/M A	As-extruded	T	T	DI	DI
	1050°C/2hr/Air Cool	T	mostly T	D	—
P/M B	As-extruded	mostly I	mostly T	DI	D
	1050°C/2hr/Air Cool	mostly I	mostly T	D	—
P/M C	As-extruded	mixed	mixed	DI	—
	1050°C/2hr/Air Cool	I	mostly I	DI	DI
P/M E	As-extruded	mostly T	mostly T	mostly I	mixed
	1050°C/2hr/Air Cool	T	T	mostly I	I
P/M F	As-extruded	T	mostly T	I	DI
	1050°C/2hr/Air Cool	T	mostly T	I	DI
P/M G	As-extruded	T	T	D	D
	1050°C/2hr/Air Cool	T	T	DI	D
P/M H	As-extruded	T	mostly T	I	D
P/M I	As-extruded	T	T	D	—
	1050°C/2hr/Air Cool	T	T	T	—

I	= Intergranular fracture
T	= Transgranular cleavage
mixed	= Both transgranular cleavage and intergranular fracture
D	= Ductile tearing
DI	= Ductile tearing plus intergranular separation

Table 11. Phase II Alloys

<u>Alloy</u>	<u>Nominal Composition (atom percent)</u>	<u>Rationale</u>	<u>Purpose</u>	<u>Form</u>
A2 (1)	Ni – 32.0 Al – 29.0 Co	} Stress-Induced Martensite $M_s < RT$	} Toughening	} Extruded VIM Ingots
A3 (1)	Ni – 32.0 Al – 25.0 Co			
C2 (3)	Ni – 31.0 Al – 16.0 Co	} $M_s \gg RT$		
C3 (3)	Ni – 30.0 Al – 15.0 Co			
B2 (2)	Ni – 30.0 Al – 25.0 Co	} Alloy B w/o boron		
AT (1)	Ni – 30.0 Al – 32.5 Co – 5.0 Ti	} Precipitation Hardening	} Strengthening	
CT (3)	Ni – 29.0 Al – 21.0 Co – 5.0 Ti			
AH (1)	Ni – 30.0 Al – 34.5 Co – 0.5 Hf	} Solid-Solution Strengthening		
CH (3)	Ni – 29.0 Al – 21.0 Co – 0.5 Hf			
M1	(Ni – 50.0 Al) + 20 v/o MERL 76	} Ductile Particle/ Brittle Matrix	} Toughening	} Extruded Powder Mixtures

Alloys based on the following Phase I Alloys:

- (1) Alloy A: Ni - 30 Al - 35 Co
- (2) Alloy B: Ni - 30 Al - 25 Co - 0.25 B
- (3) Alloy C: Ni - 29 Al - 21 Co

Table 12. Phase II Alloy Compositions (atom percent)*

Alloy		Ni	Al	Co	Hf	Ti
A2	Nominal:	39.0	32.0	29.0		
	Chemical Analysis:	38.3	34.0	27.7		
A3	Nominal:	43.0	32.0	25.0		
	Chemical Analysis:	43.0	32.7	24.3		
C2	Nominal:	53.0	31.0	16.0		
	Chemical Analysis:	52.9	31.5	15.6		
C3	Nominal:	55.0	30.0	15.0		
	Chemical Analysis:	54.6	30.9	14.5		
B2	Nominal:	45.0	30.0	25.0		
	Chemical Analysis:	44.6	31.2	24.2		
AT	Nominal:	32.5	30.0	32.5		5.0
	Chemical Analysis:	32.3	31.5	31.3		4.9
CT	Nominal:	45.0	29.0	21.0		5.0
	Chemical Analysis:	44.5	30.1	20.5		4.9
AH	Nominal:	35.0	30.0	34.5	0.50	
	Chemical Analysis:	35.1	30.9	33.5	0.51	
CH	Nominal:	49.5	29.0	21.0	0.50	
	Chemical Analysis:	49.3	29.8	20.4	0.53	

* $\pm 2\%$ of the reported value

Table 13. X-Ray Diffraction Results for Phase II Alloys

Alloy	Nominal Composition (atom percent)	X-Ray Diffraction		Optical Metallography/ Phase Diagram
		Phases Present	Lattice Parameters (nm)	
A2	Ni-32 Al-29 Co	ord. bcc	a = 0.285779	NiAl-type, B2
A3	Ni-32 Al-25 Co	tetragonal	a = 0.38868 c = 0.30844	NiAl-type, L1 ₀
		ord. ? bcc	a = 0.285969	NiAl-type, B2
B2	Ni-30 Al-25 Co	ord. fct	a = 0.38320 c = 0.30771	NiAl-type, L1 ₀
		ord. ? fcc	a = 0.357356	Ni ₃ Al-type, L1 ₂
C2	Ni-31 Al-16 Co	ord. ? fct	a = 0.38053 c = 0.30128	NiAl-type, L1 ₀
		ord. ? fcc	a = 0.357525	Ni ₃ Al-type, L1 ₂
C3	Ni-30 Al-15 Co	ord. ? fct	a = 0.38122 c = 0.31238	NiAl-type, L1 ₀
		ord. fcc	a = 0.357789	Ni ₃ Al-type, L1 ₂
AH	Ni-30 Al-34.5 Co-0.5 Hf	ord. bcc	a = 0.286023	NiAl-type, B2
		ord. ? fcc	a = 0.35729	Ni ₃ Al-type, L1 ₂ or (Ni,Co) Solid Solution, A1
AT	Ni-30 Al-32.5 Co-5 Ti	ord. bcc	a = 0.28721	NiAl-type, B2
CH	Ni-29 Al-21 Co-0.5 Hf	ord. ? fct	a = 0.38375 c = 0.31006	NiAl-type, L1 ₀
		ord. ? fcc	a = 0.359318	Ni ₃ Al-type, L1 ₂
CT	Ni-29 Al-21 Co-5 Ti	ord. ? bcc	a = 0.287092	NiAl-type, B2
		ord. ? fcc	a = 0.359197	Ni ₃ Al-type, L1 ₂
? = Assumed ordered; superlattice peaks too weak for clear identification				

Table 14. Martensitic Transformation Temperatures of NiAl-Co Alloys

Alloy	Composition (atom %)				Transformation Temperatures (°C)			
	Ni	Co	Al	B	As	Af	Ms	Mf
A	35	35	30	—	-70	-55	-25	-50
B	44.75	25	30	0.25	170	215	180	150
C	50	21	29	—	675	695		665*
P/M D	55	10	35	—	270*		165	150
A2	39	29	32	—			15+	—
A3	43	25	32	—			70+	—
B2	45	25	30	—	40	240	110	95
C2	53	16	31	—	445*		270	255
C3	55	15	30	—	330	360		160*

* = Only one transformation temperature observed on dilatometer trace in the form of a change in slope only

+ = Ms determined via quenching experiments only

Table 15. Phase II Alloys Metallography Results

Alloy	Phases Present (volume percent)	Grain Size (ASTM No.)	
		As-Extruded	1050°C/2hr/Air Cool
A2	NiAl-type, B2	5	2
A3	NiAl-type, L1 ₀	5	3
B2	95% NiAl-type, L1 ₀ + 5% Ni ₃ Al-type, L1 ₂	5	4
C2	95% NiAl-type, L1 ₀ + 5% Ni ₃ Al-type, L1 ₂	5	4-5
C3	70-65% NiAl-type, L1 ₀ + 30-35% Ni ₃ Al-type, L1 ₂	5	8
AH	90% NiAl-type, B2 + 10% Ni ₃ Al-type, L1 ₂	6	4
AT*	90% NiAl-type, B2 + 10% Ni ₃ Al-type, L1 ₂	—*	—*
CH	80% NiAl-type, B2 + 20% Ni ₃ Al-type, L1 ₂	7	7
CT	80% NiAl-type, B2 + 20% Ni ₃ Al-type, L1 ₂	8	6
M1	As-Extruded		
	80% NiAl-type, B2 + 20% MERL 76 particles	7 (matrix)	—
	1050°C/2hr/Air Cool		
	60-65% NiAl-type, B2 + 25% Ni ₃ Al-type, L1 ₂	—	7 (matrix)
	10-15% MERL 76 particles		

* As-cast ingot only

Table 16. Gamma Prime Compositions in Alloy CT at 760°C (1400°F)

Phase Location	Composition (atom percent)				Composition (weight percent)			
	Ni	Al	Co	Ti	Ni	Al	Co	Ti
Grain Boundary	63.2	13.6	17.9	5.3	68.9	6.8	19.6	4.7
Grain Interior	61.1	13.8	17.8	7.3	66.8	7.0	19.6	6.6

Table 17. Morphology and Structure of the Phases Present in Alloys A and AH at Room Temperature and 760°C (1400°F)

Phase	Alloy A		Alloy AH	
	Room Temp. Morph./Struct.	760°C (1400°F) Morph./Struct.	Room Temp. Morph./Struct.	760°C (1400°F) Morph./Struct.
Matrix	B2	B2	B2	B2
Boundary Ppts.	Blocky L1 ₂	Blocky L1 ₂	Blocky A3	Small Blocky A3 Blocky A1
Matrix Ppts.	None	Prism-shaped A1	None	Rod-shaped A3
Phase Structures:				
A1 = disordered fcc		A3 = hexagonal		
B2 = ordered bcc		L1 ₂ = ordered fcc		

Table 18. Compositions of Phases Present in Alloys A and AH at 760°C (1400°F)

Alloy A: Ni-29.3 Al-36.7 Co					Alloy AH: Ni-30.9 Al-33.5 Co-0.51 Hf				
Composition (atom percent)					Composition (atom percent)				
Phase	Ni	Al	Co	Hf	Phase	Ni	Al	Co	Hf
B ²	35.8	35.0	29.2	—	B2*	35.6	34.4	30.0	—
L1 ₂	31.0	13.5	55.5	—	A1	27.6	11.8	60.6	—
A1	23.7	13.6	62.7	—	A3	39.9	10.8	41.9	7.4

* Calculated from precipitate compositions and volume fractions

Table 19. Tensile Data of Phase II NiAlCo Alloys

Alloy	Heat Treatment Condition	Temperature °C (°F)	Percent Elongation	Ultimate Strength MPa (ksi)	0.2% Yield Strength MPa (ksi)
A2	As-extruded	Room Temp.	0.0	172 (25)	*
		540 (1000)	0.0	428 (62)	*
		760 (1400)	22.4	138 (20)	117 (17)
A2	1050°C/2hr/Air Cool	Room Temp.	0.0	117 (17)	*
		540 (1000)	0.0	435 (63)	*
		760 (1400)	30.0	138 (20)	124 (18)
		980 (1800)	188.2	28 (4)	28 (4)
A3	As-extruded	Room Temp.	0.6	172 (25)	*
		540 (1000)	1.3	372 (54)	*
		760 (1400)	89.1	152 (22)	124 (18)
		980 (1800)	220.0	28 (4)	21 (3)
A3	1050°C/2hr/Air Cool	Room Temp.	0.0	78 (11)	*
		540 (1000)	0.0	124 (18)	*
		760 (1400)	33.9	138 (20)	117 (17)
		980 (1800)	100.0	21 (3)	14 (2)
B2	As-extruded	Room Temp.	0.0	379 (55)	*
		540 (1000)	0.0	572 (83)	469 (68)
		765 (1410)	88.1	186 (27)	152 (22)
B2	1050°C/2hr/Air Cool	Room Temp.	0.0	193 (28)	*
		540 (1000)	1.3	248 (36)	*
		760 (1400)	55.6	131 (19)	103 (15)
C2	As-extruded	Room Temp.	0.0	414 (60)	*
		540 (1000)	0.0	510 (74)	*
		760 (1400)	52.2	248 (36)	200 (29)
C2	1050°C/2hr/Air Cool	Room Temp.	0.0	228 (33)	*
		540 (1000)	0.0	359 (52)	*
		760 (1400)	15.2	276 (40)	214 (31)
		980 (1800)	159.6	28 (4)	28 (4)
C3	As-extruded	Room Temp.	0.0	572 (83)	*
		540 (1000)	0.6	745 (108)	745 (108)
		760 (1400)	43.3	228 (33)	200 (29)
		980 (1800)	246.0	21 (3)	14 (2)
C3	1050°C/2hr/Air Cool	Room Temp.	1.3	366 (53)	*
		540 (1000)	1.3	559 (81)	*
		760 (1400)	96.8	186 (27)	124 (18)
		980 (1800)	229.0	28 (4)	7 (1)

* No apparent yielding on the stress-strain curve prior to fracture

Table 20. Tensile Data of Strengthening Modifications of Alloy A

Alloy	Heat Treatment Condition	Temperature °C (°F)	Percent Elongation	Fracture/ Ultimate Strength MPa (ksi)	0.2% Yield Strength MPa (ksi)
AH	As-extruded	Room Temp.	0.7	250 (36)	*
		540 (1000)	0.9	817 (118)	*
		760 (1400)	95.0	335 (49)	319 (46)
		980 (1800)	190.0	38 (6)	32 (5)
AH	1050°C/2hr/Air Cool	Room Temp.	0.0	207 (30)	*
		540 (1000)	0.3	530 (77)	*
		760 (1400)	39.7	477 (69)	464 (67)
		980 (1800)	137.0	55 (8)	51 (7)
A	As-extruded	Room Temp.	1.8	663 (96)	*
		540 (1000)	0.3	748 (108)	*
		760 (1400)	113.5	156 (23)	138 (20)
A	1050°C/2hr/Air Cool	Room Temp.	0.0	352 (51)	*
		540 (1000)	1.3	732 (106)	*
		760 (1400)	79.4	208 (30)	197 (29)

* No "classical" yielding detected on the stress-strain curve

Table 21. Tensile Data of Strengthening Modifications of Alloy C

Alloy	Heat Treatment Condition	Temperature °C (°F)	Percent Elongation	Fracture/ Ultimate Strength MPa (ksi)	0.2% Yield Strength MPa (ksi)
CH	As-extruded	Room Temp.	0.0	628 (91)	*
		540 (1000)	8.6	945 (137)	690 (100)
		760 (1400)	125.0	228 (33)	201 (29)
		980 (1800)	290.0	47 (7)	13 (2)
CH	1050°C/2hr/Air Cool	Room Temp.	0.0	329 (48)	*
		540 (1000)	1.6	653 (94)	*
		760 (1400)	74.6	323 (47)	310 (45)
		980 (1800)	170.0	44 (6)	39 (6)
CT	As-extruded	Room Temp.	0.0	637 (92)	*
		540 (1000)	0.0	519 (75)	*
		760 (1400)	93.0	314 (46)	265 (38)
		980 (1800)	300.0	46 (7)	39 (6)
CT	1050°C/2hr/Air Cool	Room Temp.	0.0	303 (44)	*
		540 (1000)	1.9	76 (11)	*
		760 (1400)	90.0	313 (45)	304 (44)
		980 (1800)	216.0	60 (9)	53 (8)
C	As-extruded	Room Temp.	2.2	821 (119)	*
		540 (1000)	3.1	766 (111)	625 (91)
		760 (1400)	133.0	192 (28)	172 (25)
		980 (1800)	191.4	26 (4)	18 (3)
C	1050°C/2hr/Air Cool	Room Temp.	1.7	588 (85)	*
		540 (1000)	2.3	864 (125)	*
		760 (1400)	19.1	341 (49)	317 (46)
		980 (1800)	149.2	31 (5)	28 (4)

* No "classical" yielding detected on the stress-strain curve

Table 22. Tensile Data of Alloy M1 with MERL 76 Reinforcement

Alloy	Heat Treatment Condition	Temperature °C (°F)	Percent Elongation	Fracture/ Ultimate Strength MPa (ksi)	0.2% Yield Strength MPa (ksi)
M1-76	As-extruded	Room Temp.	0.0	172 (25)	*
		540 (1000)	2.5	212 (31)	*
		760 (1400)	63.8	130 (19)	75 (11)
		980 (1800)	81.0	47 (7)	40 (6)
M1-76	1050°C/2hr/Air Cool	Room Temp.	0.0	238 (35)	*
		540 (1000)	0.6	213 (31)	*
		760 (1400)	47.2	161 (23)	133 (19)
		980 (1800)	87.0	54 (8)	48 (7)

* No yielding detected on the stress-strain curve

Table 23. Compression Data of First Series of Phase II Alloys*

Alloy	Composition (at.%, Ni bal.)		Phases at Room Temp.	0.2% Yield Strength, MPa (ksi)			
	Al	Co		Room Temp.	540°C (1000°F)	760°C (1400°F)	980°C (1800°F)
A	30	35	B2+10% L1 ₂	1118 (162)	1031 (150)	316 (46)	—
A2	32	29	B2	846 (123)	472 (69)	128 (19)	37 (5)
A3	32	25	L1 ₀ + B2	546 (79)	525 (76)	178 (26)	37 (5)
B2	30	25	L1 ₀ +5% L1 ₂	517 (75)	524 (76)	195 (28)	34 (5)
C	29	21	L1 ₀ +25% L1 ₂	754 (109)	558 (81)	163 (24)	—
C2	31	16	L1 ₀ +5% L1 ₂	716 (104)	900 (131)	276 (40)	34 (5)
C3	30	15	L1 ₀ +35% L1 ₂	1319 (191)	1455 (211)	303 (44)	19 (3)

* Heat Treatment: 1050°C/2hr/Air Cool

Table 24. Compression Data of Second Series of Phase II Alloys

Alloy	Alloy Composition (a/o)	Temperature °C (°F)	0.2% Yield Strength MPa (ksi)
A	Ni-30 Al-35 Co	Room Temp.	1118 (162)
		540 (1000)	1031 (150)
		760 (1400)	316 (46)
AH	Ni-30 Al-34.5 Co-0.5 Hf	Room Temp.	1045 (152)
		540 (1000)	705 (102)
		760 (1400)	411 (60)
		980 (1800)	54 (8)
C	Ni-29 Al-21 Co	Room Temp.	754 (109)
		540 (1000)	558 (81)
		760 (1400)	163 (24)
CH	Ni-29 Al-21 Co-0.5 Hf	Room Temp.	521 (76)
		540 (1000)	617 (89)
		760 (1400)	326 (47)
		980 (1800)	34 (5)
CT	Ni-29 Al-21 Co-5 Ti	Room Temp.	976 (142)
		540 (1000)	828 (120)
		760 (1400)	403 (58)
		980 (1800)	56 (8)
NiAl	Ni-50 Al	Room Temp.	310 (45)
		540 (1000)	170 (25)
		760 (1400)	90 (13)
		980 (1800)	39 (6)
M1-76	80 v/o (Ni-50 Al) + 20 v/o MERL 76 Particles	Room Temp.	413 (60)
		540 (1000)	284 (41)
		760 (1400)	154 (22)
		980 (1800)	57 (8)

Table 25. Room Temperature Fracture Toughness and Fracture Energy of Selected Alloys

Alloy	Nominal Composition (atom %)	Phases Present	K_{IC} (MPa \sqrt{m})	Fracture Energy (N-cm/cm ²)
NiAl	Ni-50 Al	100% B2 NiAl	5.4*, 5.9* 6.2°	6.5*, 7.2* —
NiAl	Ni-50 Al-0.25 B	100% B2 NiAl	5.9*, 6.2*	3.5*, 6.1*
NiAl	Ni-43 Al	100% B2 NiAl	4.3*, 6.9*	2.6*, 3.9*
NiAl	Ni-40 Al	100% B2 NiAl	6.8°	—
NiAl	Ni-38.5 Al	100% B2 NiAl	9.0°	—
NiAl	Ni-37 Al	100% B2 NiAl	7.5°	—
A	Ni-30 Al-35 Co	90% B2 NiAl 10% fcc (Co,Ni,Al)	15.6*, 18.5*	55*, 77*
A2	Ni-32 Al-29 Co	100% B2 NiAl	10.5*, 12.0+	15*, 17+
A3	Ni-32 Al-25 Co	100% L1 ₀ NiAl	8.3+, 10.9*	19+, 23*
B	Ni-30 Al-25 Co-0.25 B	95% L1 ₀ NiAl 5% boride	10.3*, 10.8*	33*, 43*
B2	Ni-30 Al-25 Co	95% L1 ₀ NiAl 5% Ni ₃ Al	14.9+, 17.8*	113+, 97*
C	Ni-29 Al-21 Co	90% L1 ₀ NiAl 10% Ni ₃ Al	22.8*, 25.3*	141*, 145*
C2	Ni-31 Al-16 Co	95% L1 ₀ NiAl 5% Ni ₃ Al	16.6+, 17.9*	72+, 70*
C3	Ni-30 Al-15 Co	70-65% L1 ₀ NiAl 30-35% Ni ₃ Al	13.2*, 15.8+	38*, 36+
D	Ni-35 Al-10 Co	100% L1 ₀ NiAl	9.1*, 10.2+	22*, 26+

* As-extruded VIM ingot (or powder of Ni-43Al and Alloy D)

+ As-extruded and heat treated at 2 hours/1050°C/air cooled

° Hot-pressed consolidated pre-alloyed powder (Reference 21)

Table 26. Room Temperature Fracture Toughness and Fracture Energy of Selected Quaternary Alloys and a NiAl Composite

<u>Alloy</u>	<u>Nominal Composition (atom %)</u>	<u>K_{max} (MPa\sqrt{m})</u>	<u>Fracture Energy (J-cm/cm²)</u>
A	Ni-30 Al-35 Co	15.6*, 18.5*	55*, 77*
AM	Ni-30 Al-34.5 Co-0.5 Hf	(10.9*)	(12*)
C	Ni-29 Al-21 Co	22.8*, 25.3*	141*, 145*
CM	Ni-29 Al-21 Co-0.5 Hf	17.7*, 22.8+	37*, 229+
CT	Ni-29 Al-21 Co-5 Ti	(7.6*), (9.3+)	(6*), (7+)
MI	(Ni-50 Al) + 20 v/o MERL 76	(17.3+)	(26+)

* Extruded VIM ingot

+ Extruded and heat treated at 2 hours/1050°C/air cooled

() Precrack did not meet ASTM standards

Table 27. Heat Treatment Studies of NiAlCo Alloys

<u>Alloy+</u>	<u>Heat Treatment</u>	<u>Gamma Prime Amount (vol. %)</u>	<u>Grain Size (ASTM)</u>	<u>Matrix Composition (atom %)</u>	<u>K_{IC} (MPa\sqrt{m})</u>
B2	As-extruded	3	5	n.d.	17.8
	2hr/800°C/AC	13	5	n.d.	17.6
	2hr/1050°C/AC	8	4	n.d.	14.9
	2hr/1300°C/AC	0	-3	n.d.	*
C	As-extruded	20	5	n.d.	22.8, 25.3
	2hr/800°C/AC	33	5	Ni - 23Co - 31Al	23.3, 33.3
	2hr/1090°C/AC	28	4	Ni - 20Co - 31Al	n.d.
	2hr/1300°C/AC	<2	-3	Ni - 22Co - 28Al	13.2, 25.3

n.d. = not determined

* = material broke apart intergranularly before testing

+ = Alloy B2 Composition: Ni - 30 Al - 25 Co

Alloy C Composition: Ni - 29 Al - 21 Co

Table 28. Compressive Stiffness of Martensitic and Nonmartensitic Alloys

Alloy	A _f Temp. °C (°F)	Test Temperature °C (F)	Loading	Unloading	Stiffness Ratio (Unload./Load.)
A	-55 (-65)	Room Temp. 205 (400)	113 (16.4) 91 (13.3)	113 (16.4) 94 (13.7)	1 1.03
A2	15 (59)	Room Temp.	123 (17.8)	123 (17.8)	1
A3	70 (160)	Room Temp. 205 (400)	53 (7.7) 88 (12.8)	118 (17.1) 95 (13.8)	2.2 1.08
B	215 (420)	Room Temp.	57 (8.3)	56 (12.5)	1.5
B2	240 (465)	Room Temp. 205 (400)	45 (6.5) 46 (6.7)	83 (12.0) 95 (13.8)	1.8 2.06
C	695 (1280)	Room Temp. 205 (400)	90 (13.0) 86 (12.4)	90 (13.0) 107 (15.5)	1 1.25
C2	445 (830)	Room Temp. 205 (400)	91 (13.2) 83 (12.1)	96 (13.9) 83 (12.1)	1.1 1.64
C3	360 (680)	Room Temp.	126 (18.2)	126 (18.2)	1
E	+	Room Temp.	145 (21.0)	145 (21.0)	1
F	+	Room Temp.	127 (18.4)	127 (18.4)	1
J	+	Room Temp.	138 (20.0)	138 (20.0)	1

+ Stable B2 Phase Alloy

Table 29. Creep Stress Exponents for Selected Alloys at 760°C (1400°F)

Alloy	Stress Exponent
Ni - 50 Al	10.5 (Reference 25)
Ni - 49 Al	7.3 (Reference 25)
Ni - 45 Al	4.9 (Reference 25)
Alloy A	3.0
Alloy CH	3.1
Alloy AH	1.0
Alloy C2	1.1
Alloy CT	1.5

Table 30. Low Cycle Fatigue Data of Selected Alloys

Alloy	Temperature °C (°F)	Applied Stress MPa (ksi)	Cycles to Failure
A	Room Temp.	Failed in loading due to porosity; see text	
C	Room Temp.	207 (30)	run-out*
		276 (40)	run-out*
		345 (50)	run-out*
		414 (60)	20
C2	Room Temp.	193 (28)	run-out*
		255 (37)	run-out*
		297 (43)	run-out*
		345 (50)	run-out*
		414 (60)	failed on first cycle
CH	Room Temp.	207 (30)	run-out*
		276 (40)	run-out*
		345 (50)	run-out*
		414 (60)	14, 160
C	760 (1400)	69 (10)	run-out*
		103 (15)	22,154
C2	760 (1400)	138 (20)	47,950

* run-out: 50,000 cycles without failure

Table 31. Metallography of As-Extruded Phase III and Baseline Materials

Material (atom percent)	Phase Present (volume percent)	Grain Size	
		(ASTM)	(mm)
Ni-29 Al-21 Co	75% L1 ₀ martensite	5	0.062
	25% L1 ₂ gamma prime		
Ni-29 Al-21 Co + PRD-166	(75% L1 ₀ martensite 25% L1 ₂ gamma prime) + 10-15% PRD-166	8	0.022

Table 32. 0.2% Compressive Yield Strength of the Phase III Material

Material	Temperature °C (°F)	0.2% Yield Strength MPa (ksi)	Percent Improvement
Ni-29 Al-21 Co + PRD-166 (tested perpendicular to the extrusion direction)	20 (68)	776 (113)	3
	540 (1000)	699 (101)	25
	760 (1400)	272 (39)	67
	870 (1600)	116 (17)	N/A
	980 (1800)	36 (5)	N/A
Ni-29 Al-21 Co + PRD-166 (tested parallel to the extrusion direction)	20 (68)	840 (122)	11
	540 (1000)	759 (110)	36
	760 (1400)	348 (51)	113
	870 (1600)	143 (21)	N/A
Ni-29 Al-21 Co	20 (68)	754 (109)	—
	540 (1000)	558 (81)	—
	760 (1400)	163 (24)	—

Table 33. Elastic Modulus of the Phase III Material

Material	Temperature °C (°F)	Elastic Modulus* GPa (Msi)
Ni-29 Al-21 Co + PRD-166 (tested perpendicular to the extrusion direction)	20 (68)	134 (20)
	540 (1000)	152 (22)
	760 (1400)	55 (8)
	870 (1600)	41 (6)
	980 (1800)	28 (4)
Ni-29 Al-21 Co + PRD-166 (tested parallel to the extrusion direction)	20 (68)	97 (14)
	540 (1000)	97 (14)
	760 (1400)	55 (8)
	870 (1600)	28 (4)

* Material measurements ± 20 GPa (3 Msi)

Table 34. Tensile Ductility of the Phase III Material

Material	Temperature °C (°F)	Percent Elongation	Fracture Strength MPa (ksi)	0.2% Yield Strength MPa (ksi)
Phase III Material	Room Temp.	0.0	543 (79)	*
	300 (572)	2.5	833 (121)	786 (114)
	400 (750)	1.9	770 (112)	770 (112)
	500 (932)	3.9	785 (114)	748 (109)
	600 (1112)	9.3	655 (95)	585 (85)
	760 (1400)	32.2	61 (9)	210 (30)
P/M C	Room Temp.	0.7	1087 (158)	968 (140)
Ni-29 a/o Al-21 a/o Co	400 (750)	4.1	1062 (154)	821 (119)
	540 (1000)	18.6	1041 (151)	611 (89)
	765 (1410)	76.3	53 (8)	80 (12)

Table 35. Fracture Toughness of the Phase III Material and Selected Alloys

Material	Condition	K _{1C} (MPa√m)
Phase III Material	Extruded Powder	18.9, 20.5
Alloy C	Extruded Ingot with	23.3, 33.3
Ni-29 a/o Al-21 a/o Co	2hr/800°C/Air Cool Heat Treatment	
	Extruded Ingot	22.8, 25.3
Alloy B2	Extruded Ingot	17.8
Ni-30 a/o Al-25 a/o Co		
Alloy A	Extruded Ingot	15.6, 18.5
Ni-30 a/o Al-35 a/o Co		
Ni-(38-50) a/o Al	Extruded Ingot	9.0, 5.7

Table 36. $\Delta\sigma^2$ Values for 300°K Versus 77°K, Taken on Bulk, Annealed CoAl and NiAl by Glancing Exit Angle Fluorescence*

<u>Alloy</u>	<u>Shell</u>	<u>$\Delta\sigma^2$ (Å)²</u>
CoAl	1	0.0028
CoAl	2	0.0024
CoAl	3	0.0036
NiAl	1	0.0025
NiAl	2	0.0058
NiAl	3	0.0049

*Note: These $\Delta\sigma^2$ values are determined for different temperatures than those of Table 37, and will not yield corresponding values of $\Delta T/\Delta\sigma^2$.

Table 37. Third Nearest-Neighbor $\Delta T/\Delta\sigma^2$ from EXAFS

<u>Bond</u>	<u>$\Delta T/\Delta\sigma^2$ ($\times 10^3$ °K/Å²)</u>
Zn-Zn in CuZn	18.3
Fe-Fe in FeAl	32.0
Ni-Ni in NiAl	30.0
Co-Co in CoAl	42.0
Fe-Fe in FeCo(ordered)	40.0
Co-Co in FeCo(ordered)	49.0

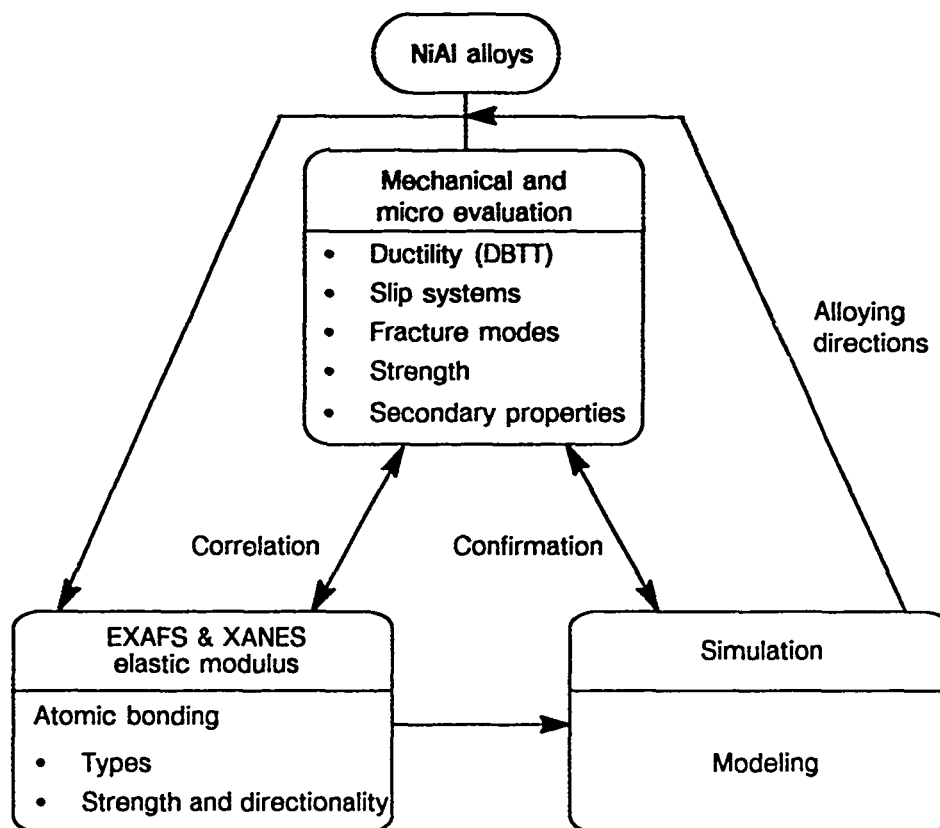


Figure 1. Schematic of the Approach Used in this Program Showing the Relationship Between the Various Types of Studies

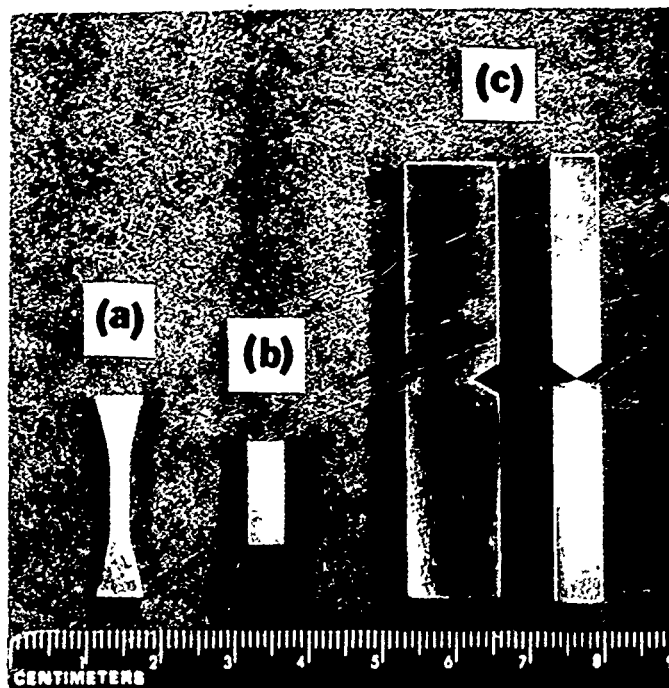


Figure 2. Specimen Geometries Used in Mechanical Testing for: (a) Tensile Strength and Ductility, (b) Compressive Strength and Deformability and Compressive Creep, and (c) Fracture Toughness

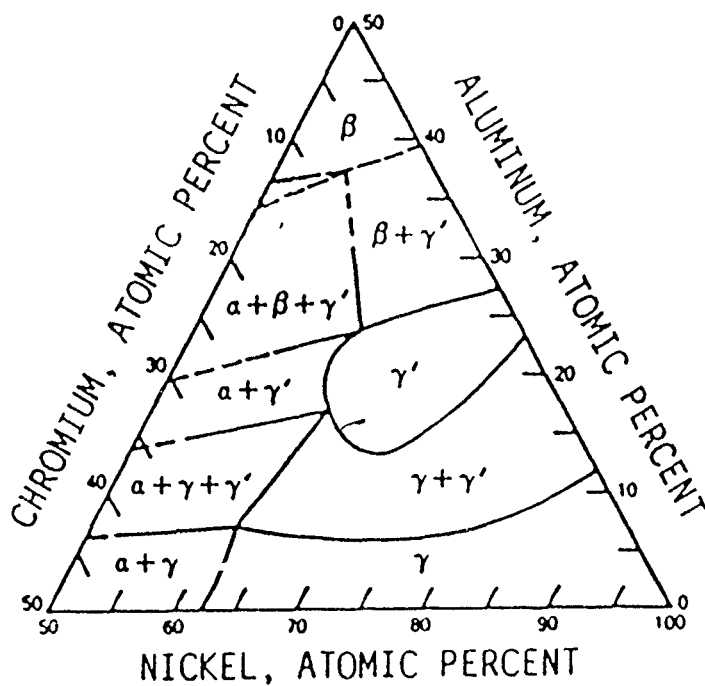


Figure 3. Ni-Al-Cr Isothermal Section at 750°C (Reference 5)

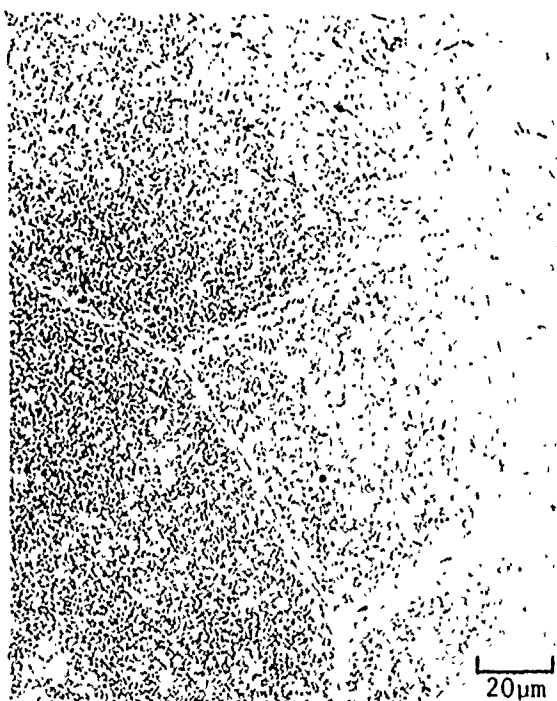
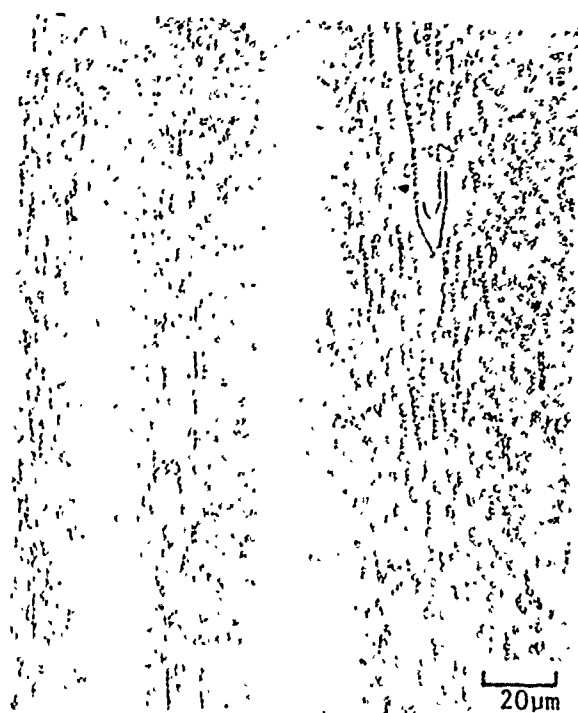
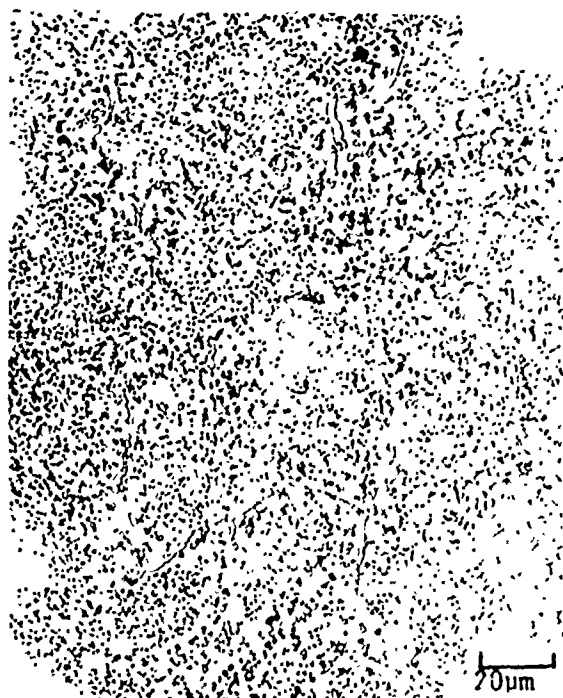


Figure 4. Microstructures of the Baseline Alloy Produced as VIM Ingot After Extrusion at 1000°C , Extrusion Ratio 9:1 (top) and After Heat Treatment for 2 Hours at 1300°C (bottom); Left-Transverse Section, Right-Longitudinal Section

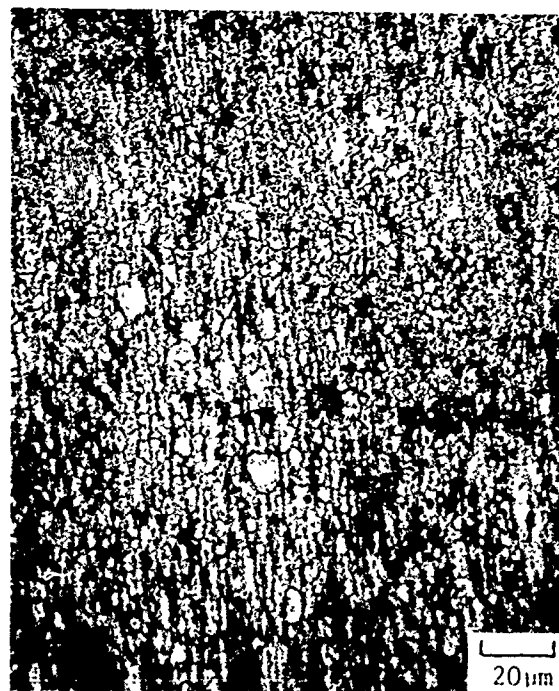
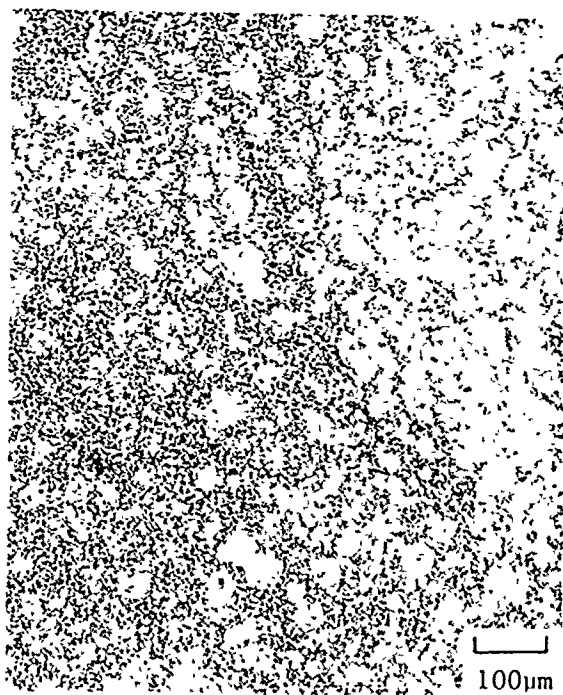


Figure 5. Microstructures of the Baseline Alloy Produced in Powder Form After Extrusion at 1000°C , Extrusion Ratio 9:1 (top) and After Heat Treatment for 2 Hours at 1300°C (bottom); Left-Transverse Section, Right-Longitudinal Section



Figure 6. Microstructure of the Extruded and Heat Treated Baseline Alloy Showing a Uniform Distribution of Fine Alpha Chromium Particles and Denuded Zones at Grain Boundaries

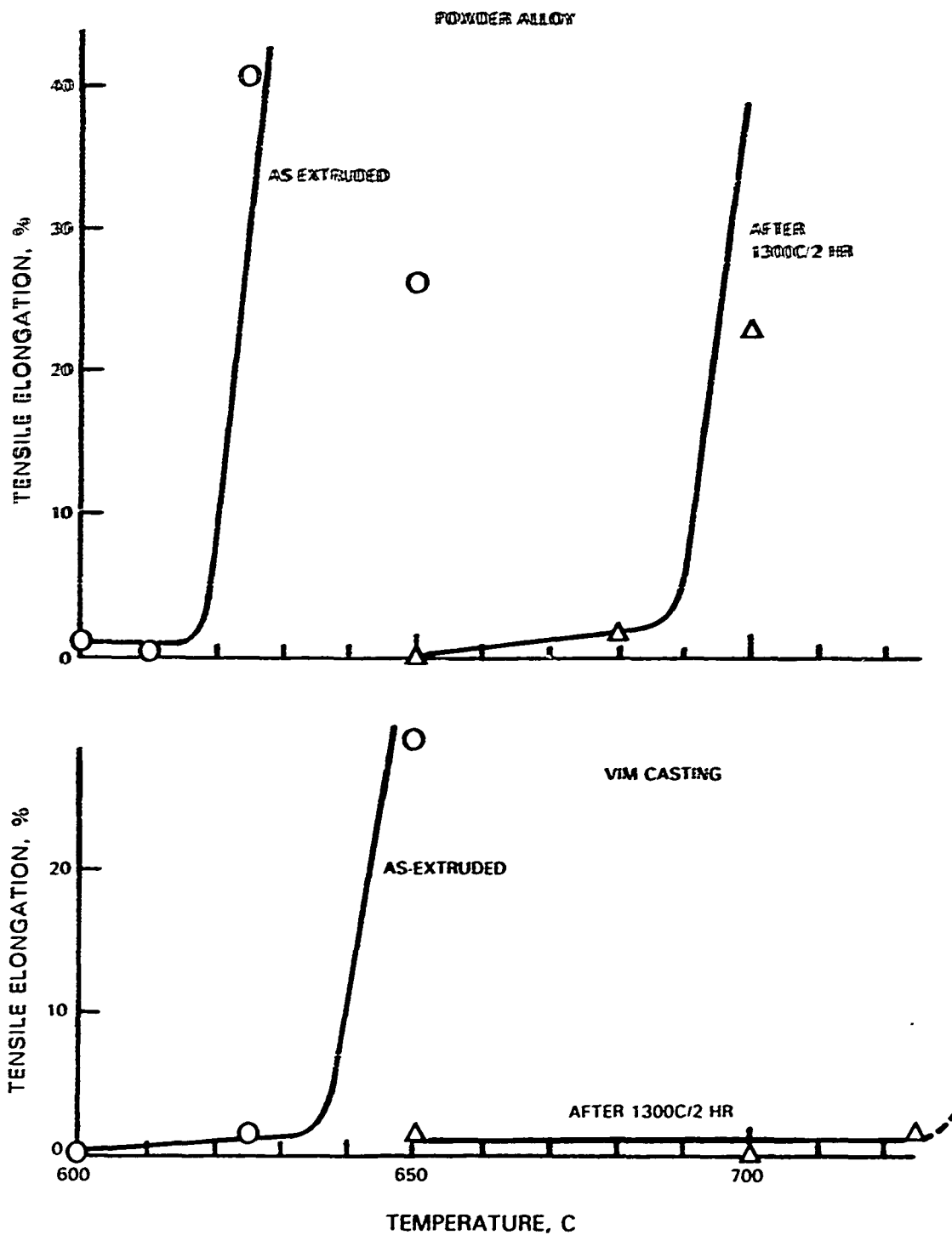


Figure 7. Tensile Elongation Versus Temperature Plots for the Baseline Alloy Initially in Powder Form (top) and Produced as Cast Ingot (bottom)

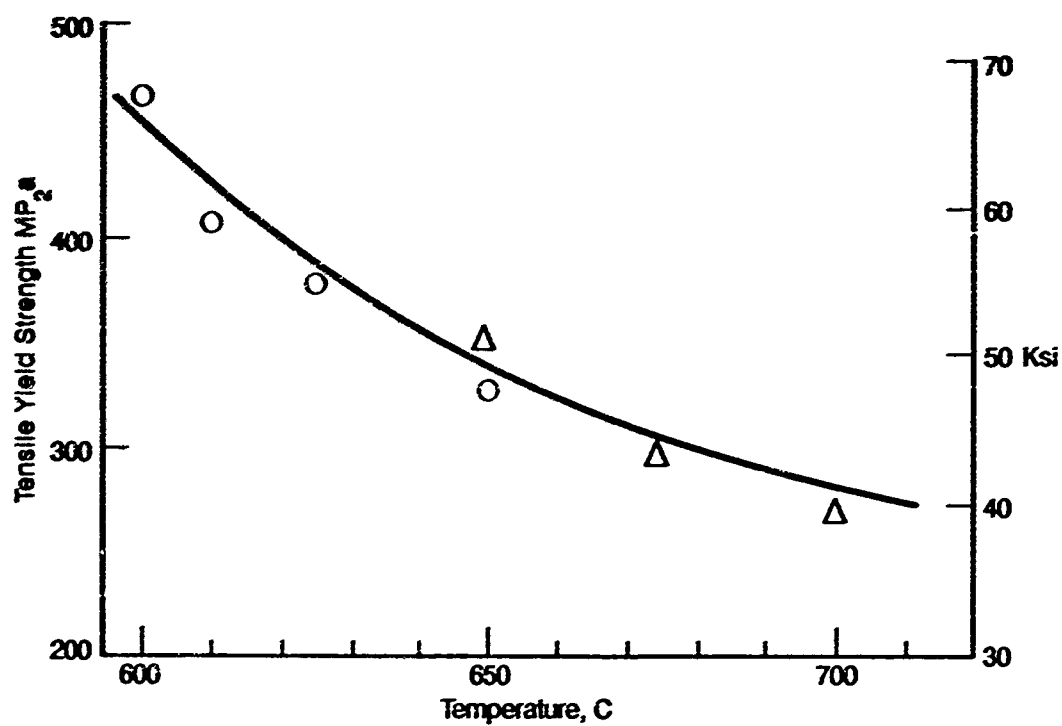


Figure 8. Tensile Yield Strength of the PIM Baseline Alloy in As-Extruded Condition (○) and After Heat Treatment for 2 Hours at 1300°C (Δ)

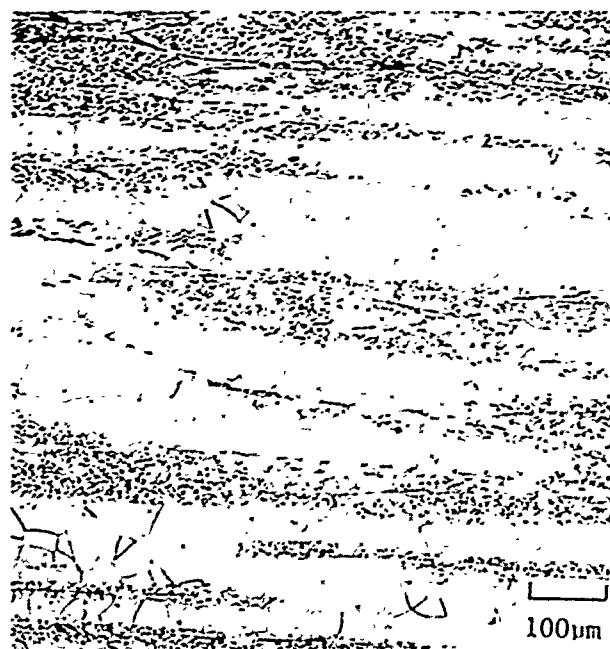
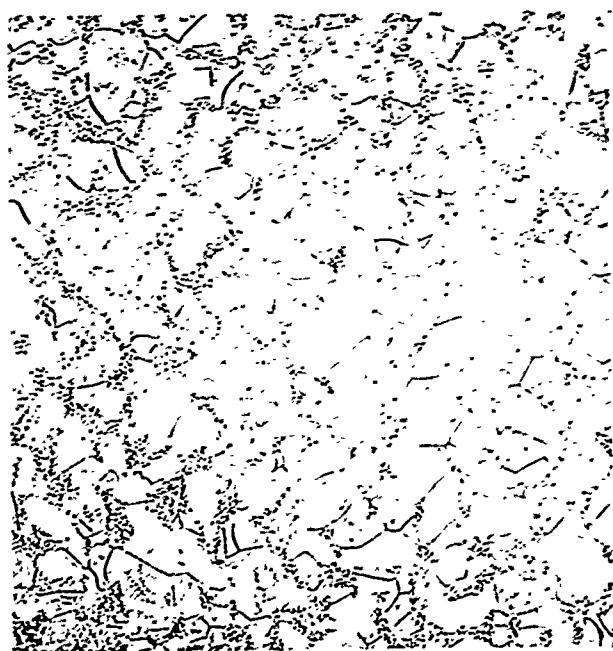
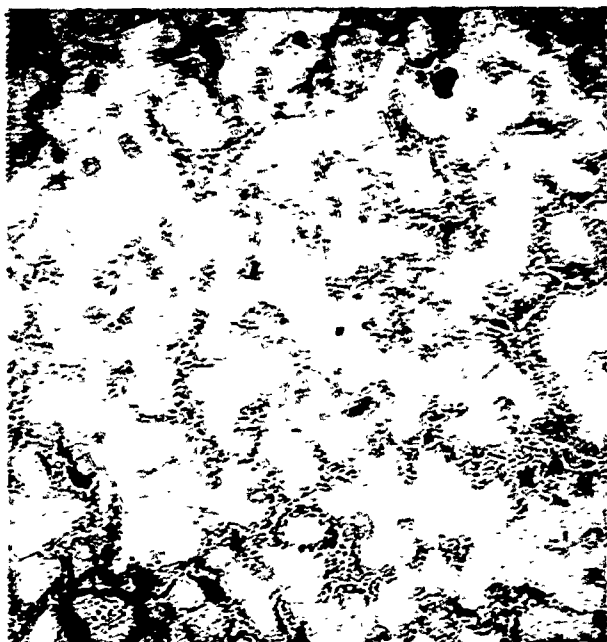


Figure 9. Microstructures of the Alloy A (Ni-30 a/o Al-35 a/o Co) Produced as a VIM Ingot After Extrusion at 1000°C, Extrusion Ratio 9:1 (top) and After Heat Treatment for 2 Hours at 1050°C (bottom); Left-Transverse Section, Right-Longitudinal Section

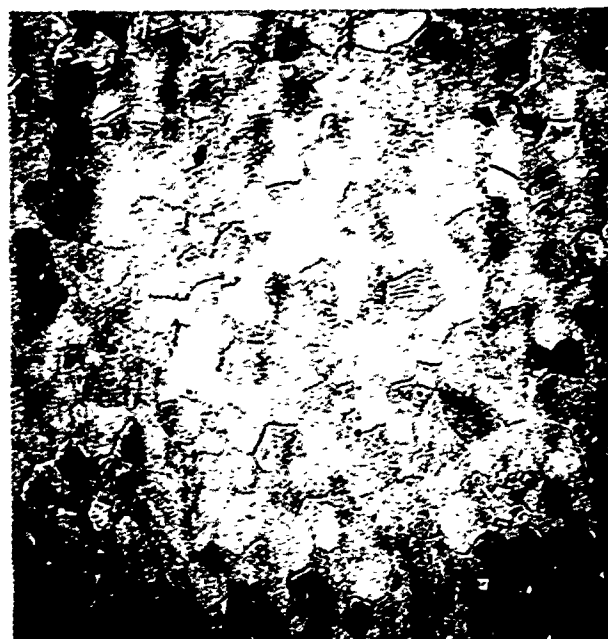


Figure 10. Microstructures of the Alloy B (Ni-30 a/o Al-25 a/o Co-0.25 a/o B) Produced as a VIM Ingot After Extrusion at 1000°C, Extrusion Ratio 9:1 (top) and After Heat Treatment for 2 Hours at 1050°C (bottom); Left-Transverse Section, Right-Longitudinal Section

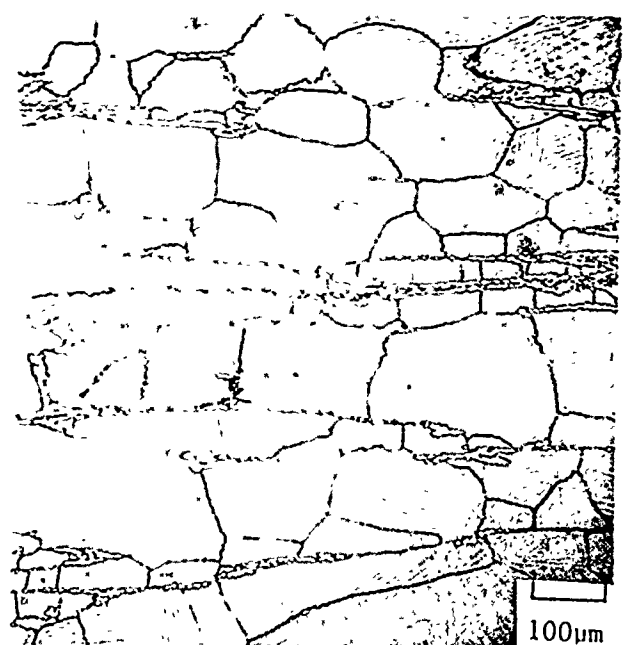
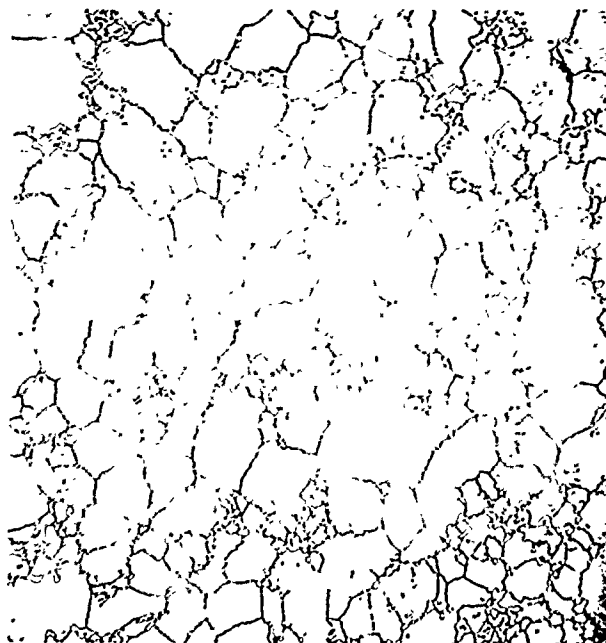
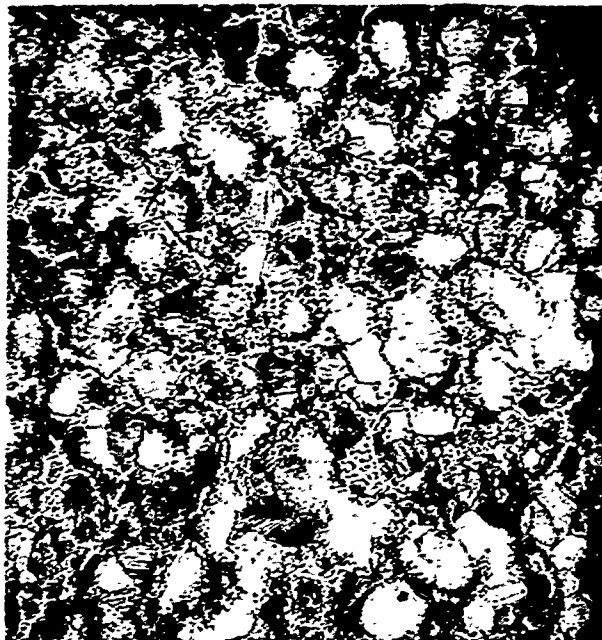


Figure 11. Microstructures of the Alloy C (Ni-29 a/o Al-21 a/o Co) Produced as a VIM Ingot After Extrusion at 1000°C, Extrusion Ratio 9:1 (top) and After Heat Treatment for 2 Hours at 1050°C (bottom); Left-Transverse Section, Right-Longitudinal Section

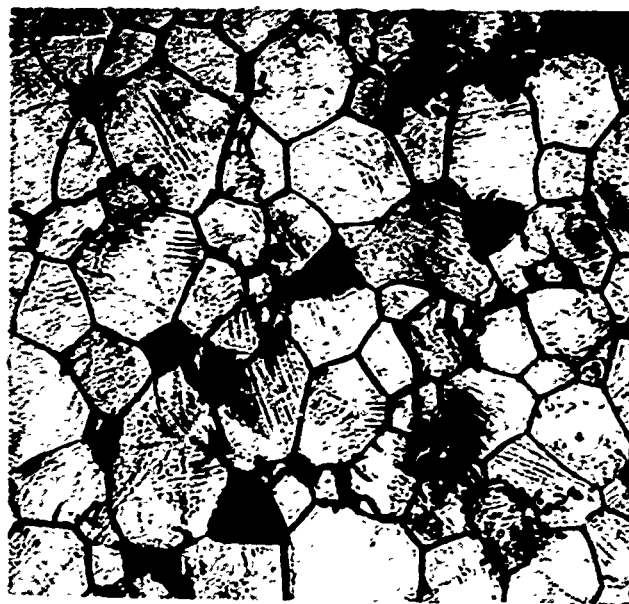


Figure 12. Microstructures of the Alloy D (Ni-35 a/o Al-10 a/o Co) Produced as a VIM Ingot After Extrusion at 1000°C, Extrusion Ratio 9:1; Top-Transverse Section, Bottom-Longitudinal Section. Note that numerous grains have been liberated from the surface indicating weak grain boundaries.

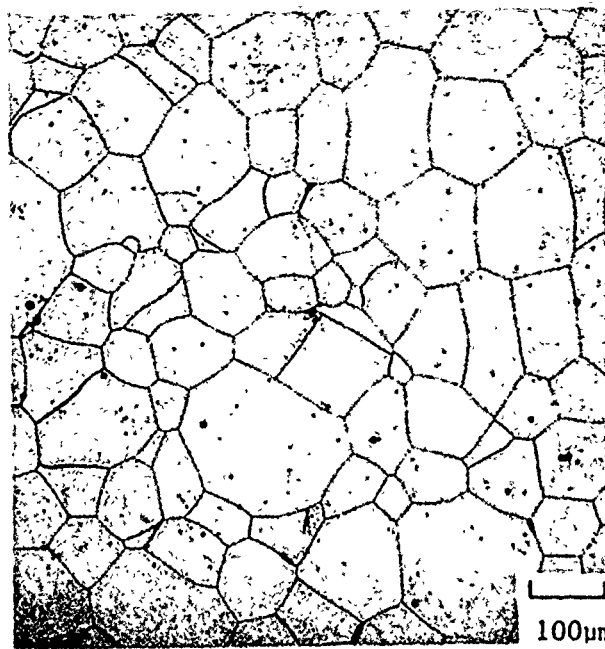
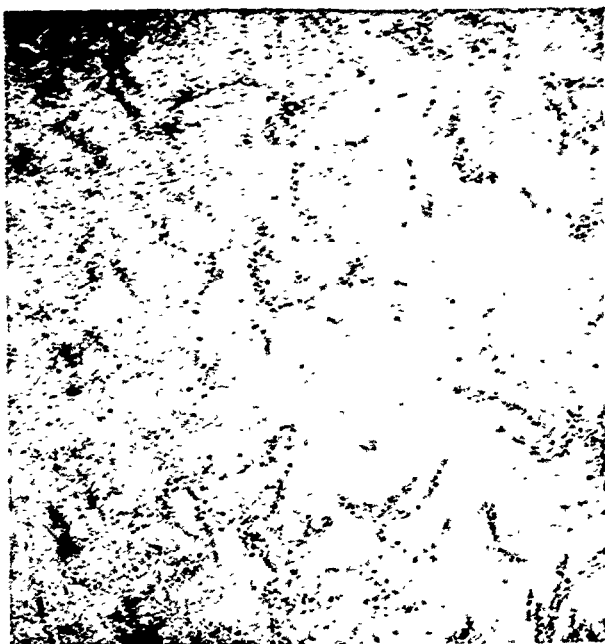


Figure 13. Microstructures of the Alloy E (Ni-33 a/o Al-28 a/o Fe) Produced as a VIM Ingot After Extrusion at 1000°C, Extrusion Ratio 9:1 (top) and After Heat Treatment for 2 Hours at 1050°C (bottom); Left-Transverse Section, Right-Longitudinal Section

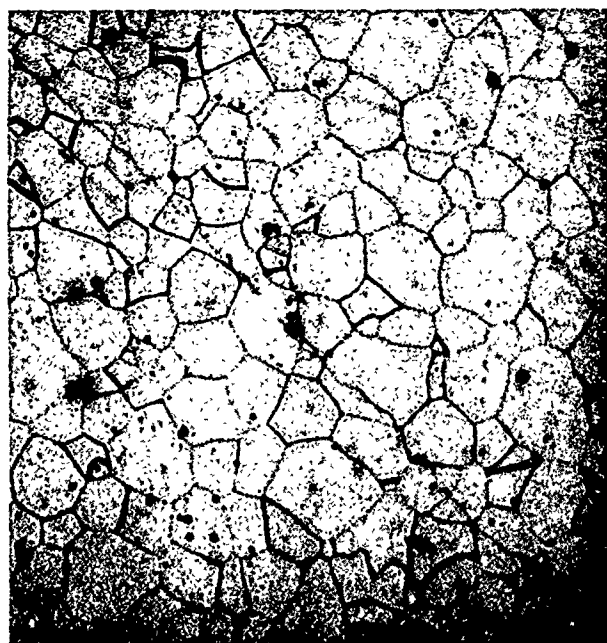
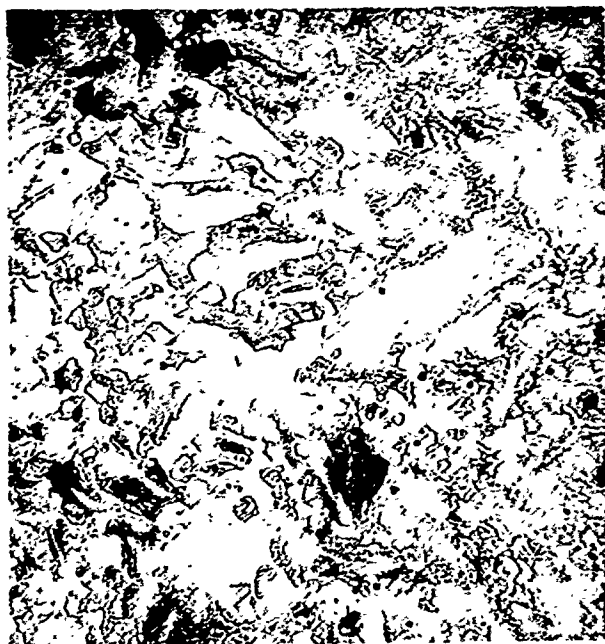


Figure 14. Microstructures of the Alloy F (Ni-33 a/o Al-20 a/o Fe) Produced as a VIM Ingot After Extrusion at 1000°C, Extrusion Ratio 9:1 (top) and After Heat Treatment for 2 Hours at 1050°C (bottom); Left-Transverse Section, Right-Longitudinal Section

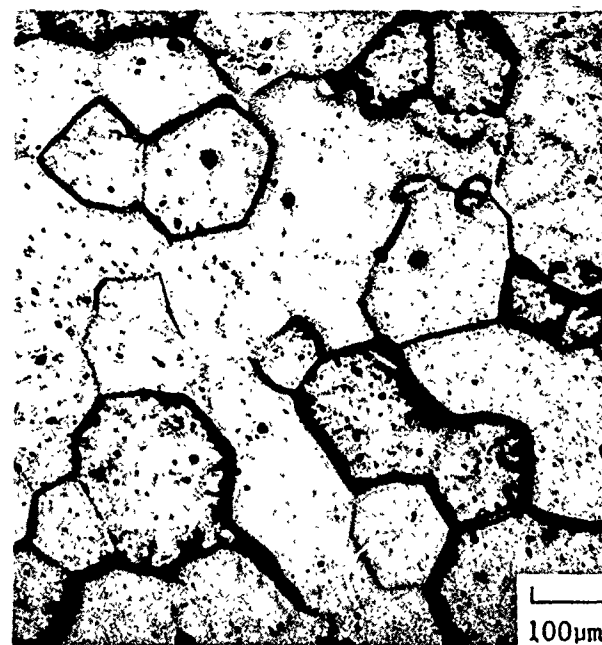
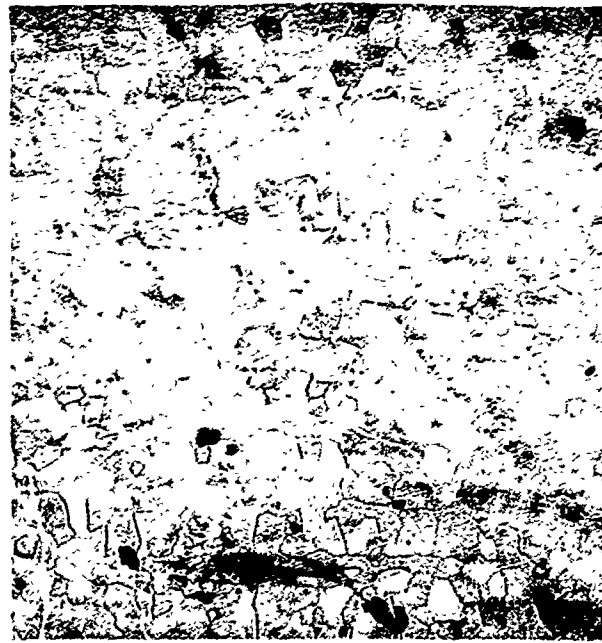
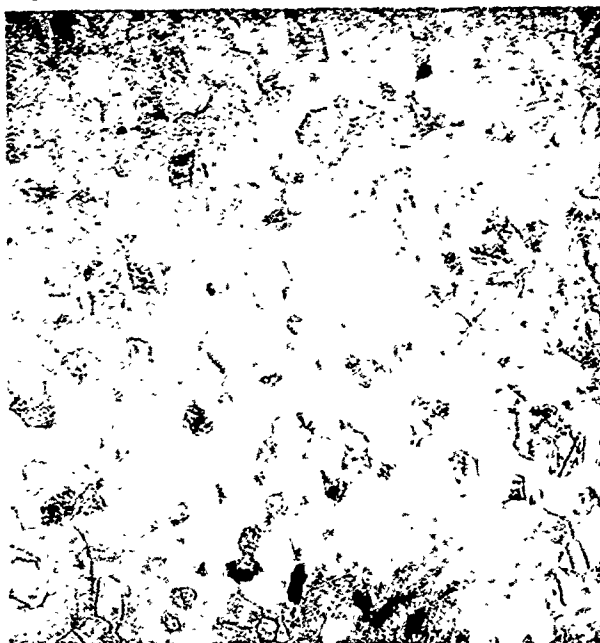


Figure 15. Microstructures of the Alloy G (Ni-35 a/o Al-5 a/o V) Produced as a VIM Ingot After Extrusion at 1000°C, Extrusion Ratio 9:1 (top) and After Heat Treatment for 2 Hours at 1050°C (bottom); Left-Transverse Section, Right-Longitudinal Section



Figure 16. *Microstructures of the Alloy H (Ni-35 a/o Al-5 a/o V-3 a/o Cr) Produced as a VIM Ingot After Extrusion at 1000°C, Extrusion Ratio 9:1 (top) and After Heat Treatment for 2 Hours at 1050°C (bottom); Left-Transverse Section, Right-Longitudinal Section*

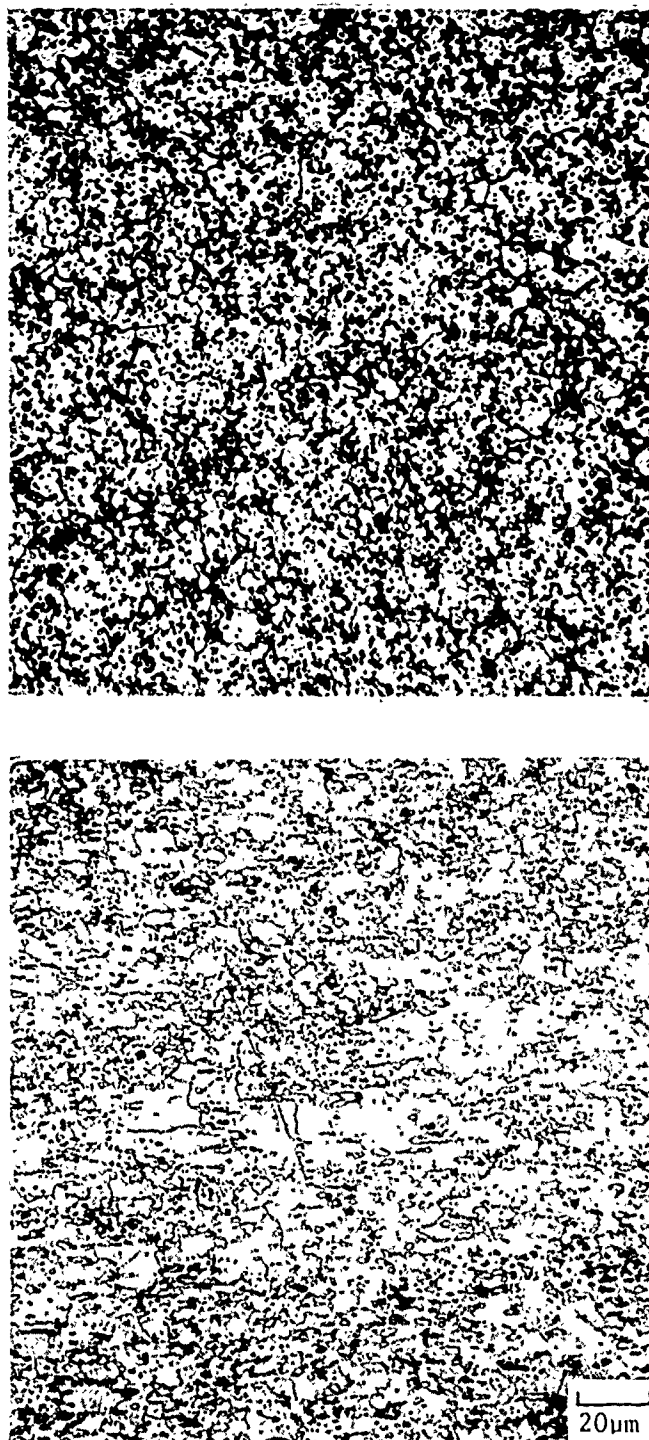
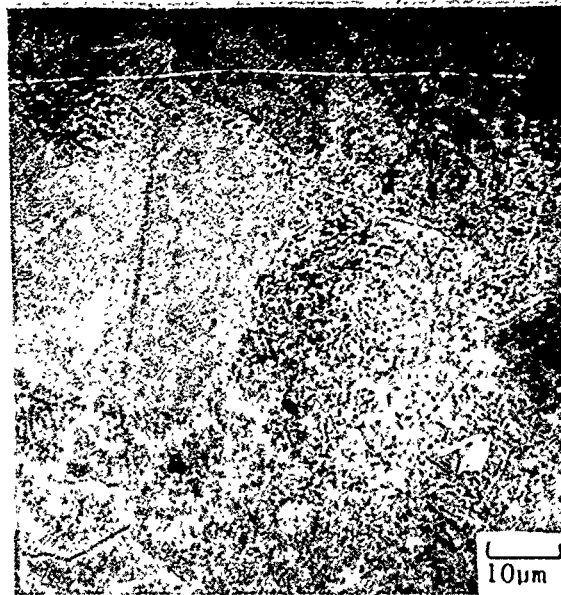
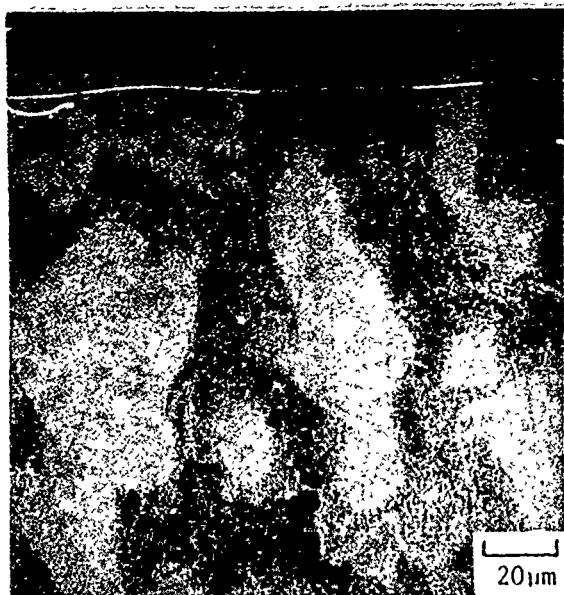
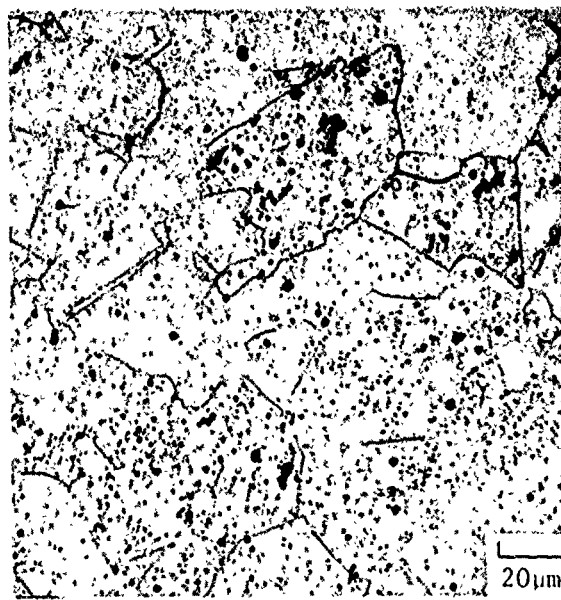
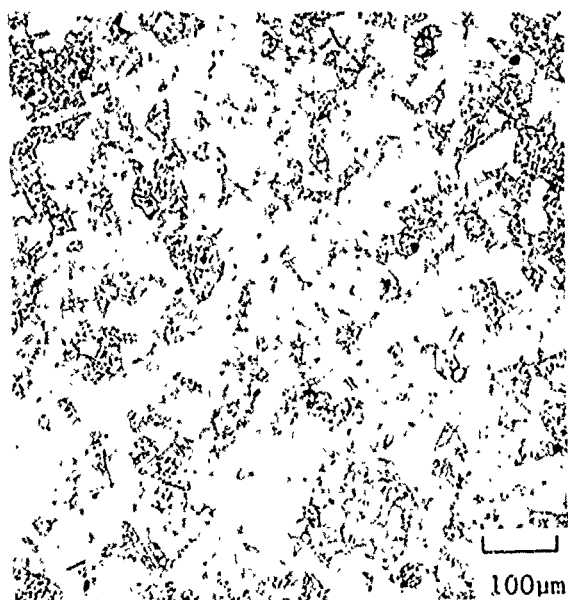


Figure 17. Microstructures of the Alloy I (Ni-35 at% Al-5 at% Ti) Produced in Powder Form After Extrusion at 1000°C, Extrusion Ratio 9:1; Top-Transverse Section, Bottom-Longitudinal Section



(a)



(b)

Figure 18. Microstructures of the Alloy J (Ni-40 a/o Al-10 a/o Ti) Produced as a VIM Ingot: (a) As Cast, and (b) As Partially Extruded. Alloy J exceeded the load capacity of the extrusion press and was not extruded. The microstructures shown are from the leading end of the extrusion preform from one of the attempted extrusions.

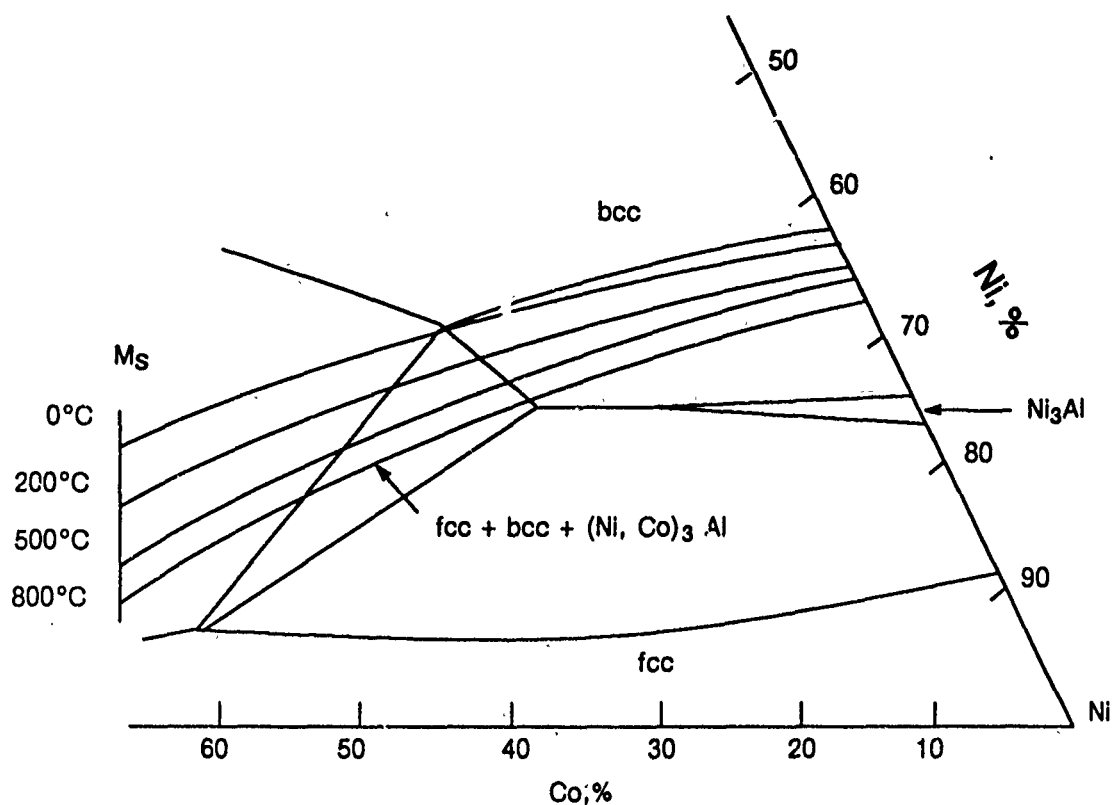
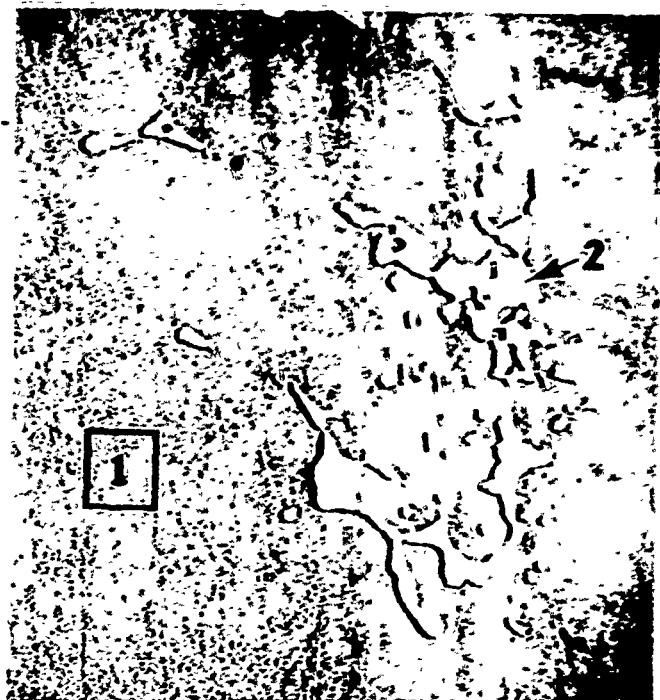


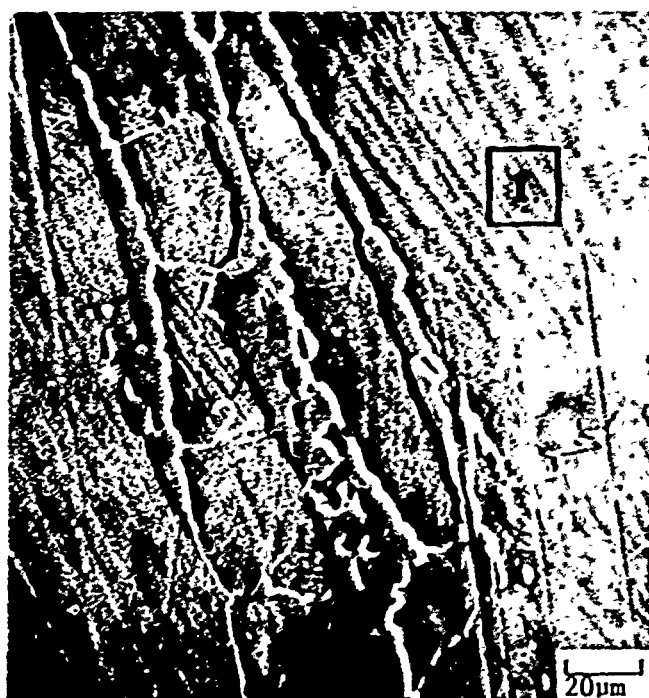
Figure 19. Ni-Co-Al Phase Diagram at 800K (Reference 9) with Estimated Martensitic Transformation Temperature Contours (from References 10 and 11)



(a)



(b)



(c)

Figure 20. Scanning Electron Micrographs of NiAlCo Alloys A, B and C (a, b and c, respectively). The compositions of the phases indicated are given in Table 6.

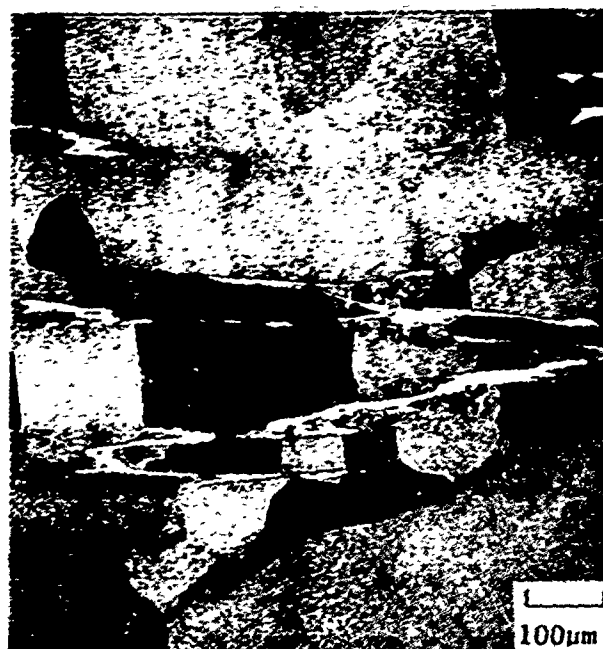
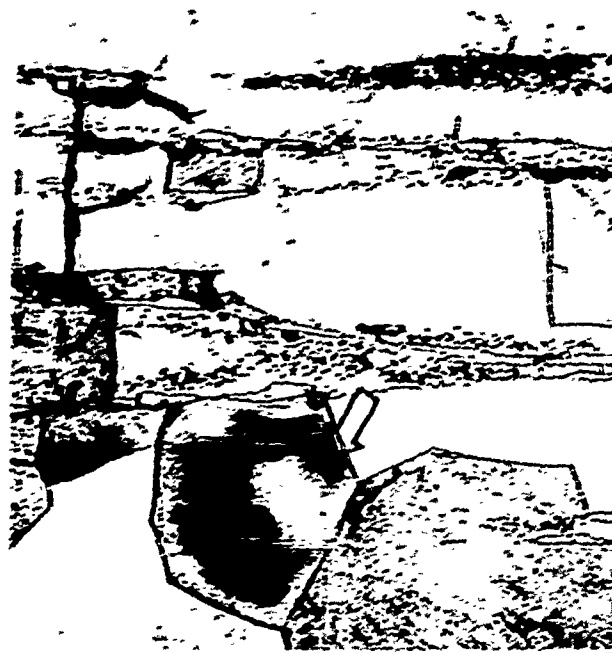


Figure 21. Optical Micrographs of Alloy A After Compression at Room Temperature (top) and 760°C (1400°F) (bottom)

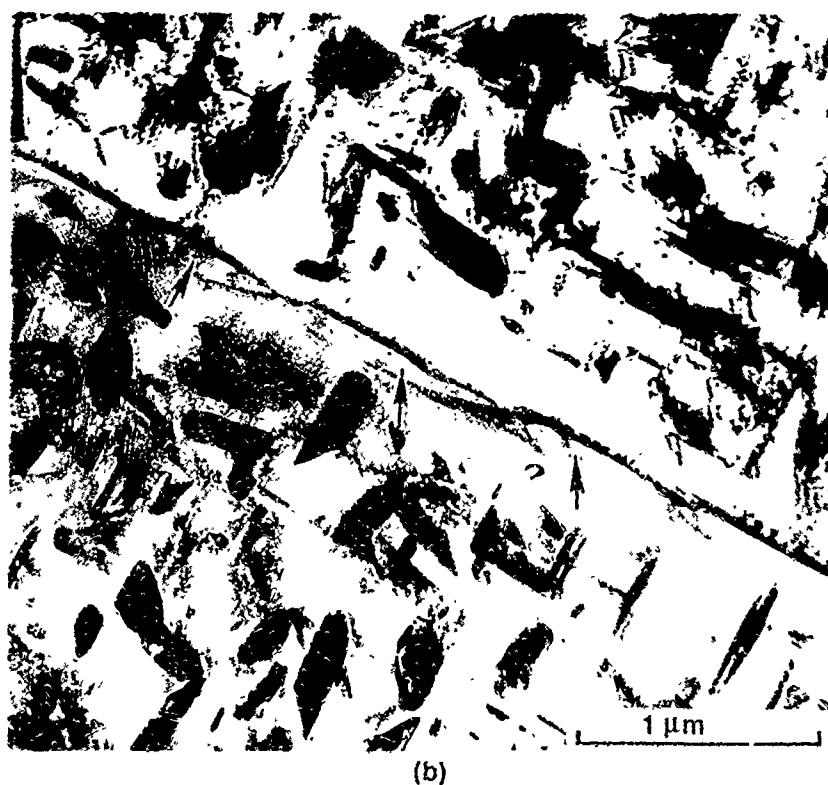
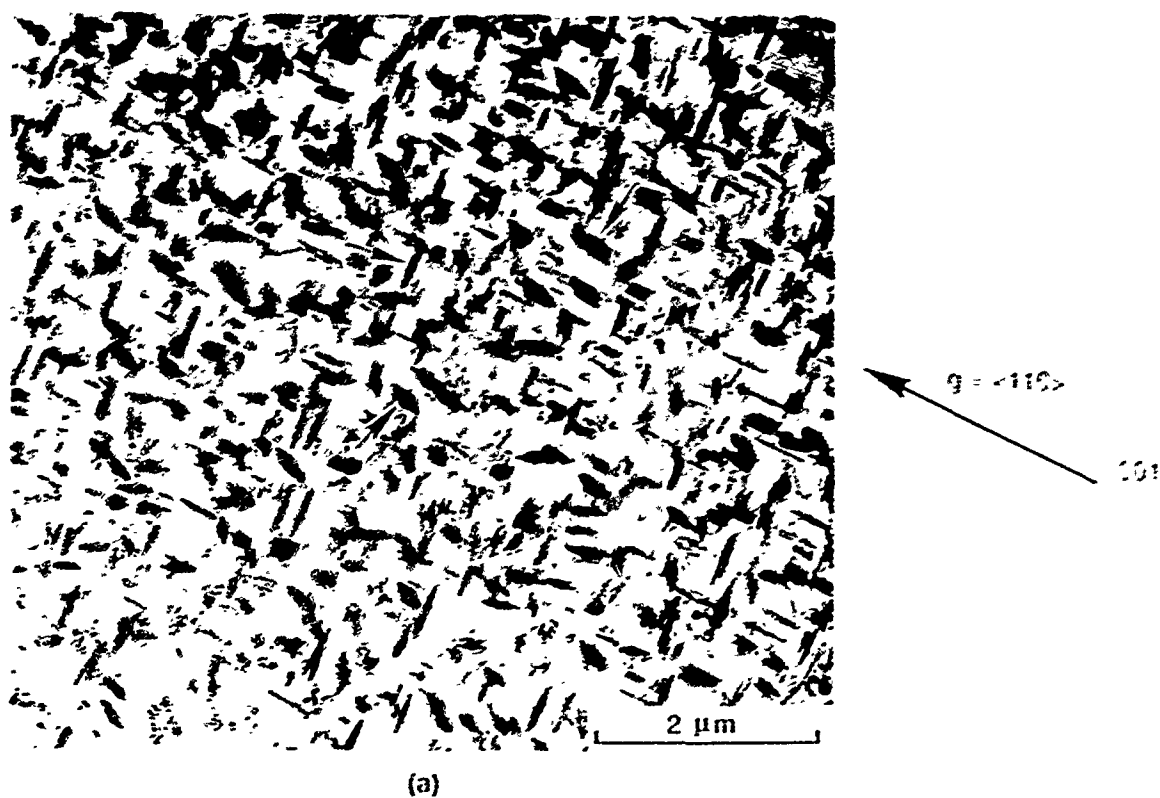


Figure 22. TEM of VIM Alloy A, As Extruded + Heat Treatment of 2 Hrs/1050°C/Air Cool After Compression at 760°C (1400°F). (a) Micrograph of matrix containing a high density of prismatic precipitates. (b) Higher magnification micrograph of grain boundary showing elongated gamma prime.

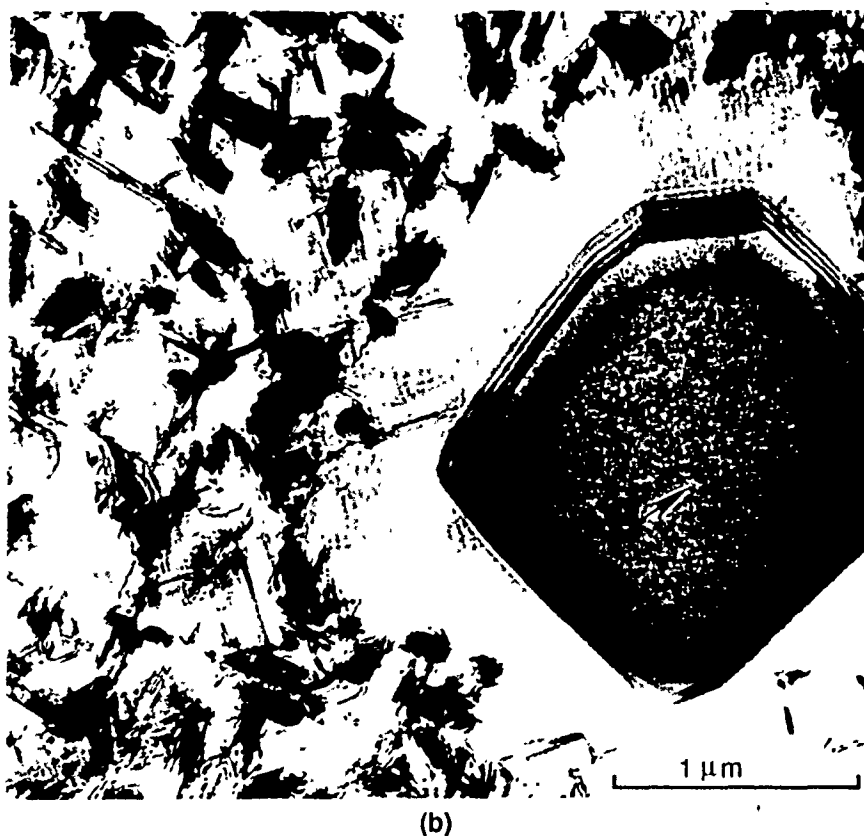
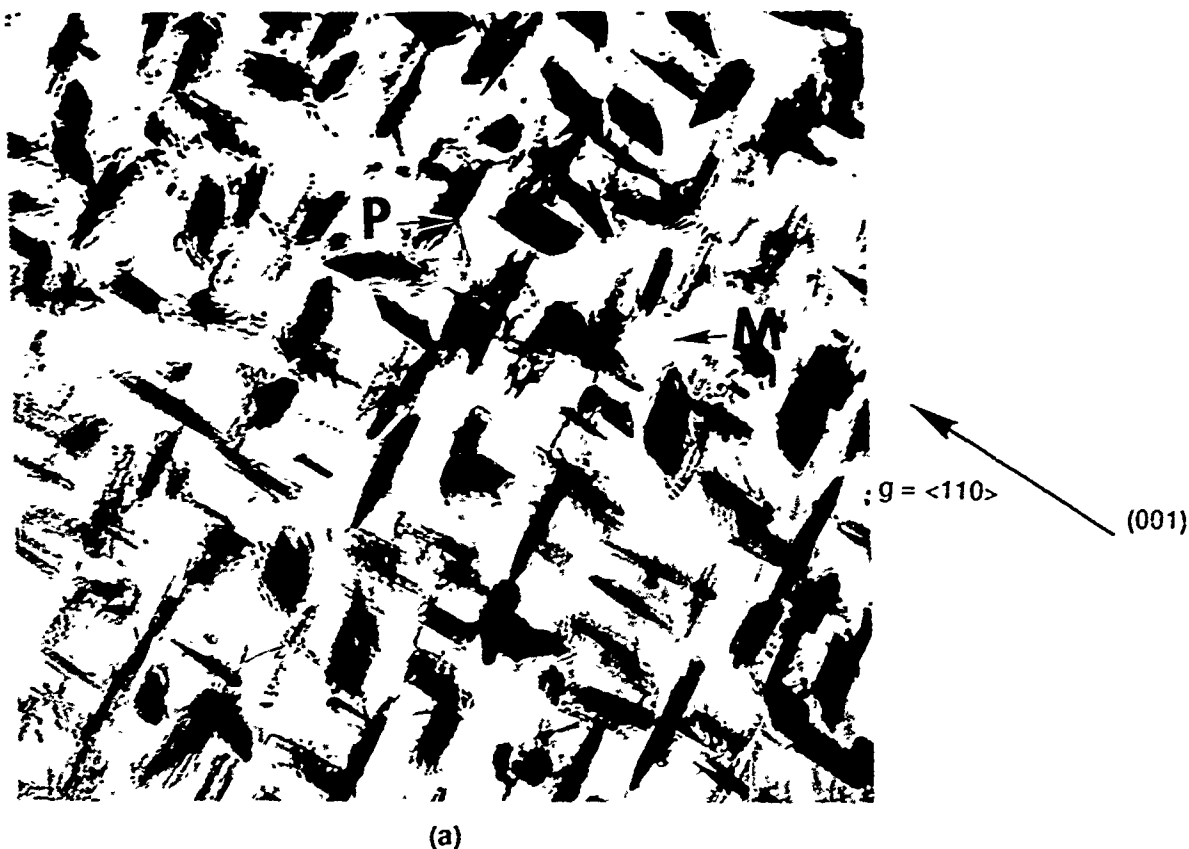
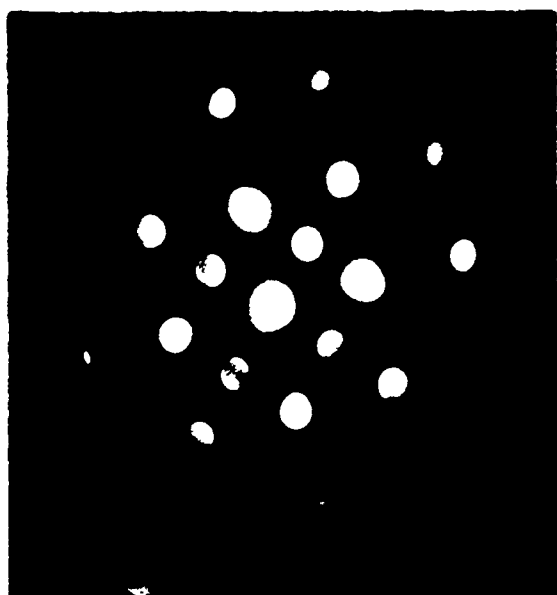
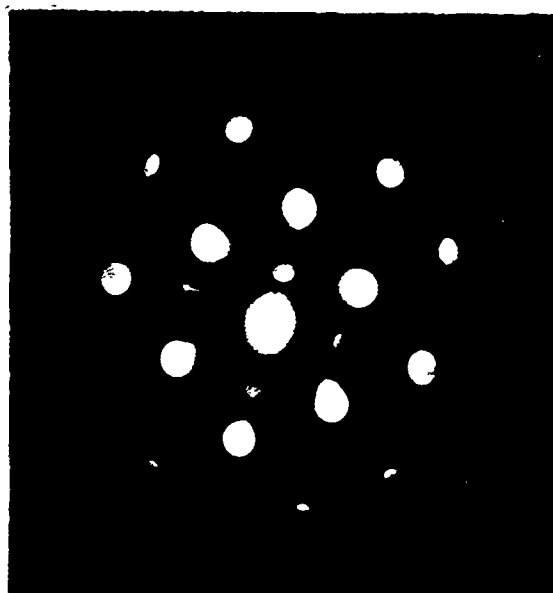


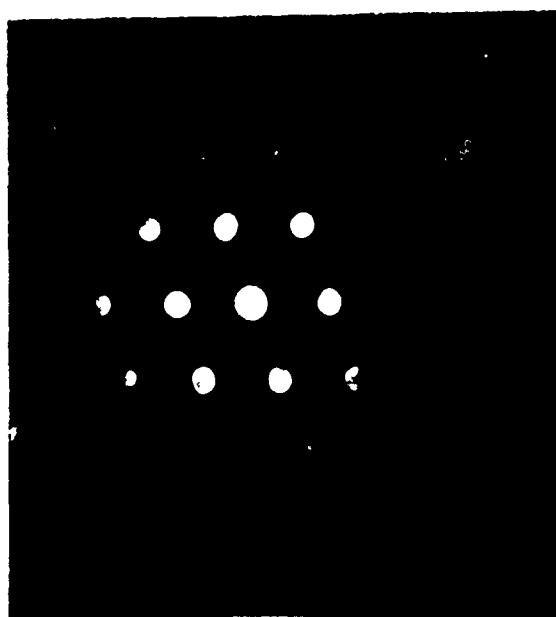
Figure 23. TEM of VIM Alloy A, As Extruded + Heat Treatment of 2 Hrs/1050° C/Air Cool After Compression at 760° C (1400° F) to 0.2% Strain. (a) Higher magnification micrograph of matrix showing the prism-shaped precipitates which are seen to lie predominantly along $\langle 110 \rangle$ B2 directions. (b) Micrograph of blocky matrix precipitate with the same structure ($L1_2$) as the grain boundary phase seen in Figure 22.



(a)



(b)

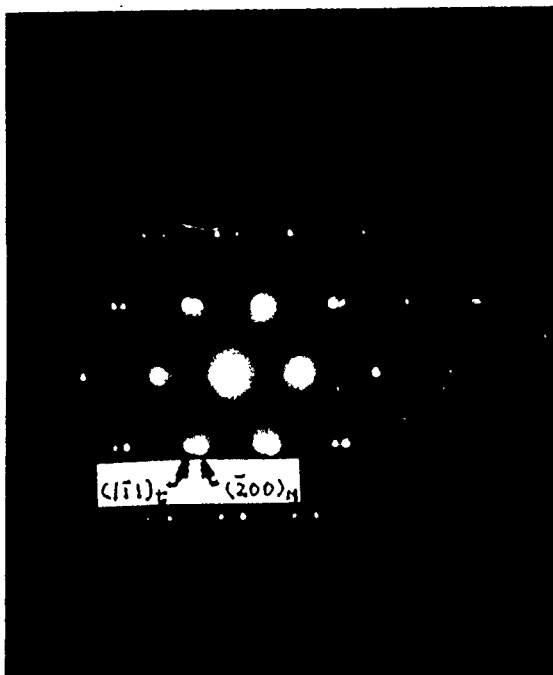


(c)

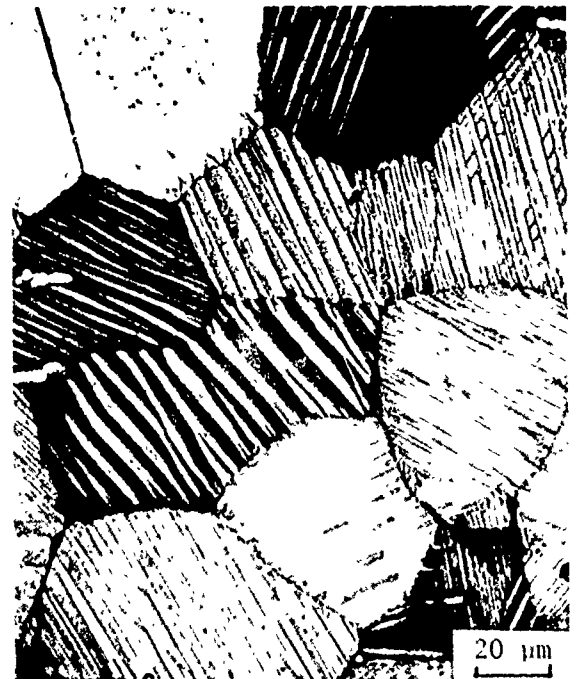
Figure 24. Selected Area Diffraction of VIM Alloy A (As Extruded + Heat Treatment at 2 Hrs/1050°C/ Air Cool After Compression at 760°C (1400°F) to 0.2% Strain) on the Phases Seen in Figure 23. (a) Matrix, (001) zone axis pattern – ordered bcc (B2) with $a = 0.286$ nm. (b) Blocky precipitate, (011) zone axis pattern – ordered fcc (L1₂) with $a = 0.355$ nm. (c) Prism precipitate, (011) zone axis pattern – fcc (Al) with $a = 0.355$ nm.



(a)

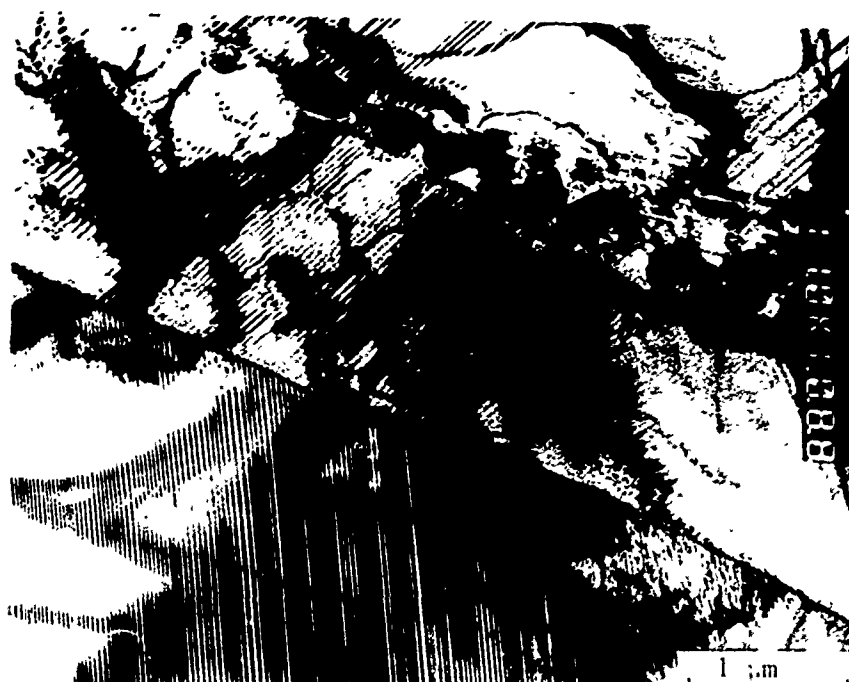


(b)

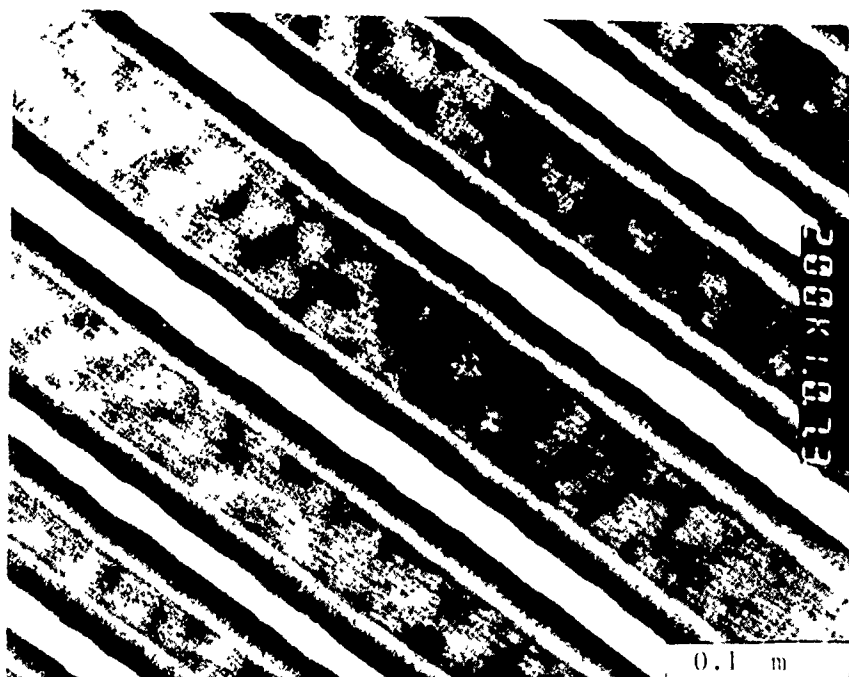


(c)

Figure 25. Microstructures of VIM Alloy B After Extrusion and a Heat Treatment at 2 Hrs/1050°C/Air Cool. (a) TEM micrograph of the martensitic plates, corresponding to the (b) selected area diffraction pattern, showing that the plates are twin related. Subscripts "m" and "t" correspond to arbitrary selection of "matrix" and "twin." (c) Optical micrograph showing parallel martensitic plates in various grains.



(a)

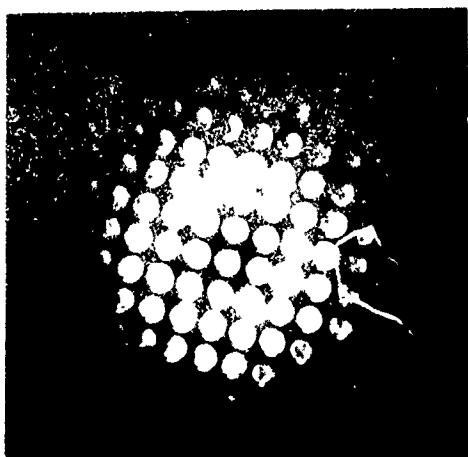


(b)

Figure 26. TEM Micrographs of Fine Twin Lamellae within the Martensitic Plates of V1M Alloy B. The orientation of the lamellae is related to the orientation of the larger martensitic plates.



(a)



(b)

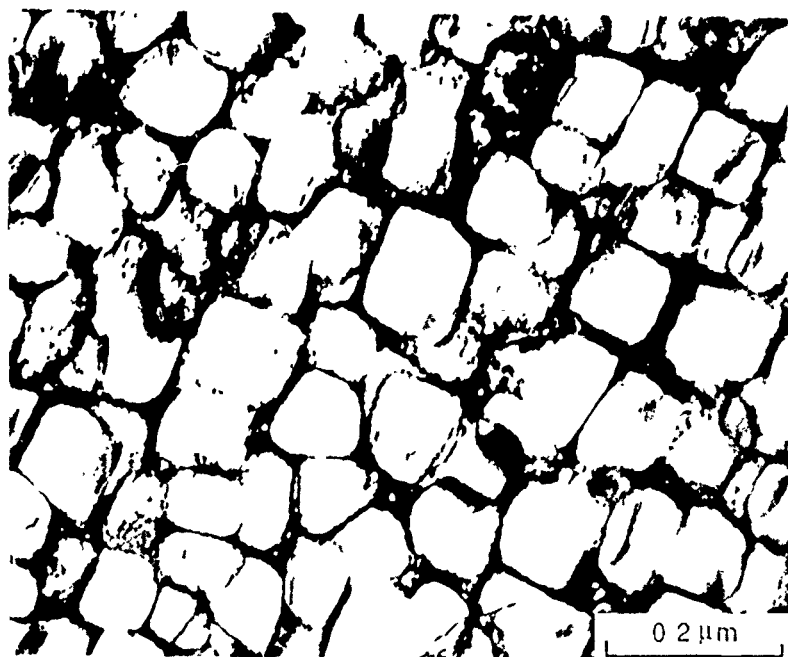


(c)

Figure 27. (a) TEM Micrograph of Grain Boundary Precipitates in VIM Alloy B, with Corresponding Selected Area Diffraction Patterns with Zone Axes of (b) (001) and (c) (123). The precipitates are identified as $(\text{Ni,Co})_{20}\text{Al}_3\text{B}_6$.



(a)



(b)

Figure 28. TEM of VIM Alloy C, As Extruded + Heat Treatment of 2 Hrs/1050°C/Air Cool. (a) TEM micrograph of grain boundary phases. (b) Higher magnification TEM dark field micrograph of gamma/gamma prime phase mixture.

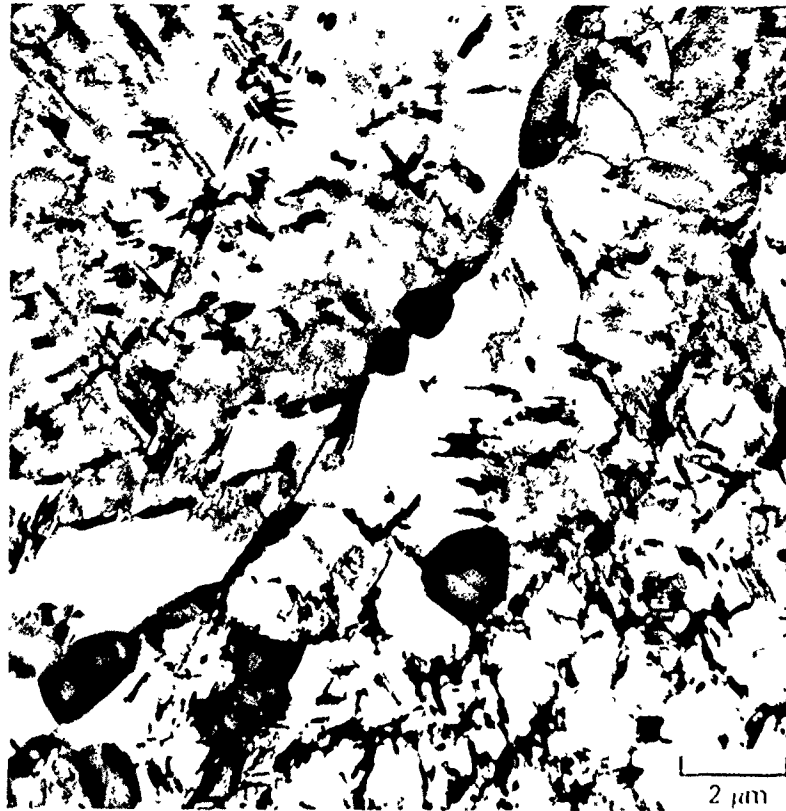


Figure 29. TEM of Powder Alloy G, As Heat Treated (2 Hrs/1050° C/Air Cool) and After Tensile Testing at 760° C (1400° F) to >30% Strain, Showing the Beta Phase Matrix Containing Gamma Prime in Equiaxed and Rod-Shaped Morphologies

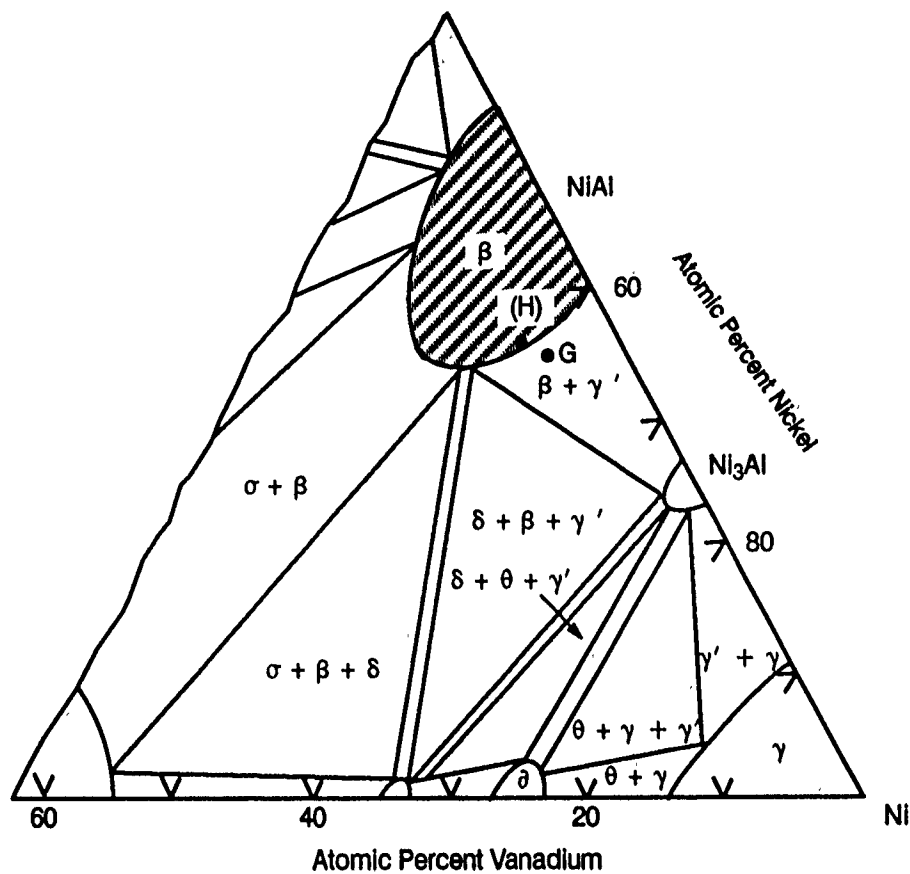


Figure 30: Isothermal Section of the Ni-V-Al Phase Diagram at 1150°C (Reference 13), Showing the Location of Phase I Alloy G and the Pseudo-Ternary Location of Alloy H



Figure 31. TEM of Powder Alloy G, As Heat Treated (2 Hrs/1050° C/Air Cool) and After Tensile Testing at 760° C (1400° F) to > 30% Strain, Showing Microstructure in Greater Detail. Note the mottled matrix and the rod-shaped and planar gamma prime phases.

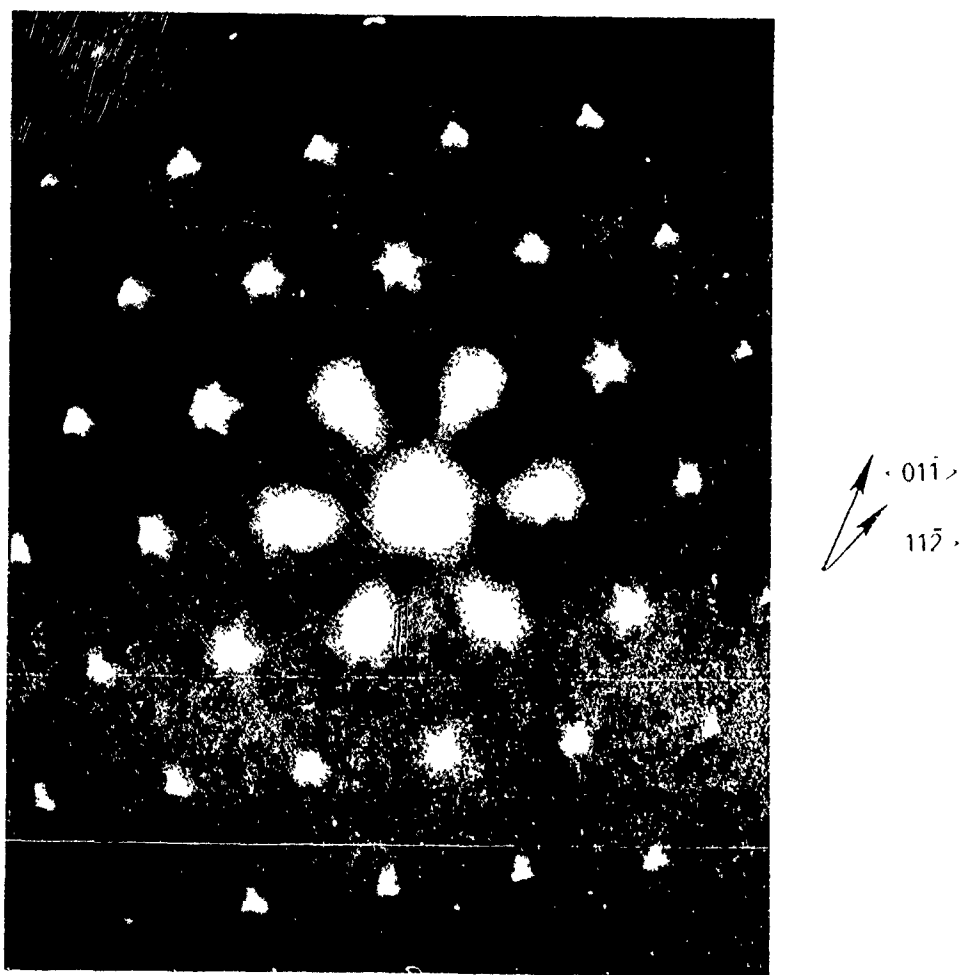


Figure 32. $\{111\}$ Electron Diffraction Pattern Taken from Powder Alloy G, As Heat Treated (2 Hrs/1050°C/Air Cool) and After Tensile Testing at 760°C (1400°F) to >30% Strain. The pattern was taken from a region of the mottled matrix free of gamma prime phase. Note the $\langle 01\bar{1} \rangle$ streaking indicative of lattice instability and the $\langle 11\bar{2} \rangle$ streaking associated with the higher order diffraction spots.

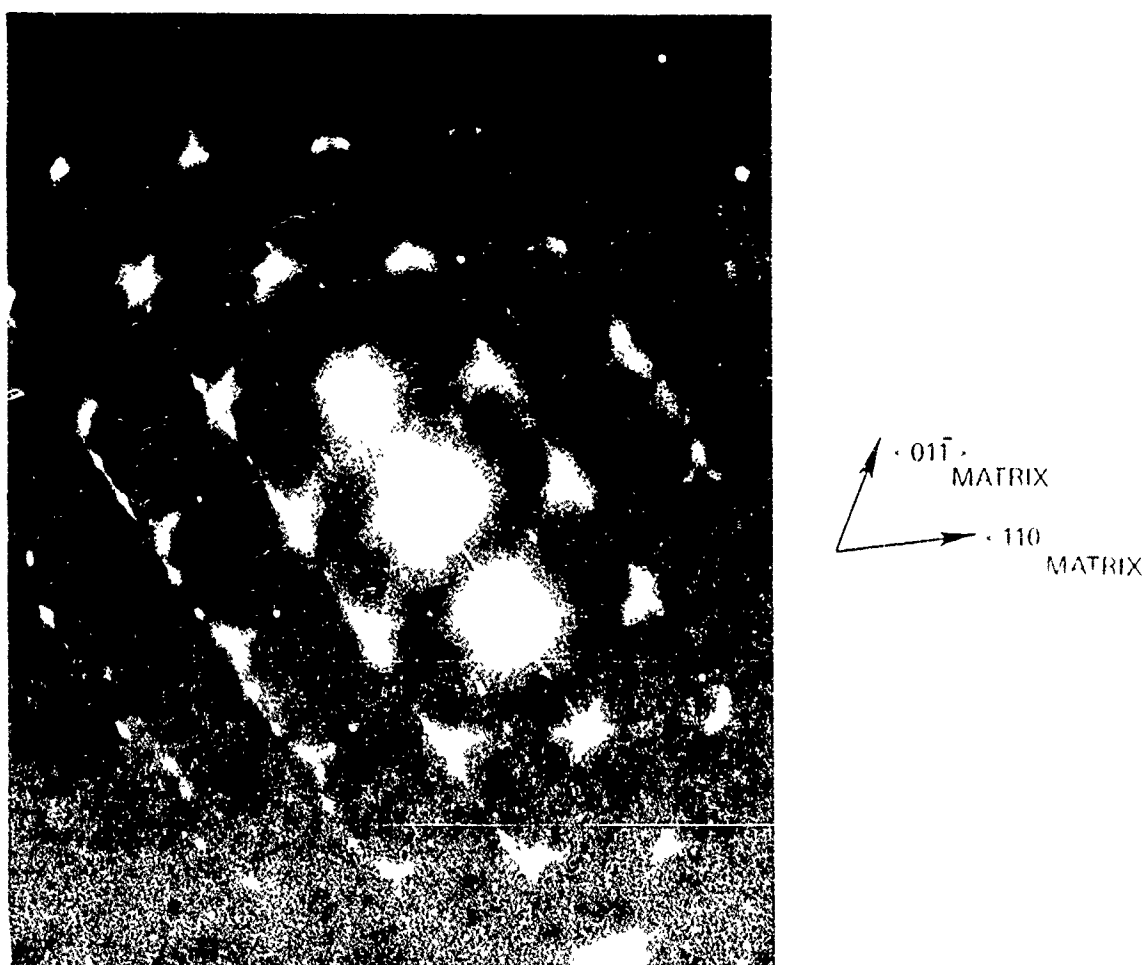


Figure 33. Electron Diffraction Pattern of the $\{111\}$ NiAl Matrix and the $\langle 101 \rangle$ Gamma Prime Precipitates Taken from Powder Alloy G, As Heat Treated (2 Hrs 1050°C /Air Cool) and After Tensile Testing at 760°C (1400°F) to $> 30\%$ Strain

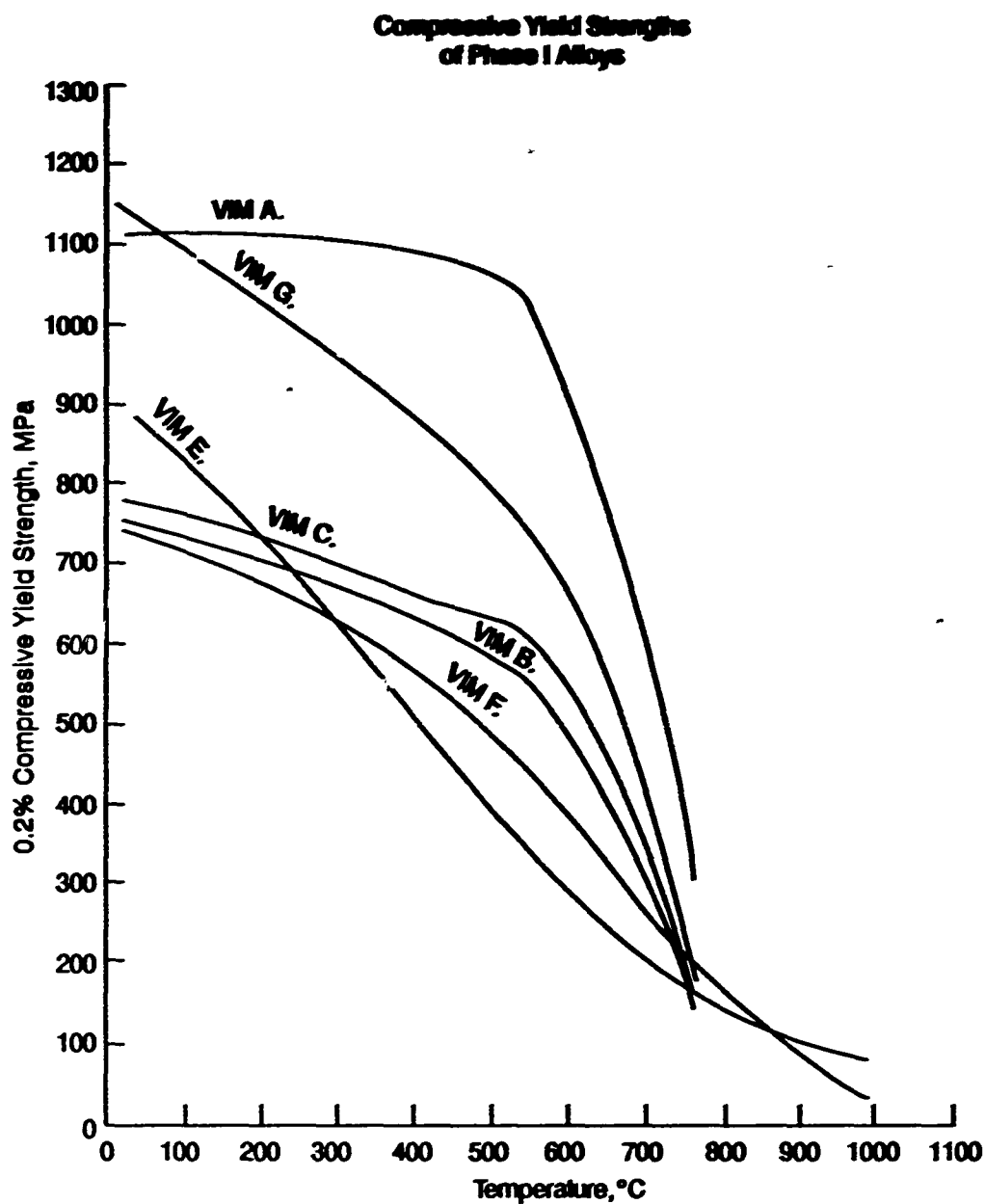


Figure 34. 0.2% Compressive Tensile Yield Strength Versus Temperature Curves for NiAl VIM Alloys A, B, C, E, F and G, Tested After a Homogenization Heat Treatment (2 Hrs/1050°C/Air Cool)

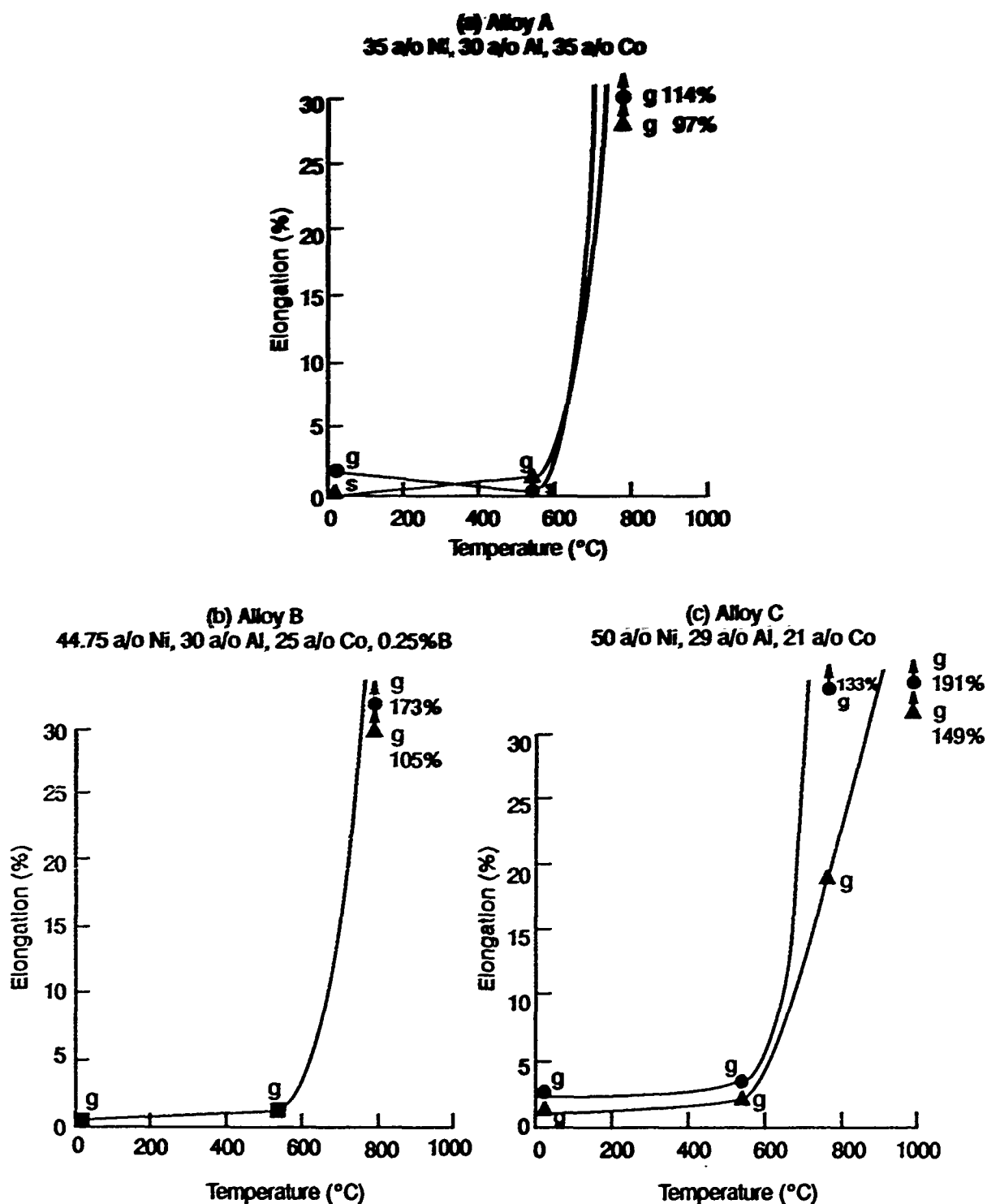
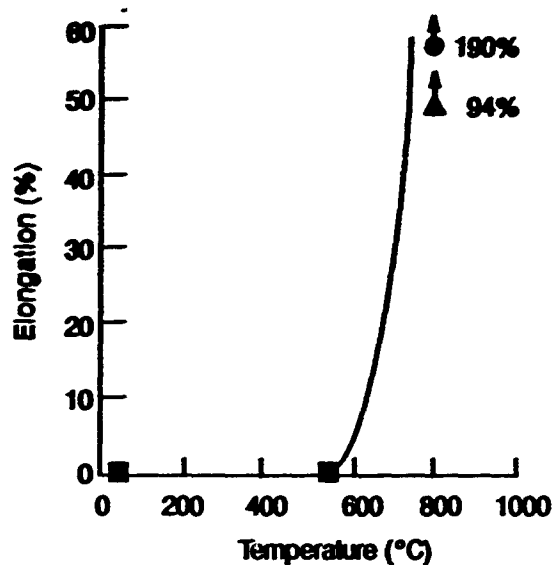
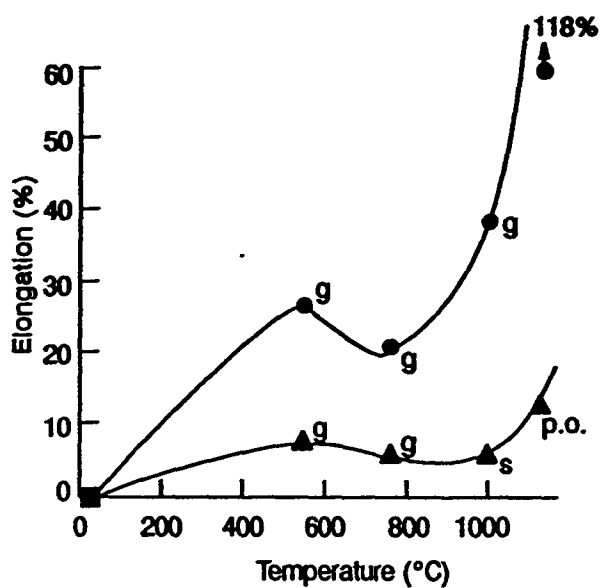


Figure 35. Tensile Elongation Versus Temperature Curves for Phase I NiAl Alloys Produced as VIM Ingots and Extruded at 1000°C with an Extrusion Ratio of 9:1. Specimens were tested as-extruded (●) and after a homogenization heat treatment for 2 hours at 1050°C and air cooled (▲). (Data points which correspond to both forms are designated ■.) The fracture locations in the specimens are indicated by "g" for gage fracture, "s" for fracture at the shoulder or grip section of the specimen, and "p.o." for specimens deformed at the shoulder and pulled out of the grip without fracture.

(d) Alloy D
55 a/o Ni, 35 a/o Al, 10 a/o Co



(e) Alloy E
39 a/o Ni, 33 a/o Al, 28 a/o Fe



(f) Alloy F
47 a/o Ni, 33 a/o Al, 20 a/o Fe

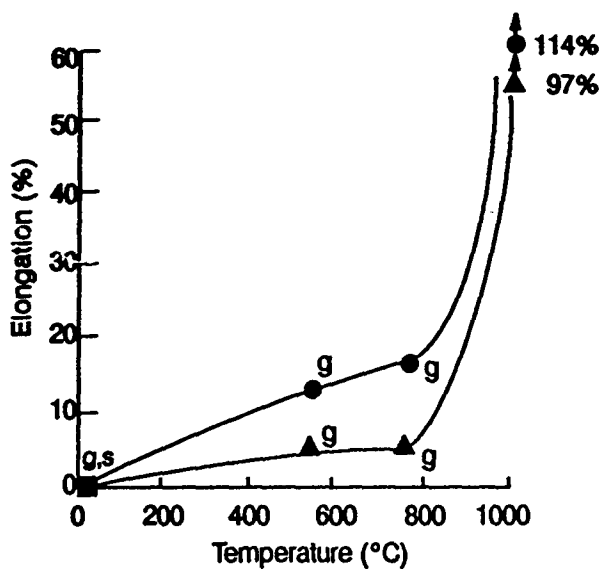
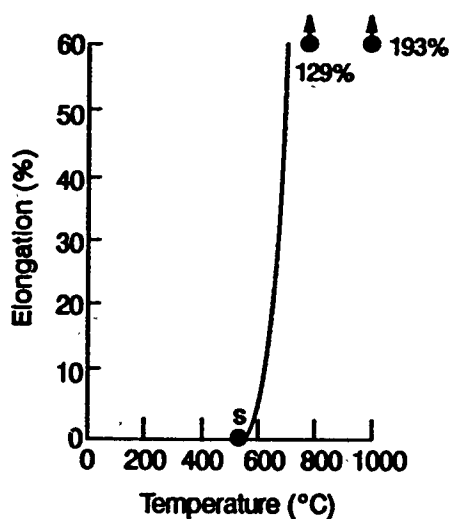
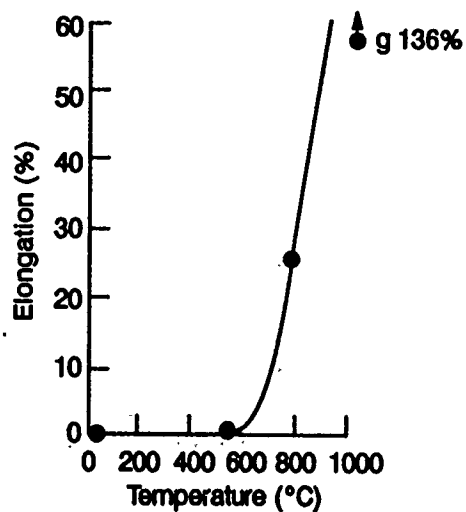


Figure 35 (continued)

(g) Alloy G
60 a/o Ni, 35 a/o Al, 5 a/o V



(h) Alloy H
57 a/o Ni, 35 a/o Al, 5 a/o V, 3 a/o Cr



(i) Alloy J
60 a/o Ni, 35 a/o Al, 5 a/o Ti

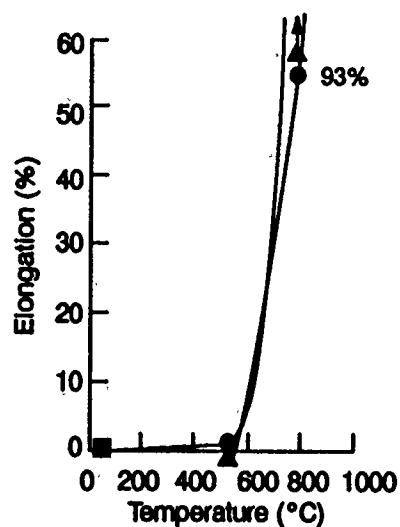
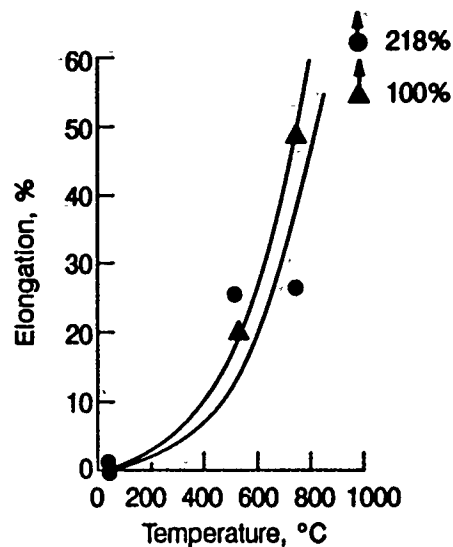
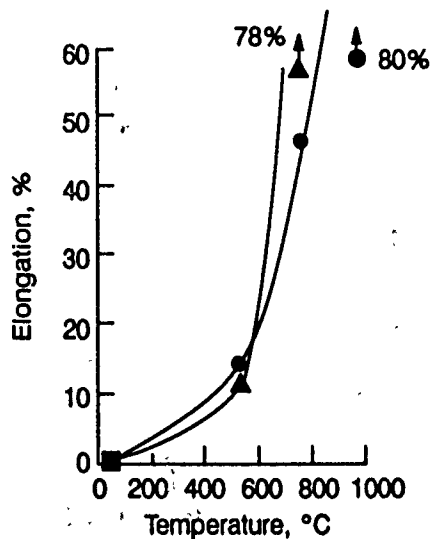


Figure 35 (continued)

(a) Alloy A
35 a/o Ni, 30 a/o Al, 35 a/o Co



(b) Alloy B
44.75 a/o Ni, 30 a/o Al, 25 a/o Co, 0.25 a/o B



(c) Alloy C
50 a/o Ni, 29 a/o Al, 21 a/o Co

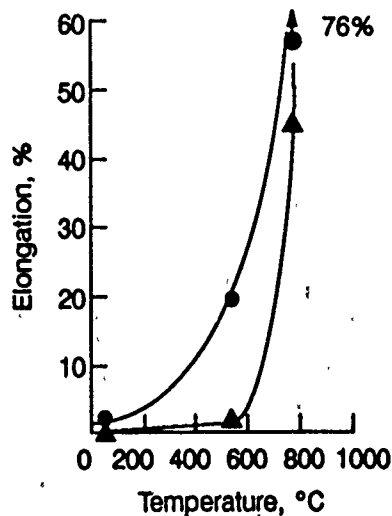
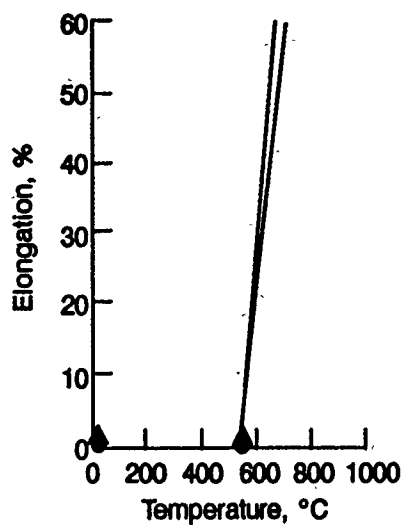
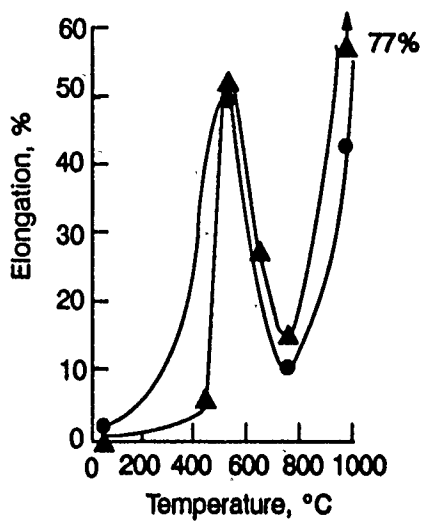


Figure 36. Tensile Elongation Versus Temperature Curves for Phase I NiAl Alloys Produced in Powder Form and Extruded at 1000°C with an Extrusion Ratio of 9:1. Specimens were tested as-extruded (●) and after a homogenization heat treatment for 2 hours at 1050°C and air cooled (▲). Overlapping data points are indicated by ■.

(d) Alloy D
55 a/o Ni-35 a/o Al-10 a/o Co



(e) Alloy E
39 a/o Ni, 33 a/o Al, 28 a/o Fe



(f) Alloy F
47 a/o Ni, 33 a/o Al, 20 a/o Fe

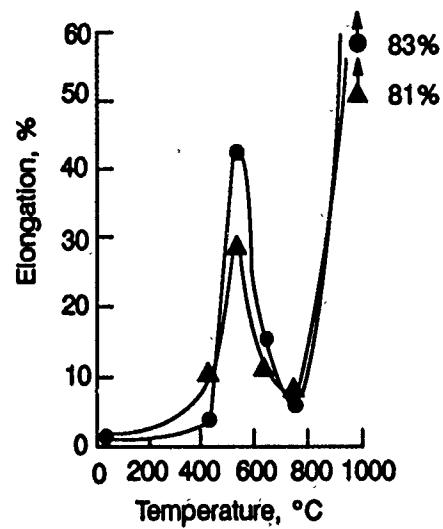


Figure 36 (continued)

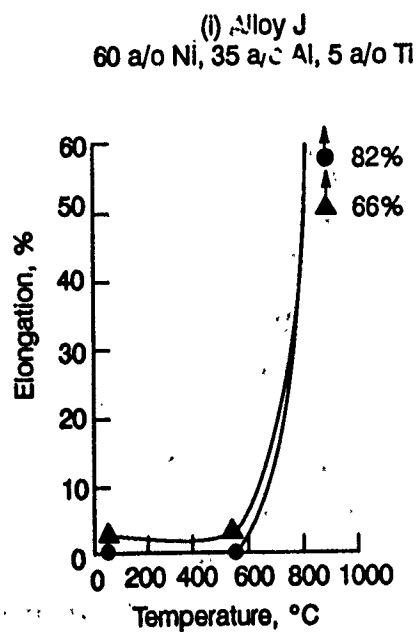
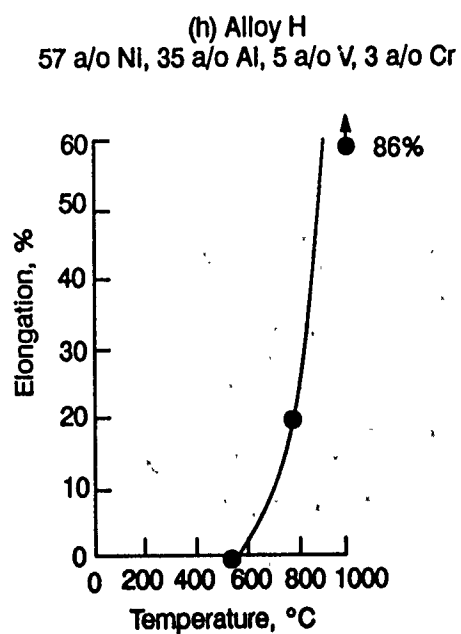
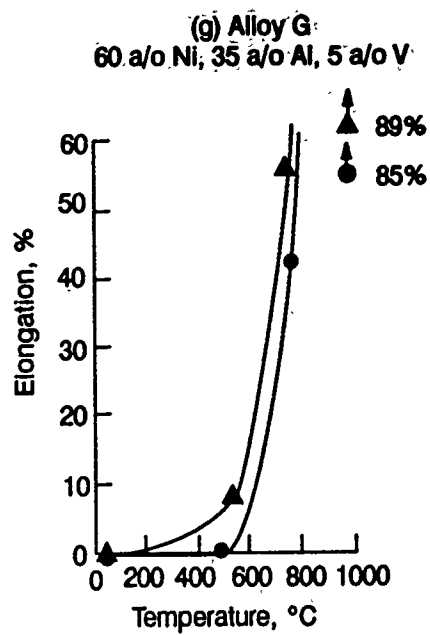


Figure 36 (continued)



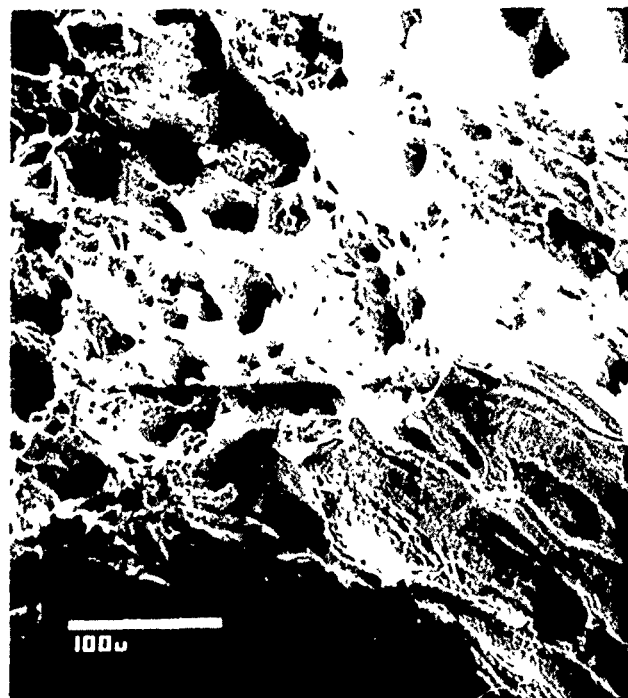
(a)



(b)



(c)



(d)

Figure 37. Typical Examples of Tensile Fracture Surfaces of Phase I VIM Alloys. (a) Intergranular fracture (Alloy E, tested at 760°C), (b) transgranular cleavage (Alloy F, tested at 540°C), (c) mixed mode (Alloy A, tested at 540°C), and (d) ductile tearing (Alloy A, tested at 760°C). All alloys tested after a homogenization heat treatment at 1050°C for 2 hours, air cooled.



Figure 38. *Optical Micrographs of Alloy A Compression Specimens Before Deformation (top) and After 4% Strain at Room Temperature (bottom). Note the stress-induced martensite (arrow).*

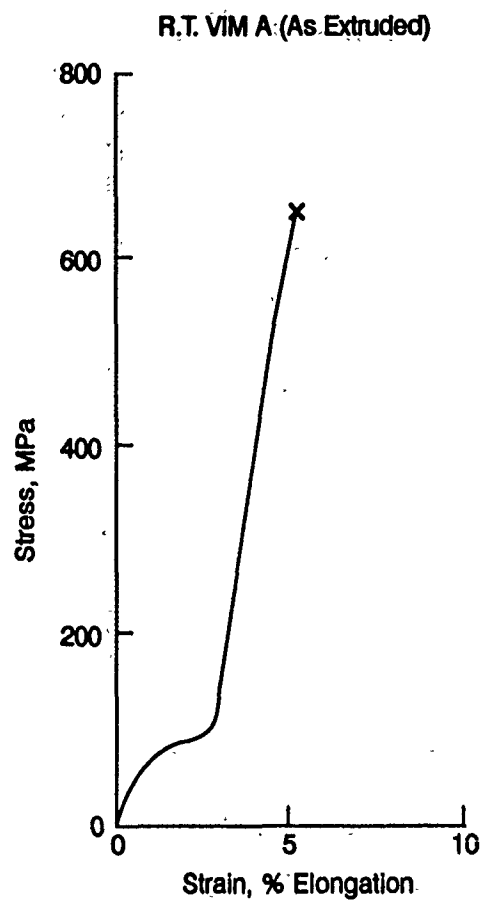
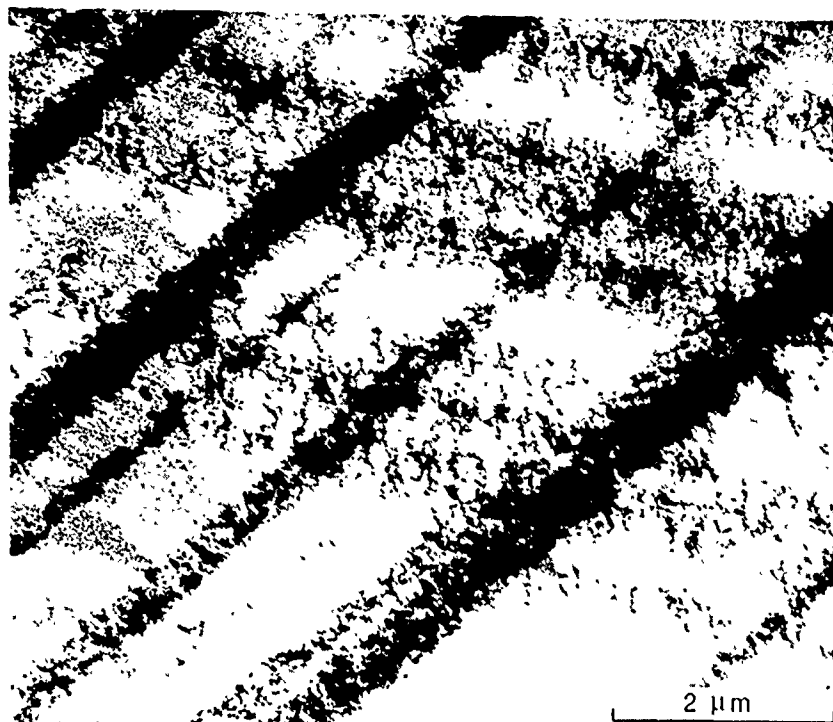
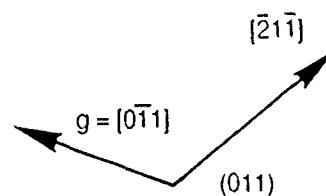


Figure 39. Room Temperature Tensile Stress-Strain Curve for Extruded VIM Alloy A Showing Evidence of a Stress-Induced Martensitic Transformation at About 80 MPa



(a)



(b)

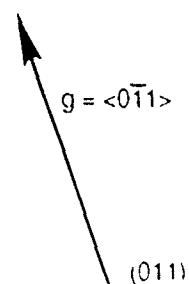


Figure 40. TEM of VIM Alloy A, As-Extruded + Heat Treatment of 2 Hrs/1050°C/Air Cool After Compression at Room Temperature to 0.2% Strain. (a) Micrograph of matrix showing dislocation bands along $\langle 112 \rangle$ and $\langle 110 \rangle$ B2 directions. (b) Micrograph of blocky phase with stacking faults on the same structure ($L1_2$) as the grain boundary phase. Note the poorly defined tweed contrast in the matrix.

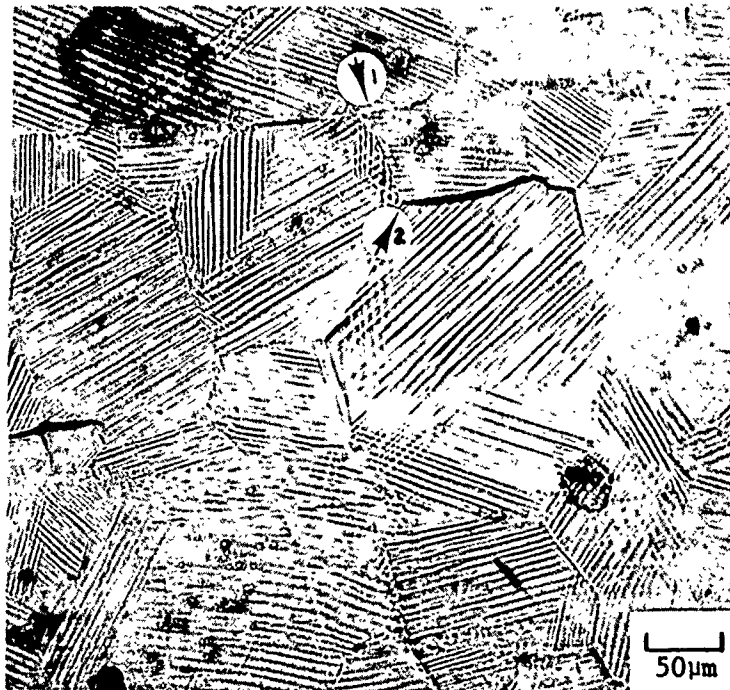
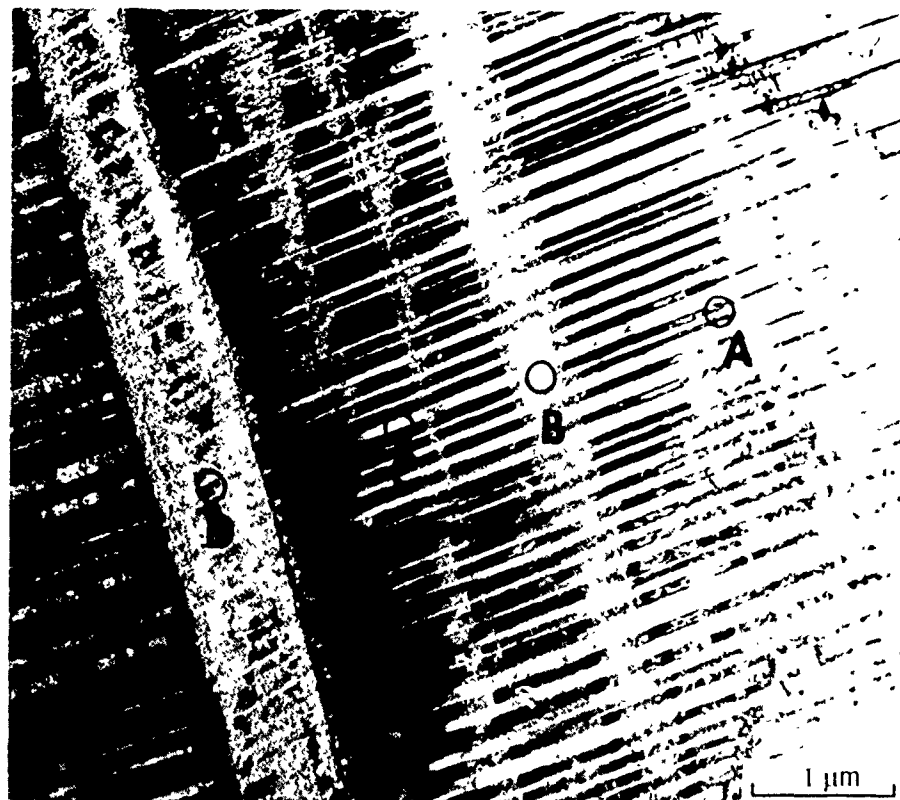


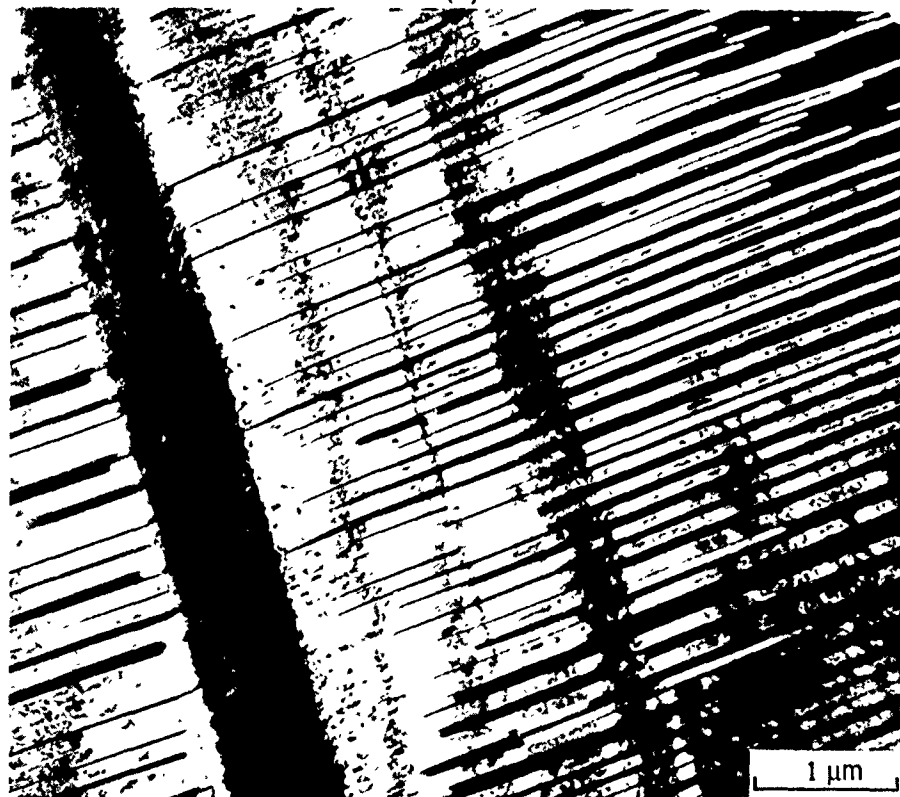
Figure 41. *Optical Micrographs of Alloy B Room Temperature Compression Specimen (top) After 0.35% Strain, and (bottom) After 1.65% Strain. Note the nucleation of the intergranular crack labeled #2 after 1.65% strain. (Applied force direction – horizontal to the photographs.)*



Figure 42. Optical Micrographs of Alloy B Room Temperature Compression Specimen (top) After 4.0% Strain, and (bottom) After 7.5% Strain. Note that at 4.0%, cracks #1 and #2 have widened and both cracks continue to widen with 7.5% strain. However, the grains exhibit good toughness as seen by the blunting of the crack and resistance to propagation into the grain at the point indicated by #2. (Applied force direction – horizontal to the photographs.)



(a)

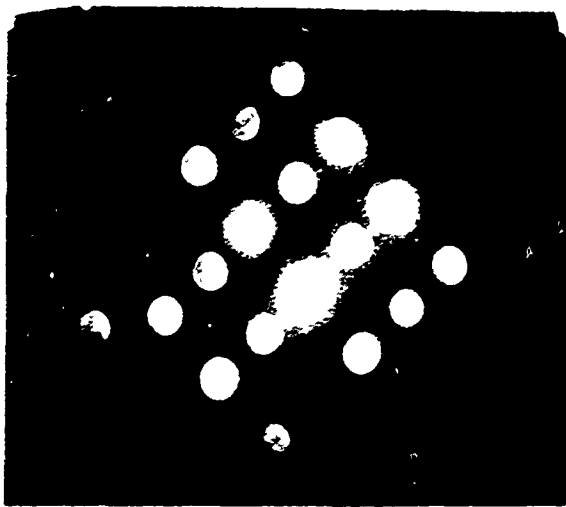


(b)

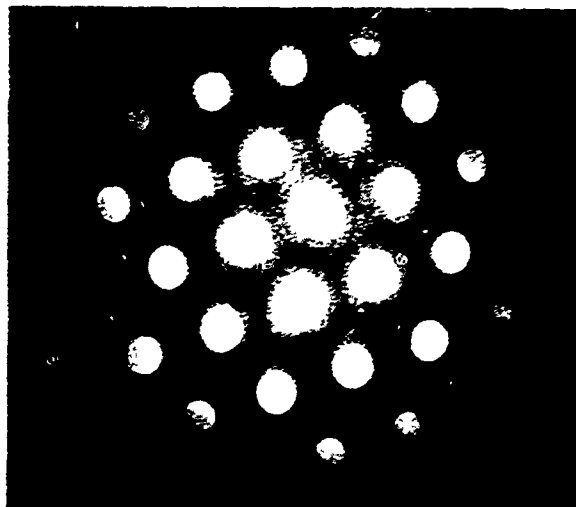
Figure 43. TEM Micrographs of VIM Alloy B After Compression to 3% at Room Temperature. (a) Bright field image showing lamellae of different orientations—A: $\bar{1}\bar{1}2$, B: $\bar{1}\bar{5}2$, C: $\bar{1}\bar{1}2$, D: $\bar{1}\bar{3}2$. (b) Dark field image of the same area. Note that the twin lamellae maintain their orientation as they continue through martensitic plates of different (twin related) orientations. The average thickness of the twin lamellae is 65 nm.



(a)



(b)



(c)

Figure 44. TEM Micrographs of VIM Alloy B After Compression to 3% at Room Temperature. (a) Bright field image showing lamellae of different orientations. Selected area diffraction patterns using a convergent beam and zone axes of (b) $(1\bar{1}2)$ and (c) $(0\bar{1}1)$, indicating the structure of the martensite to be face-center tetragonal with lattice parameters of $a = 0.384$ nm and $c = 0.314$ nm.

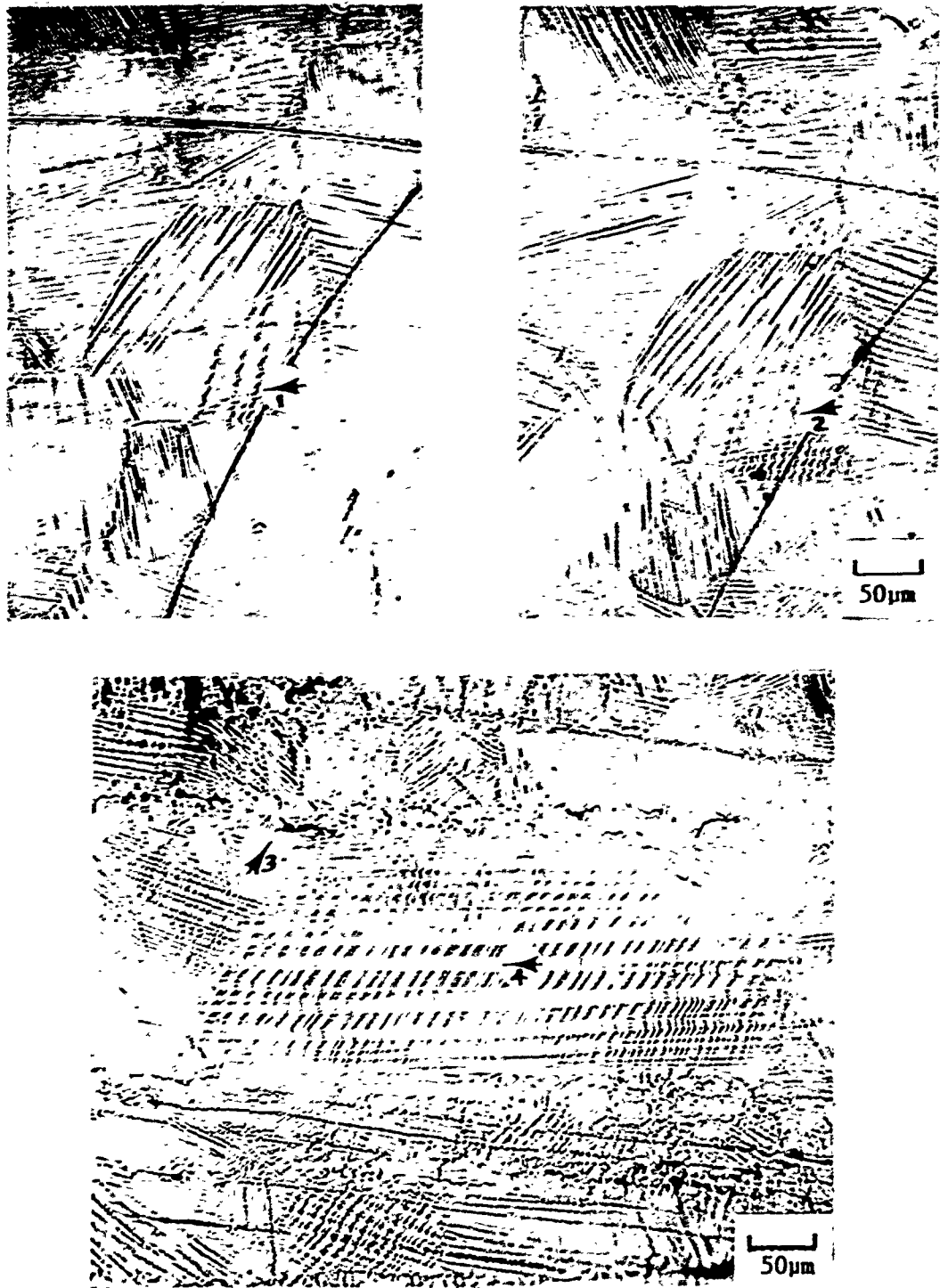


Figure 45. Optical Micrographs of Alloy C Room Temperature Compression Specimen After 1.5% Strain (top left), After 4.0% Strain (top right), and After 9.0% Strain (bottom). Note the origination of what appears to be cross-twinning at 1.5% strain (#1). At 4.0% strain, the number of cross-twins has increased (#2). A different grain shown at 9.0% strain contains a very large number of these features. #3 and #4 indicate areas to be examined in greater detail in Figure 46. (Applied force direction – horizontal to the photographs.)

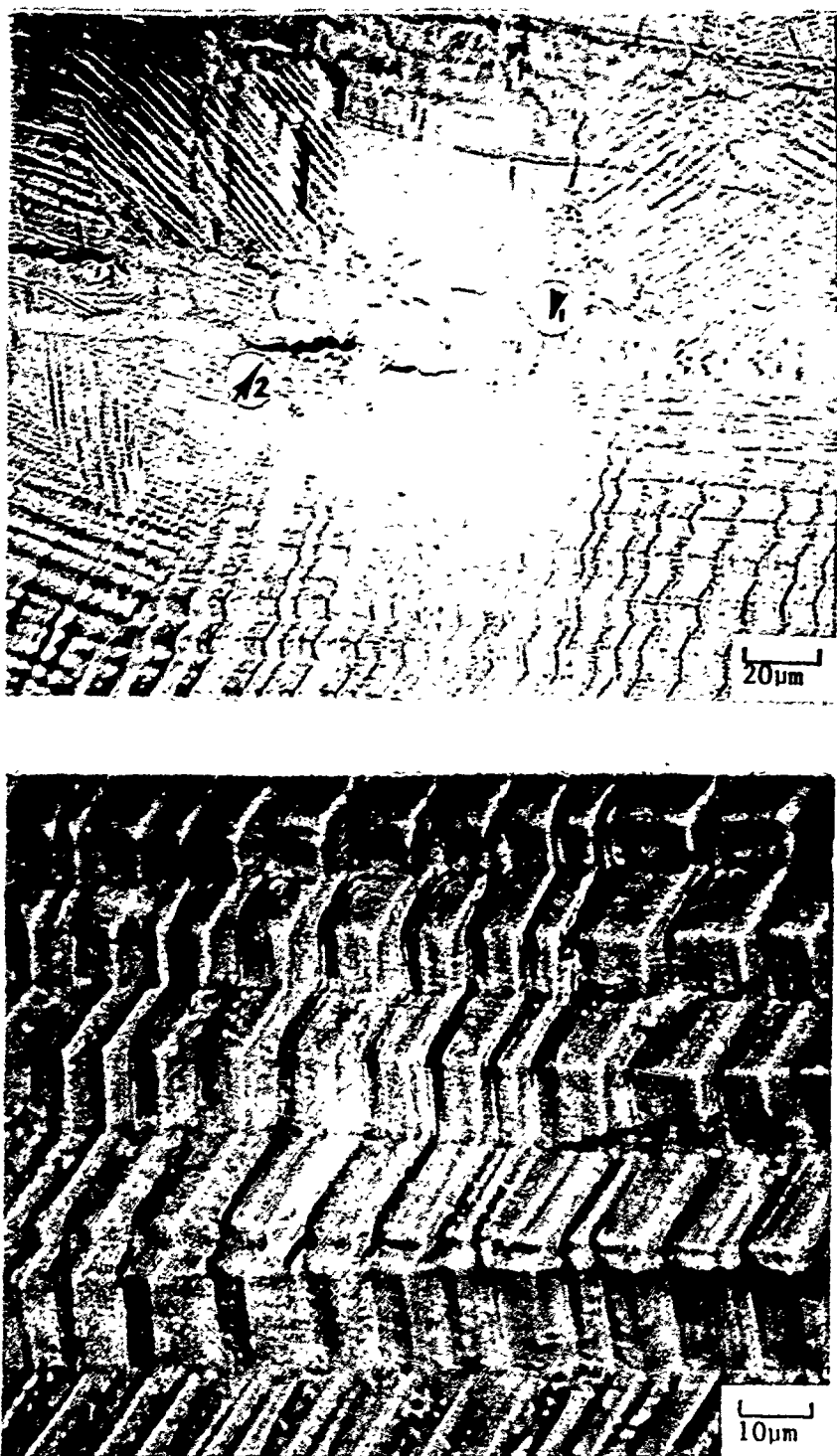


Figure 46. Optical Micrographs of Alloy C Room Temperature Compression Specimen After 9.0% Strain Showing the Detail in Figure 45 at (top) #3 and (bottom) #4. The top micrograph shows the region at the grain boundary, with the secondary grain boundary phase seen here at #1. The crack (#2) is typical of cracks in Alloy C, which appear at the interface between the martensitic grains and the secondary phase. The bottom micrograph shows the lines which appear to be cross-twinning. (Applied force direction ~ horizontal to the photographs.)

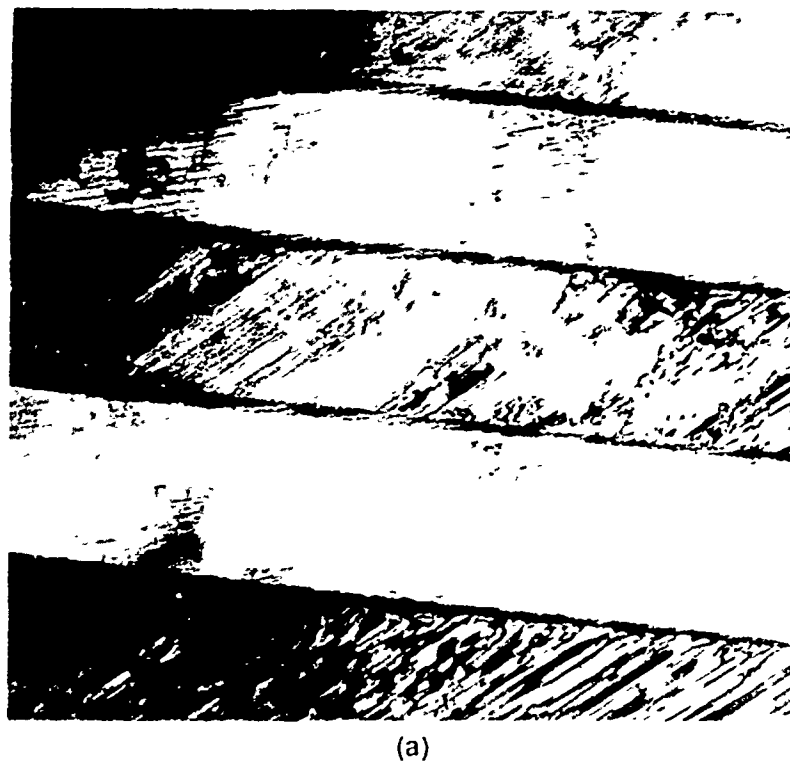


Figure 47. TEM Micrographs of VIM Alloy C, As Extruded + Heat Treatment of 2 Hrs/1050°C/Air Cool. (a) Undeformed microstructure of parallel martensitic laths. (b) Intersecting martensitic laths produced by plastic deformation.

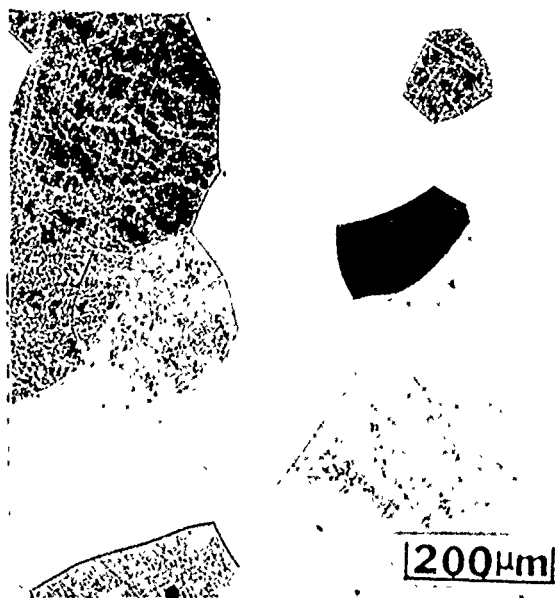
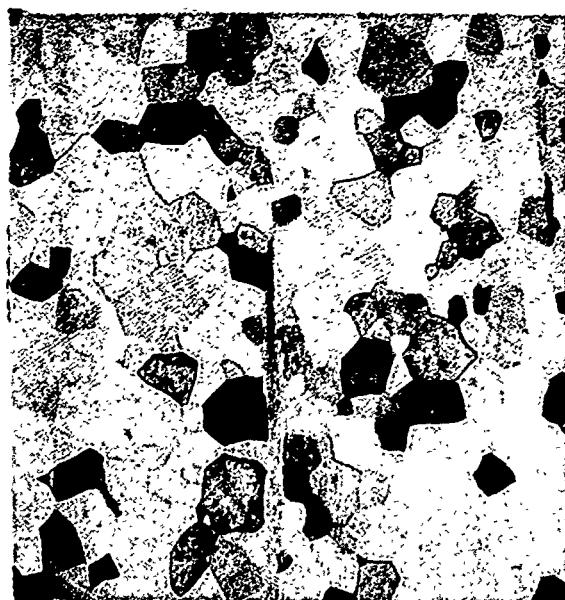
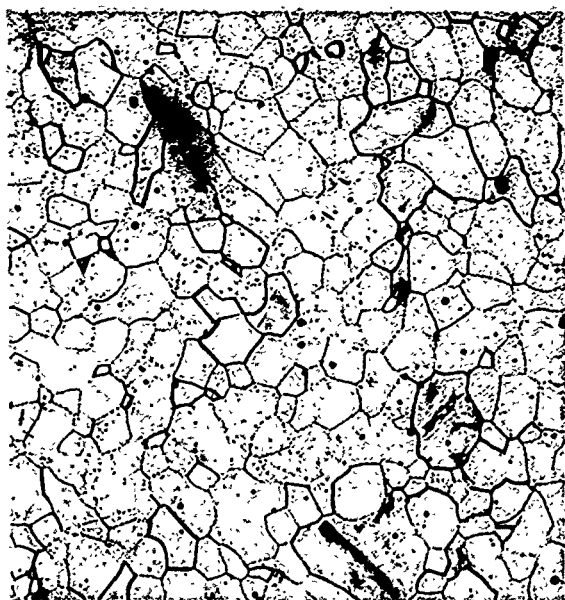


Figure 48. Microstructures of Alloy A2 (Ni-32 a/o Al-29 a/o Co) Produced as a VIM Ingot After Extrusion at 1000°C, Extrusion Ratio 9:1 (top) and After Heat Treatment for 2 Hrs/1050°C/Air Cool (bottom); Left - Transverse Section, Right - Longitudinal Section



Figure 49. Microstructures of Alloy A3 (Ni-32 a/o Al-25 a/o Co) Produced as a VIM Ingot After Extrusion at 1000°C, Extrusion Ratio 9:1 (top) and After Heat Treatment for 2 Hrs/1050°C/Air Cool (bottom); Left - Transverse Section, Right - Longitudinal Section

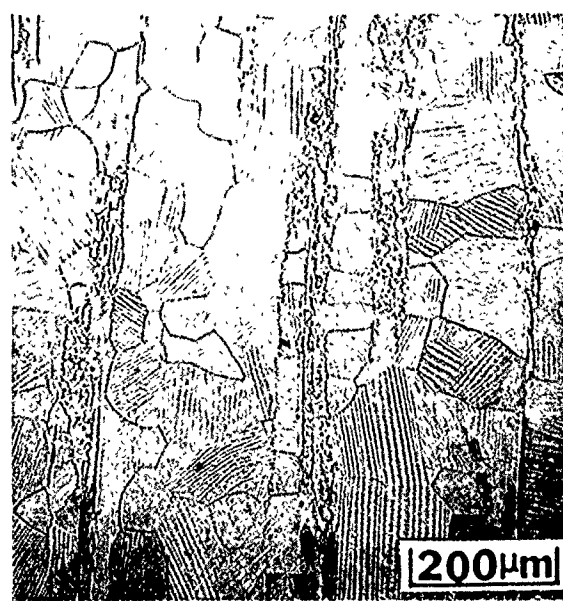
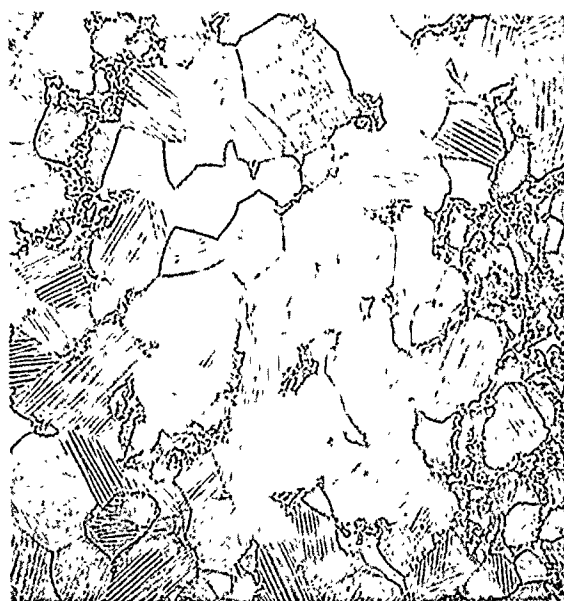
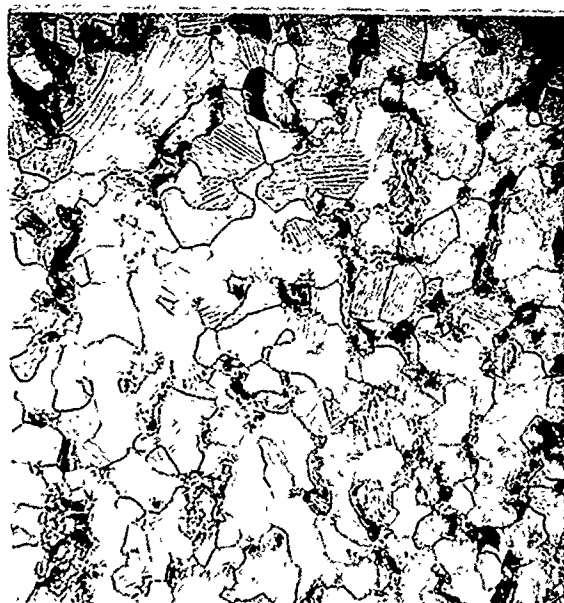


Figure 50. *Microstructures of Alloy B2 (Ni-30 a/o Al-25 a/o Co) Produced as a VIM Ingot After Extrusion at 1000°C, Extrusion Ratio 9:1 (top) and After Heat Treatment for 2 Hrs/1050°C/Air Cool (bottom); Left - Transverse Section, Right - Longitudinal Section*

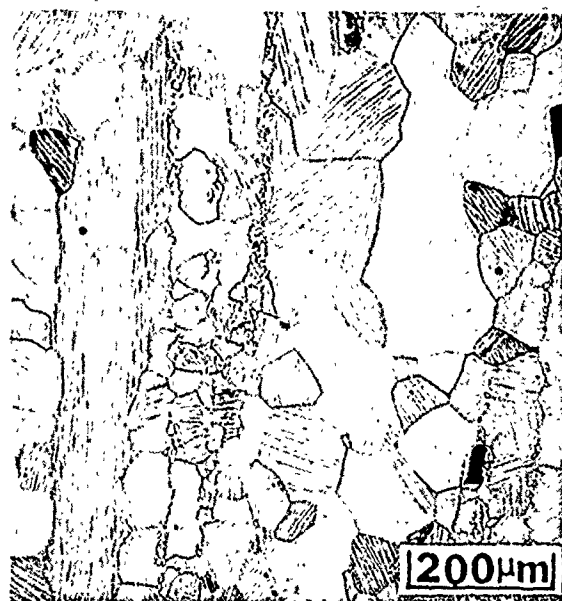
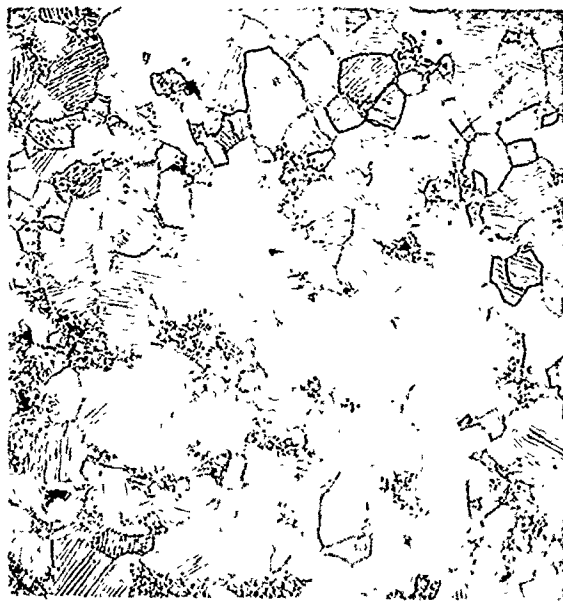


Figure 51. Microstructures of Alloy C2 (Ni-31 a/o Al-16 a/o Co) Produced as a VIM Ingot After Extrusion at 1000°C, Extrusion Ratio 9:1 (top) and After Heat Treatment for 2 Hrs/1050°C/Air Cool (bottom); Left - Transverse Section, Right - Longitudinal Section

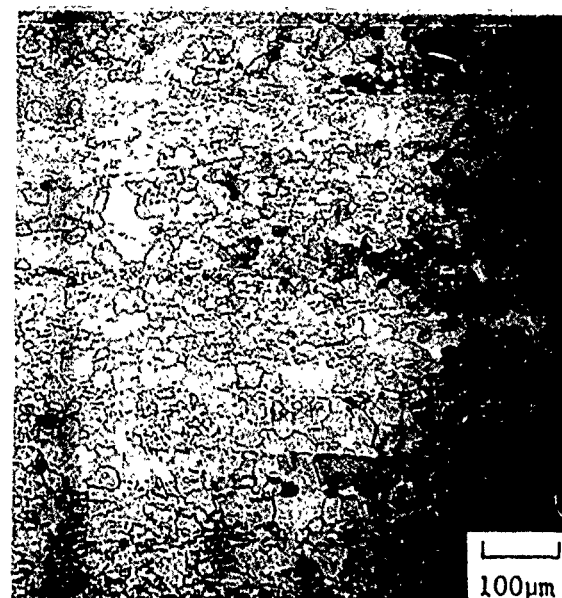
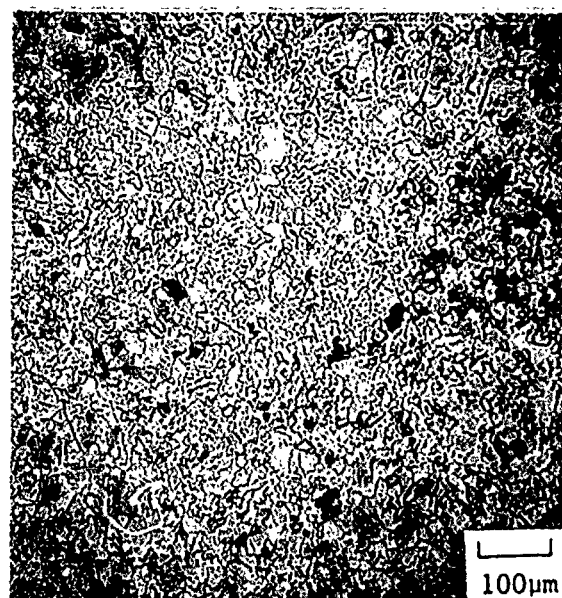
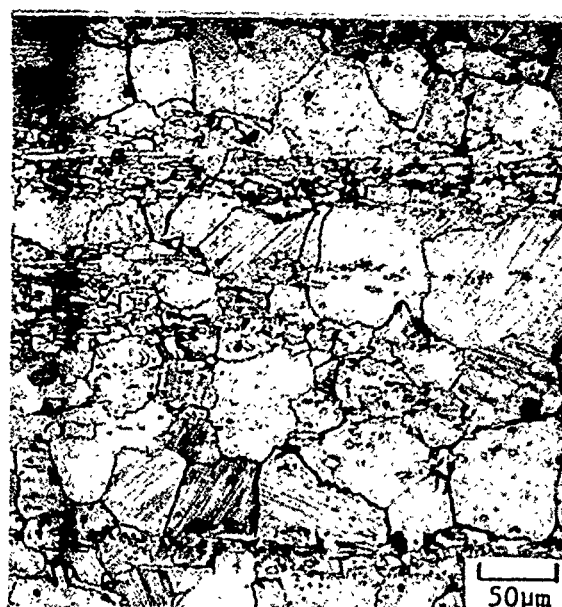
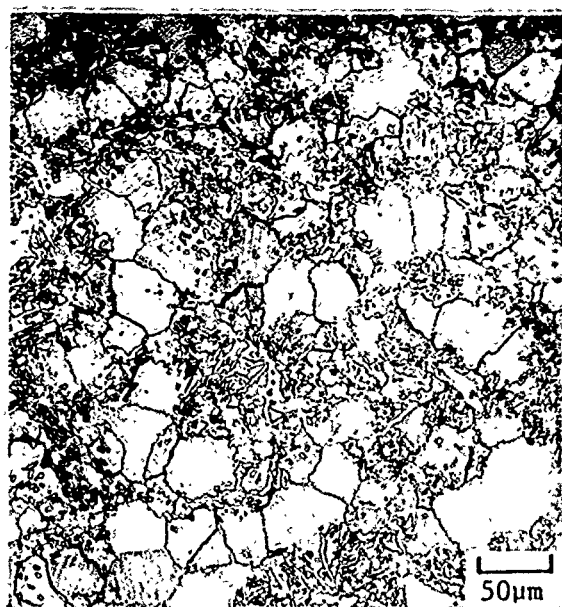


Figure 52. Microstructures of Alloy C3 (Ni-30 a/o Al-15 a/o Co) Produced as a VIM Ingot After Extrusion at 1000°C, Extrusion Ratio 9:1 (top) and After Heat Treatment for 2 Hrs/1050°C/Air Cool (bottom); Left - Transverse Section, Right - Longitudinal Section

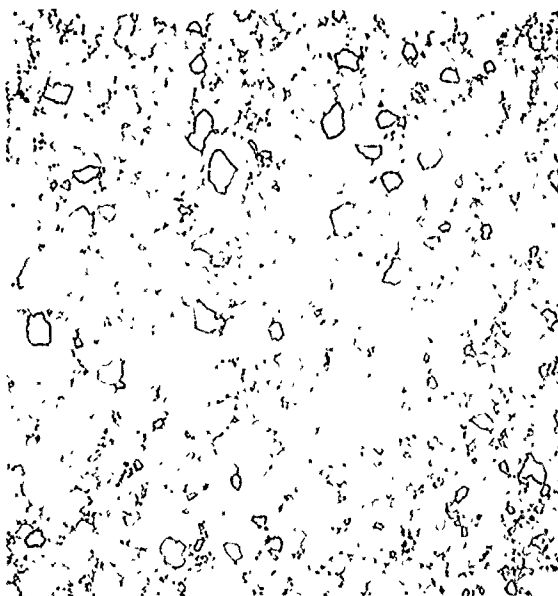
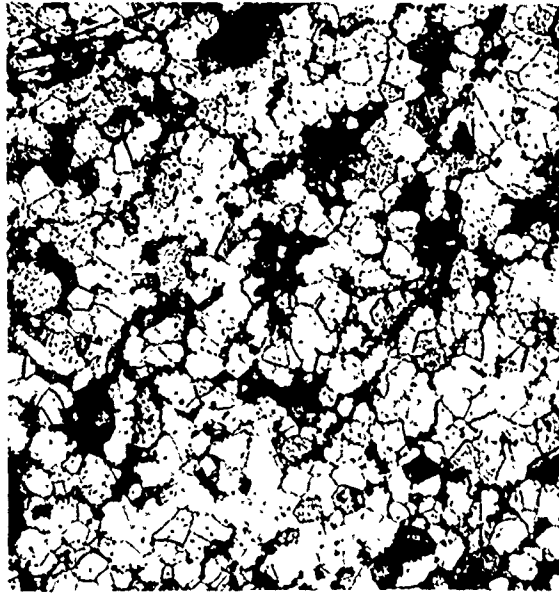


Figure 53. Microstructures of Alloy AH (Ni-30 a/o Al-34.5 a/o Co-0.5 a/o Hf) Produced as a VIM Ingot After Extrusion at 1000°C, Extrusion Ratio 9:1 (top) and After Heat Treatment for 2 Hrs/1050°C/Air Cool (bottom); Left - Transverse Section, Right - Longitudinal Section

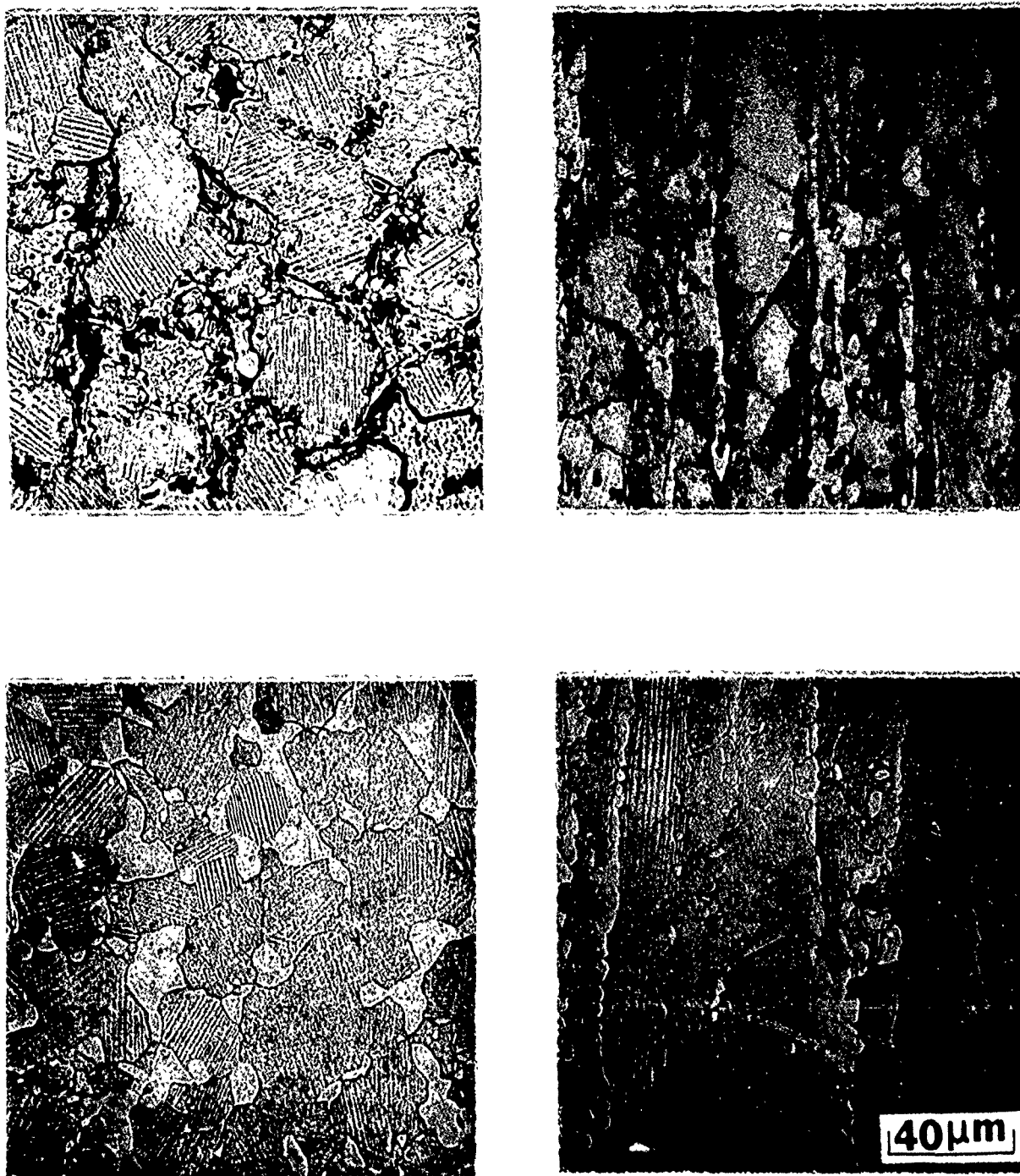


Figure 54. Microstructures of Alloy CH (Ni-29 a/o Al-21 a/o Co-0.5 a/o Hf) Produced as a VIM Ingot After Extrusion at 1000°C, Extrusion Ratio 9:1 (top) and After Heat Treatment for 2 Hrs/1050°C/Air Cool (bottom); Left - Transverse Section, Right - Longitudinal Section

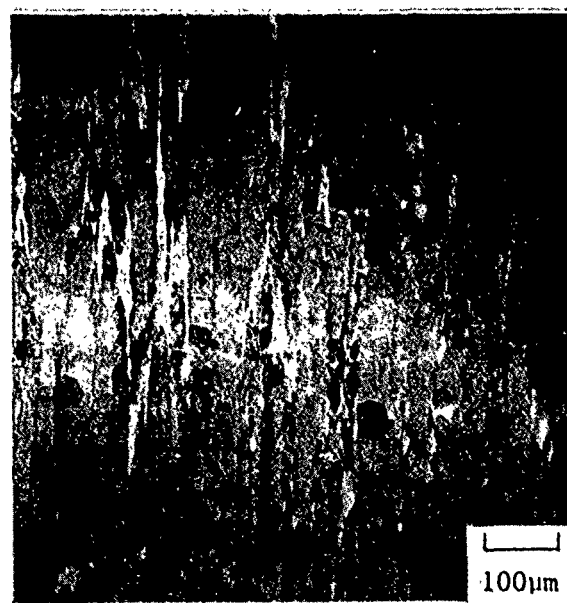
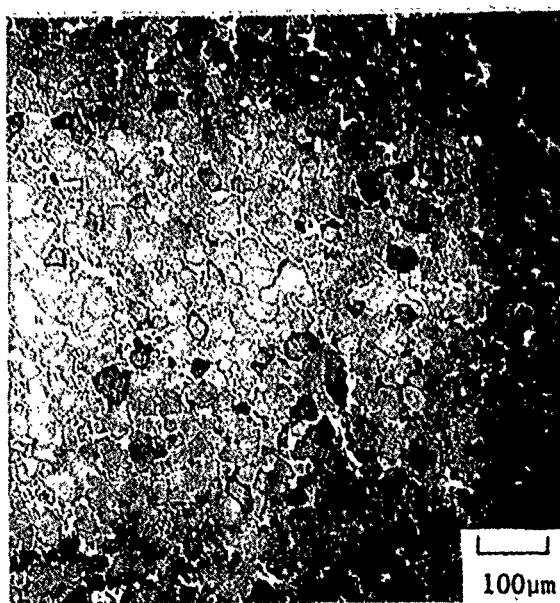
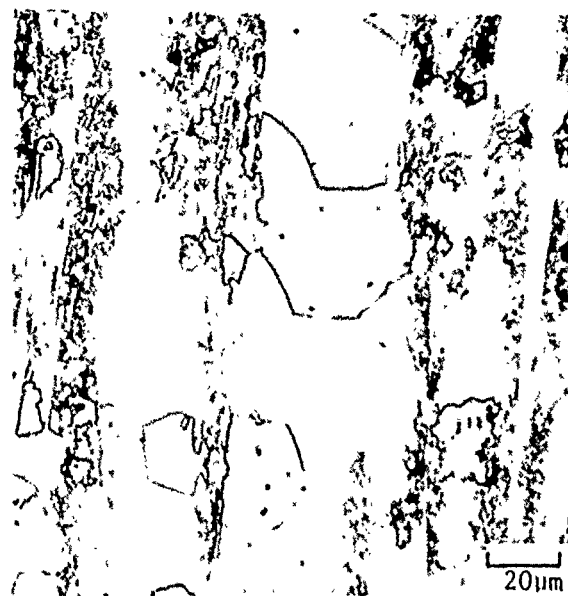
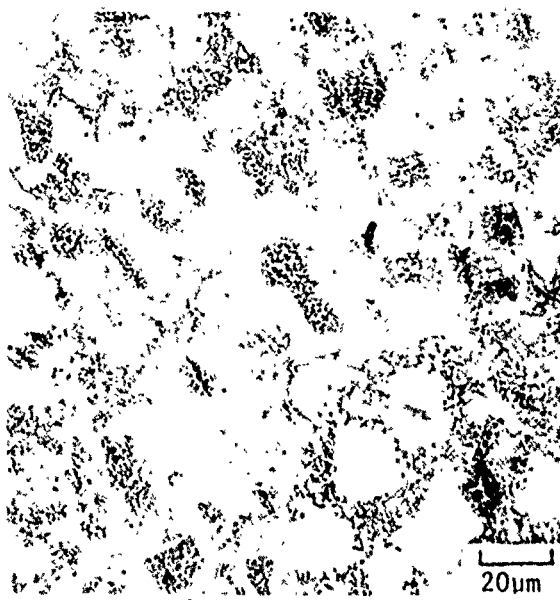


Figure 55. Microstructures of Alloy CT (Ni-29 a/o Al-21 a/o Co-5 a/o Ti) Produced as a VIM Ingot After Extrusion at 1000°C, Extrusion Ratio 9:1 (top) and After Heat Treatment for 2 Hrs/1050°C/Air Cool (bottom); Left - Transverse Section, Right - Longitudinal Section

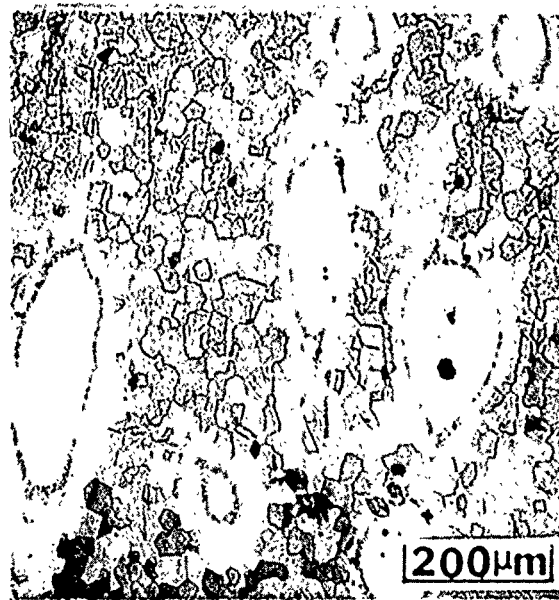
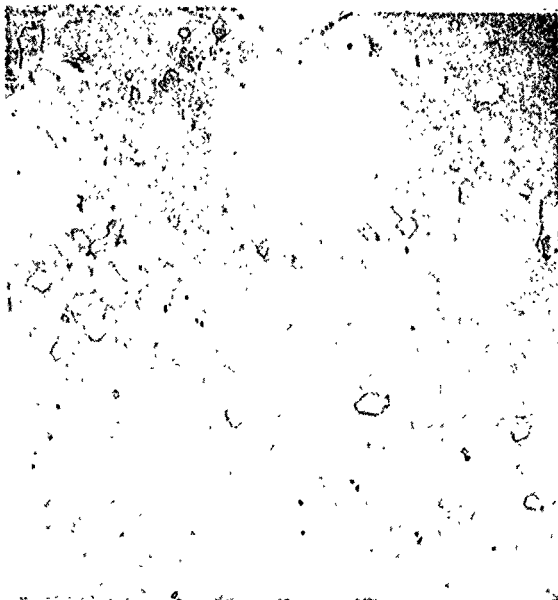
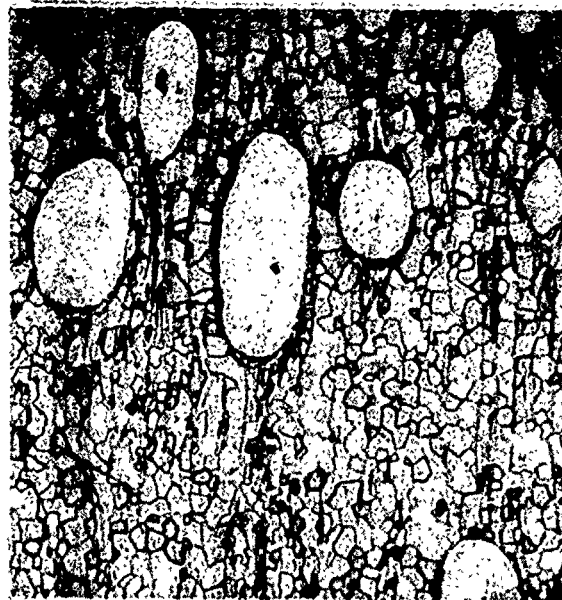
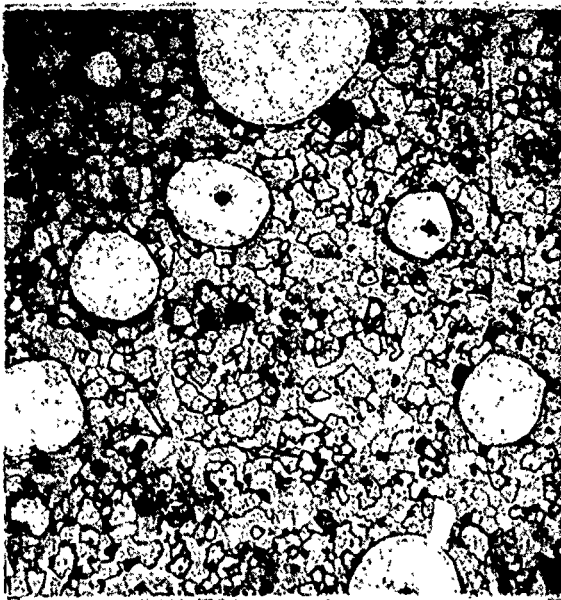


Figure 56. Microstructures of Alloy M1 (Ni-50 a/o Al-20 v/o MERL 76 Particles) After Extrusion at 1000°C, Extrusion Ratio 9:1 (top) and After Heat Treatment for 2 Hrs/1050°C/Air Cool (bottom); Left - Transverse Section, Right - Longitudinal Section

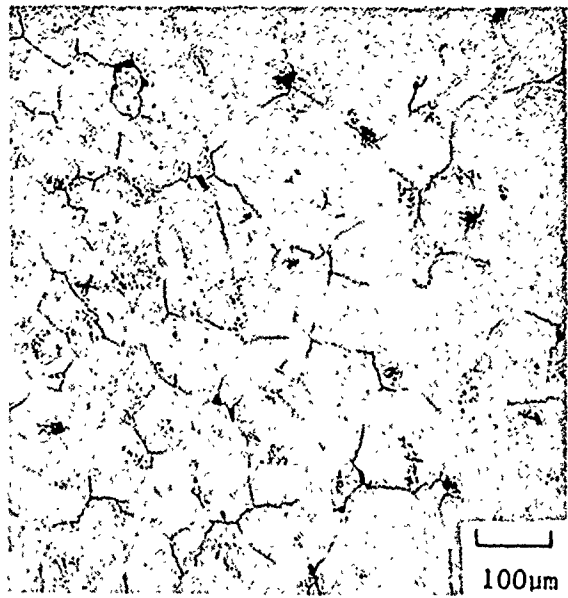
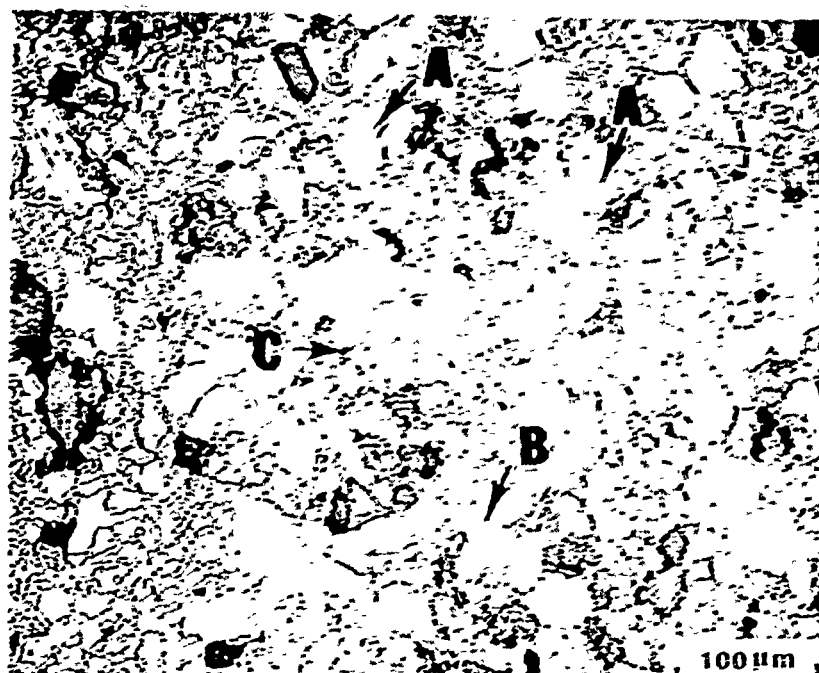
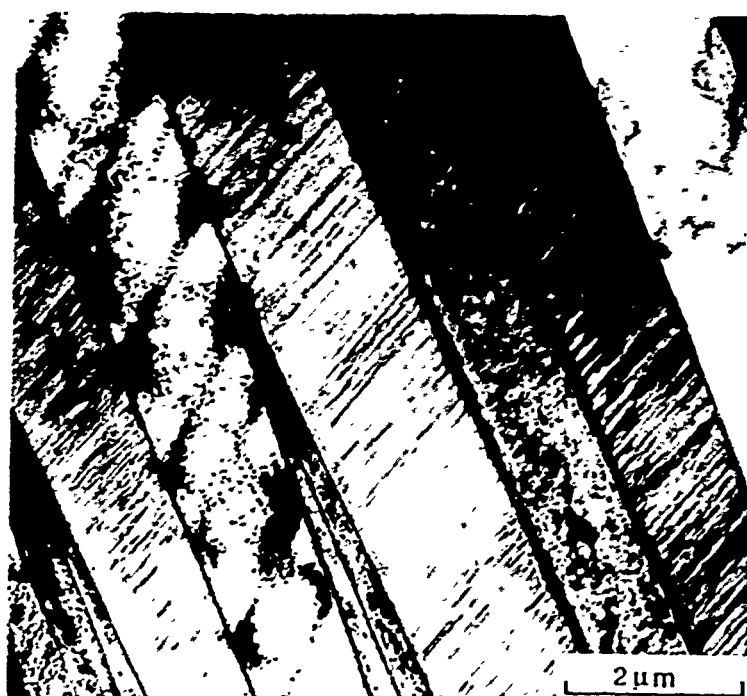


Figure 57. Microstructures of Alloy AT (Ni-30 a/o Al-32.5 a/o Co-5 a/o Ti) Produced as a VIM Ingot. Alloy AT broke apart during the canning stage and was not extruded.

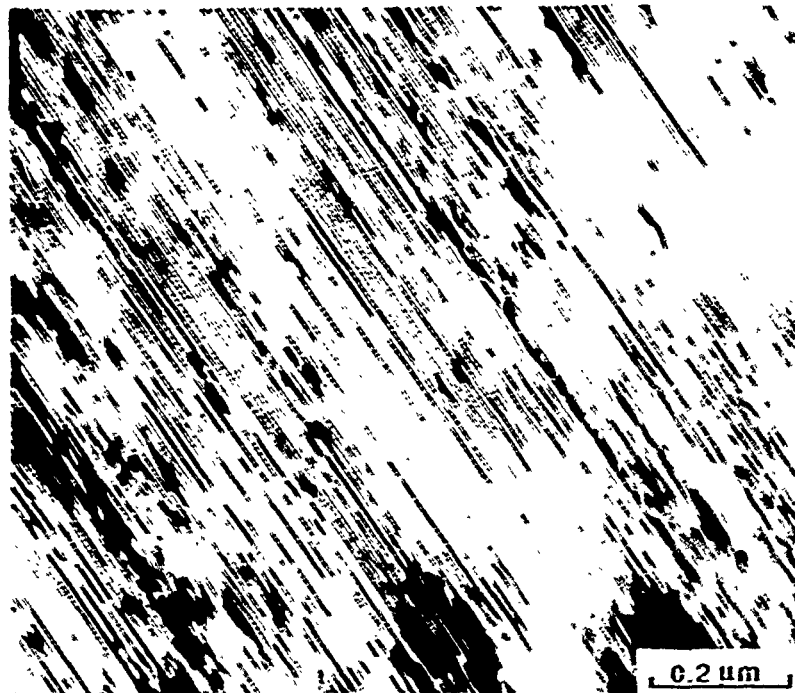


(a)

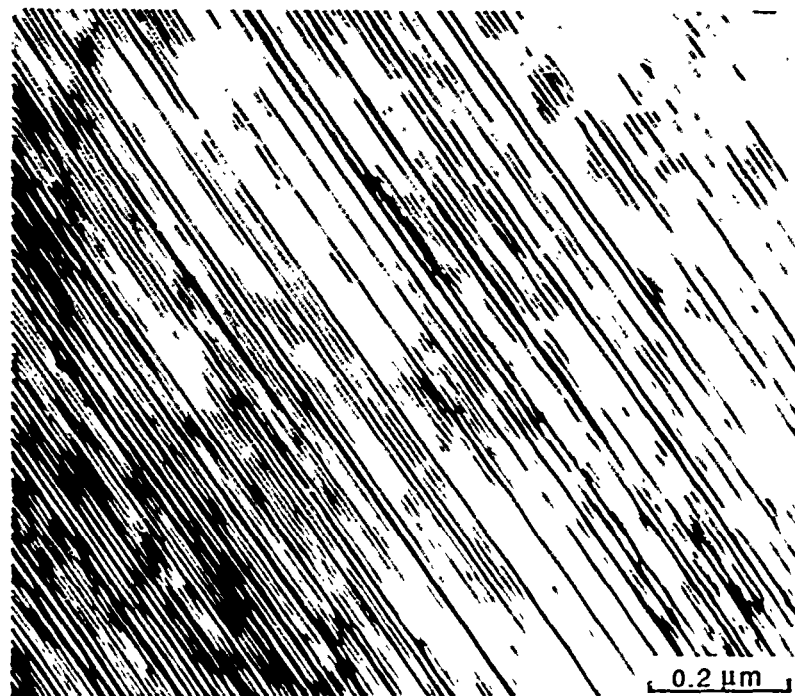


(b)

Figure 58. (a) Optical Micrograph, and (b) TEM Micrograph of Alloy C3 After Compression at Room Temperature Showing Gamma Prime Distribution and Fine Twin Lamellae

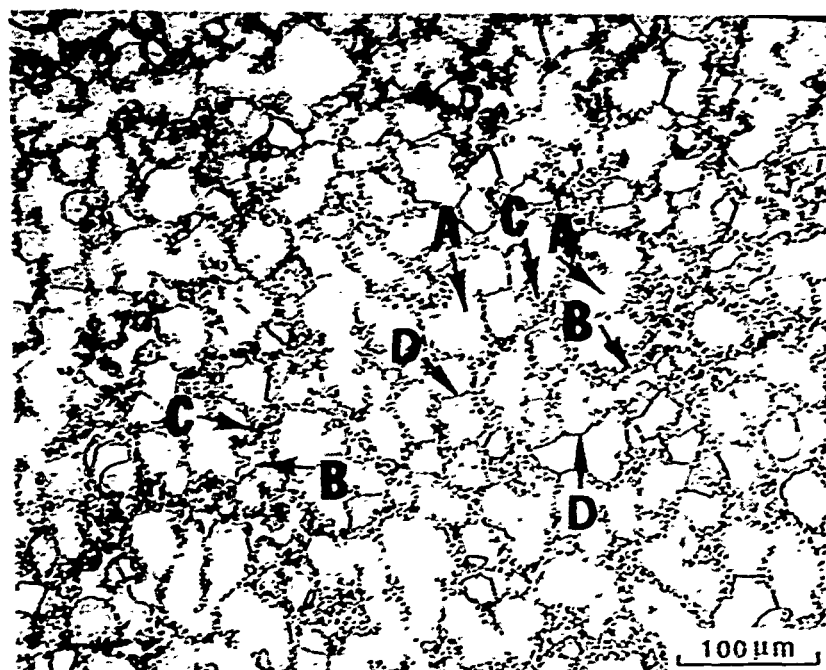


(a)

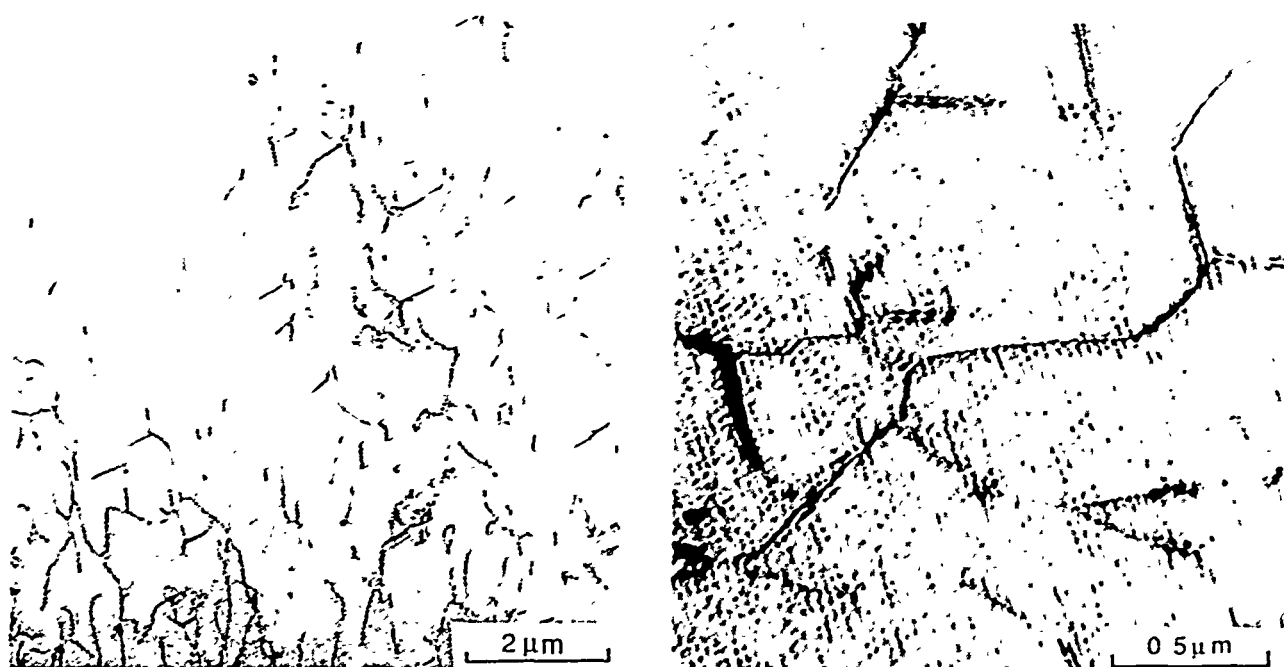


(b)

Figure 59. Higher magnification of the Fine Twin Lamellae Seen in Figure 58b: (a) Bright Field, and (b) Dark Field

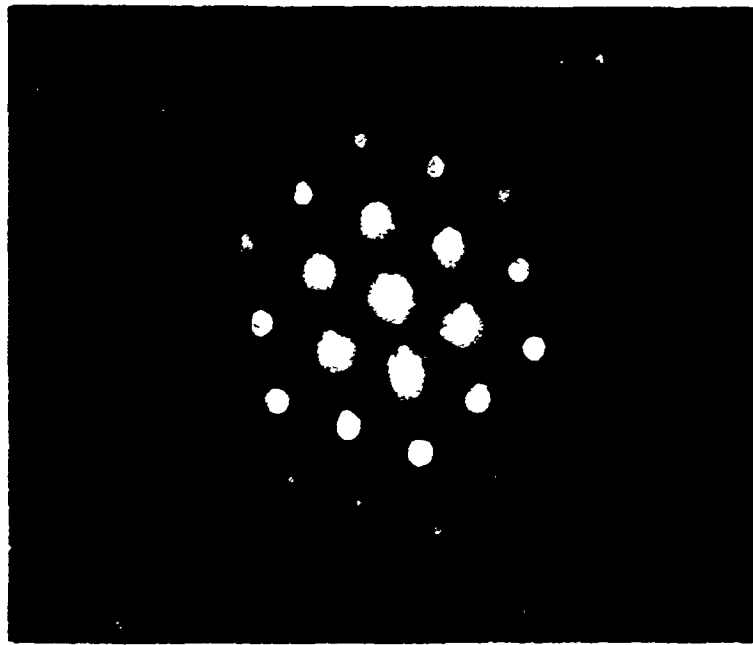


(a)

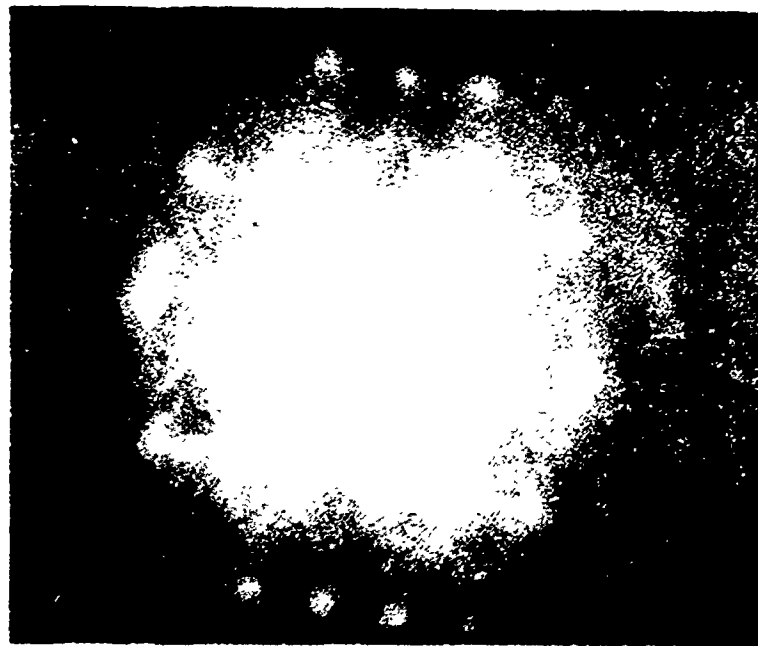


(b)

Figure 60. Alloy CT After Compression at Room Temperature: (a) Optical Micrograph, and (b) TEM Micrographs of Matrix (Region A) Showing a Tweed Structure



(a)



(b)

Figure 61. SAD of Matrix Region of Alloy CT as Shown in Figure 60 After Compression at Room Temperature Showing $\langle 111 \rangle$ Streaking Corresponding to the Tweed Structure: (a) $\langle 111 \rangle$ Zone Axis, and (b) $\langle 311 \rangle$ Zone Axis



(a)



(b)

Figure 62. TEM Micrographs of Alloy CT After Compression at Room Temperature Showing the Gamma Prime Morphologies at the Grain Boundaries: (a) Regions of Equiaxed Grains at Areas B and C Indicated in Figure 60a, and (b) Stringers at Area D of Figure 60a

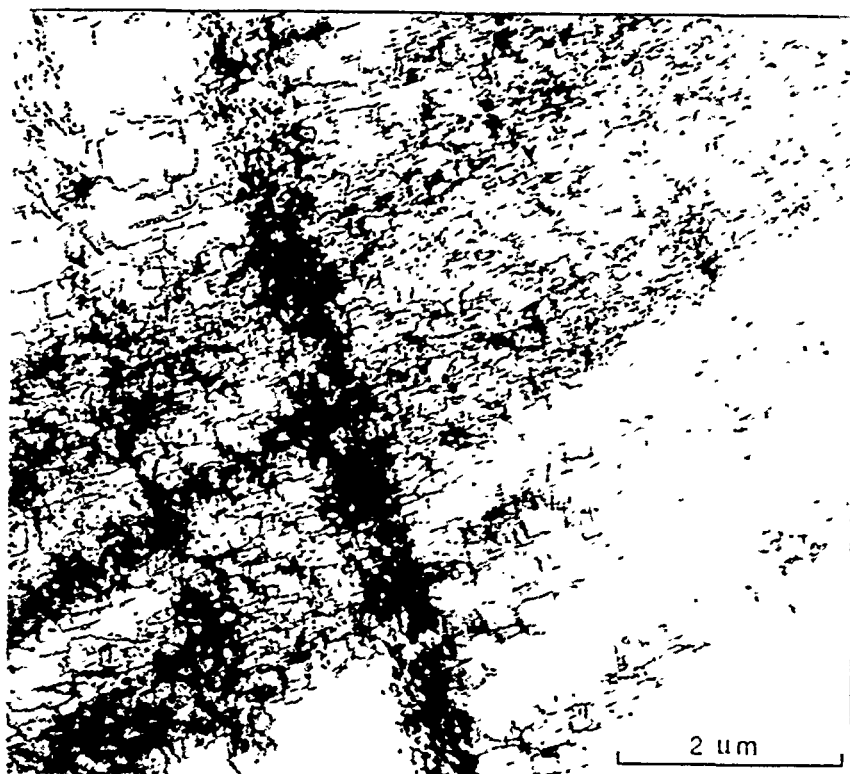


(a)



(b)

Figure 63. (a) Optical Micrograph, and (b) TEM Micrograph of Alloy CT After Compression at 760°C (1400°F) Showing the Gamma Prime at the Grain Boundaries and Randomly-Oriented, Elongated Gamma Prime in the Grain Interior



(a)



(b)

Figure 64. TEM of VIM Alloy AH, As Extruded + Heat Treatment of 2 Hrs/1050°C/Air Cool After Compression at Room Temperature to 0.2% Strain. (a) Micrograph of matrix showing dislocation bands. (b) Higher magnification micrograph of stringer of a Hf-rich hexagonal blocky phase with numerous stacking faults.

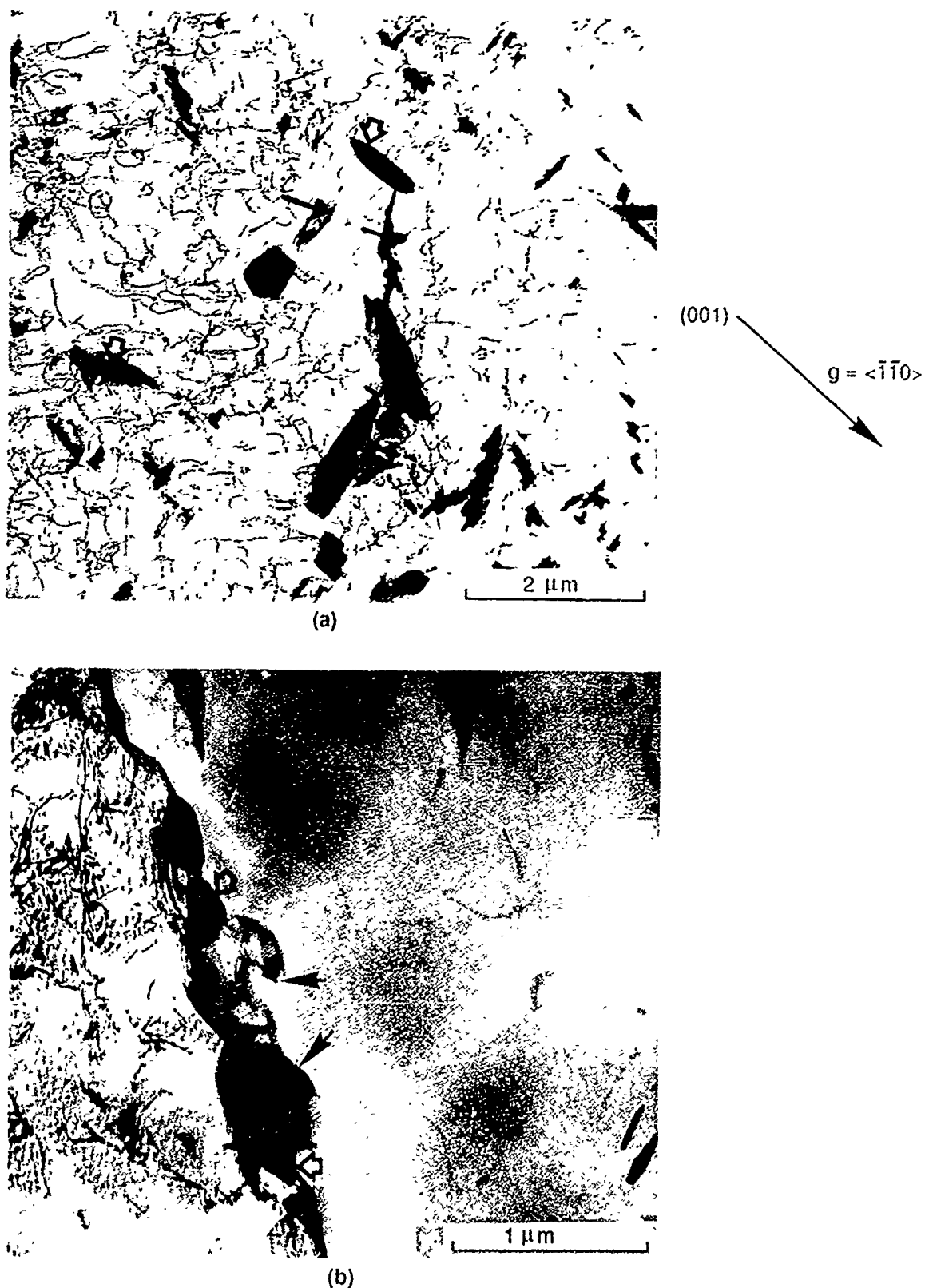
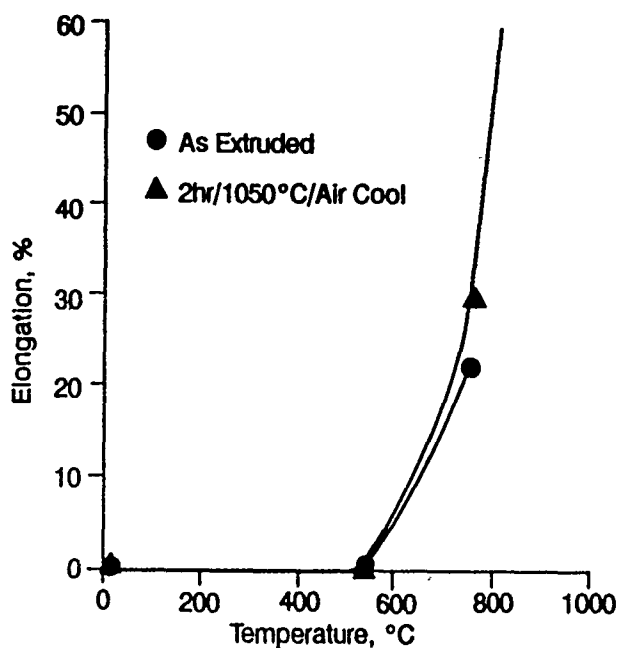
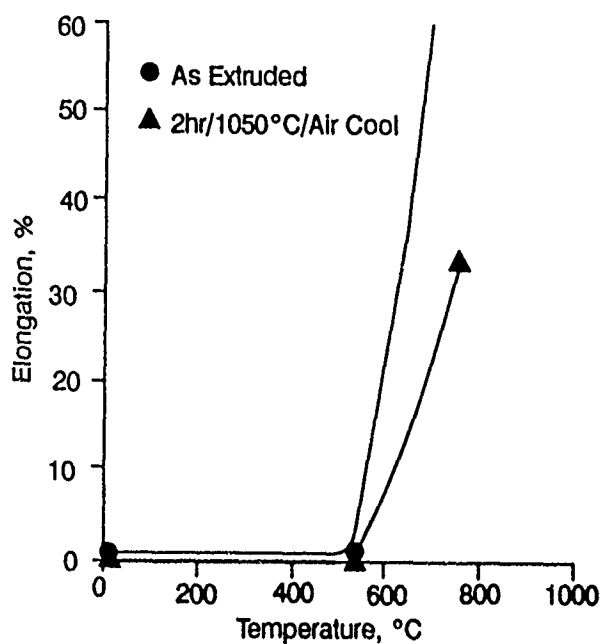


Figure 65. TEM of VIM Alloy AH, As Extruded + Heat Treatment of 2 Hrs/1050°C/Air Cool After Compression at 760°C (1400°F). (a) Micrograph of matrix containing a small amount of Hf-rich rod-shaped precipitates and a high dislocation density. (b) Higher magnification micrograph of grain boundary showing small Hf-rich particles (open arrows) and a disordered fcc (Al) blocky phase (solid arrows).

(a) Alloy A2: Ni-32Al-29Co



(b) Alloy A3: Ni-32Al-25Co



(c) Alloy C2: Ni-31 Al-16Co

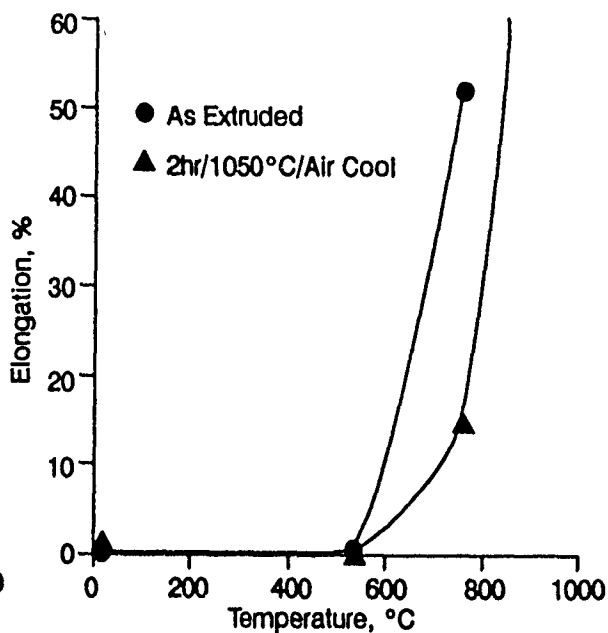
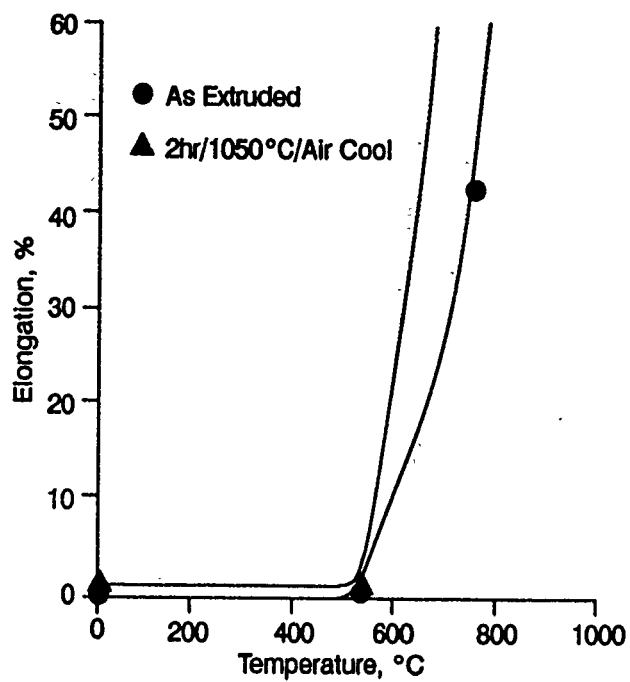


Figure 66. Tensile Elongation Versus Temperature Curves for Phase II NiAl Alloys. Specimens were tested as-extruded (●) and after a recrystallization heat treatment for 2 hrs/1050°C/Air Cool (▲).

(d) Alloy C3: Ni-30 Al-15 Co



(e) Alloy B2: Ni-30Al-25Co

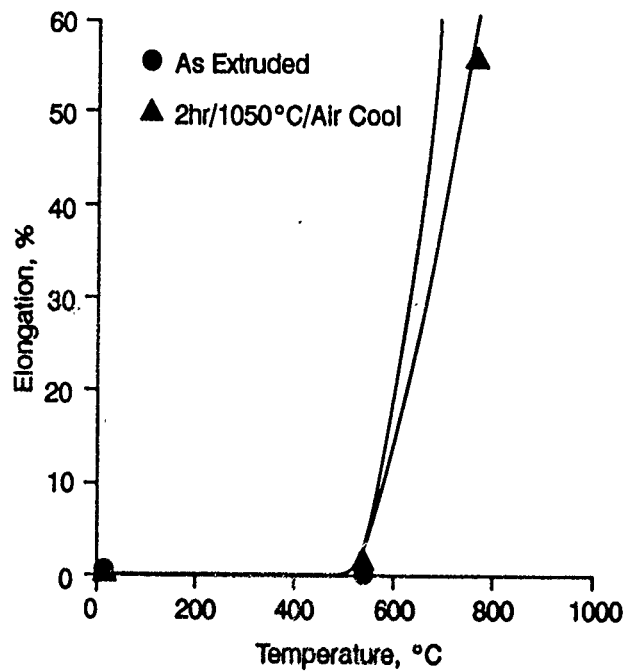


Figure 66 (continued)

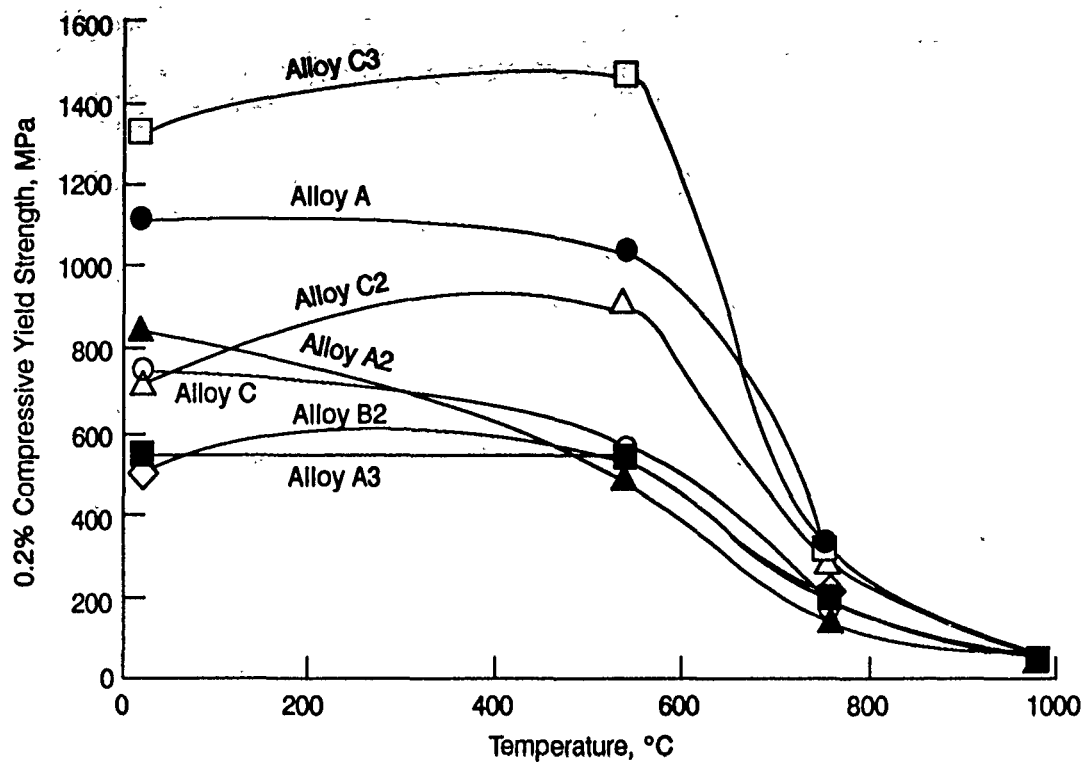


Figure 67. 0.2% Compressive Yield Strength Versus Temperature of Selected Phase II Ternary Alloys

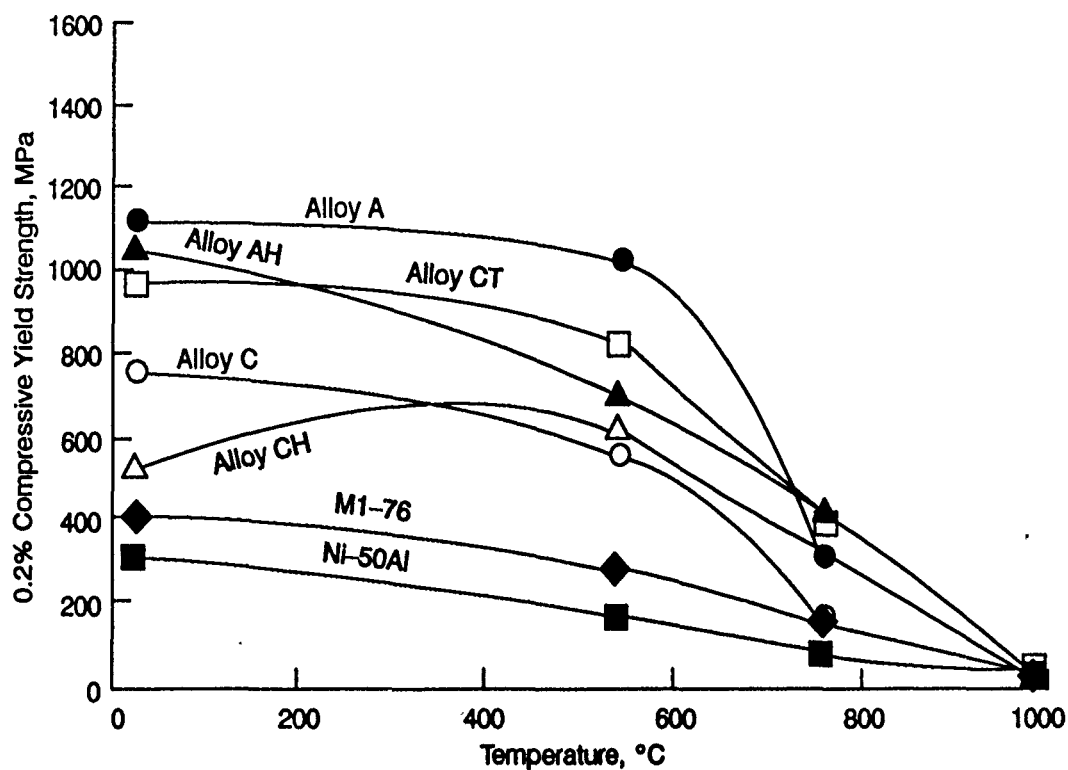


Figure 68. 0.2% Compressive Yield Strength Versus Temperature of Selected Phase II Alloys Formulated for Strengthening

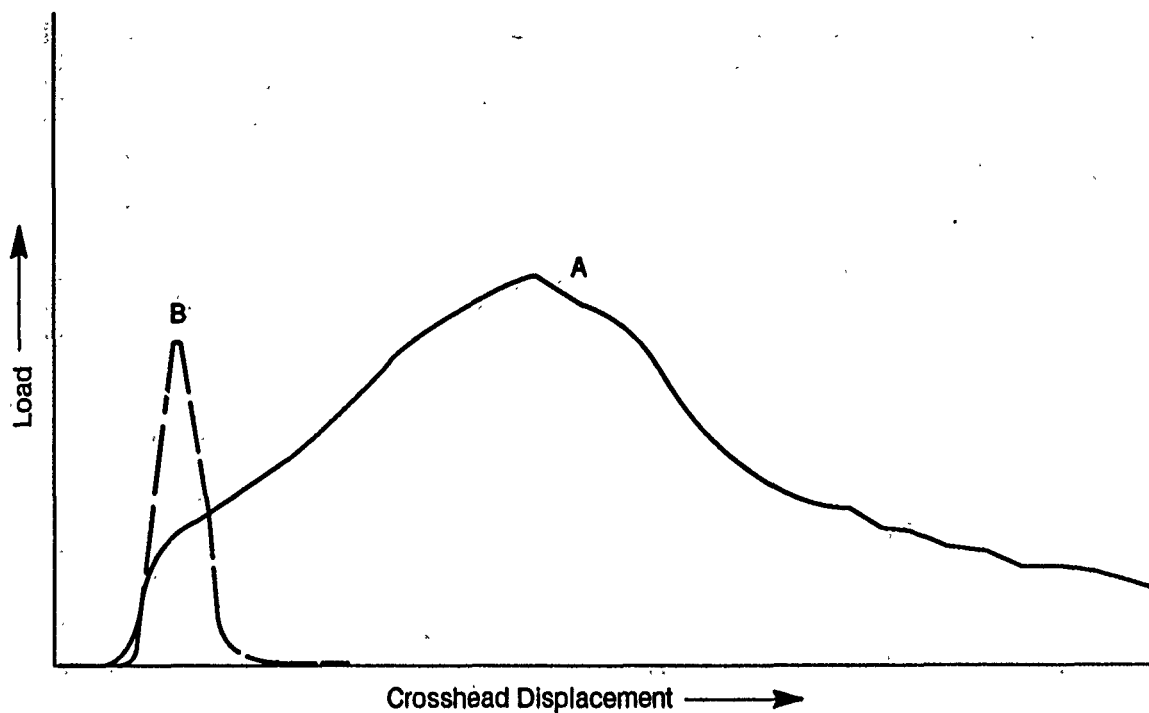


Figure 69. Load Versus Load Point Displacement Traces of Chevron-Notched Precracked Specimens Tested at 20°C. (A): A cobalt-modified martensitic alloy (B2). Note the apparent yielding during loading and slow rates of the load drop as the crack propagates. (B) A nonmartensitic (stoichiometric) binary alloy.

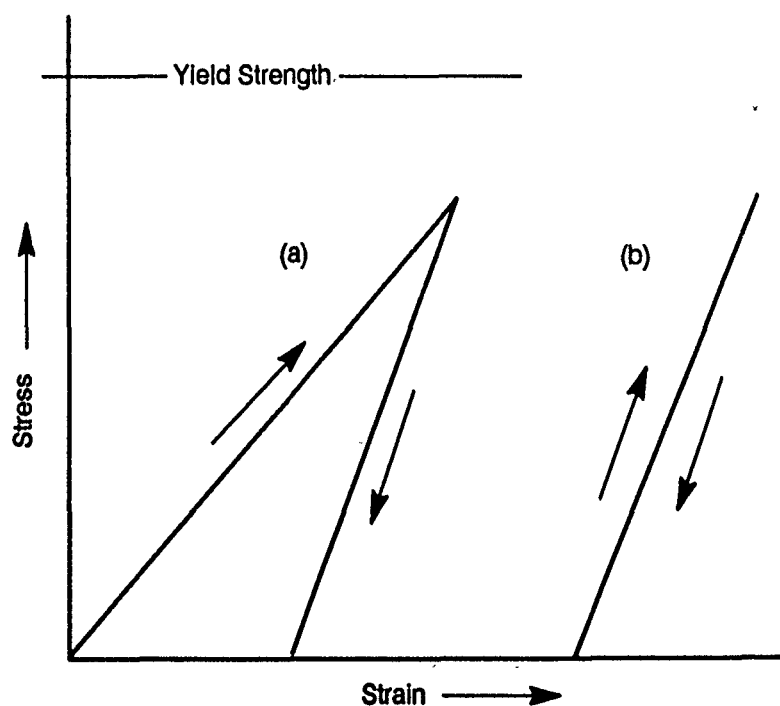


Figure 70. Stress-Strain Curve for: (a) a Martensitic Alloy that Undergoes Preyield Deformation, and (b) an Alloy that Does Not

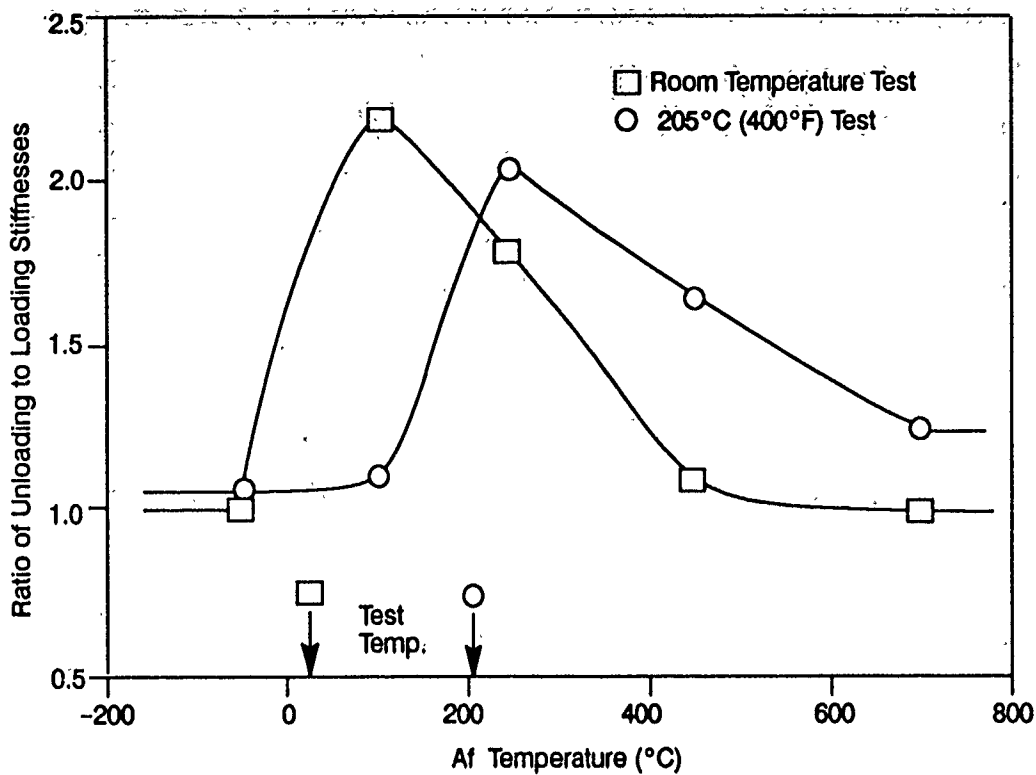


Figure 71. Ratio of Unloading/Loading Stiffness Versus A_f Temperature for Various Martensitic NiAlCo Alloys. Note the abrupt change in stiffness ratio when the test temperature is near the A_f temperature of the material.

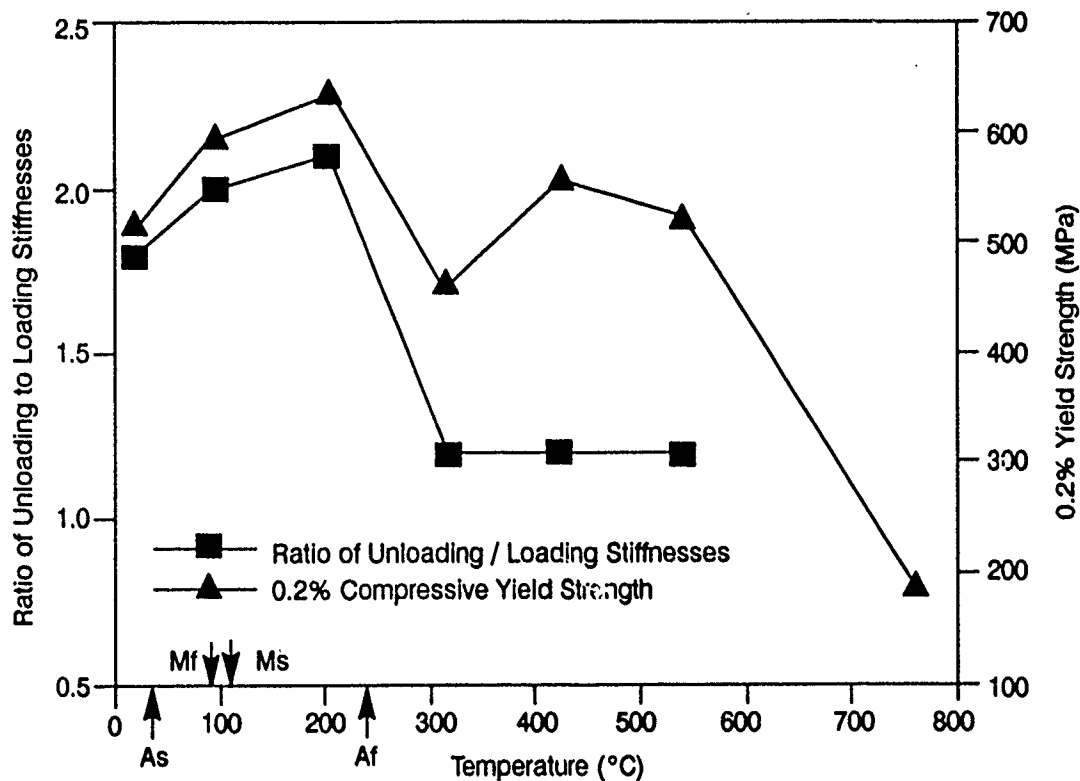


Figure 72. Ratio of Unloading/Loading Stiffness and 0.2% Compressive Yield Strength Versus Temperature for Alloy B2. Note the abrupt changes near the A_f temperature.

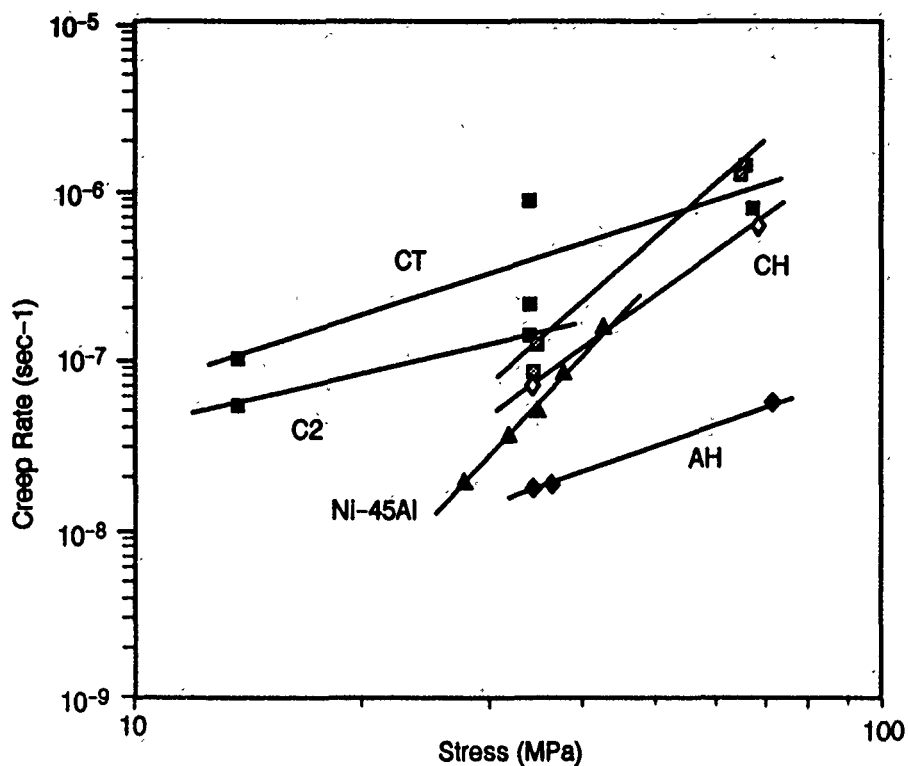


Figure 73. Compressive Creep Strength Versus Secondary Creep Rate at 760°C (1400°F) of Selected Alloys

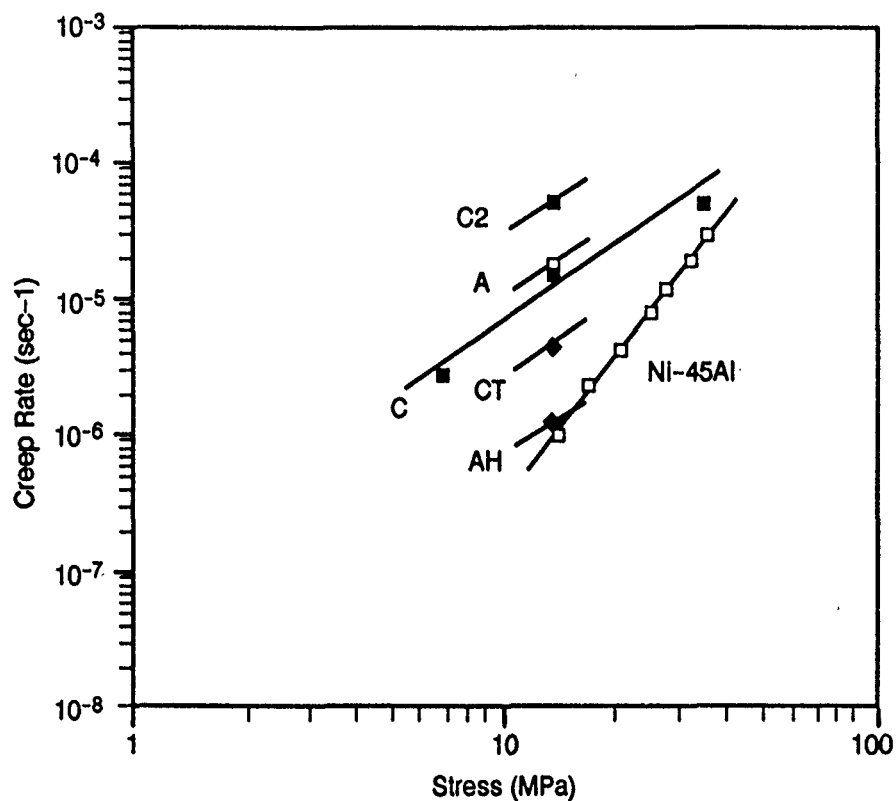
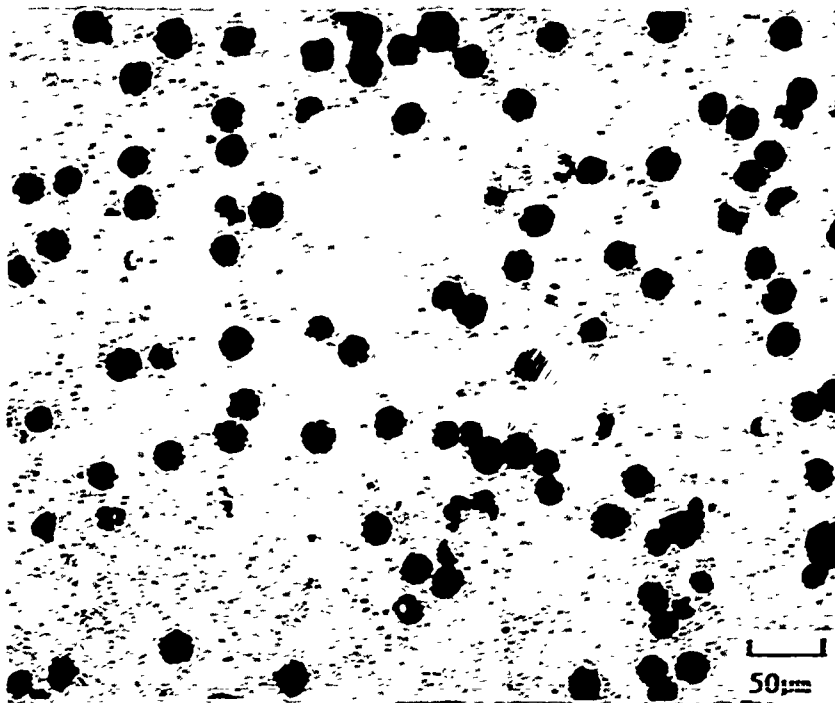
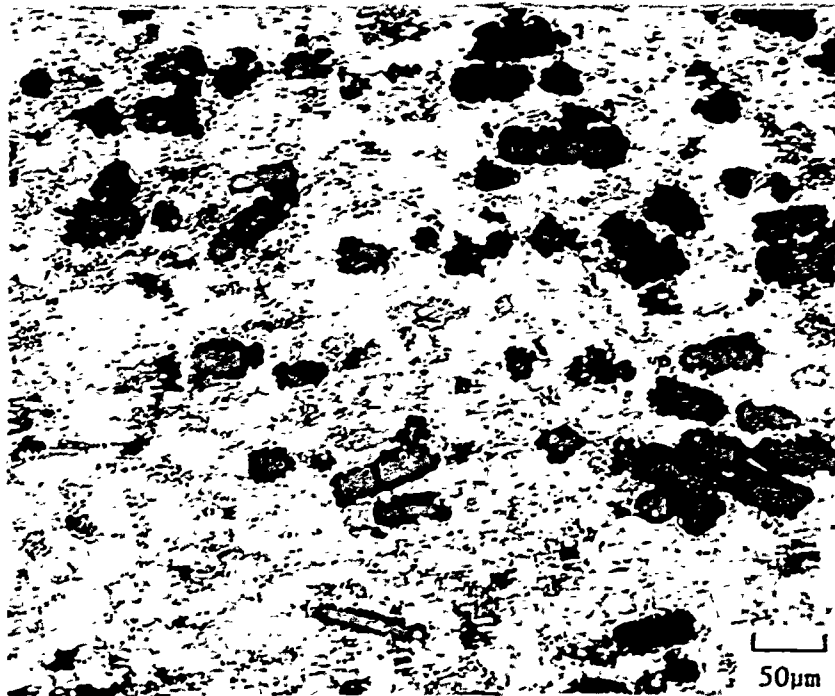


Figure 74. Compressive Creep Strength Versus Secondary Creep Rate at 980°C (1800°F) of Selected Alloys

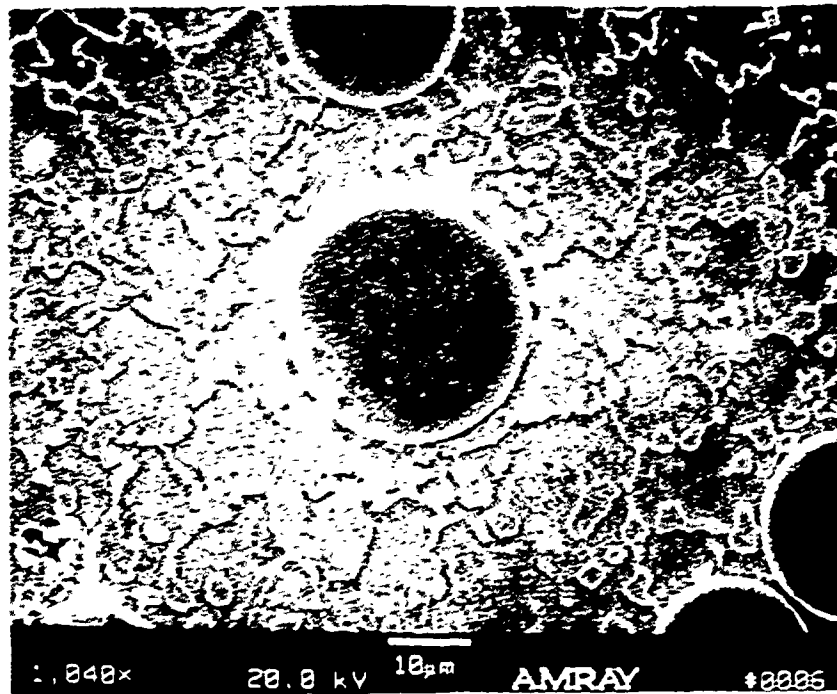


(a)



(b)

Figure 75. Optical Micrographs of Ni-29 Al-21 Co + PRD-166 Mixture. Note the fine grain size and uniform reinforcement distribution. (a) Transverse section, and (b) longitudinal section.



(a)



(b)

Figure 76. Scanning Electron Micrographs of Ni-29 Al-21 Co + PRD-166 Mixture. Note the martensitic structure of the NiAlCo matrix and the blocky gamma prime at the grain boundaries. (a) Transverse section showing no reaction zone between the reinforcement and the matrix. (b) Longitudinal section showing evidence of fiber breakup and void formation at the ends of the fibers during extrusion.

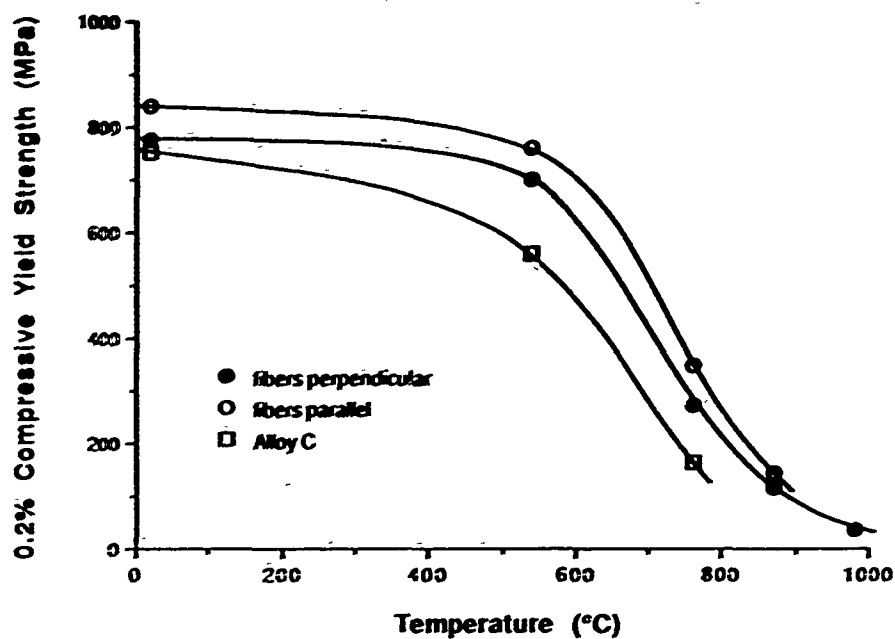


Figure 77. 0.2% Compressive Yield Strength of the Phase III Material Tested with the Stress Direction Both Parallel and Perpendicular to the Fiber/Extrusion Axis. Alloy C (Ni-29 a/o Al-21 a/o Co) is the matrix alloy.

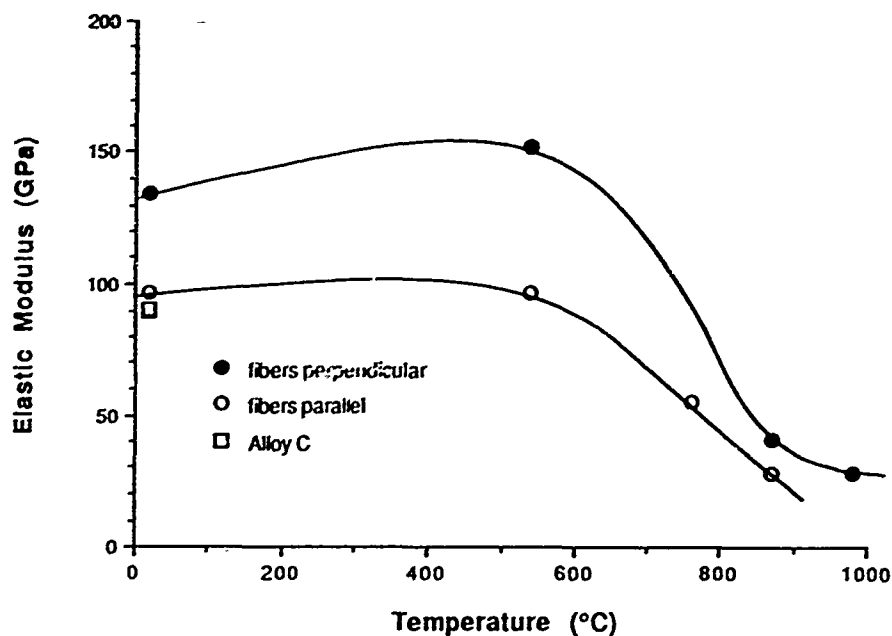


Figure 78. Elastic Modulus of the Phase III Material Tested in Compression with the Stress Direction Both Parallel and Perpendicular to the Fiber/Extrusion Axis. Alloy C (Ni-29 a/o Al-21 a/o Co) is the matrix alloy.

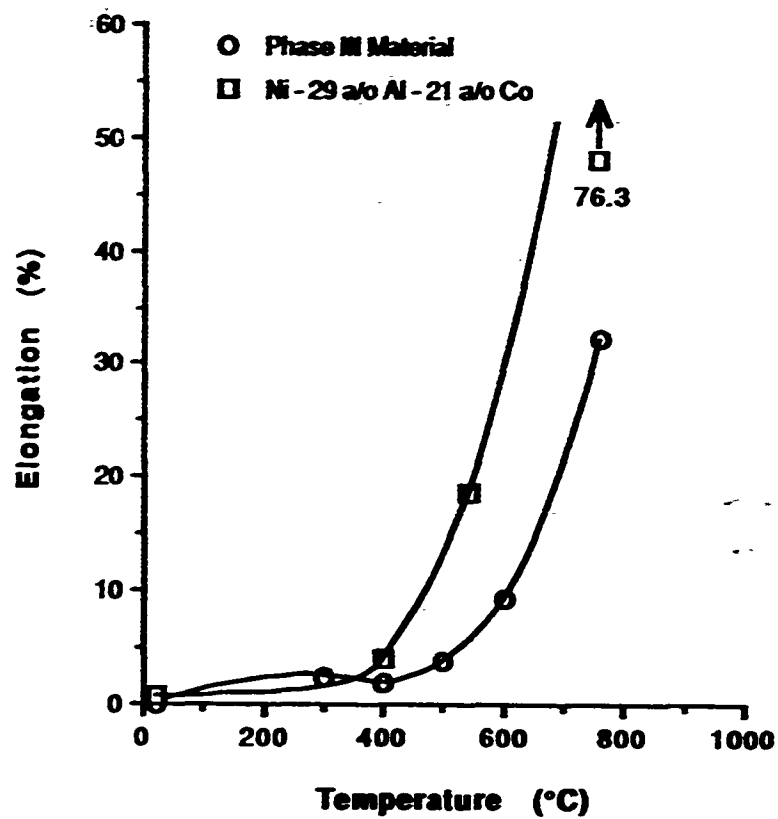
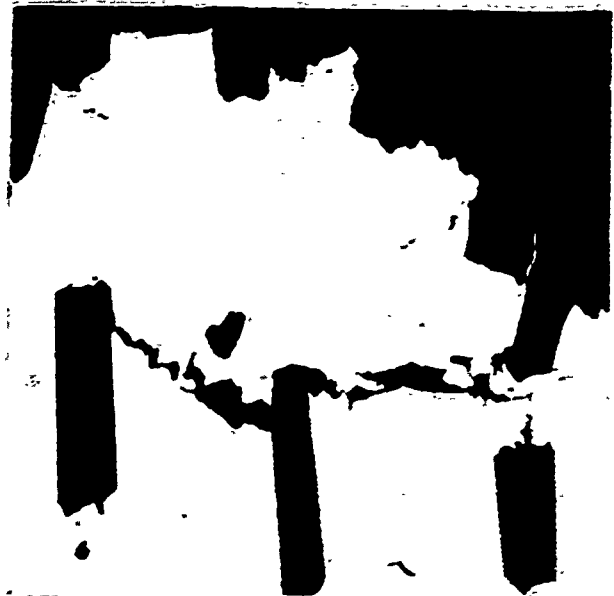


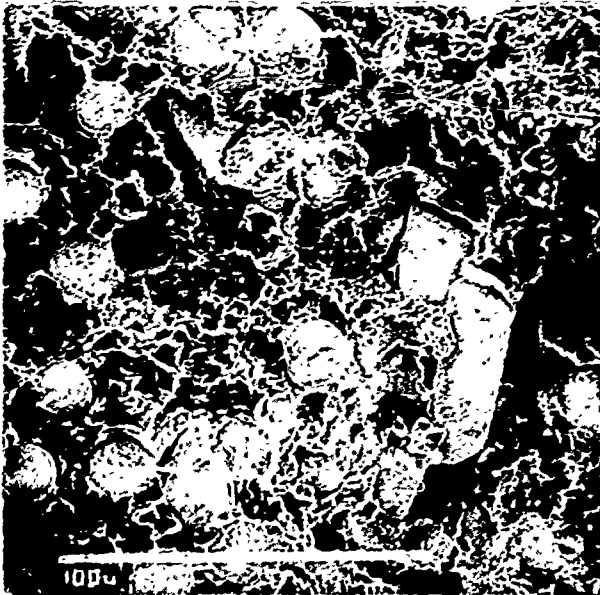
Figure 79. *Elongation Versus Temperature of the Phase III Material Tested Parallel to the Extrusion Axis Compared to the Matrix Material (Ni-29 a/o Al-21 a/o Co) in Extruded Powder Form*



(a)



(b)



(c)



(d)

Figure 80. Tensile Fracture Surfaces of the Phase III Material at Room Temperature (a through c) and 760°C (d)

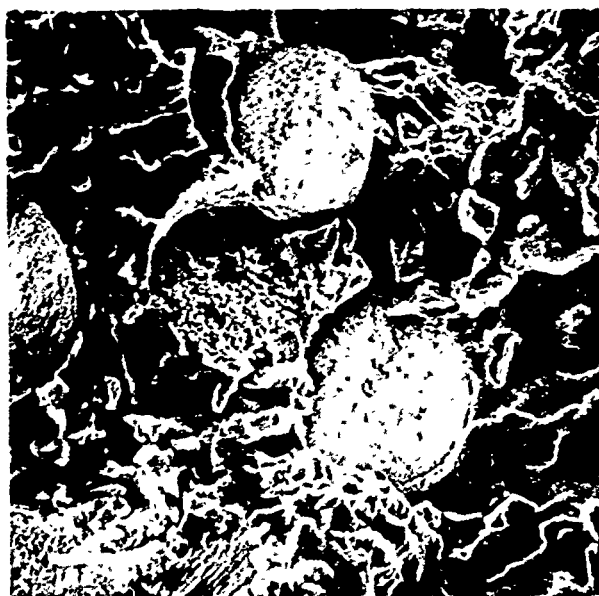
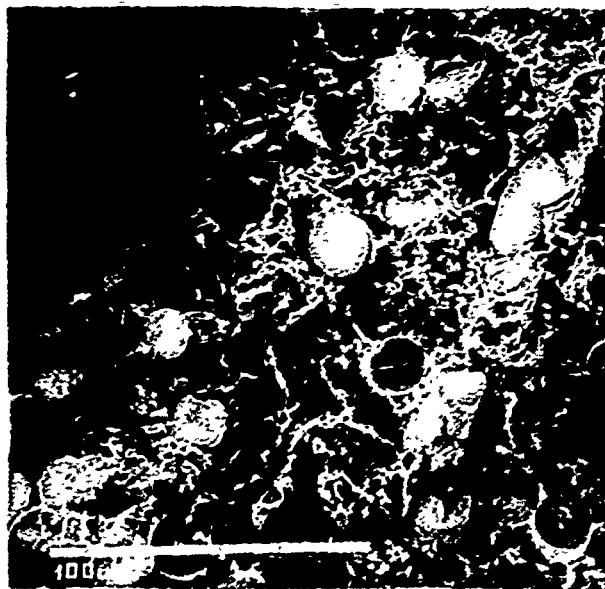


Figure 81. Room Temperature Fracture Toughness Specimen Fracture Surfaces of the Phase III Material Showing Fiber Breakage and Limited Fiber Pull-Out

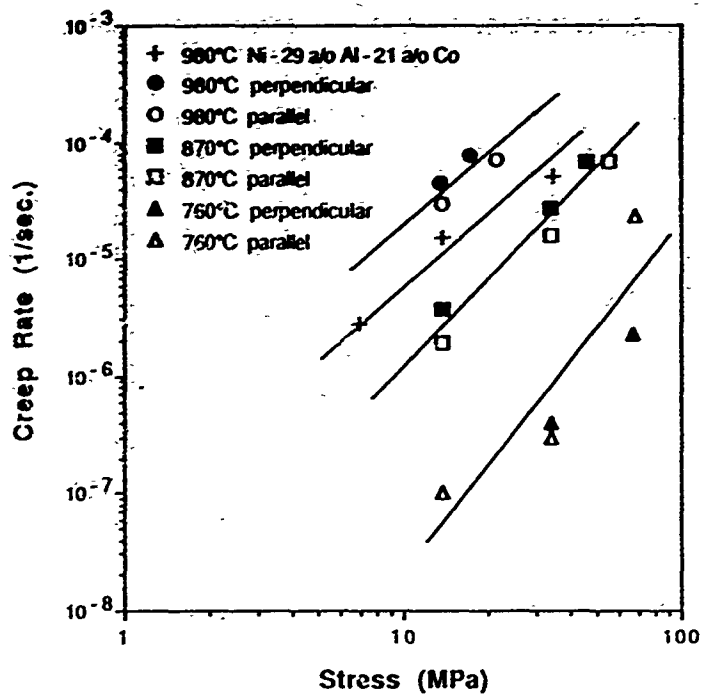


Figure 82. Compressive Creep Rate as a Function of Applied Stress of the Phase III Material at Different Temperatures Tested with the Stress Direction Both Parallel and Perpendicular to the Fiber/ Extrusion Axis. Ni-29 a/o Al-21 a/o Co is the matrix material.

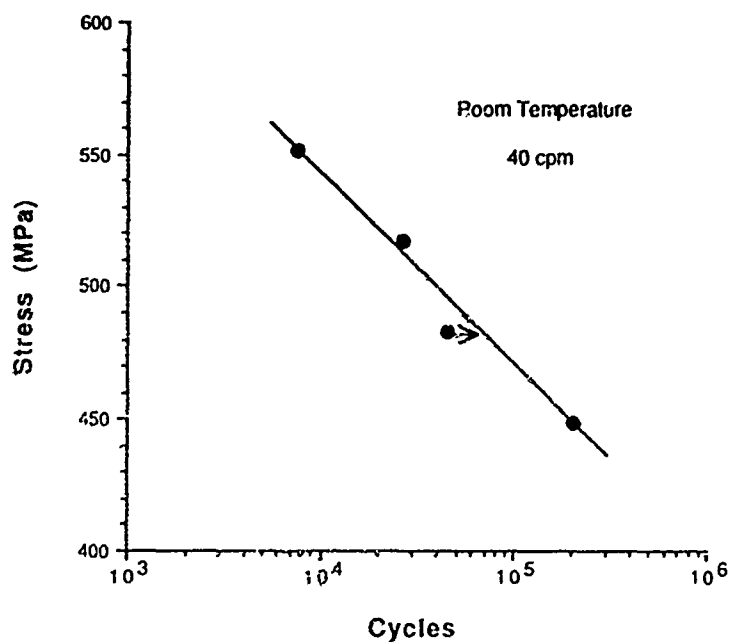
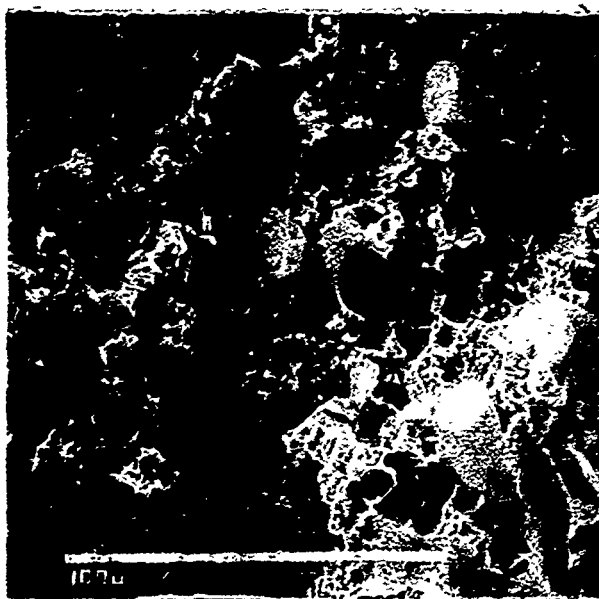
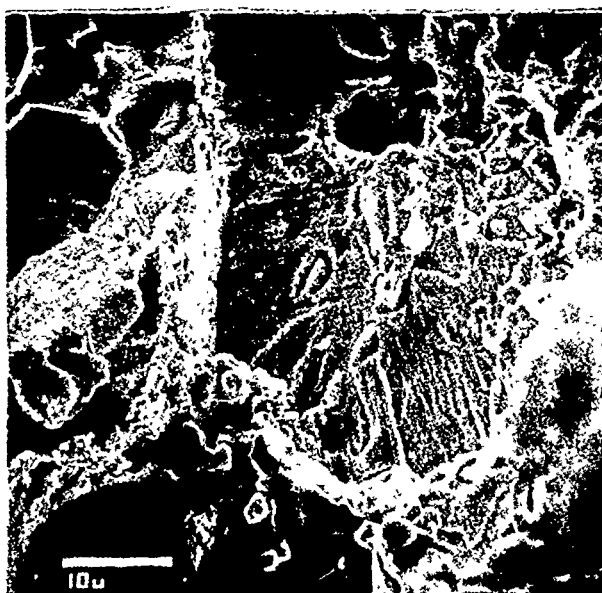


Figure 83. Room Temperature Low Cycle Fatigue Behavior of the Phase III Material. The stress was cycled between zero and the maximum stress at 40 cpm.



(a)



(b)



(c)

Figure 84. Fracture Surface of Room Temperature LCF Specimen of the Phase III Material. Note the chisel-edge fracture of the gamma prime precipitates (b and c)

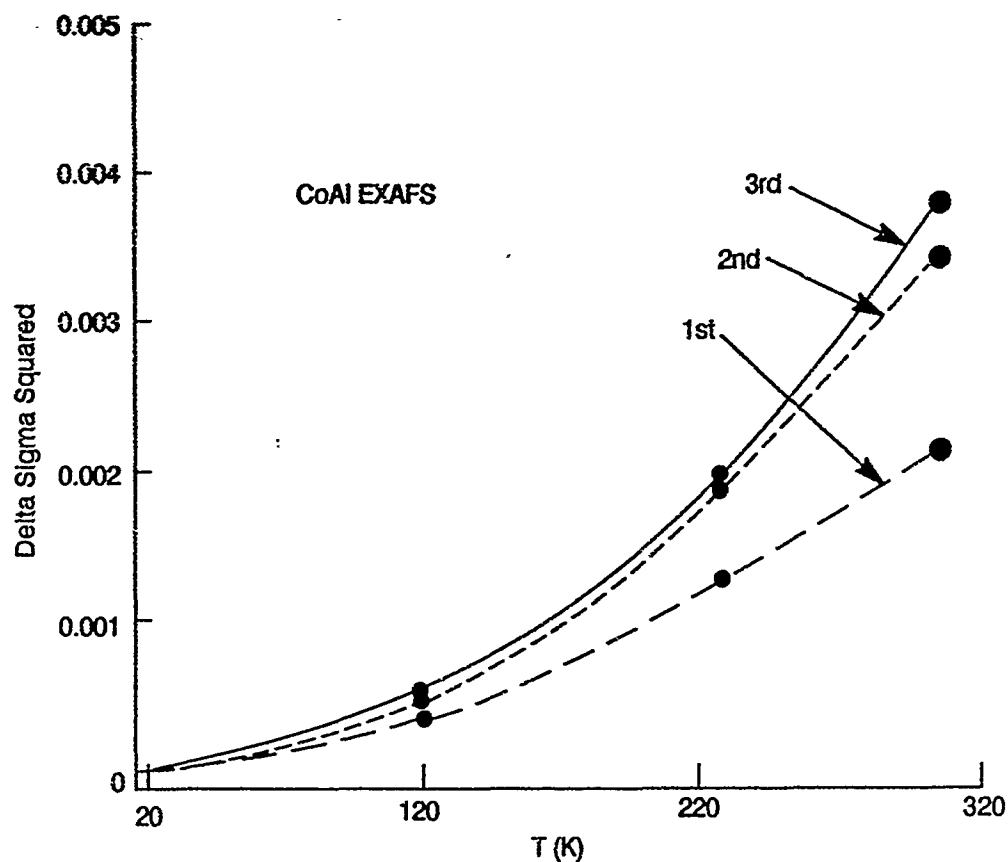


Figure 85. Plot from EXAFS of $\Delta\sigma^2$ Versus Temperature for the First, Second and Third Nearest-Neighbor Bonds for CoAl

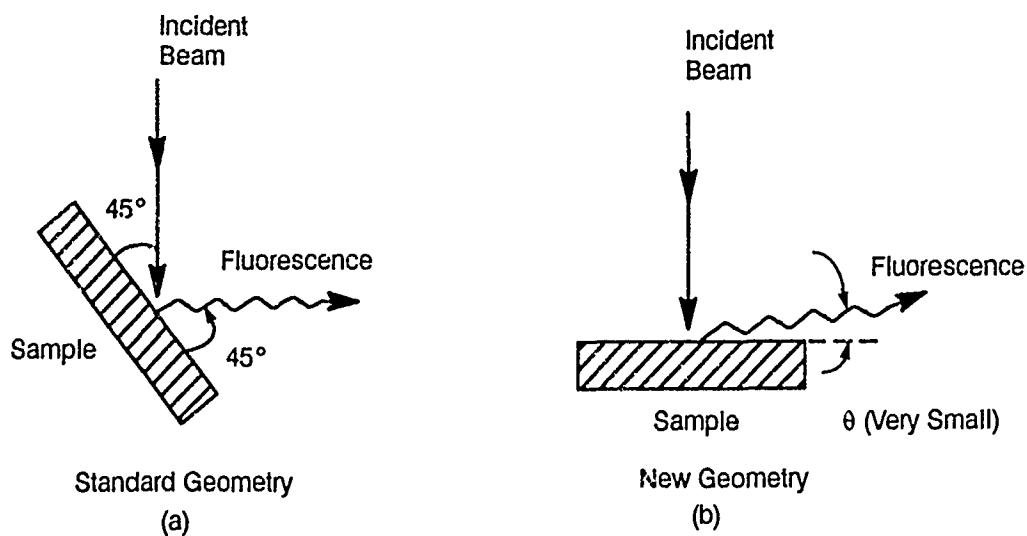


Figure 86. Comparison of Standard Geometry (a) and the Improved Geometry (b) for Performing EXAFS on Bulk Samples Using Fluorescence Detection

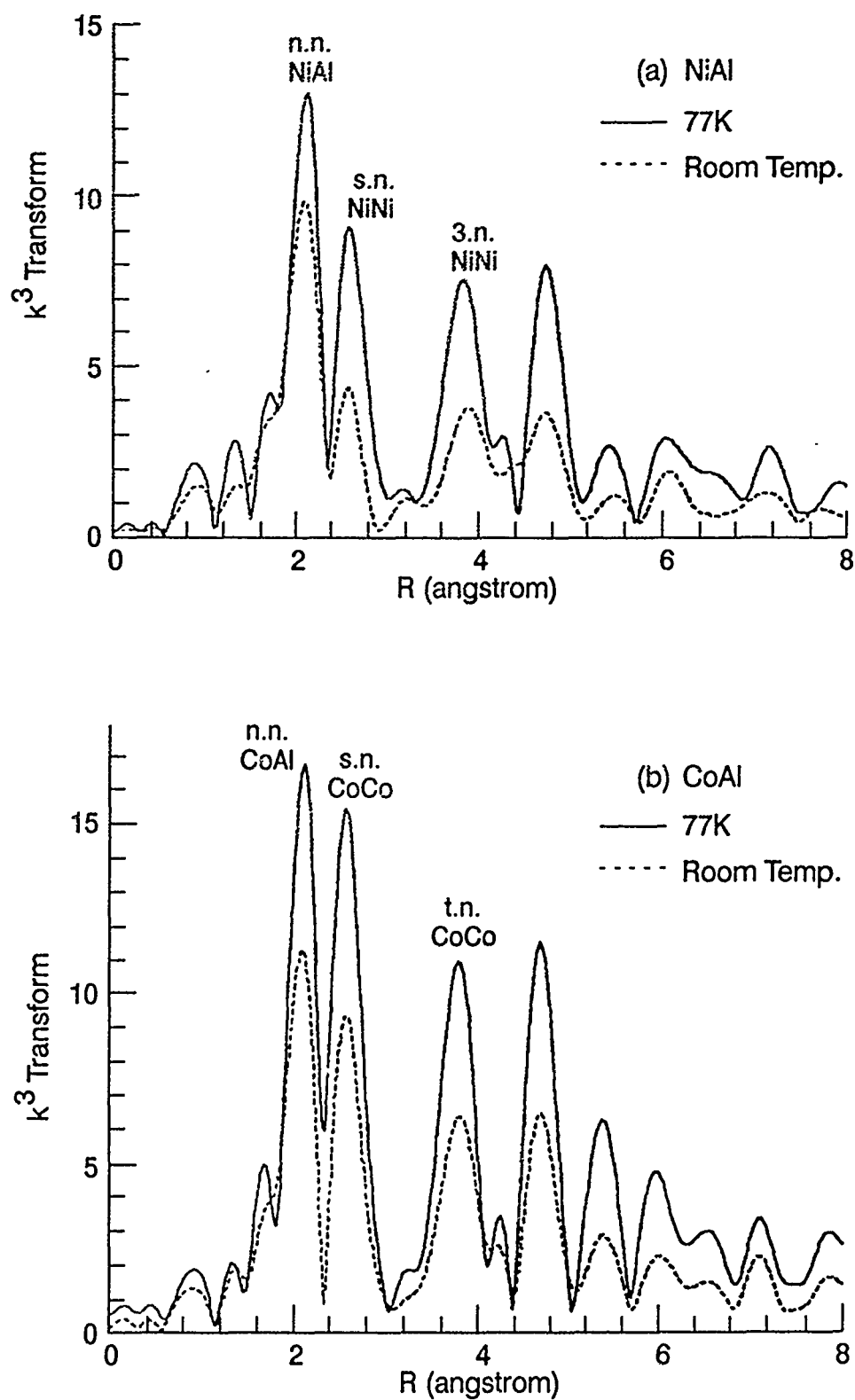


Figure 87. k^3 Transforms for (a) Ni-Edge in NiAl and (b) Co-Edge in CoAl, Both at 7°K

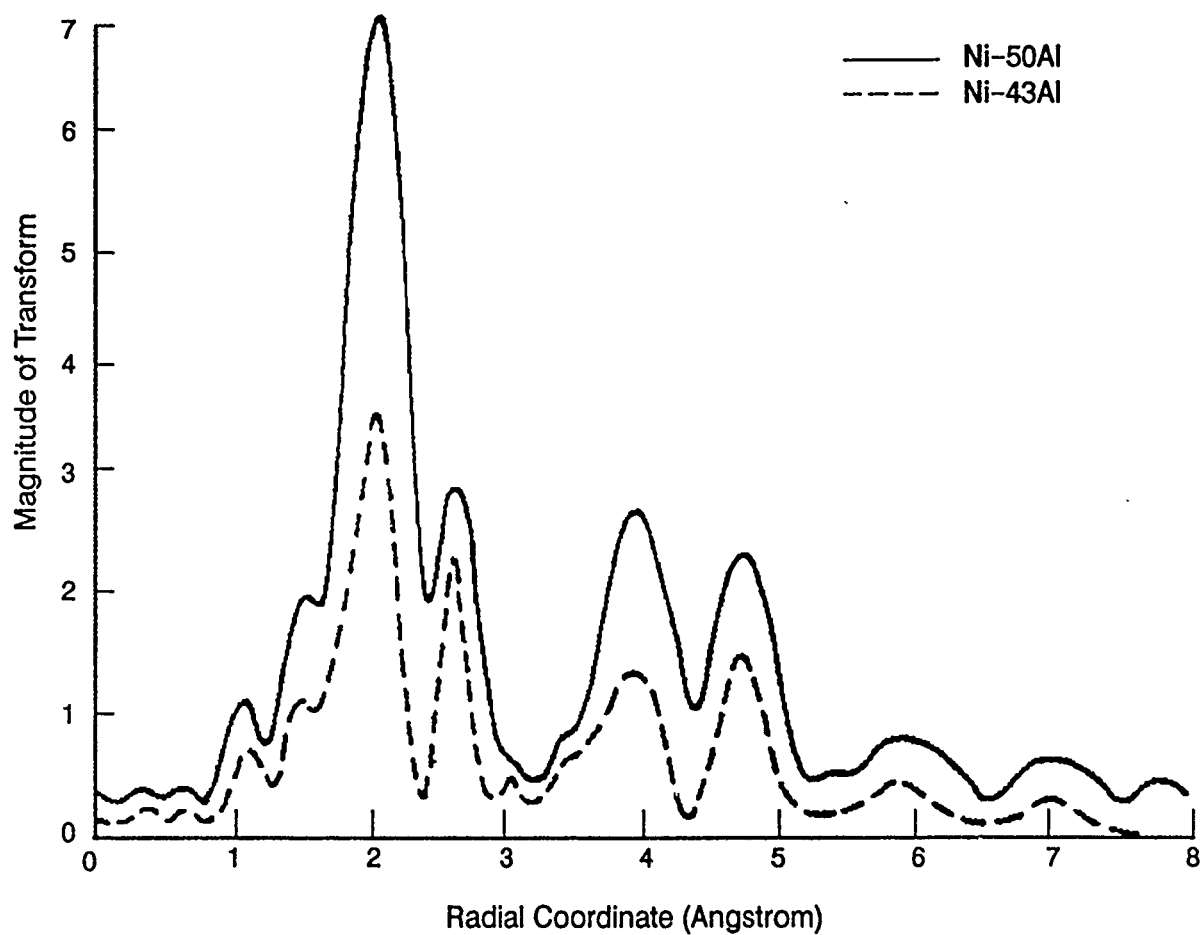


Figure 88. k^3 Transform of EXAFS Data for Ni-50Al and Ni-43Al. The reduced amplitude for the Ni-43Al alloy is indicative of structural disorder in the material.

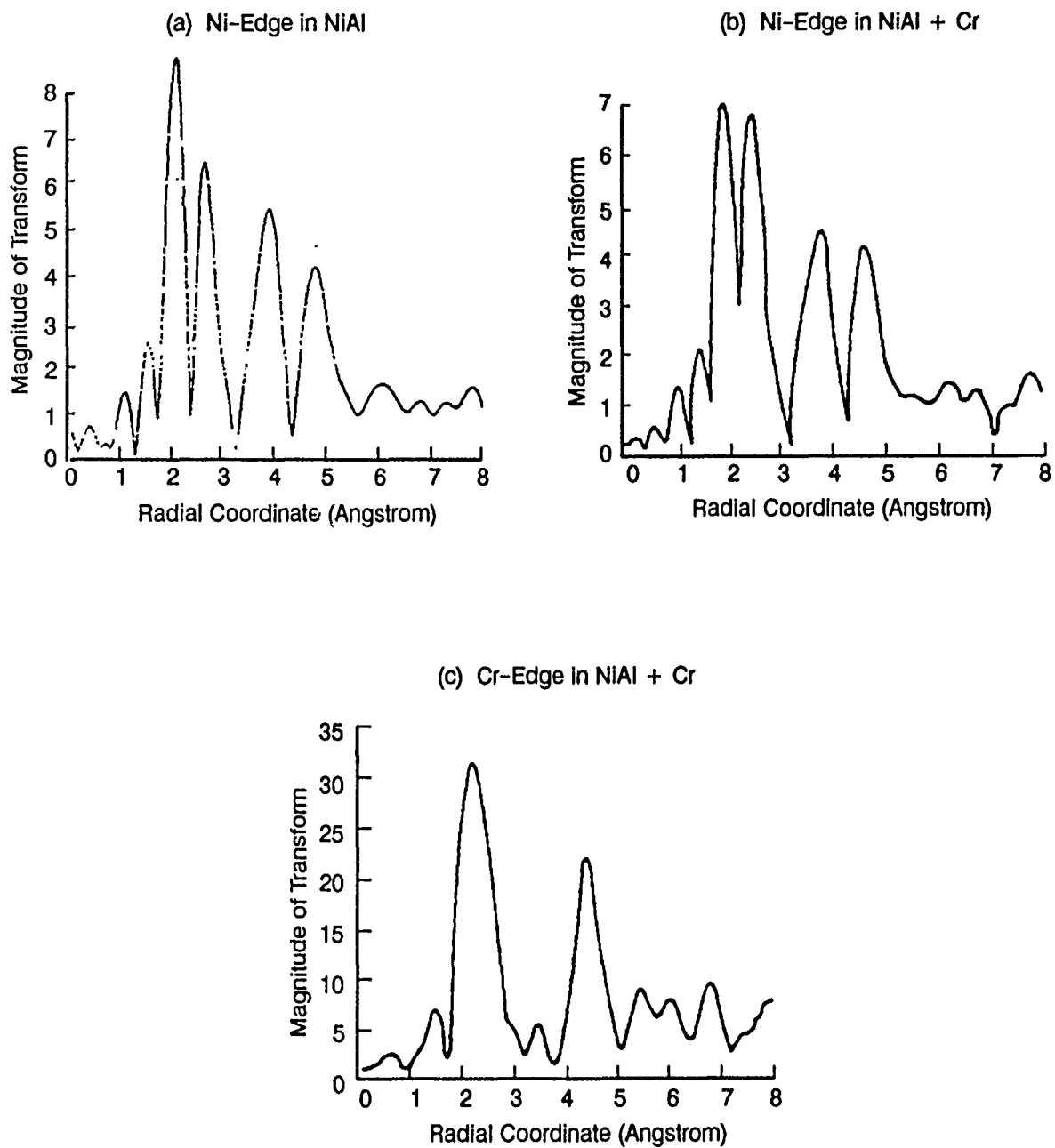


Figure 89. k^3 Transforms of EXAFS Data for: (a) the Ni-Edge in Ni-50Al, (b) the Ni-Edge in Ni-42Al-6Cr, and (c) the Cr-Edge in Ni-42Al-6Cr. Addition of Cr to NiAl reduces the first nearest-neighbor bond strength and the Cr atoms are seen to occupy Al sites.

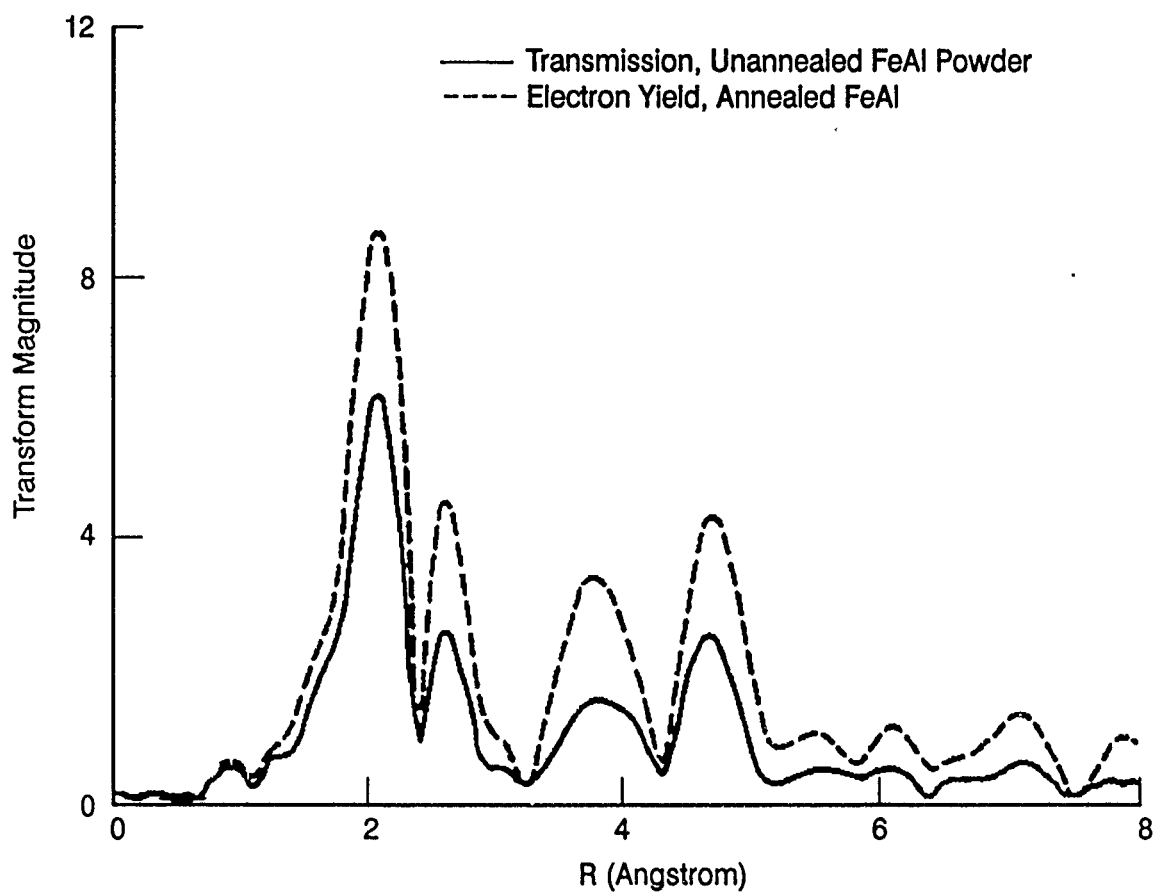


Figure 90. Comparison of EXAFS Spectra from Annealed and Cold-Worked FeAl. Note the decreased amplitude in the cold-worked case indicative of disorder.

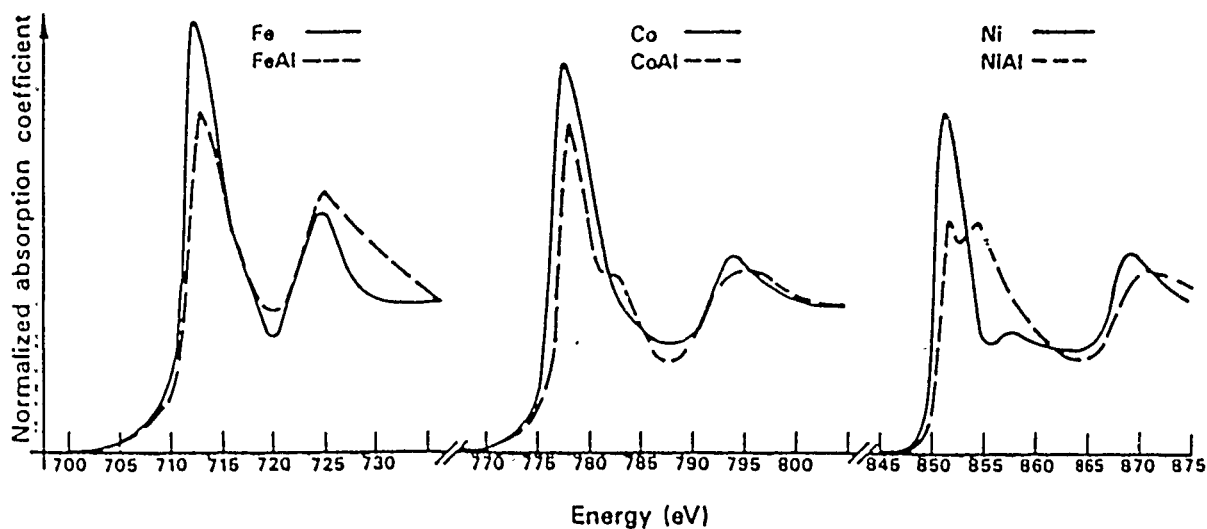


Figure 91. $L_{3,2}$ Edge XANES Data from EELS Measurements. The splitting of the transition metal L_3 and L_2 edge white lines becomes more pronounced going from FeAl to CoAl to NiAl, indicating a filling of the third band as electrons are added across the series. It also appears that the effect of the Al in CoAl is to increase the Co occupied states (References 35 and 36); this is not seen in the FeAl or NiAl.

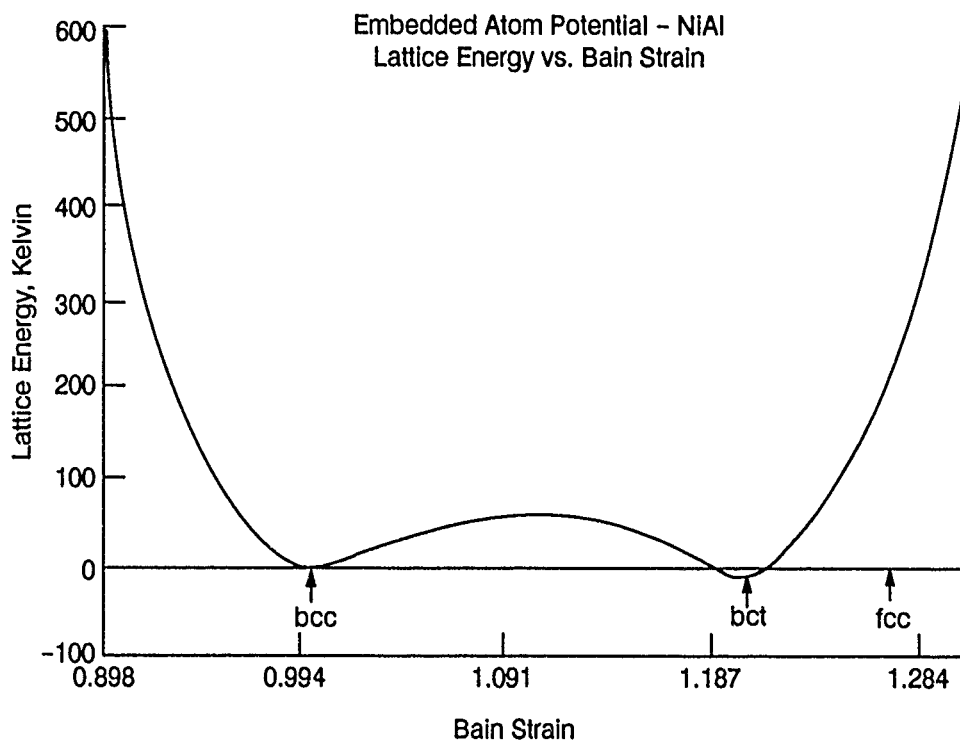


Figure 92. Lattice Energy Versus Bain Strain for NiAl Using the Embedded Atom Method

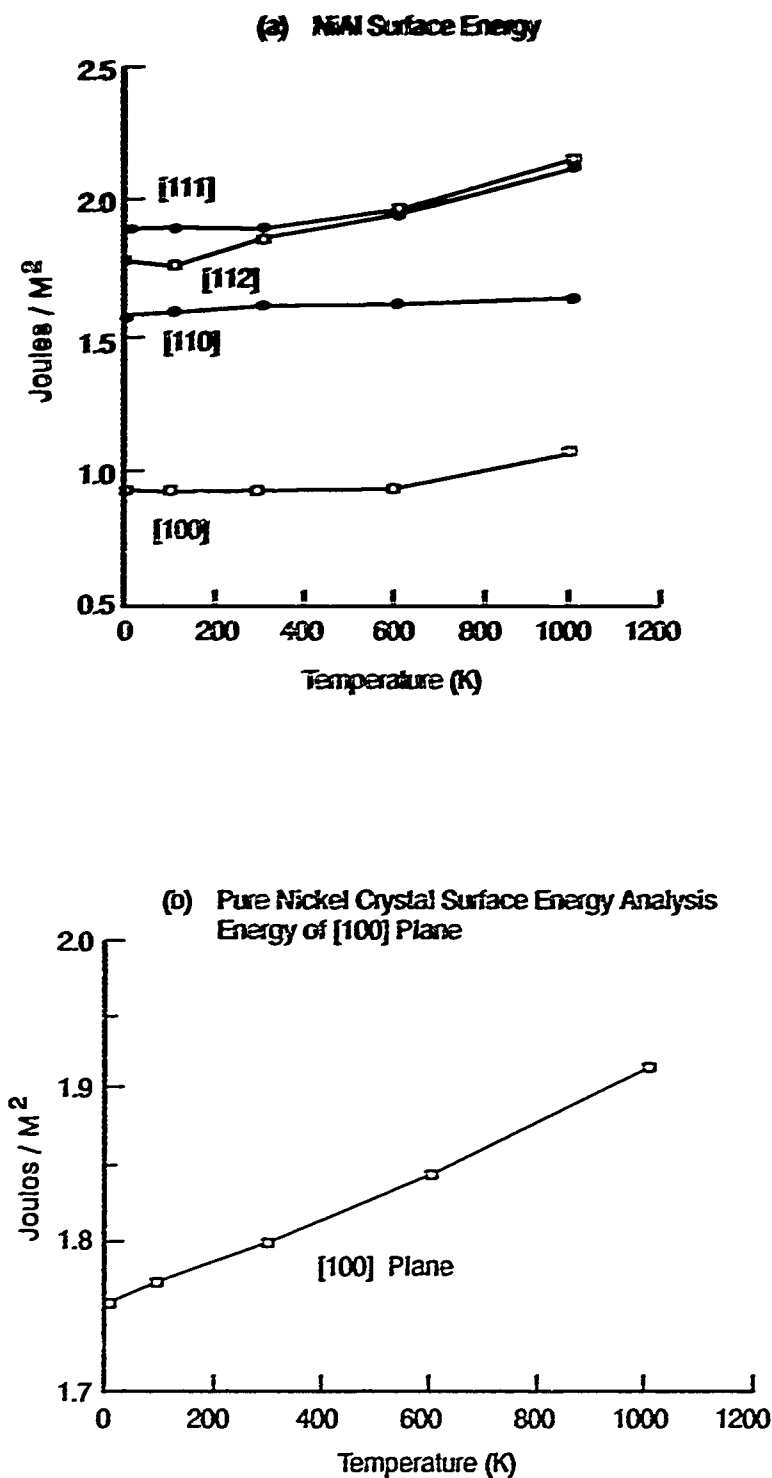


Figure 93. Surface Energies (γ) of. (a) NiAl, and (b) Ni as Calculated from the Embedded Atom Method Simulation Arrays

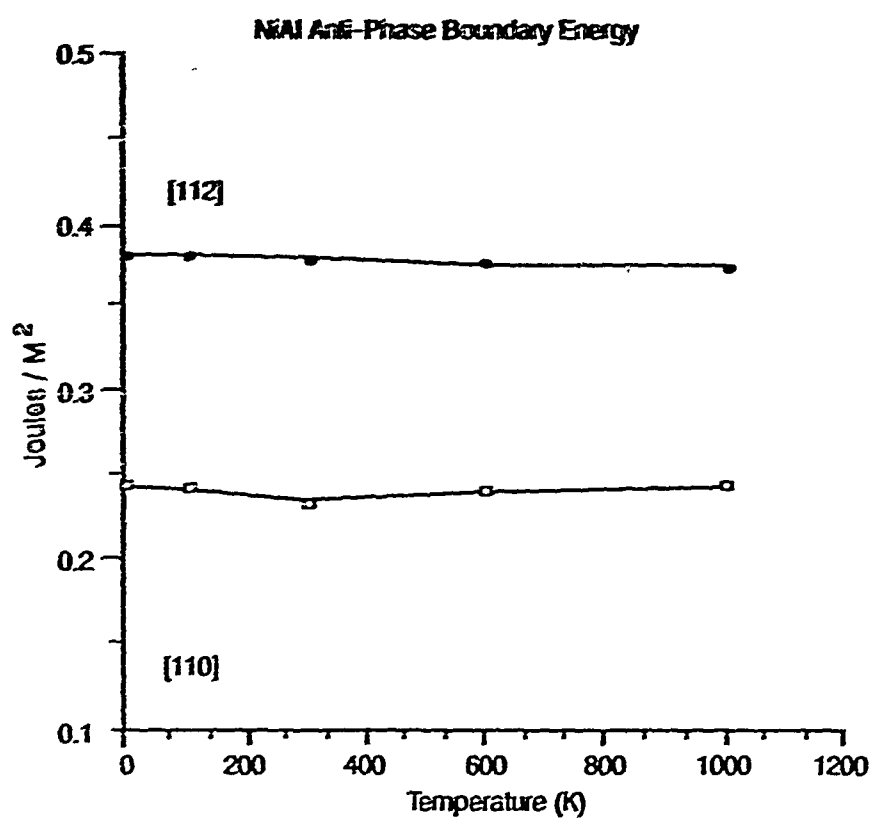


Figure 94. Anti-Phase Boundary Energy of NiAl as Calculated from the Embedded Atom Method Simulation Arrays

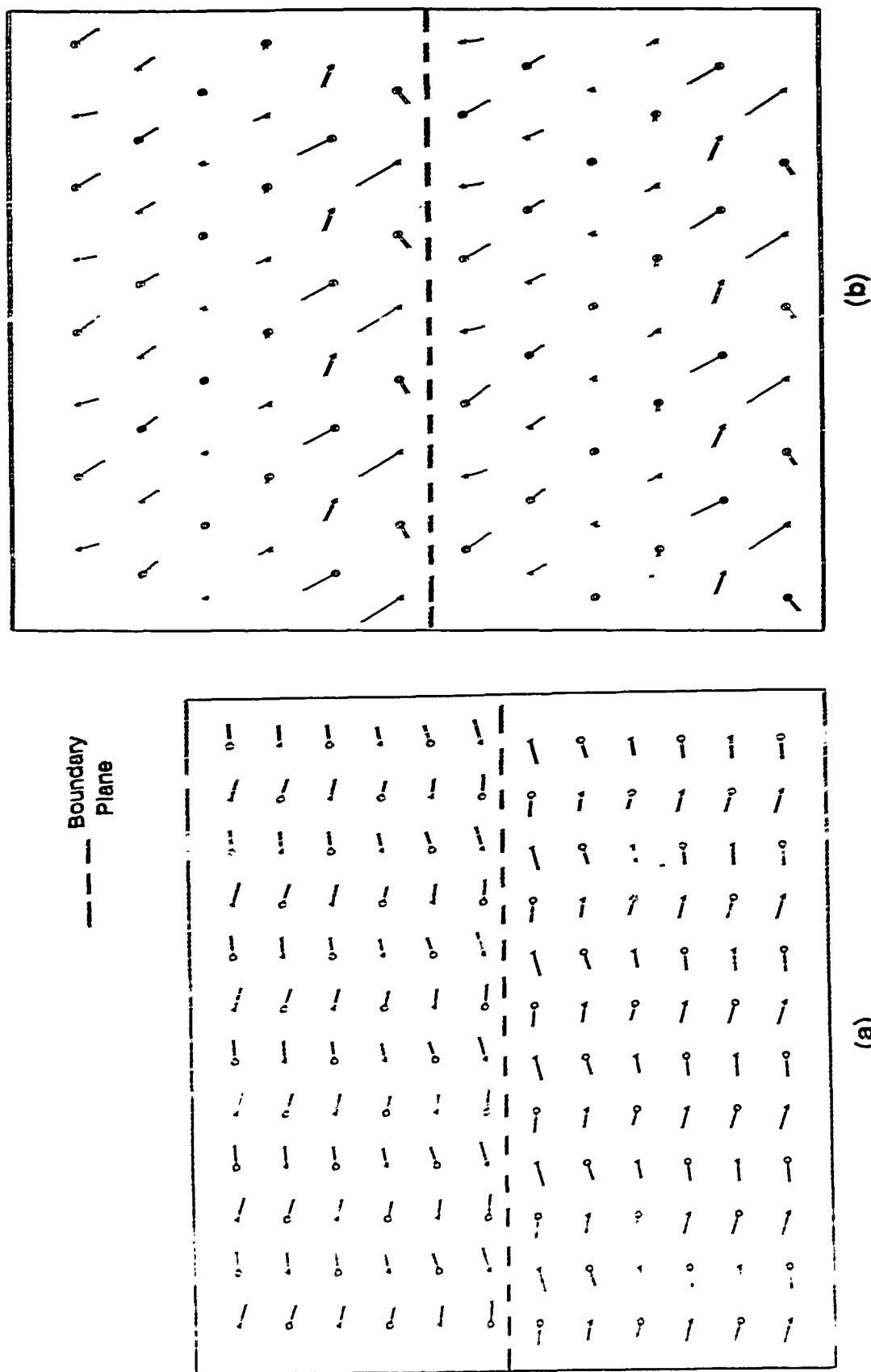


Figure 95. Appearance of the: (a) $\{110\}$, and (b) $\{112\}$ Anti-Phase Boundaries in NiAl at 1K as Determined from the Embedded Atom Method Simulation Array. Ni atoms are marked by circles and Al atoms by triangles. The diagrammed movements are 4X and 16X the actual movements for the $\{110\}$ and $\{112\}$ boundaries, respectively.

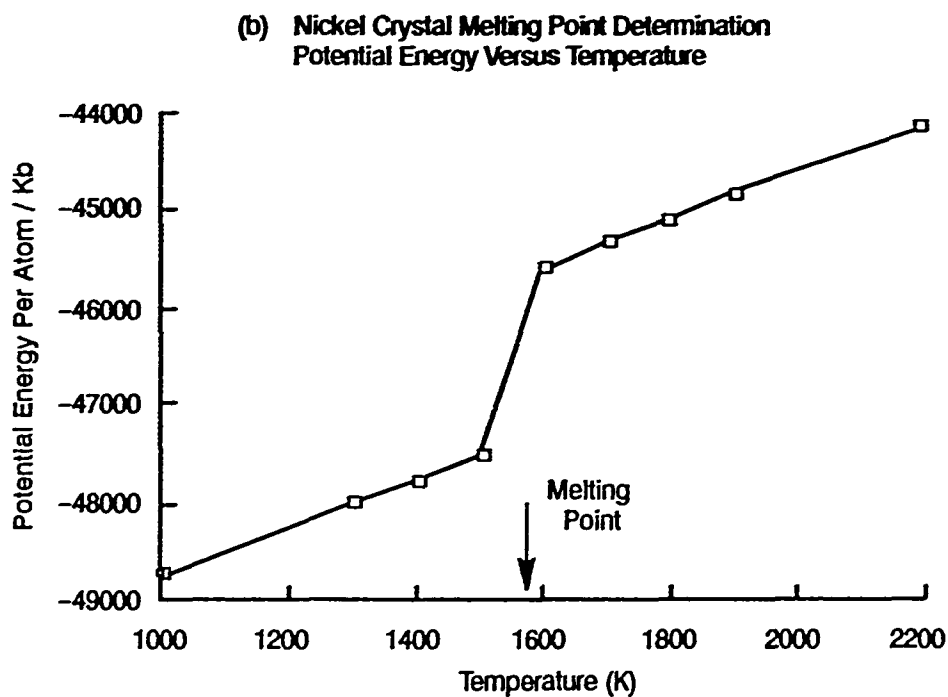
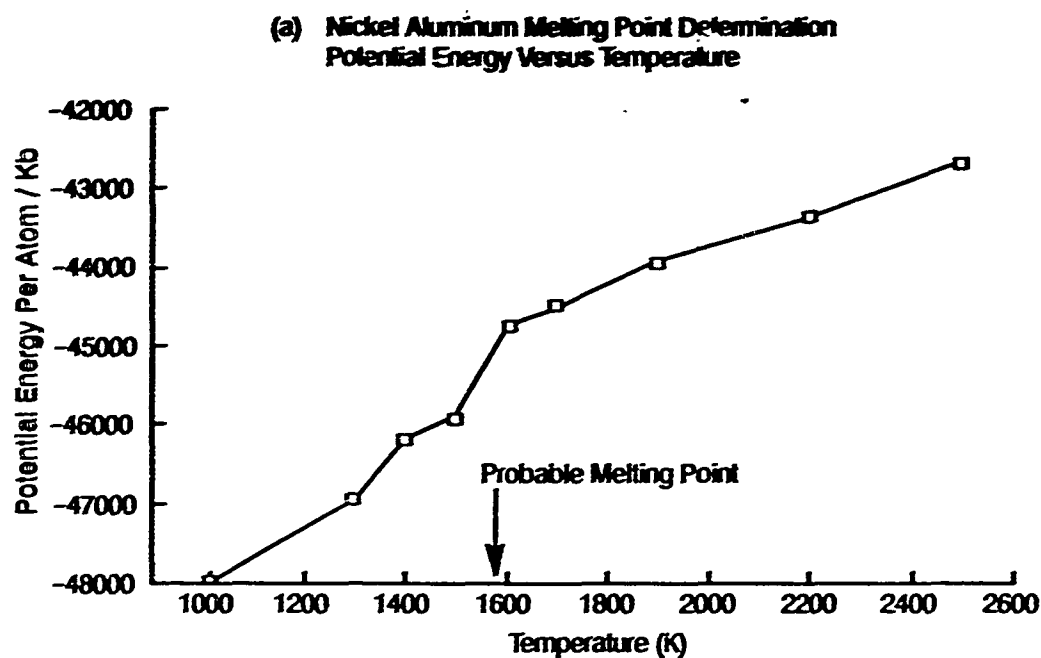


Figure 96. Potential Energy Versus Temperature Plots from the Embedded Atom Method Simulation Arrays of: (a) NiAl, and (b) Ni for Determination of the Melting Points

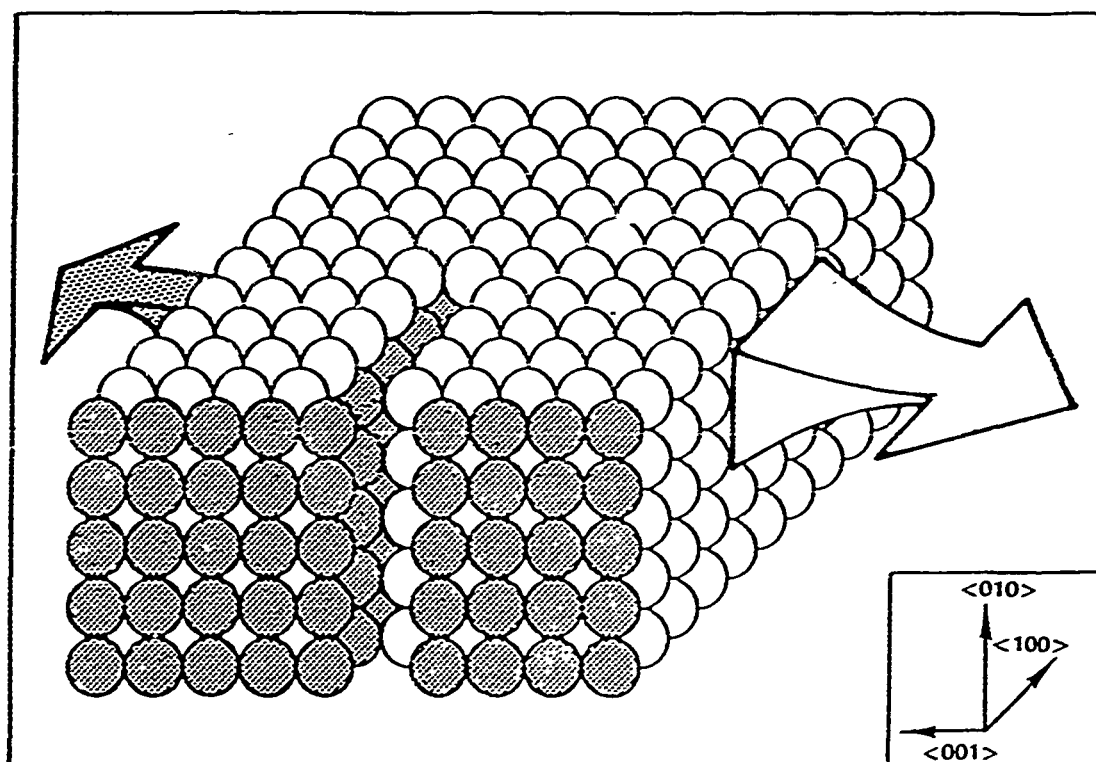


Figure 97. Three-Dimensional Diagram of the Simulated Lattice Containing a Crack. The white circles represent Al atoms, while the grey circles represent Ni atoms. The arrows indicate the direction of the applied force. Note that the force is being applied only to the outermost layer of atoms. In the $\langle 001 \rangle$ direction, the force is acting only on the Ni atoms (grey arrow), while in the $\langle 00\bar{1} \rangle$ direction, the force is acting only on the Al atoms (white arrow).

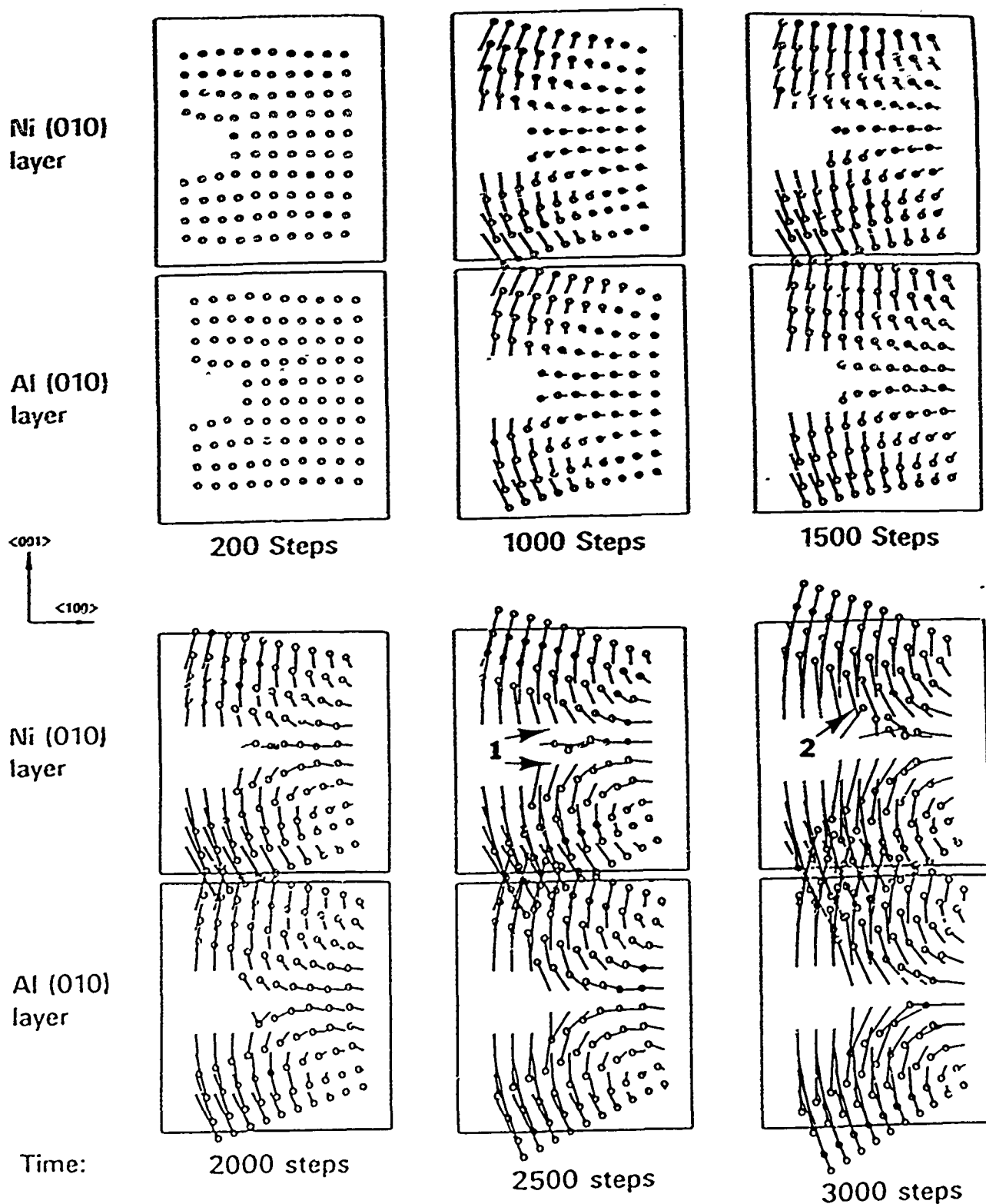
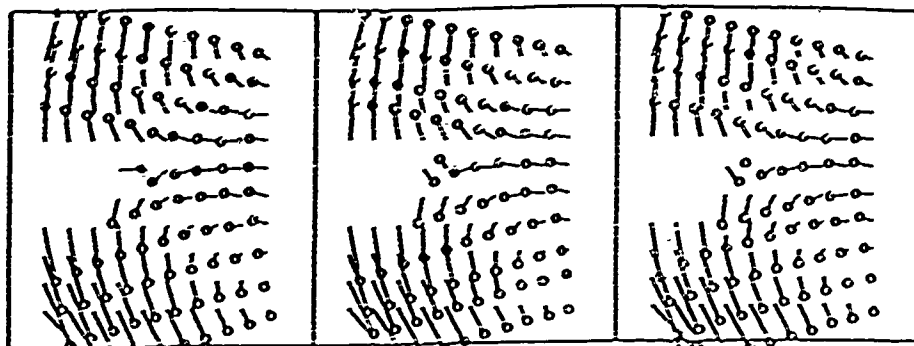
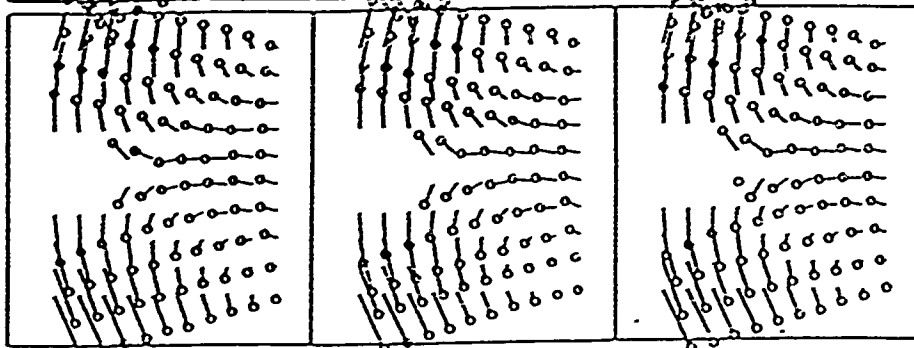


Figure 98. Typical Layers in EAM Simulation Array at 100°K, Showing the Array at Various Simulation Steps (40 Steps = 1 Atomic Vibration). Some rebonding of atoms after bond breaking can be seen in the vicinity of the crack tip in the later steps. At #1, the middle layer has separated from the top and bottom sections of the array. At #2, the middle layer has rebonded to the top portion. The "tails" attached to the atoms show displacements from their initial positions.

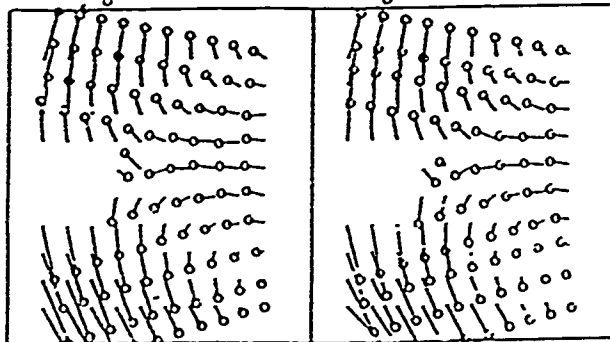
Ni (010)
layer



Al (010)
layer



Ni (010)
layer



Al (010)
layer

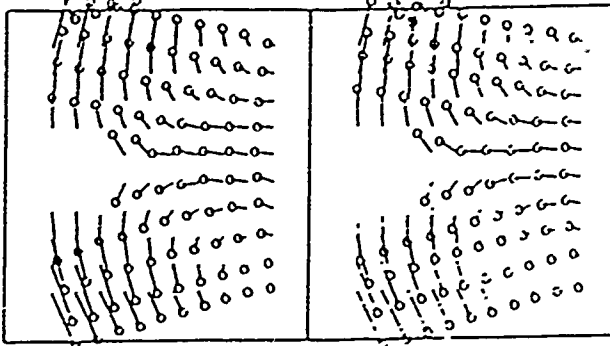


Figure 99. EAM Simulation Array at 300° K, Showing the Array at Step 2000. Rebonding of atoms after bond breaking can be seen in the vicinity of the crack tip. The "tails" attached to the atoms show displacements from their initial positions.

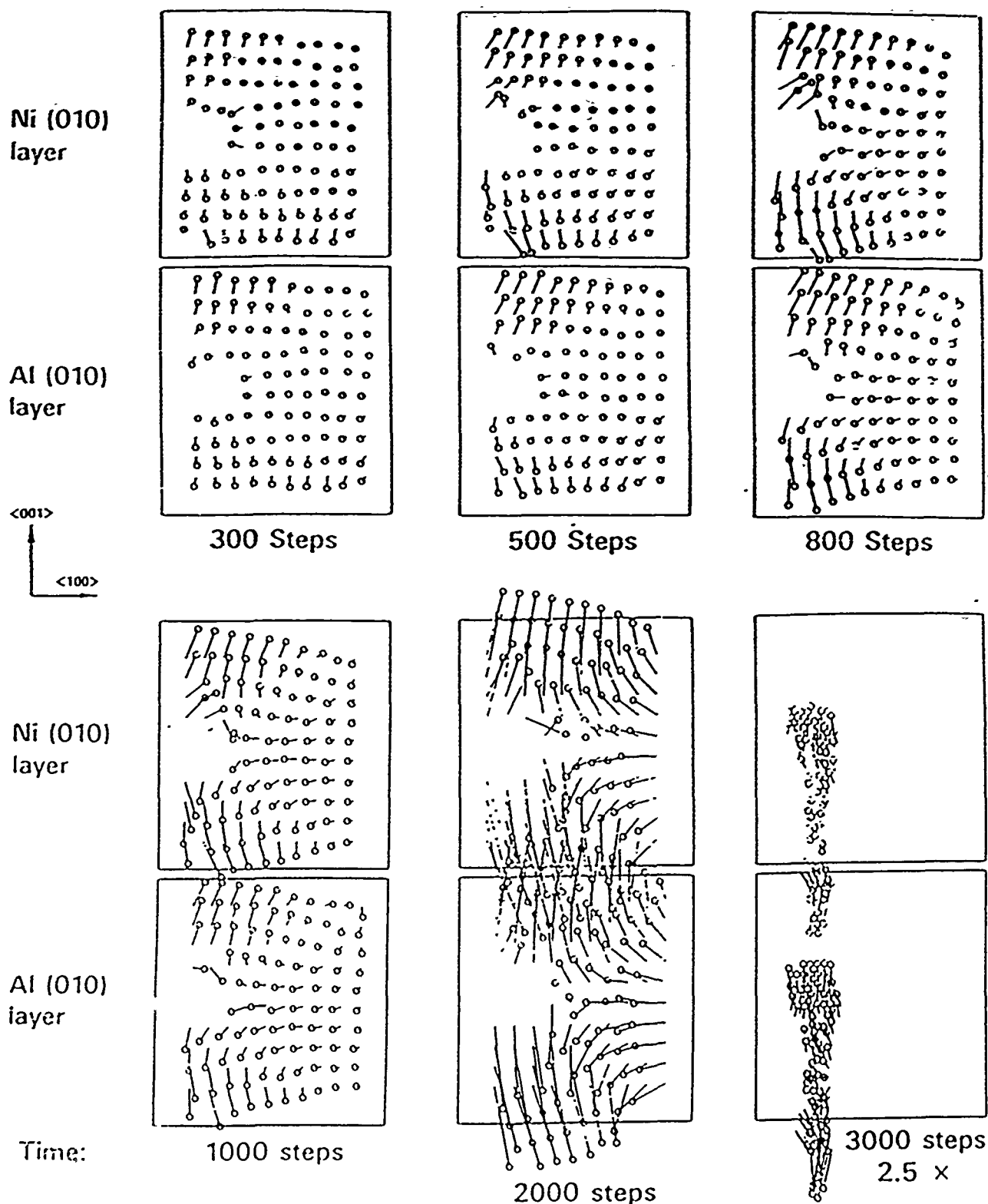


Figure 100. Typical Layers in EAM Simulation Array at 1000°K, Showing the Array at Various Simulation Steps (1 Step = 40 Atomic Vibrations). A description of the deformation processes in this simulation is provided in the text. Note: Step 3000 is plotted with displacements indicated relative to Step 2500 (not shown) and at a different scale (2.5X smaller). The "tails" attached to the atoms show displacements from their initial positions.

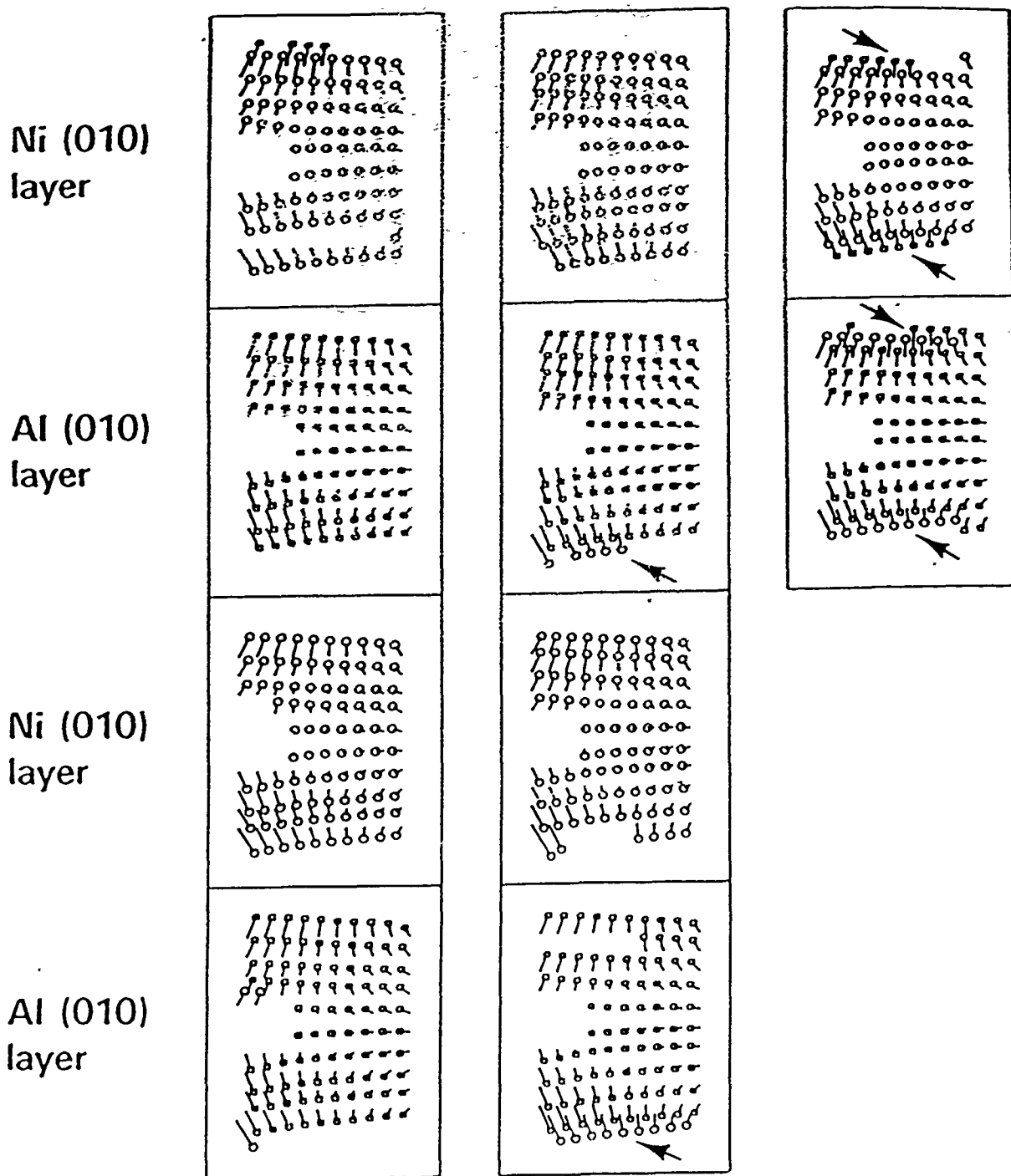
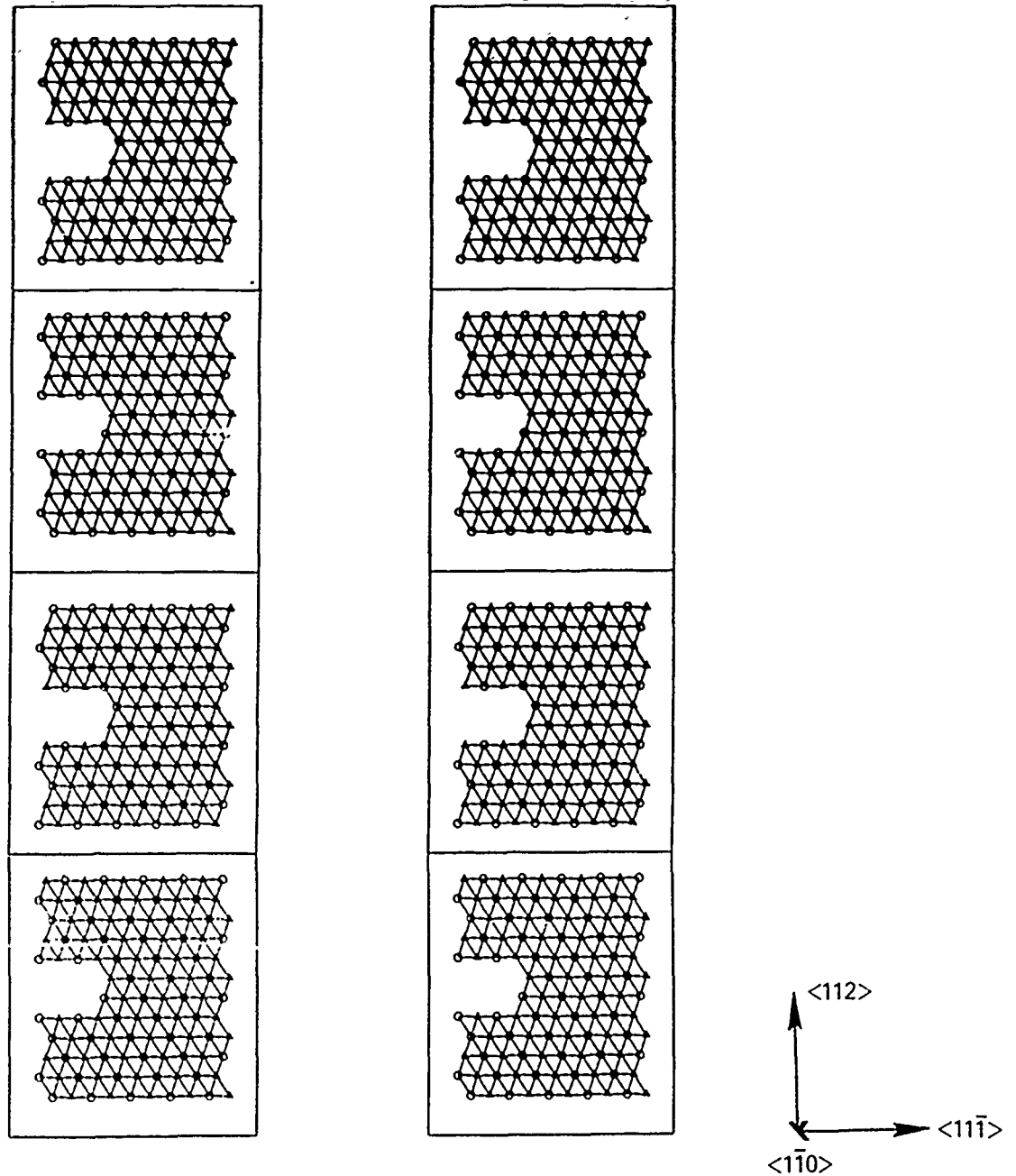
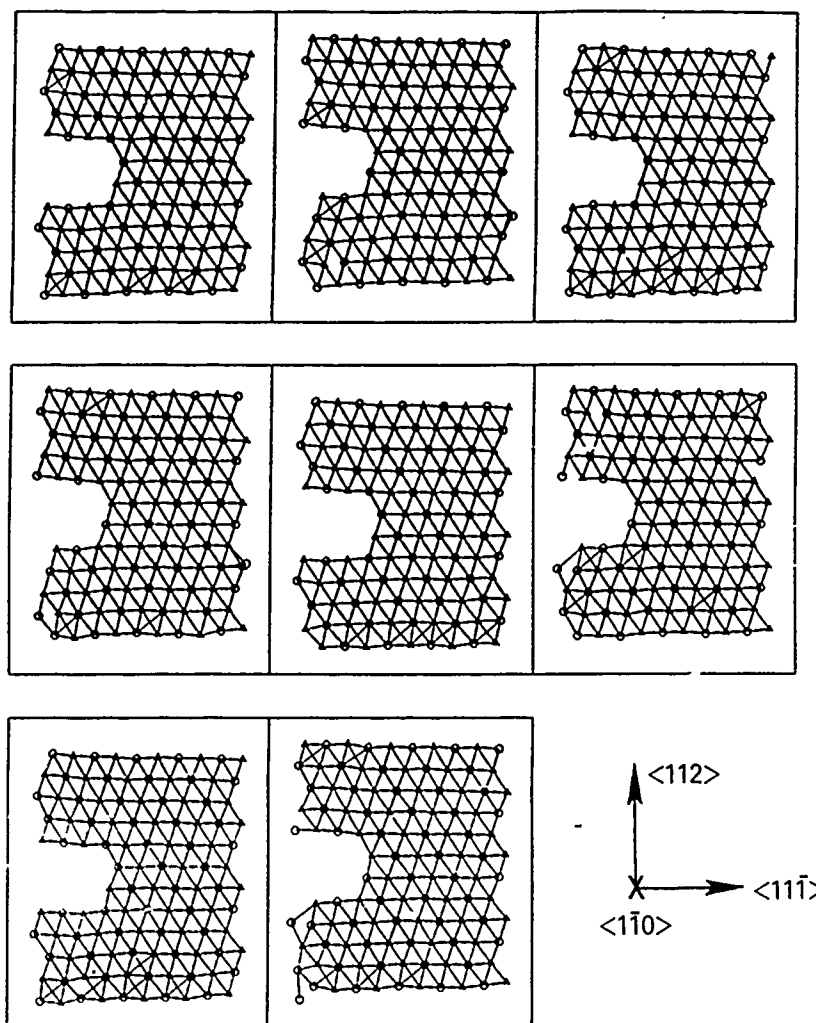


Figure 101. EAM Simulation Array at 1°K, Showing the Array at Step 4000. Ni atoms are represented by circles and Al atoms by squares. At this step, there is evidence of slip on the (001) plane (arrows), for the outermost layer of atoms has apparently shifted down a layer. The "tails" attached to the atoms show displacements from their initial positions.



STEP 0

Figure 102. $\{1\bar{1}0\}$ Slices through the Initial Embedded Atom Method Simulation Array for a Stress Applied in the $\langle 112 \rangle$ direction. Ni atoms are marked by circles and Al atoms by triangles. A load of 1750 MPa is applied to the top and bottom of the array at Step 0. This stress orientation should favor dislocation generation as the (110) planes are at 45° to the stress axis, making the resolved shear stress on these planes high.



STEP 400

Figure 103. $\{1\bar{1}0\}$ Slices through the Embedded Atom Method Simulation Array at 100K After 400 Steps. Only elastic distortions are present at this time. The stress of 1250 MPa is applied in the $\langle 112 \rangle$ direction and Ni atoms are marked by circles and Al atoms by triangles. Note: the array has been redrawn for ease of interpretation.

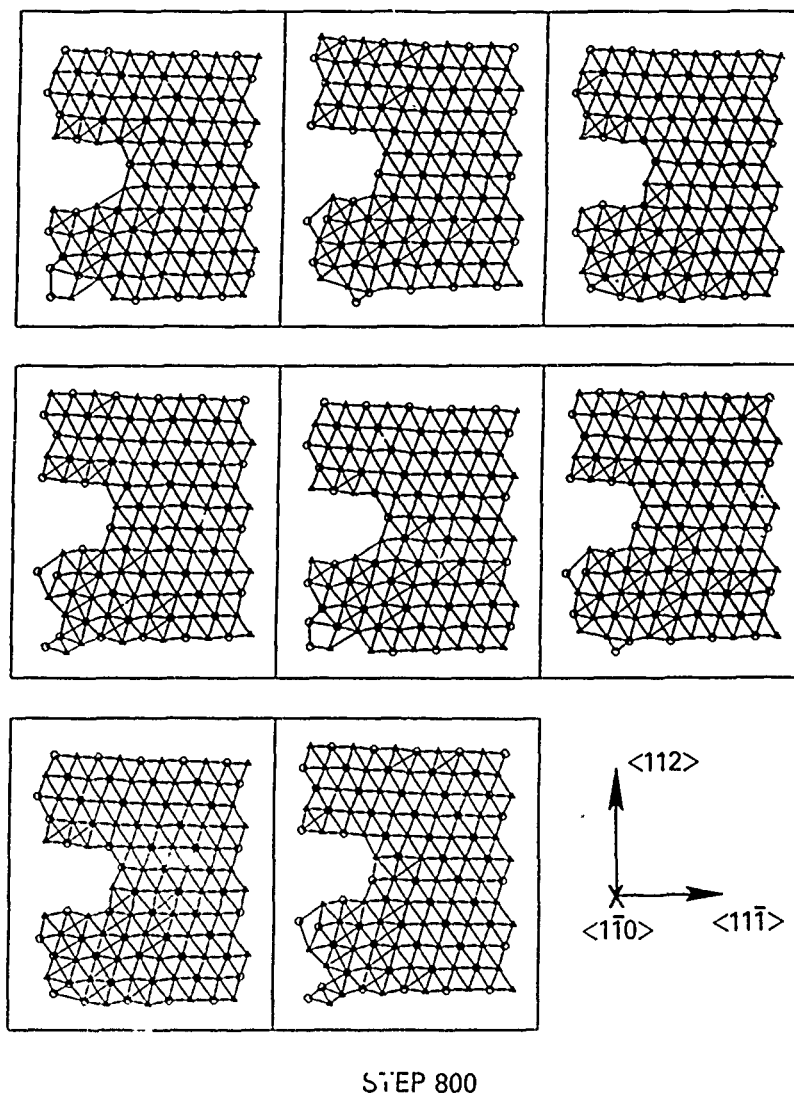
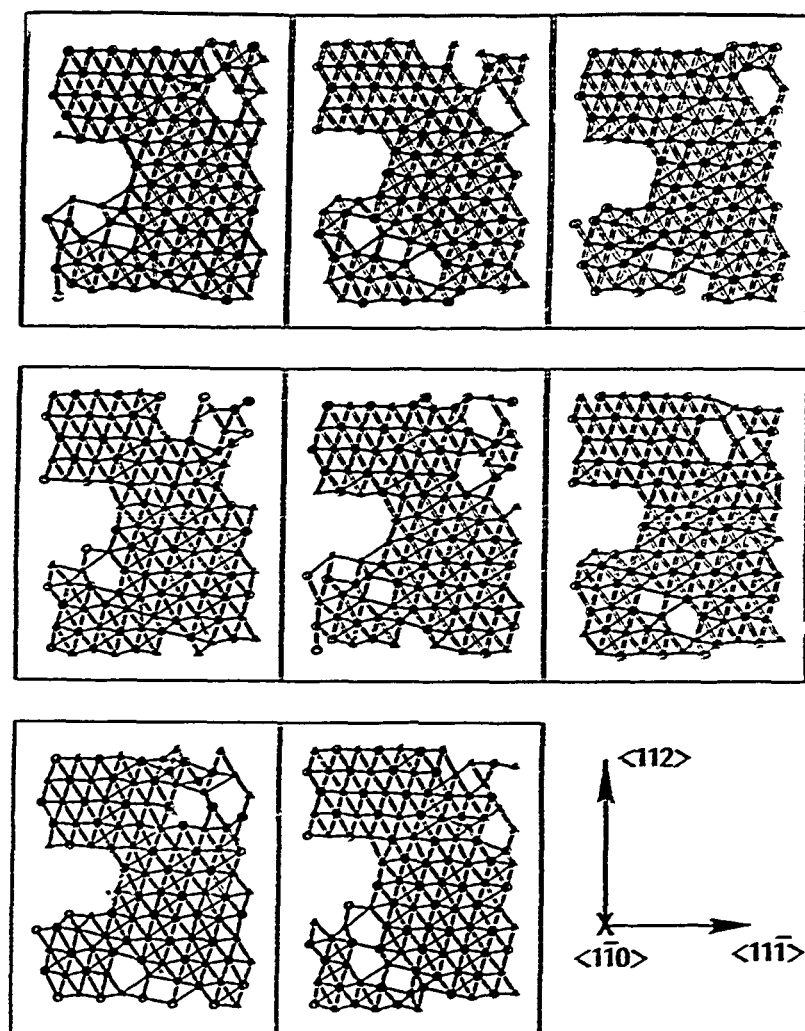


Figure 104. $\{1\bar{1}0\}$ Slices through the Embedded Atom Method Simulation Array at 100K After 800 Steps. Some sort of dislocation has propagated in the array as seen from the jog that has appeared in the lower left corner of some of the slices. The stress of 1250 MPa is applied in the $\langle 112 \rangle$ direction and Ni atoms are marked by circles and Al atoms by triangles. Note: the array has been redrawn for ease of interpretation.



STEP 1400

Figure 105. $\{1\bar{1}0\}$ Slices through the Embedded Atom Method Simulation Array at 100K After 1400 Steps. Some new dislocations have propagated in the array as seen from the new jogs that have appeared in the upper right-hand side of some of the slices. The stress of 1250 MPa is applied in the $\langle 112 \rangle$ direction and Ni atoms are marked by circles and Al atoms by triangles. Note: the array has been redrawn for ease of interpretation.

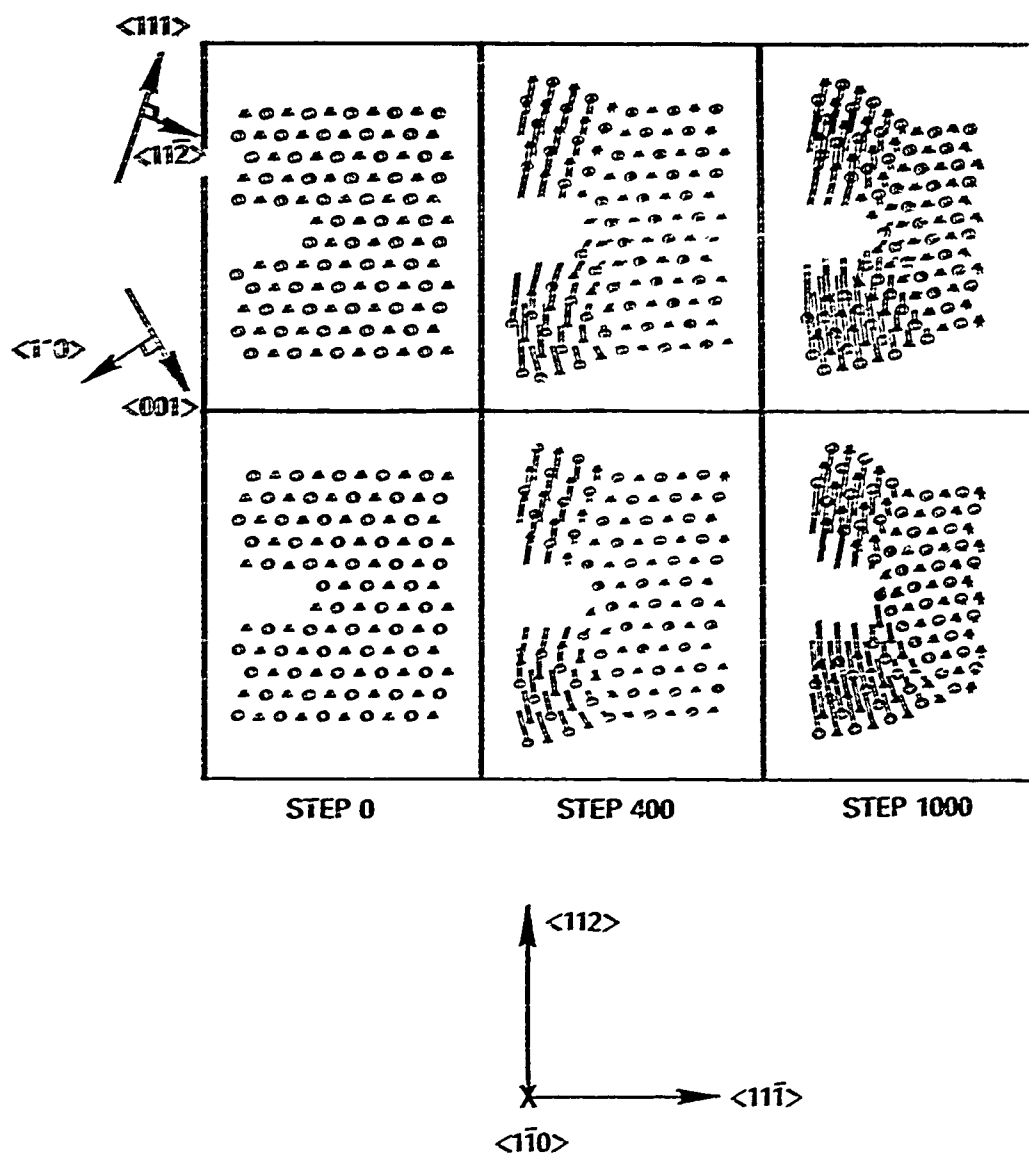


Figure 106. Typical $\{1\bar{1}0\}$ Slices through the Embedded Atom Method Simulation Array at 100K After 0, 400 and 1000 Steps. The stress of 5000 MPa has been applied in the $\langle 112 \rangle$ direction by coordinated atomic movements on (110) planes in a $\langle 001 \rangle$ direction in the lower portion of the array, and slip on $(11\bar{2})$ planes in a $\langle 111 \rangle$ direction in the upper portion of the array. However, no dislocations are evident. At 1000 steps, slip appears to be well advanced, but still no dislocations are evident. Ni atoms are marked by circles and Al atoms by triangles.

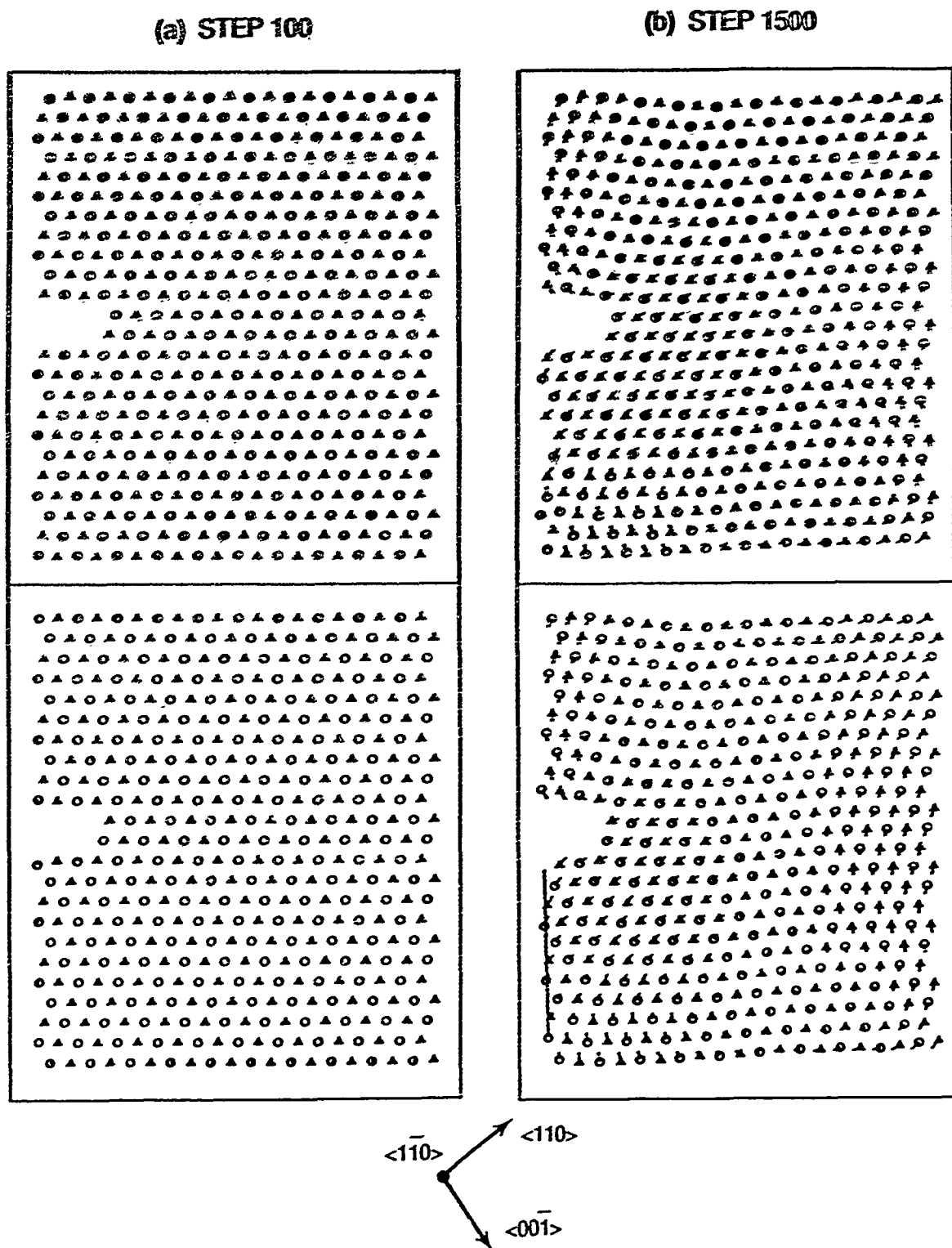
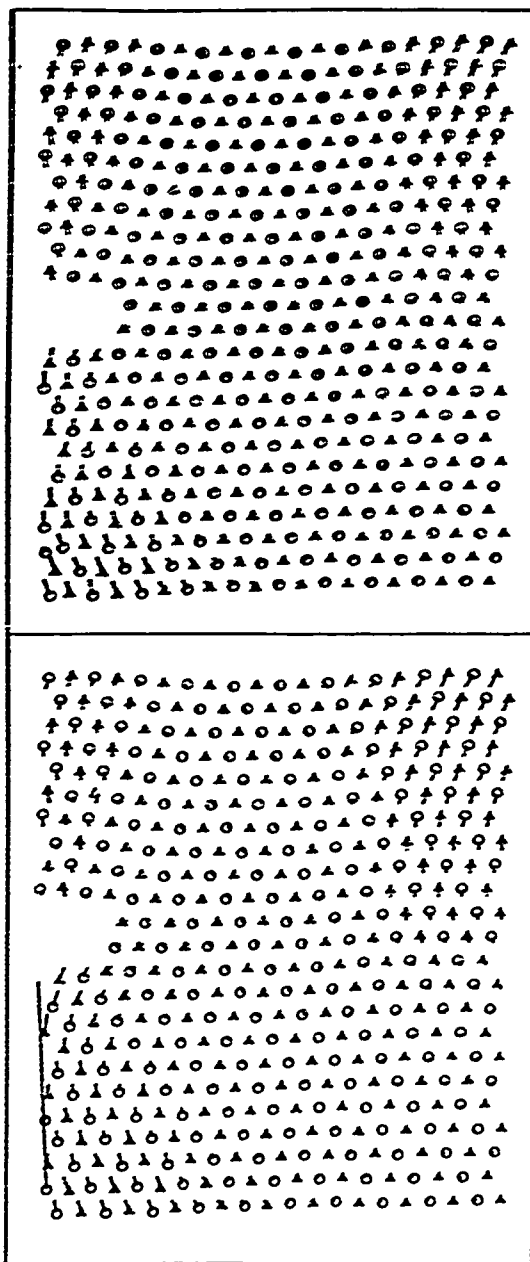


Figure 107. Typical $\{110\}$ Slices through the 4000 Atom Embedded Atom Method Simulation Array at 100K After 100, 1500, 1800, 2000, 2500 and 2700 Steps. A stress of 2500 MPa was applied in the $\langle 112 \rangle$ direction at Step 0, which was increased to 3750 MPa after Step 1500. In Steps 2000 through 2700, there appear to be dislocation events occurring in the form of coordinated slip. Further details of this simulation are provided in the text. Ni atoms are marked by circles and Al atoms by triangles.

(c) STEP 1800



(d) STEP 2000

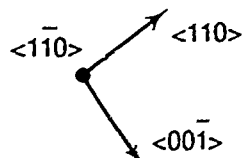
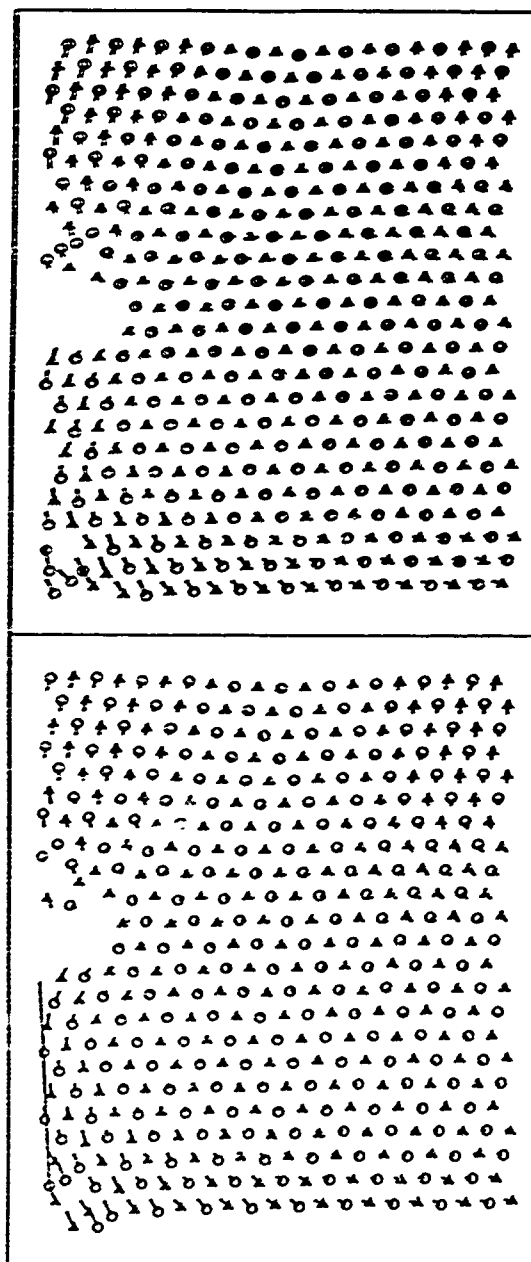


Figure 107 (continued)

(e) STEP 2500

(f) STEP 2700

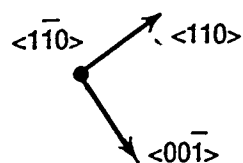
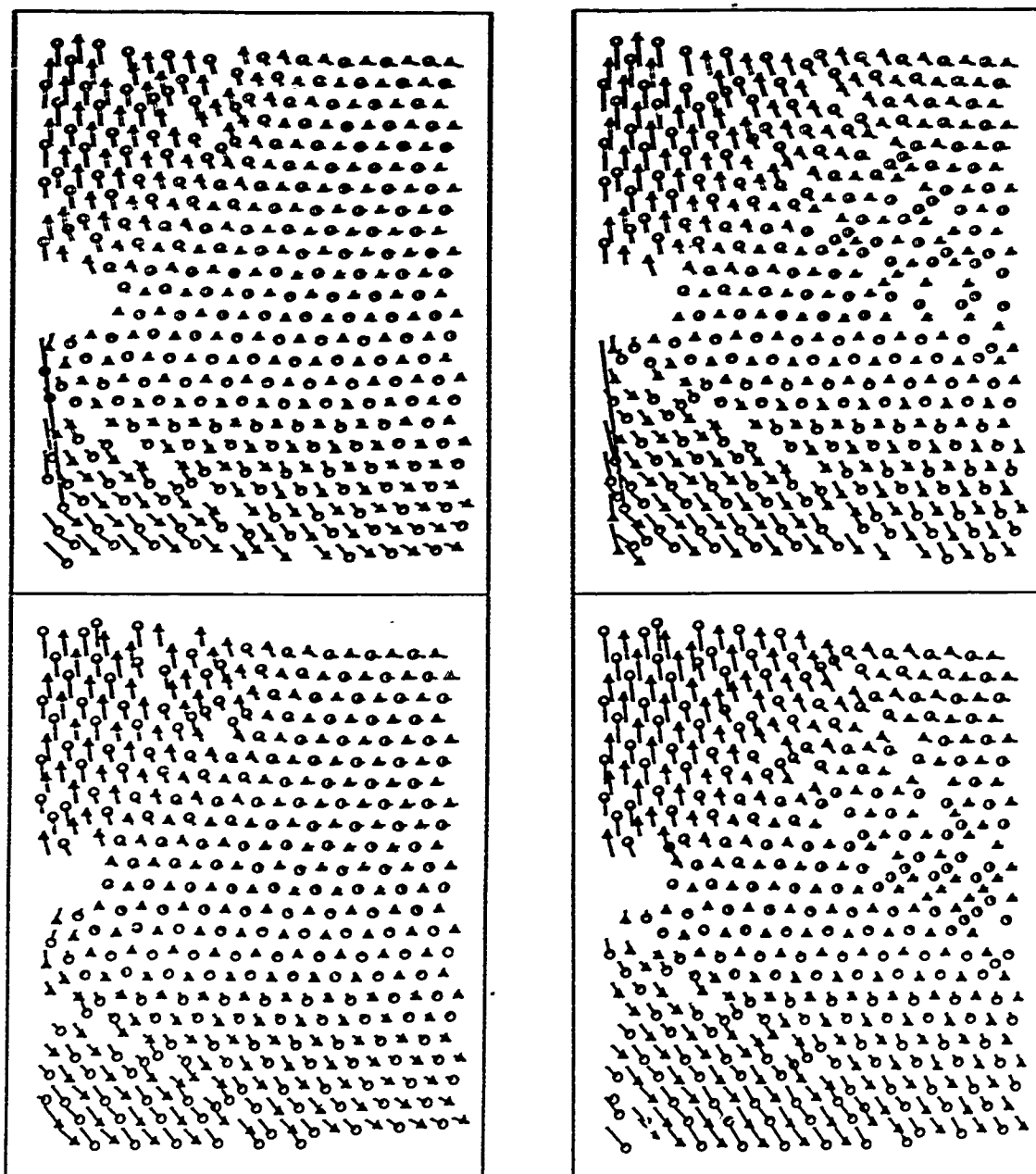


Figure 107 (continued)

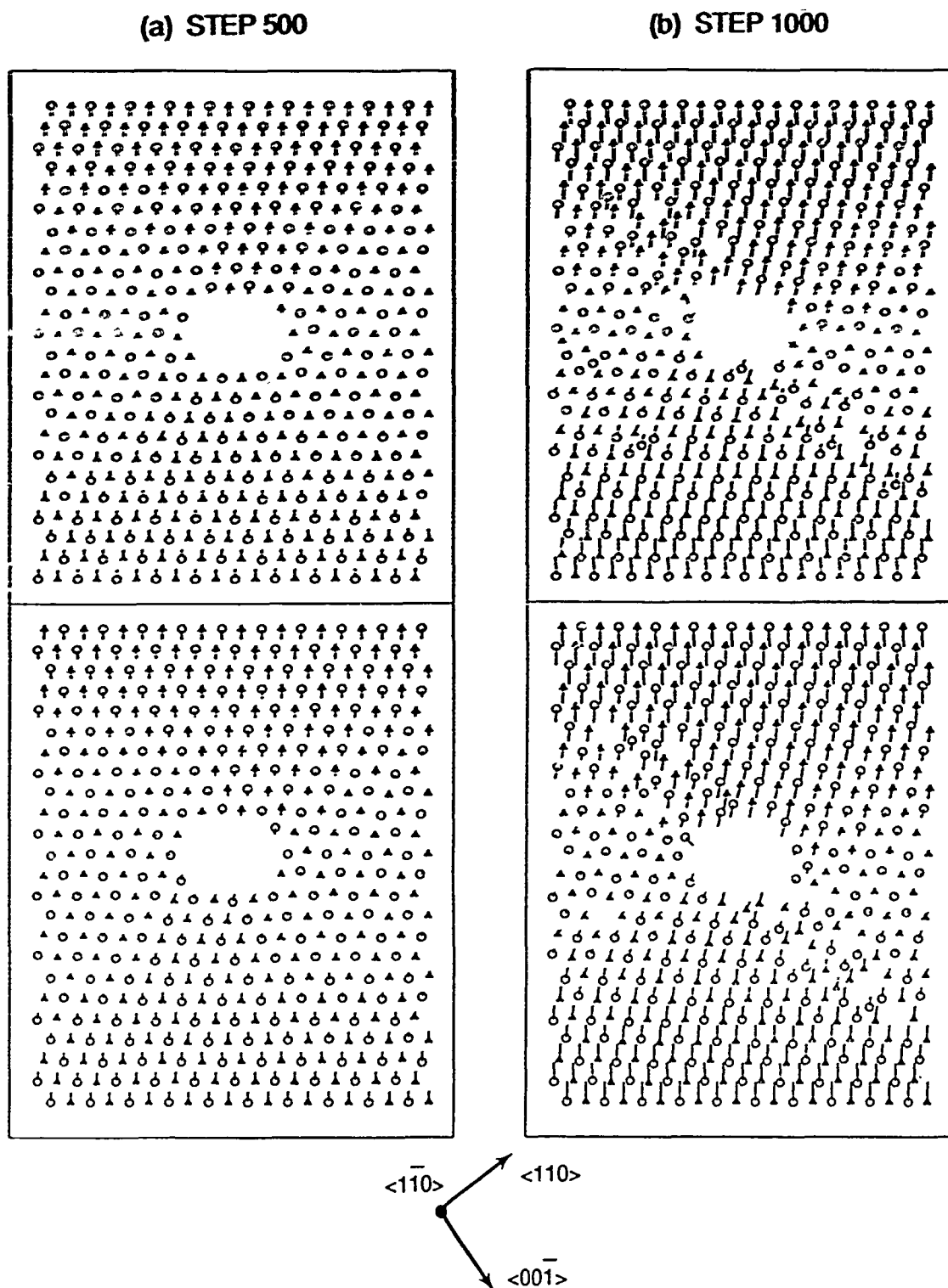


Figure 108. Typical $\{110\}$ Slices through the 4000 Atom Embedded Atom Method Simulation Array at 100K After 500, 1000, 1500 and 2000 Steps. The array is loaded at a constant strain rate, with a center crack and periodic boundary conditions between the left and right faces. The strains are applied in the $\langle 112 \rangle$ direction and Ni atoms are marked by circles and Al atoms by triangles.

(c) STEP 1500

(d) STEP 2000

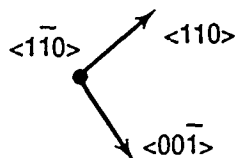
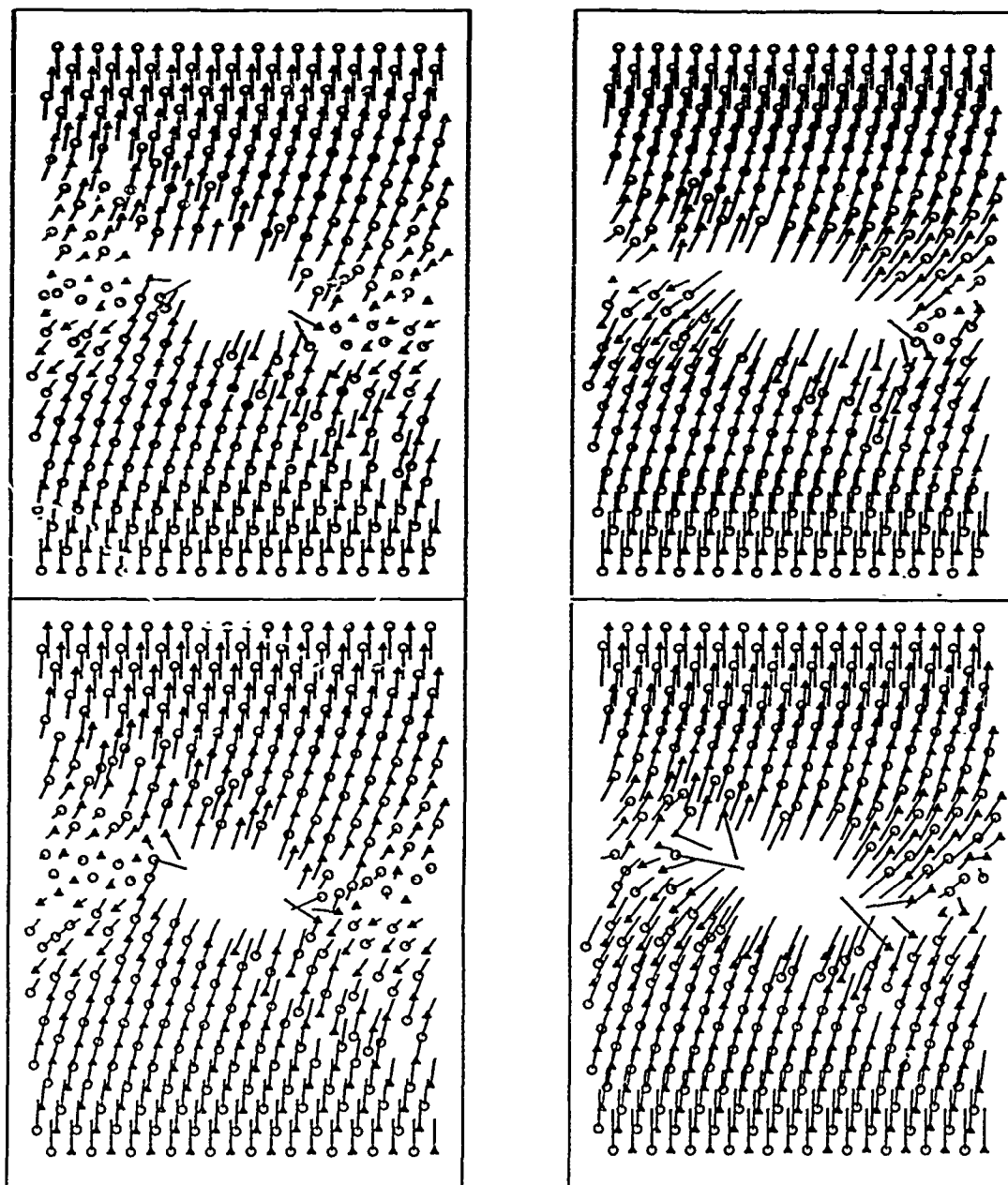


Figure 108 (continued)

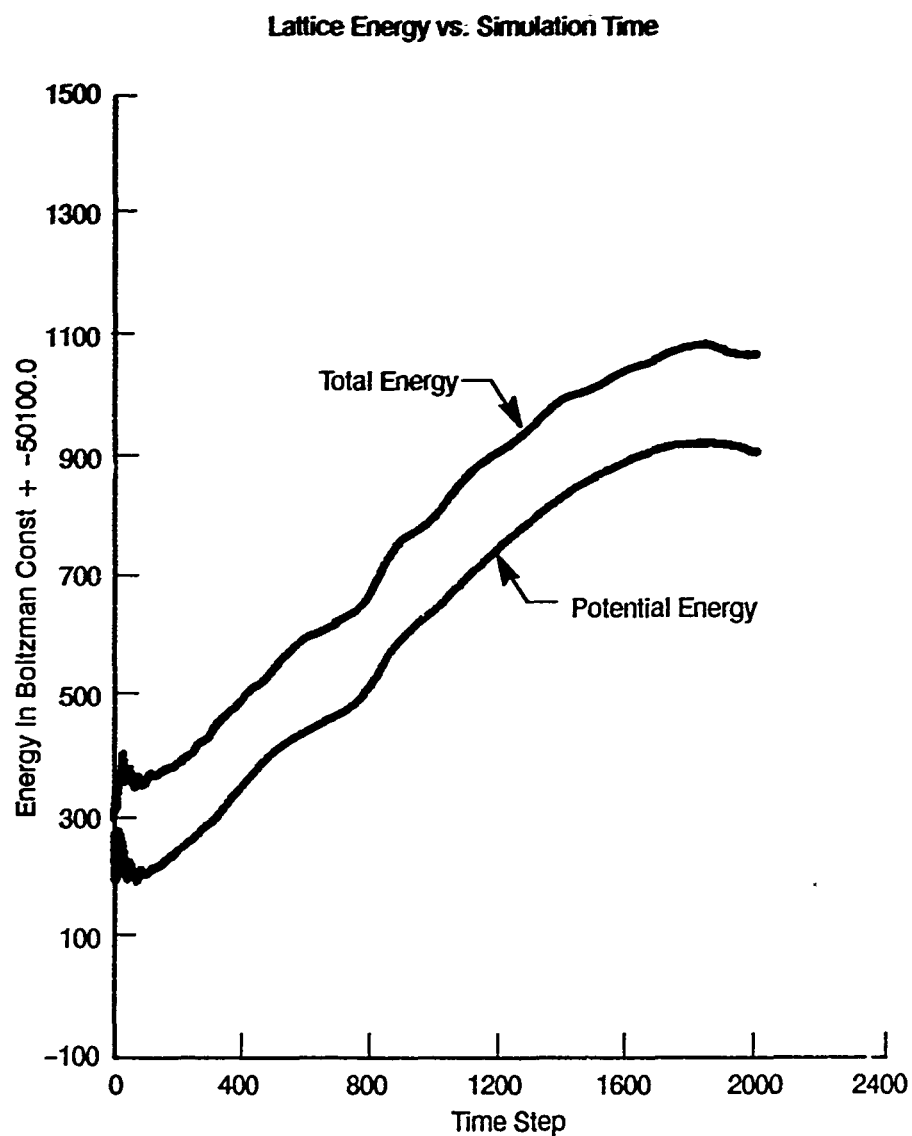
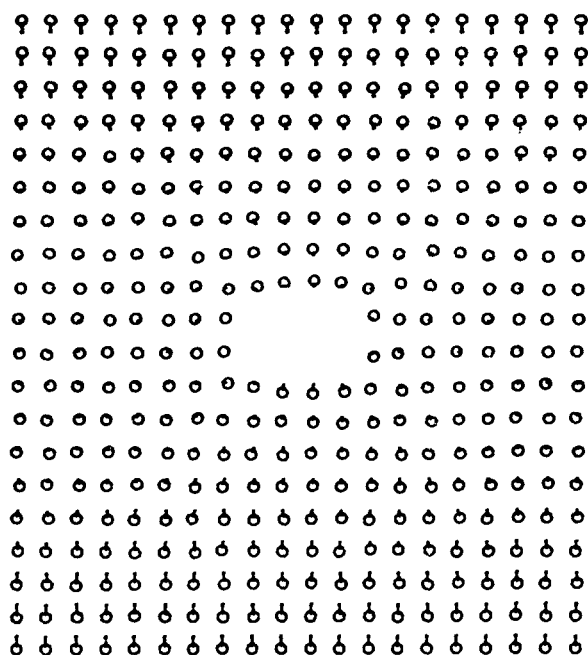
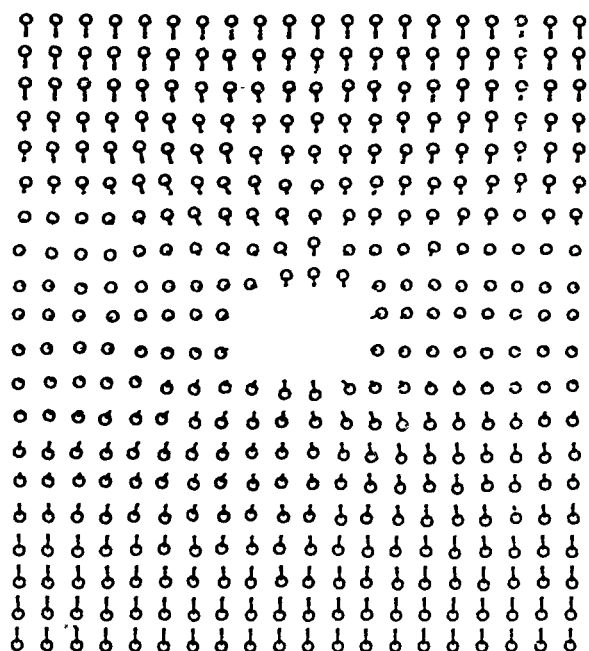


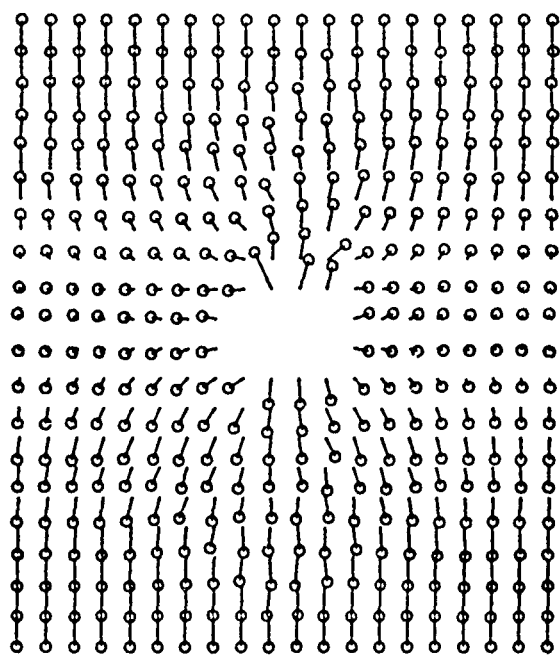
Figure 109. Lattice Energy Versus Simulation Time Plot for the Simulation Shown in Figure 108. The lattice energy is topping out and beginning to drop near Step 2000 owing to the fracture that is becoming evident in Figure 108(d).



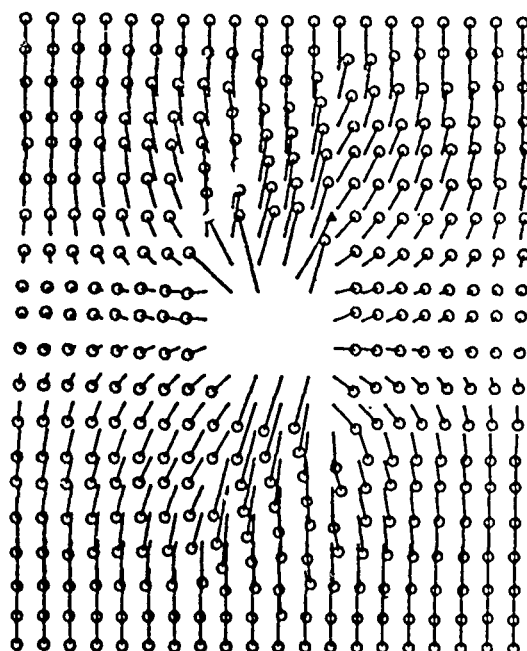
(a)



(b)

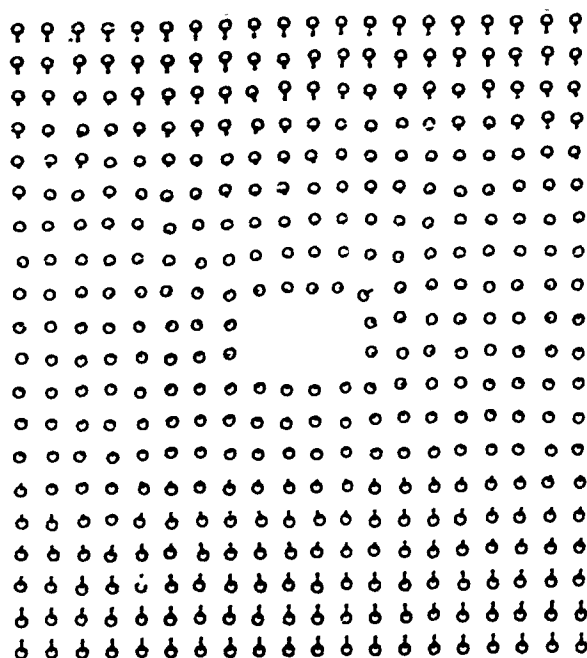


(c)

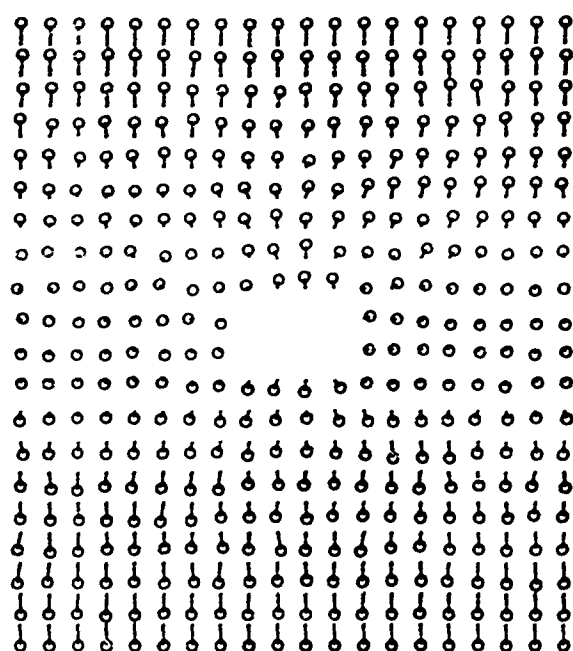


(d)

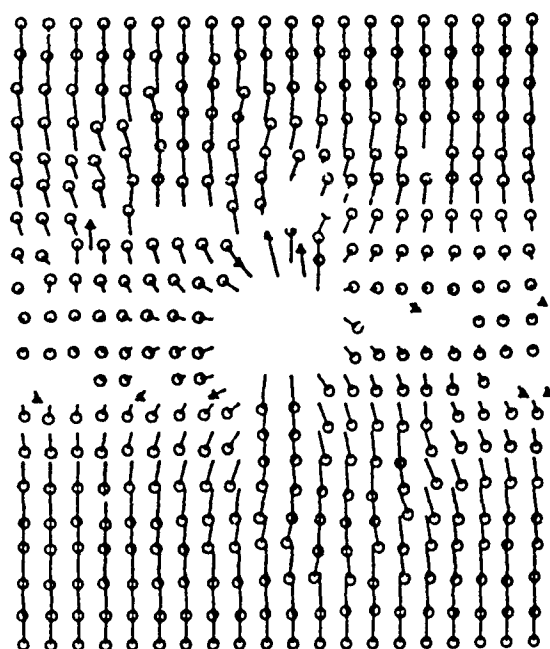
Figure 110. $\{001\}$ Slices through the Embedded Atom Array at 100K After: (a) 1500, (b) 2000, (c) 3500, and (d) 6000 Steps. Ni atoms are marked by circles and Al atoms by triangles.



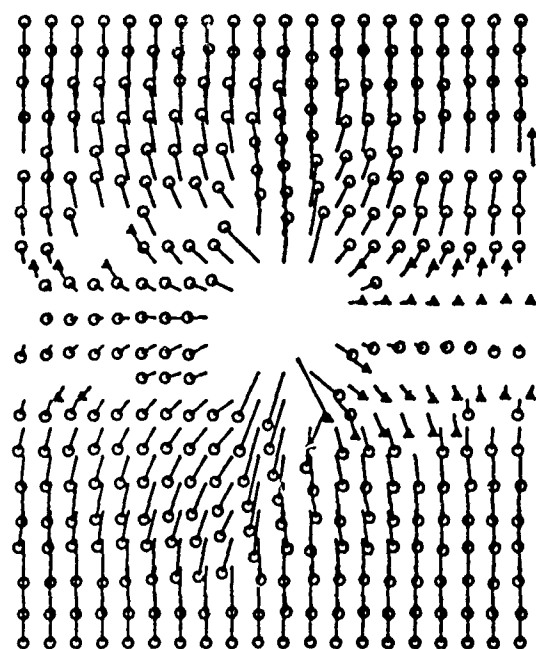
(a)



(b)



(c)



(d)

Figure 111. $\{001\}$ Slices through the Embedded Atom Array at 300K After: (a) 1500, (b) 2500, (c) 5000, and (d) 6000 Steps. Ni atoms are marked by circles and Al atoms by triangles.

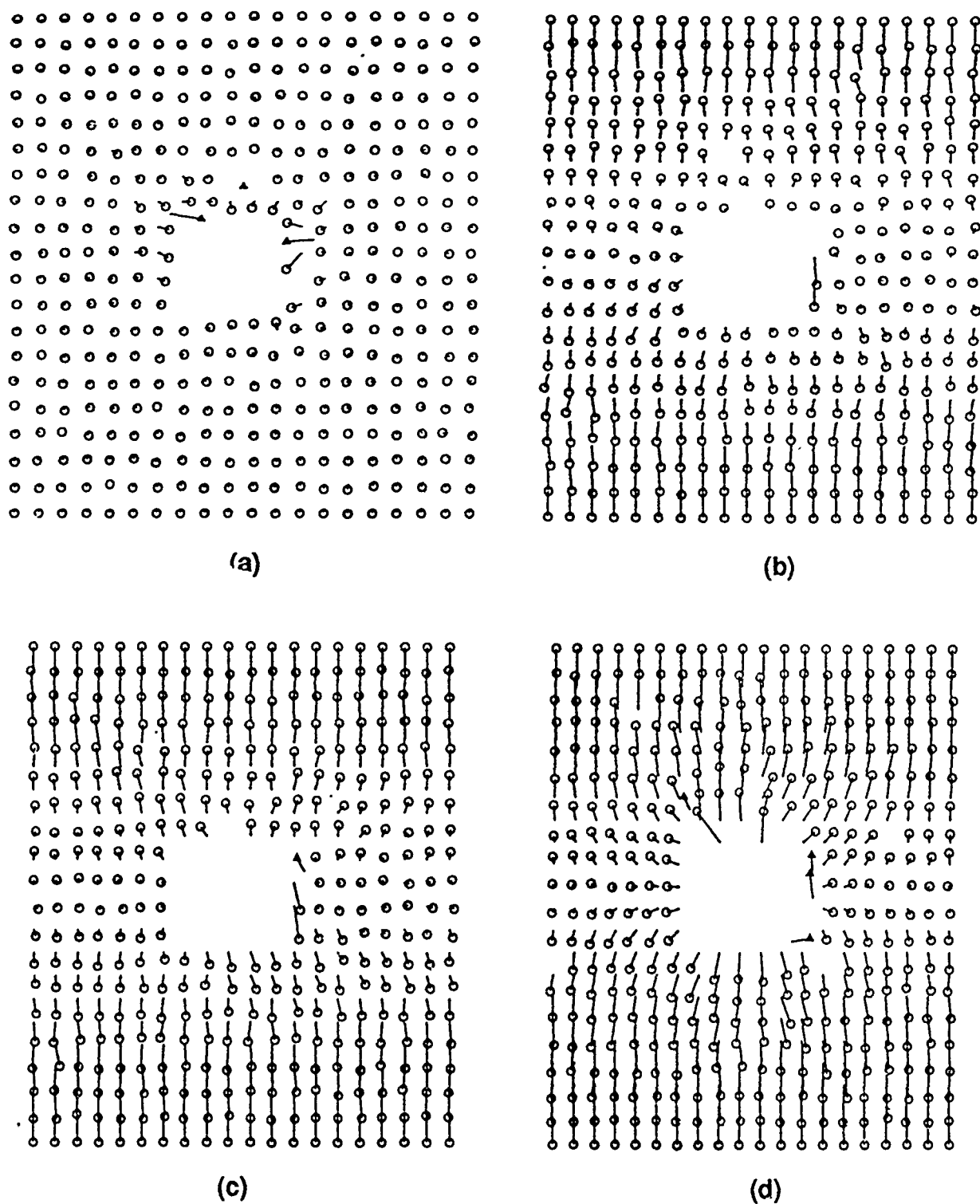
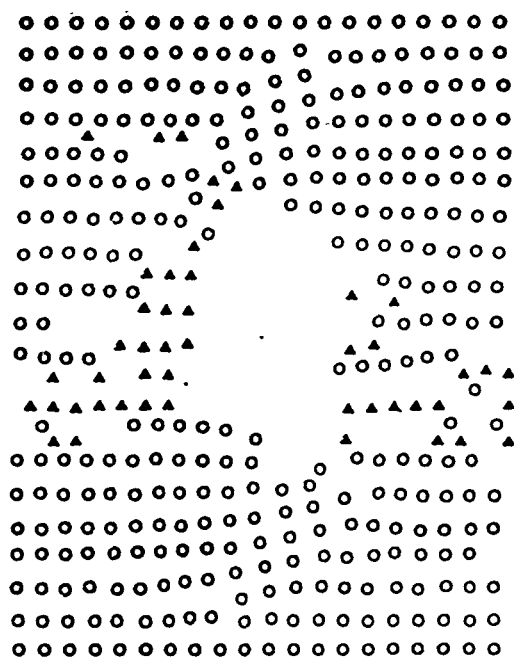
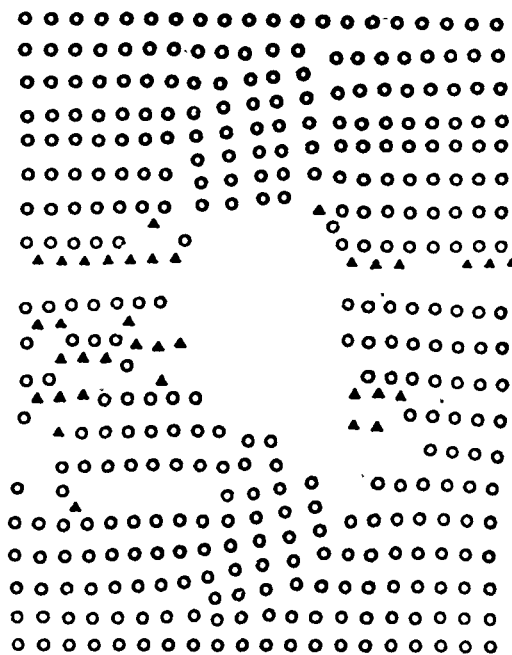


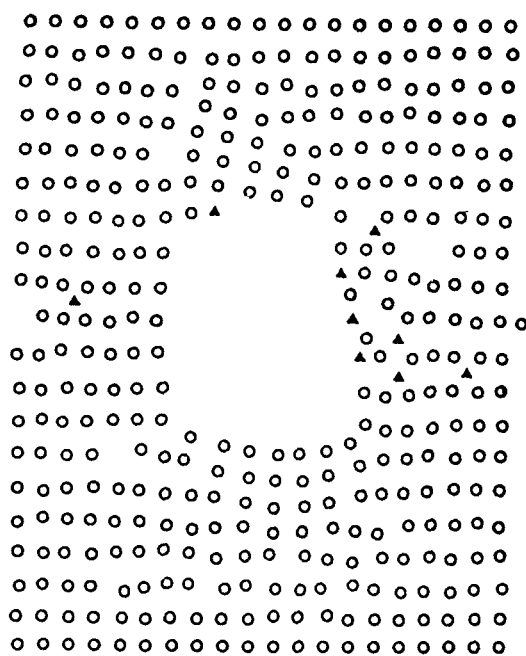
Figure 112. $\{001\}$ Slices through the Embedded Atom Array at 800K. After: (a) 500, (b) 3500, (c) 4000, and (d) 6000 Steps. Ni atoms are marked by circles and Al atoms by triangles.



(a)



(b)



(c)

Figure 113. $\{001\}$ Slices through the Embedded Atom Array at: (a) 100K, (b) 300K, and (c) 800K After 8000 Steps. Ni atoms are marked by circles and Al atoms by triangles.

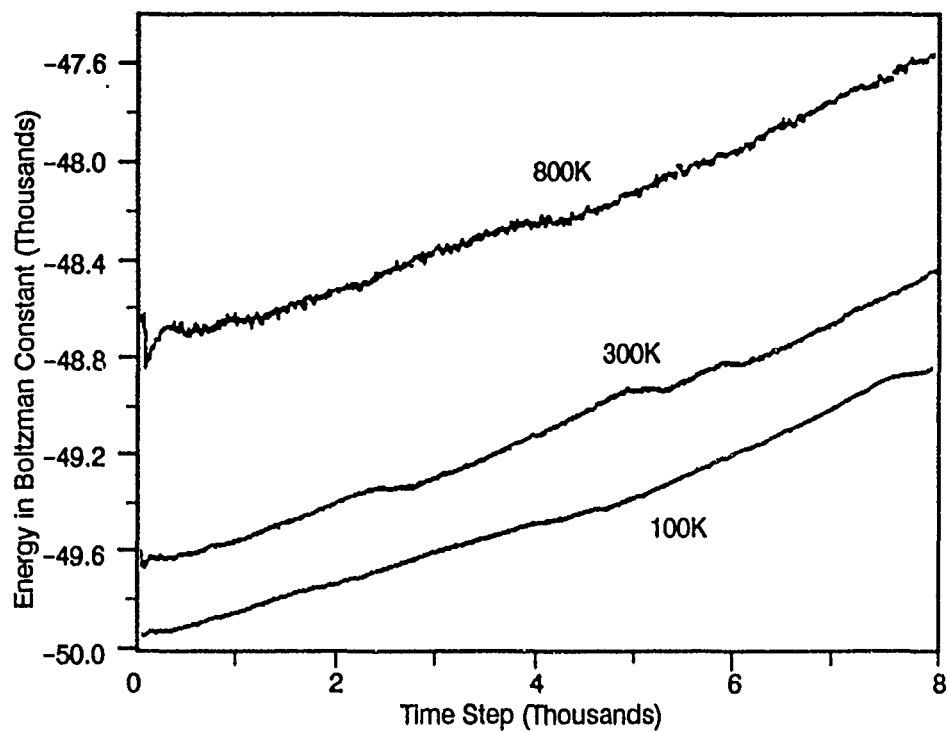


Figure 114. Potential Energy Versus Simulation Time Plot for the Simulations Shown in Figures 110 through 113

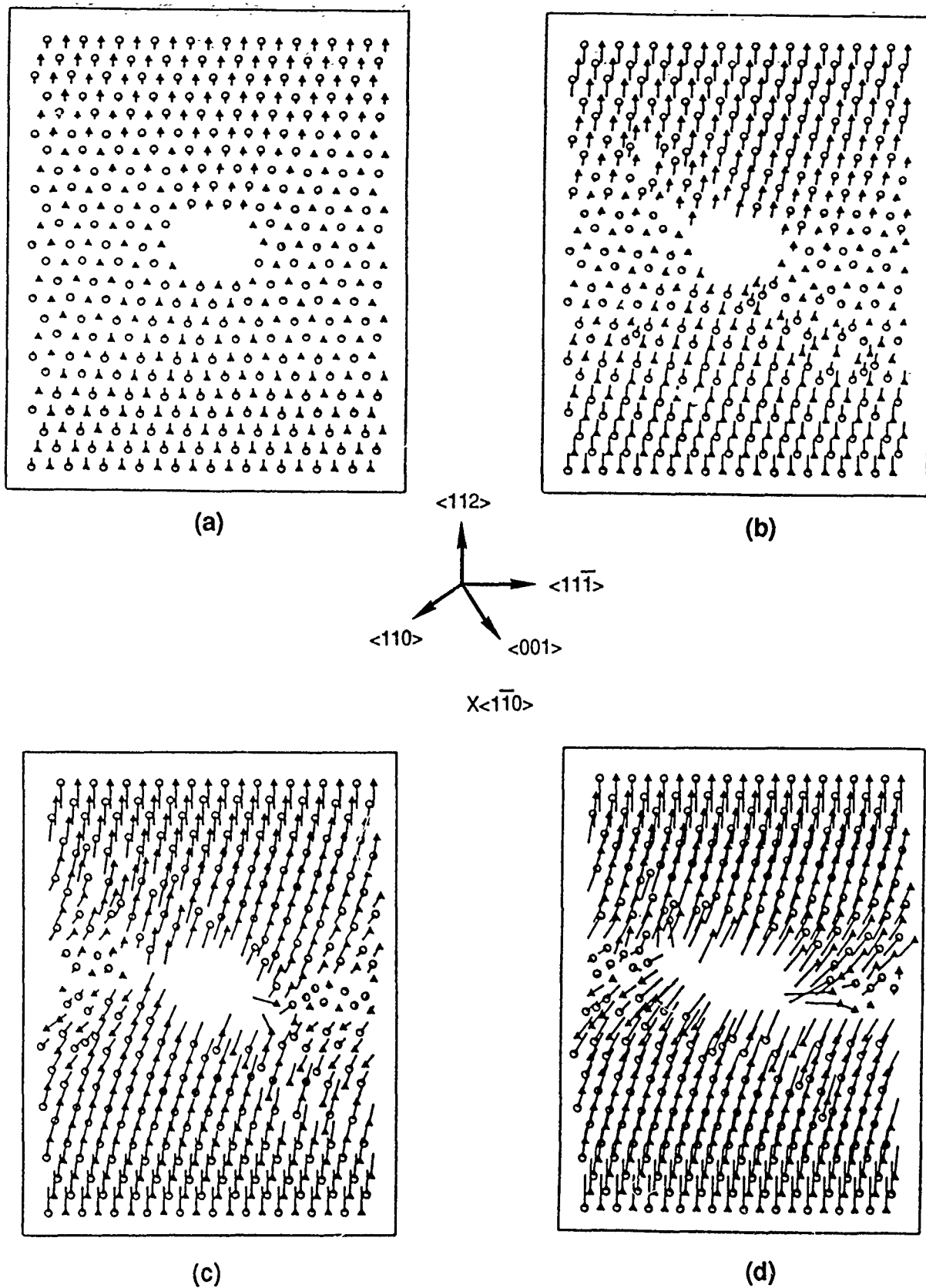


Figure 115. $\{1\bar{1}0\}$ Slices through the Embedded Atom Array Strained in the $\langle 112 \rangle$ Direction at 100K After: (a) 500, (b) 1000, (c) 1500, and (d) 2000 Steps. Ni atoms are marked by circles and Al atoms by triangles.

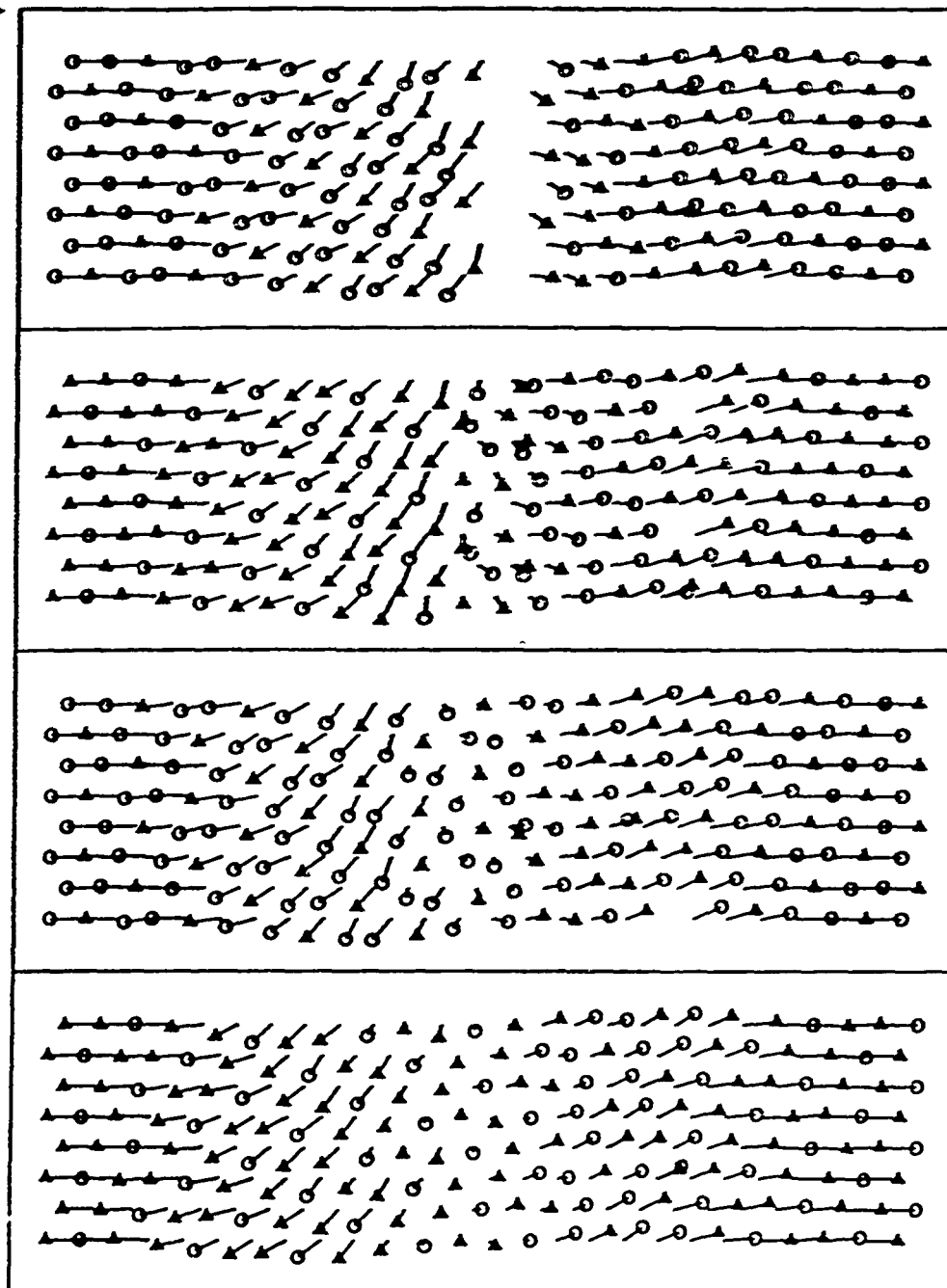
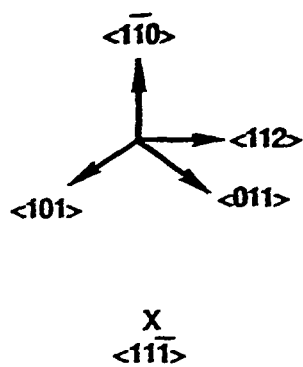


Figure 116. Side View (Looking at a $\{11\bar{1}\}$ Plane) of the Array Shown in Figure 115(b) After 1000 Steps

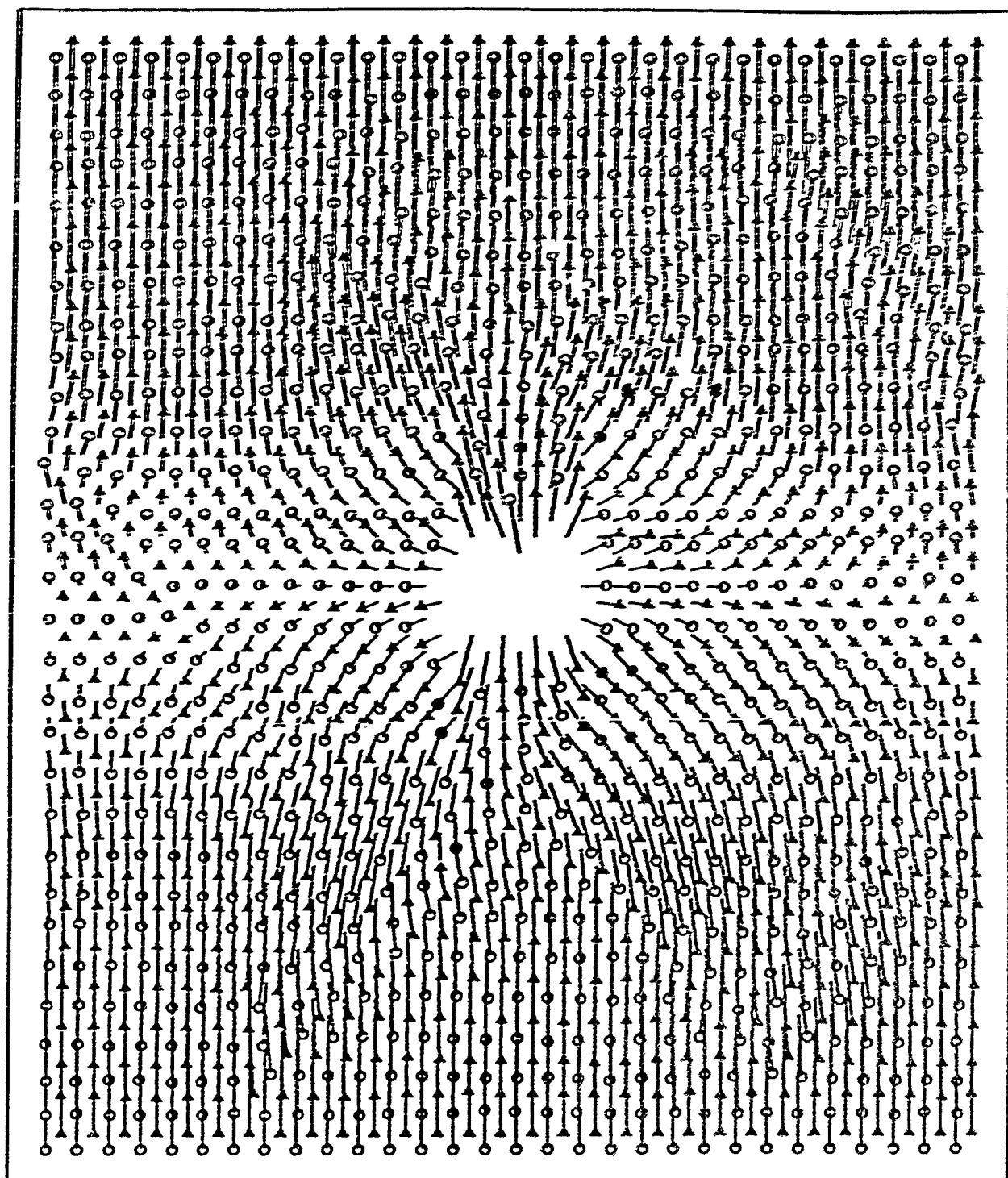


Figure 117. Slice through the Embedded Atom Method 9000 Atom Array at 300K After 2000 Steps, Showing the Atomic Displacements in the Form of "Tails" on the Atoms. Ni atoms are marked by circles and Al atoms by triangles.

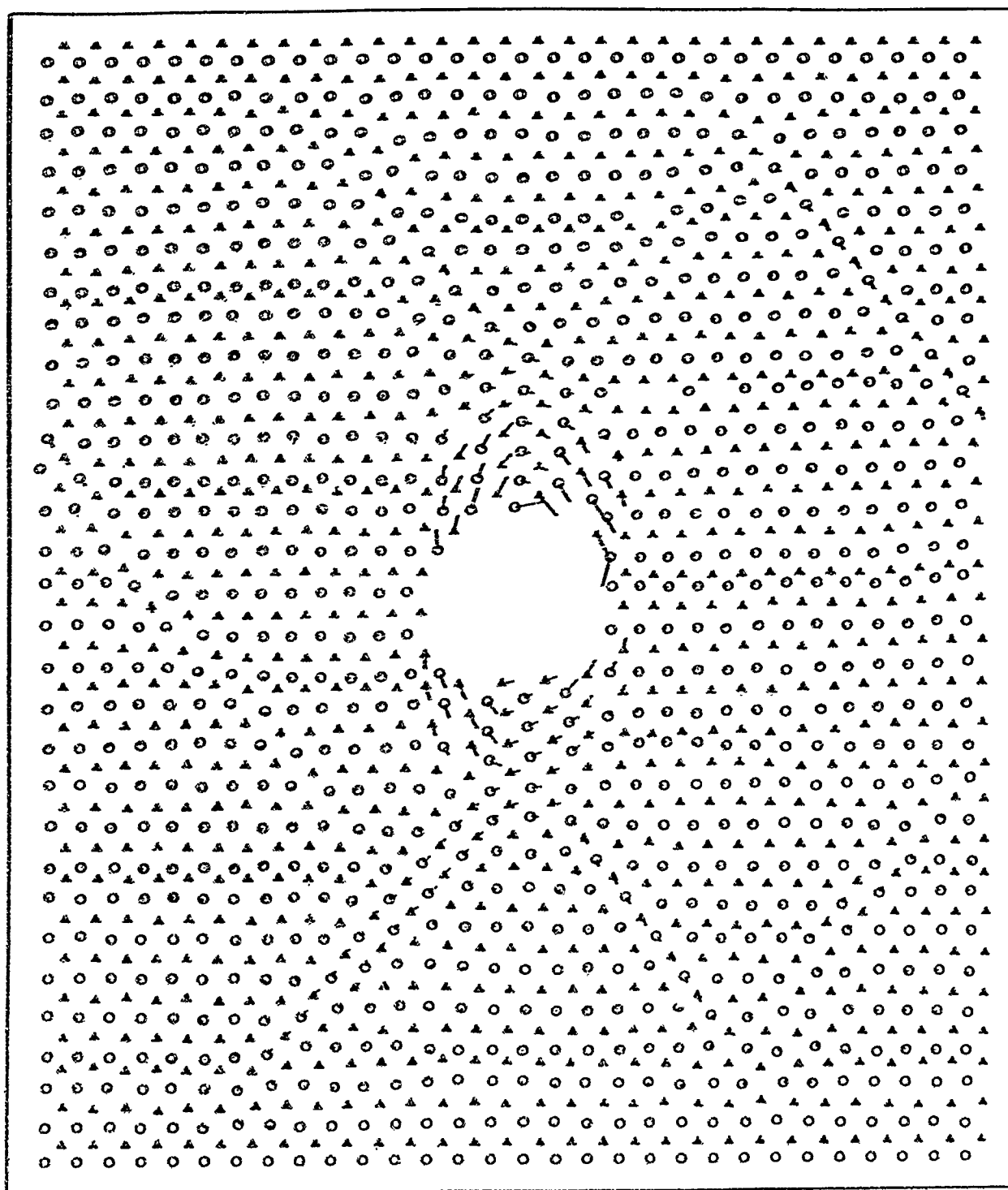


Figure 118. Slice through the Embedded Atom Method 9000 Atom Array at 300K After 2000 Steps, Showing the Strain Field. Ni atoms are marked by circles and Al atoms by triangles.

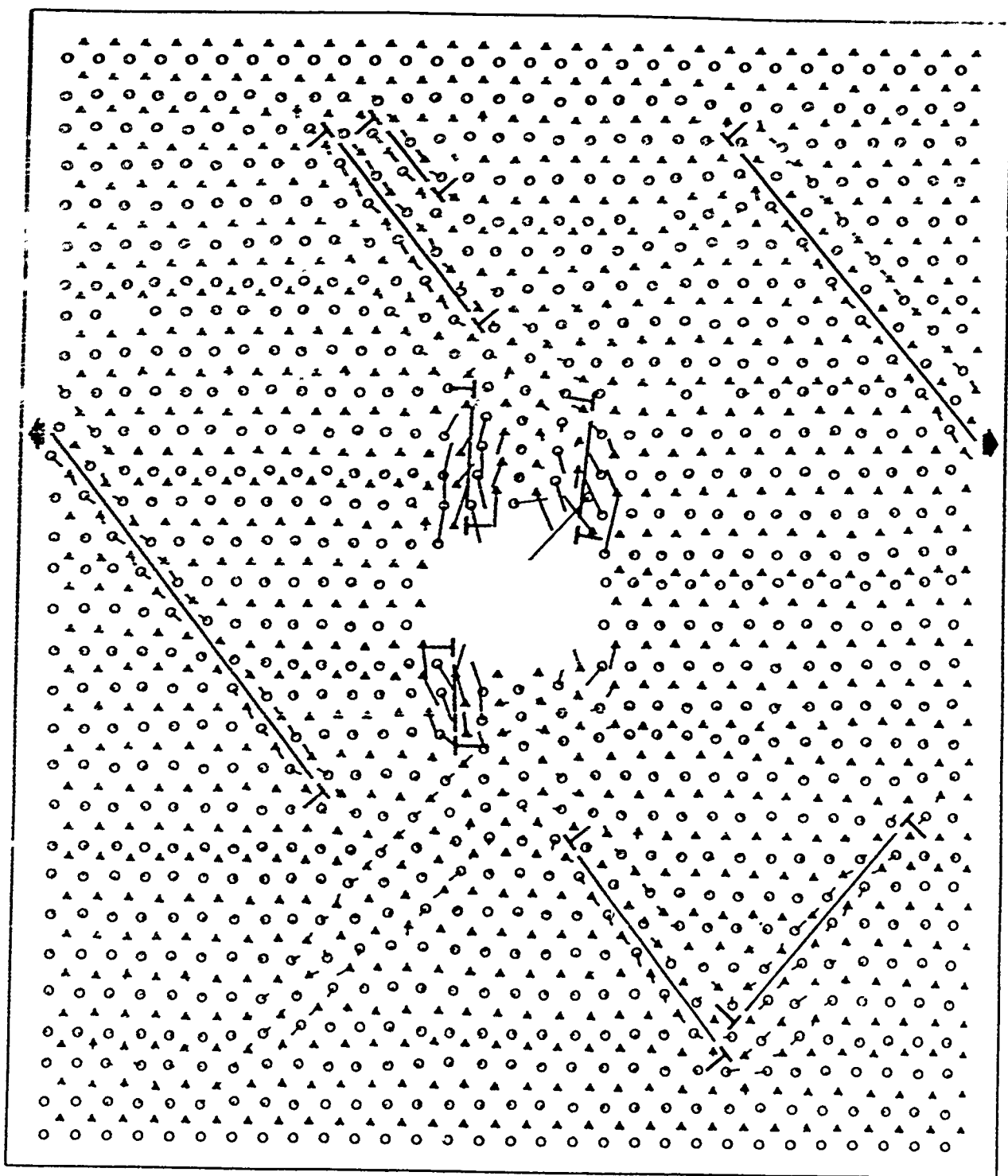


Figure 119. Slice through the Embedded Atom Method 9000 Atom Array at 300K After 2000 Steps, Showing the Strain Gradient Field and the Dislocation Loops Present in the Array. Ni atoms are marked by circles and Al atoms by triangles.

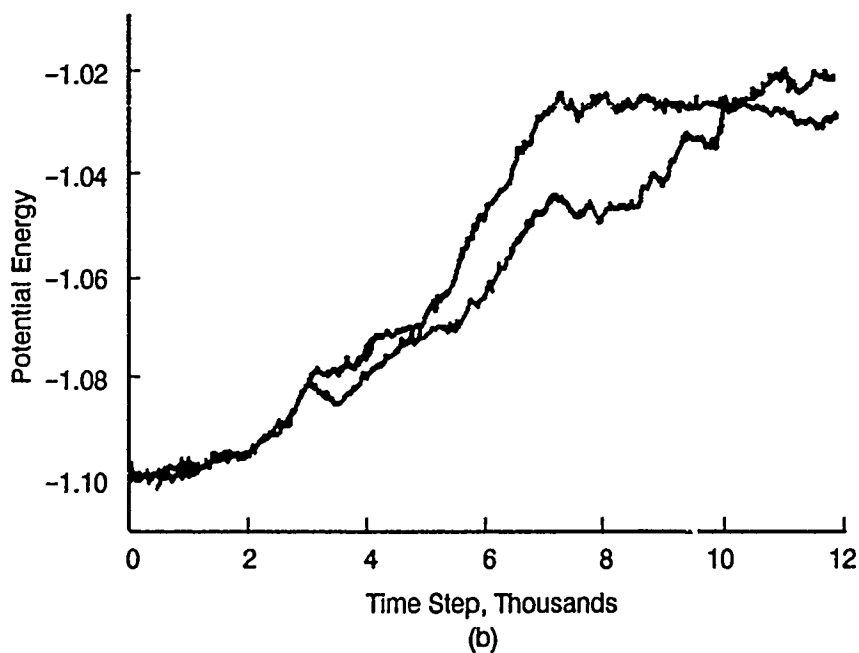
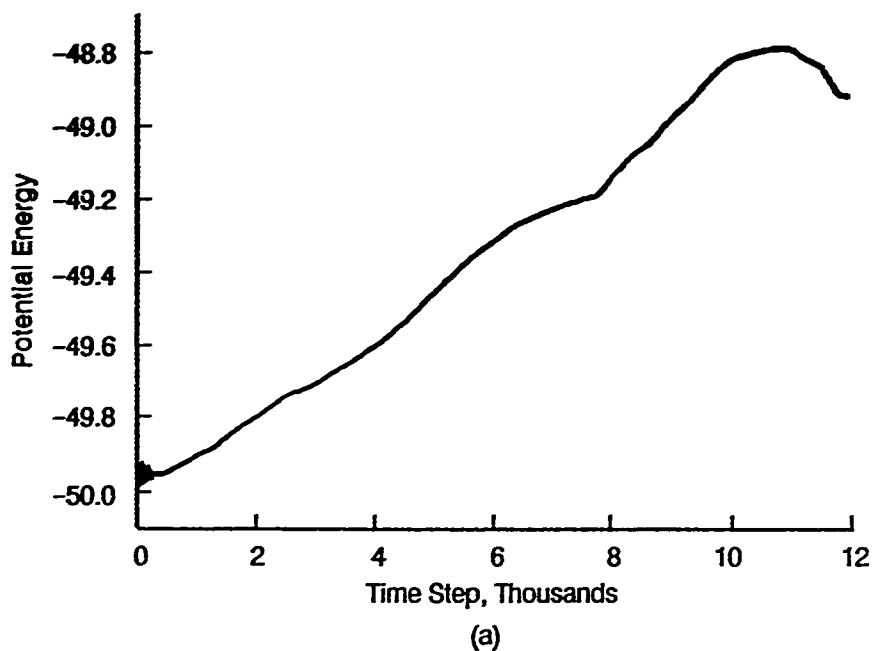


Figure 120. Potential Energy Versus Simulation Time Plot for a 9000 Atom Simulation, Recorded for: (a) the Total Simulation Array, and (b) a Few Hundred Atoms at Either Side of the Crack. The observed peaks have been seen to correspond fairly well with dislocation nucleation and/or bond breaking events.

*U.S. GOVERNMENT PRINTING OFFICE: 1991-548-076/44299 Region 5.